

**EVALUATION OF SURFACE-WAVE WAVEFORM MODELING
FOR LITHOSPHERE VELOCITY STRUCTURE**

Tao-Ming Chang, B.S., M. Prof. Geophys.

A Digest Presented to the Faculty of the Graduate School
of Saint Louis University in Partial Fulfillment of
the Requirements for the Degree of
Doctor of Philosophy

1997

DIGEST

Surface-waveform modeling methods will become standard tools for studying the lithosphere structures because they can place greater constraints on earth structure and because of interest in the three-dimensional earth. The purpose of this study is to begin to learn the applicabilities and limitations of these methods.

A surface-waveform inversion method is implemented using generalized seismological data functional theory. The method has been tested using synthetic and real seismic data and show that this method is well suited for teleseismic and regional seismograms. Like other linear inversion problems, this method also requires a good starting model.

To ease reliance on good starting models, a global search technique, the genetic algorithm, has been applied to surface waveform modeling. This method can rapidly find good models for explaining surface-wave waveform at regional distance. However, this implementation also reveals that criteria which are widely used in seismological studies are not good enough to indicate the goodness of waveform fit.

These two methods with the linear waveform inversion method, and traditional surface wave dispersion inversion method have been applied to a western Texas earthquake to test their abilities. The focal mechanism of the Texas event has been reestimated using a grid search for surface wave spectral amplitudes. A comparison of these four algorithms shows some interesting seismic evidences for lithosphere structure.

**EVALUATION OF SURFACE-WAVE WAVEFORM MODELING
FOR LITHOSPHERE VELOCITY STRUCTURE**

Tao-Ming Chang, B.S., M. Prof. Geophys.

A Dissertation Presented to the Faculty of the Graduate School
of Saint Louis University in Partial Fulfillment of
the Requirements for the Degree of
Doctor of Philosophy

1997

COMMITTEE IN CHARGE OF CANDIDACY :

Professor Robert B. Herrmann,
Chairperson and Advisor

Professor Brian J. Mitchell

Assistant Professor Charles J. Ammon

ACKNOWLEDGEMENTS

I would like to thank my advisor, Dr. Robert B. Herrmann, for his constant advice and guidance throughout this study.

I like to express my appreciation to Dr. Robert B. Herrmann, Dr. Chien-Ying Wang, and Dr. David R. Russell since their previous works forms a solid foundation for this study. I would also like to thank Dr. Jiakang Xie for his advice during his stay in Saint Louis University. I acknowledge the importance of Dr. Tzay-Chyn Shin and Dr. Chien-Ying Wang for leading me into the field of geophysics.

Finally, I express my gratitude to my family for their support.

The comments and reviews by Dr. Brian J. Mitchell, and Dr. Charles J. Ammon are greatly appreciated.

TABLE OF CONTENTS

CHAPTER 1 INTRODUCTION	1
1.1 The Problem	1
1.2 Review of Related Literature	2
1.2.1 Development of Global Seismology	3
1.2.2 Development of Exploration Seismology	5
1.2.3 The Possible Future Direction of Seismology	7
1.2.4 Emphasis of This Study	9
CHAPTER 2 THE WEST-TEXAS EARTHQUAKE OF APRIL 14 1995	12
CHAPTER 3 REVIEW OF GSDF THEORY AND FORMULATION OF THE INVERSION ALGORITHM USING GSDF	28
3.1 Introduction	28
3.2 Theory of Generalized Seismological Data Functionals	29
3.3 Structure Inversion	37
3.4 Forming Inversion Kernel	48
3.5 Synthetic Test	52
3.6 Real Data Test	52
3.7 Inversion Procedure	56
3.8 Inversion Results	60
3.9 Conclusion	65
CHAPTER 4 GENETIC ALGORITHMS	73
4.1 Workflow of Simulated Annealing Method	76
4.2 Workflow of the Genetic Algorithm	77
4.3 Smoothing Mechanism	78
4.4 Generation Number and Population Size	79
4.5 Criteria of Goodness-of-Fit	81
4.6 Test on the Western Texas Earthquake	83
4.7 Test for Teleseismic Traces	89
4.8 Discussion	101
CHAPTER 5 COMPARISON OF TECHNIQUES	111
5.1 Genetic Algorithms	111
5.2 Inversion of Dispersion Data	112
5.3 Linear Waveform Inversion	124

5.4	GSDF Inversion	125
5.5	How to Judge the Waveform Fit	126
5.6	Discussion	157
CHAPTER 6 DISCUSSION AND CONCLUSION		160
BIBLIOGRAPHY		163
VITA AUCTORIS		170

LIST OF TABLES

2.1	The station informations	13
2.2	Source parameters for different solutions	16

LIST OF FIGURES

2.1	Station distribution map. The stations are shown as triangles. The focal mechanism used in this study is shown as the beach ball. This map is generated using GMT (Wessel and Smith, 1991)	15
2.2	For teleseismic records, a general 9 seconds travel time difference for sP - P is observable.	17
2.3	Compare the observed teleseismic P seismogram at DAWY with synthetics, the preferred source depth is 20 km. The synthetics are generated using CUS model for different depths; 13, 15, 17, 19, 21, 23, and 25 km. The used focal mechanism is the reestimated one in this study.	18
2.4	The Love wave radiation patterns for the preferred focal mechanism at 20 km depth. The bars indicate attenuation corrected spectral amplitudes in cm-sec normalized for geometrical spreading to 1000 km.	19
2.5	The Love wave radiation patterns for Harvard CMT solution at 15 km depth.	20
2.6	The Love wave radiation patterns for Sipkin's USGS solution at 13 km depth.	21
2.7	The Rayleigh wave radiation patterns for the preferred focal mechanism at 20 km depth.	22
2.8	The Rayleigh wave radiation patterns for Harvard CMT solution at 15 km depth.	23
2.9	The Rayleigh wave radiation patterns for Sipkin's USGS solution at 13 km depth.	24
2.10	This figure shows the observed P-wave polarities and the reestimated focal mechanism which will be used for testing several surface-waveform modeling algorithms.	25
2.11	This figure shows the focal mechanism of Harvard CMT solution and the observed P-wave polarities.	26
2.12	This figure shows the focal mechanism of Sipkin's USGS solution and the observed P-wave polarities.	27

3.1a	This is an example showing how unexpected signal interference affects the extracting procedure in GSDF theory. There are five traces presented to show the different processing stages. The top two traces are the prefiltered isolation filter and observed seismogram, respectively. The third trace shows the Gaussian filtered cross-correlation at a target period of 20.0 seconds. The five extracted parameters are shown. The dashed curve inside the envelope is from the synthetics and the solid curve is from the observed data. The fourth trace is the windowed cross-correlogram from the third trace. The bottom trace is the filtered windowed cross-correlogram and its five Gaussian wavelet parameters which are to be used in further processing. Due to improper rotation, the Love wave appears on radial component before the Rayleigh wave arrival. The Love wave wavetrain may causes error (a) wrong determination of Gaussian wavelet parameters, and	50
3.1b	(cont'd). (b) Misalignment of signals which produces significant bias phase and group delay. This arises because a period of 25 seconds is considered compared to 20 seconds in Fig. 3.1a.	51
3.2	The starting model (dashed line) used in synthetic test of the GSDF inversion algorithm and the 'true' model (solid line) used to create the 'observed data'.	53
3.3	The velocity time histories of 'observed seismograms' (solid line) and the those from the starting model (dashed line) are both filtered in the frequency band 0.01-0.05 Hz by using a Butterworth filter with four poles. The plotted seismograms are normalized according the maximum amplitude of each component in the current frequency band. It is clear that the starting model is not close to the 'true' model and this may test the ability of the inversion programs to resolve structure.	54
3.4	After 12 iterations, the final inversion result shows a predicted waveforms that closely agree with 'observed seismograms'.	55
3.5	The comparison between the final model and the 'true model'. We can see that the 2-layer crust is very close to the 'true' model, but that in the upper mantle the model fluctuates around the 'true model'.	56

3.6	The result of inversion using the second procedure. This inversion procedure first obtains the S wave velocity from the Love wave and then inverts for the P wave velocity from Rayleigh wave by assuming no anisotropy effect. This shows a acceptable waveform match in phase, but not in envelope.	58
3.7	The model inverted by the second inversion procedure.	59
3.8a	Waveform fit of the final inverted model for ALE in the frequency band of 0.005-0.03 Hz. The signal which arrives at 1020 seconds and around 1300 seconds are the S and SS phases, respectively. From the S phase waveform, we can say that the source time function used in this inversion is a little short but is close enough.	61
3.8b	(Cont'd). Waveform fit in the 0.005-0.05 Hz frequency band.	62
3.9	The inverted models for ALE. Two models (PSV and SH) were obtained from the Love wave and Rayleigh Wave. Comparing these two models, there is one slight anisotropic zone above 200 km.	63
3.10	The final inverted model for FCC. There is 4.5% anisotropy effect exists between 70 and 140 km.	64
3.11a	The waveform fit for the final model for FCC is shown at three frequency bands : (a) 0.01-0.03 (b) 0.01-0.05 (c) 0.01-0.1 Hz. The SS phase arrives at 660 seconds. The inverted model can fit fundamental mode Love wave and Rayleigh wave waveforms as high as 0.1 Hz, but it lacks the ability to simulate the high frequency higher modes.	66
3.11b	(Cont'd). (b) 0.01-0.05 Hz.	67
3.11c	(Cont'd). (c) 0.01-0.1 Hz. The SS phase arrives at 660 seconds. The inverted model can fit fundamental mode Love wave and Rayleigh wave waveforms as high as 0.1 Hz, but it lacks the ability to simulate the higher modes.	68
3.12	The inverted models for PAS. There are no clear anisotropy effects. The crustal Q is very low.	69

3.13a	Waveform fitting is shown on three frequency bands: (a) 0.01-0.03 (b) 0.01-0.05 and (c) 0.01-0.1 Hz. The S wave signal arrives at 350 seconds.	70
3.13b	(Cont'd). (b) 0.01-0.05 Hz.	71
3.13c	(Cont'd). (c) 0.01-0.1 Hz.	72
4.1	In GA, models are randomly generated, so there always will be some 'ZIG-ZAG' patterns. To obtaining a smooth background velocity model, a smoothing mechanism is introduced. Without changing the vertical shear wave travel time, the smoothed model (dashed line) has less 'ZIG-ZAG' pattern than the original model (solid line).	80
4.2	To know how many generations is necessary for surface-waveform modeling, an experiment with large generation number (500) is tested. The result shows that GA can find a fairly good model within 50 generations. After that, the model improvement is less rapidly.	82
4.3a	Using GA to model the surface-waveform of station ANMO. In this test, separate GA runs were conducted for Love and Rayleigh wave respectively. The searched models are shown in these figures, the heavy lines are the search bounds, the thin lines are models which have goodness-of-fit greater than a certain value shown at the left bottom, and the best model is plotted as thick black line. (a) Models for Love wave.	85
4.3b	(cont'd). (b) Models for Rayleigh wave.	86
4.4	For ANMO, the observed waveforms (solid line) and predicted waveforms (dashed line) which generated for the best searched models for Love and Rayleigh wave at frequency range 0.01 to 0.1 Hz.	87
4.5	For ANMO, the filtered cross-correlations of observed and synthetic waveforms at different frequency bands. The number at the right of cross-correlation traces is the cross-correlation value at zero-lag which is used to construct the value of goodness-of-fit.	88
4.6a	Separate GA search results for Love and Rayleigh wave recorded at TUC. (a) Love-wave model.	90

4.6b	(cont'd). (b) Rayleigh-wave model.	91
4.7	A joint GA search using both Love and Rayleigh waveforms at TUC.	92
4.8a	For TUC, filtered waveforms at frequency range 0.01 to 0.1 Hz for observed and predicted seismograms. (a) The predicted seismograms were generated using the best models from individual searches for Love and Rayleigh wave (Figures 4.6ab).	93
4.8b	(cont'd). (b) The predicted seismograms were generated using the best model from a joint searches for both Love and Rayleigh wave (Figure 4.7).	94
4.9a	For TUC, the cross-correlations for the observed and synthetic seismograms which were generated using GA searched models. (a) The synthetics were computed using the best models from the separate search models for Love and Rayleigh wave (Figures 4.6ab).	95
4.9b	(cont'd). (b) The synthetics were computed using the best model from a joint search for both Love and Rayleigh wave (Figure 4.7).	96
4.10	The models from GA search for Rayleigh wave recorded at WMOK.	98
4.11	The waveform comparison of observed and synthetic seismograms for WMOK (Figure 4.10).	99
4.12	The cross-correlation of the best GA searched model for WMOK (Figure 4.10).	100
4.13	The waveform fit of the best GA searched model for HRV.	102
4.14	The GA searched models for HRV.	103
4.15	The waveform fit of the best GA searched model for FRB.	104
4.16	The GA search models for FRB.	105
4.17	The waveform fit of the best GA searched model for LMN.	106
4.18	The GA search models for LMN.	107

4.19	The waveform fit for INK. INK is located in the most northwest of Canada. From the Rayleigh wave trace, we can see the wavetrain due to the multipathing effect arrives after the 1600 seconds. The currently used criteria of goodness-of-fit can not properly represent the crustal wave and may cause an overly extended synthetic trace.	108
4.20	The GA search models for INK. The unreasonable low crustal velocity value is due to the criteria of goodness-of-fit which can not properly represent the crust wave.	109
5.1	First stage 4-layers GA search result.	113
5.2	The waveform fit for the best model in first step GA search.	114
5.3	Second stage GA search results.	115
5.4	The waveform fit of the best model in second step GA search.	116
5.5	The extracted surface wave dispersion data using multiple filtering techniques. The top plot shows the spectrum amplitudes at different periods. The bottom plot shows the group velocity dispersion curve.	118
5.6	This figure shows the extracted traces using the phase match filter technique. The top trace is the vertical component displacement seismogram of CCM. The second trace is extracted fundamental mode. The third trace is the extracted first higher mode. The bottom trace is the residual.	119
5.7	The comparison of observed phase (circle), group velocities (triangle), and predicted (line) from inversion for the fundamental and first higher mode Rayleigh-wave.	120
5.8	The inversion model.	121
5.9a	The waveform fit of observed and predicted seismograms. The model is shown as figure 5.8. (a) Displayed at frequency range 0.01-0.1 Hz.	122
5.9b	(Cont'd) (b) The waveform fit for the frequency range 0.01-0.5 Hz.	123

5.10	The waveform comparison of observed, synthetic, and the residual seismograms at two different frequency bands. The top panel which corresponds to apparent velocities of 3.3-2.5 km/sec is plotted at 0.02-0.05 Hz. The bottom panel is for a 4.5-2.5 km/sec window and a 0.02-0.1 Hz frequency band.	126
5.11a	The waveform fit for the model obtained from GSDF inversion. Three different frequency ranges are shown: (a) for 0.01-0.05 Hz.	127
5.11b	(Cont'd) (b) for 0.01-0.1 Hz.	128
5.11c	(Cont'd) (c) for 0.01-0.5 Hz.	129
5.12	The partial derivatives of first higher mode at 10 seconds which computed for the GSDF inversion.	132
5.13a	Waveform fit for the model which increasing the upper mantle Q. Three different frequency ranges are displayed: (a) 0.01-0.05 Hz.	133
5.13b	(Cont'd) (b) 0.01-0.1 Hz.	134
5.13c	(Cont'd) (c) 0.01-0.5 Hz.	135
5.14	This figure shows a better model which based on GSDF inversion result, and using trial and error to do the fine tuning.	136
5.15a	The waveform fit of the model shown as figure 5.14. Three frequency ranges are displayed: (a) 0.01-0.05 Hz.	137
5.15b	(Cont'd) (b) 0.01-0.1 Hz.	138
5.15c	(Cont'd) (c) 0.01-0.5 Hz.	139
5.16	The observed, synthetic, and seven single-mode seismograms.	140
5.17	This figure shows a better model which based on linear waveform inversion result, and using trial and error to do the fine tuning.	141

5.18a	The waveform fit of the fine-tuning model shown at figure 5.17. Three different frequency ranges are shown: (a) 0.01-0.05 Hz.	143
5.18b	(Cont'd) (b) 0.01-0.1 Hz.	144
5.18c	(Cont'd) (c) 0.01-0.5 Hz.	145
5.19	The P_{nl} waveform fit which computed using locked mode approximation for the fine-tuning model shown at figure 5.17.	146
5.20	The observed, synthetic, and seven single-mode seismograms were shown here.	147
5.21	The resolving kernel for the model shown on figure 5.18.	148
5.22	The measurements of four GSDF functionals for the model shown on figure 5.18.	149
5.23	The group velocity dispersion curve and spectrum amplitudes for station CBKS.	151
5.24	The waveform fit for station CBKS at frequency band 0.01-0.5 Hz.	152
5.25	The fine-tuning model for station CBKS which is based on the GSDF inversion result.	153
5.26	The group velocity dispersion curve and spectral amplitudes for station WMOK.	154
5.27	The waveform fit at 0.01-0.5 Hz of station WMOK for the model shown on figure 5.28.	155
5.28	The fine-tuning model for WMOK which based on GSDF inversion result.	156

CHAPTER 1

INTRODUCTION

1.1 The Problem

To verify seismological inferences about the Earth, matching observed seismograms is an ultimate challenge. Given past success in modeling long-period seismograms and routinely estimating earthquake mechanisms in the 80s, seismologists are now trying to model entire regional seismograms at the high frequencies. In this study, two different methods were used to model the surface-wave waveform. One of the proposed algorithms uses the gradient information from the hypersurface of the misfit function to find an optimal solution, and the second approach is based on a global search technique. The advantages and weaknesses of each algorithm were examined in terms of robustness. The ultimate purpose of this type of research is to quantify the limitations of one-dimensional earth models as an initial step in approximating 3-D structures.

1.2 Review of Related Literature

Since the birth of quantitative seismology, seismologists have shared the goal that one day we can use all geophysical knowledge to design an intelligent system which can routinely analyze all near real-time earthquake data, predict future earthquakes, and systematically update our knowledge about the Earth. To reach this goal, there are several important tasks to accomplish: collecting earthquake data, developing more sophisticated computational techniques, and finding a better way to interpret data systematically.

For the past half century, seismological research into Earth structure can be roughly divided into three scales: planetary (global seismology), regional (regional seismology; a few hundred kilometers), and small (exploration seismology; a few tens of kilometers). The seismology development for these three scales has not been uniform. Global and exploration seismology were developed more systematically than regional seismology. The reasons are differences in interests of science and industry, in data coverage, and in the available theoretical computational methods in each of the three types of studies. In this review, historical seismology developments will be briefly described, possible future developing directions will be outlined, and the emphasis of this study will be addressed.

1.2.1 Development of Global Seismology

Although earthquakes happen in the world everyday, the currently available data are very limited in both spatial and temporal distribution. Confined by the dataset, only the low-wavenumber (harmonic) global structural features can be estimated. In fact, even though research in global seismology has been boosted by specific scientific interests, global earth structures determined are not unique.

Global seismology developed systematically. For example, scientists inferred earth structure using free oscillations, surface waves, and body wave travel times, and reference models are well established (e.g. Dziewonski and Anderson 1981). Based on the reference models, routine analysis of seismic sources for large earthquakes became possible (Dziewonski, Chou, and Woodhouse, 1981; Dziewonski and Woodhouse, 1983; Sipkin, 1986). On the other hand, global heterogeneity (obtained using tomographic techniques) has been studied using different data such as phase and group velocities of long-period surface waves (Nakanishi and Anderson, 1983, 1984; Nataf, Nakanishi, and Anderson, 1986), long-period waveforms (Woodhouse and Dziewonski, 1984), P-velocities from teleseismic events (Dziewonski, 1984), and normal modes (Masters *et al.*, 1982). In these studies, the horizontal resolution is greater than 1000 km (Zhang and Tanimoto, 1992), and many significant features, such as mid-ocean ridges, require better resolution.

There are several ways to increase the resolving power of seismological techniques. The first way is to use more data. The number of global seismic stations is increasing, the earthquake dataset is also increasing steadily, but slowly. A few decades may be needed to resolve the details of Earth structure. Under such a limitation, seismologists have to find better ways to increase the usable data which means to effectively use the current data. One possibility is to use waveforms directly, another is to use shorter period data from smaller earthquakes. A difficulty associated with using waveforms is the availability of accurate source mechanisms of smaller regional earthquakes. A second way to increase resolution is to reduce some uncertainties caused by the inaccurate shallow structure. Mooney *et al.* (1996) obtained improvement of the resolving power in global structure when using an improved global crustal model for station corrections. The third way to increase resolution is to find new ways to interpret data. Two such experiments have been reported. One uses body wave travel-time residuals (Su and Dziewonski, 1992), the other uses differential travel times (Woodward and Masters, 1991). The typical horizontal resolving length for such experiments is 550 km (Su *et al.* 1992).

It is clear that the current effort in global seismology is directed toward increasing resolution. To achieve this, more knowledge is required about the regional structure. More complicated techniques to invert different types of data simultaneously must also be developed and proven.

1.2.2 Development of Exploration Seismology

The purpose of exploration seismology is to search for resources by obtaining a high-resolution image of subsurface geology. To do this, artificial sources and dense receiver coverage are necessary. This approach contrasts with most crustal- and mantle-scale studies which rely on natural earthquakes and sparse seismic stations. Huge exploration datasets enable seismologists to investigate the heterogeneity of shallow structure, even when only travel time data are used. In the early stages of exploration seismology, it was natural to use first arrival data (refraction signal) to infer layered structures. But the problem of non-uniqueness of solutions has pushed the joint use of both refraction and wide-angle reflection data. The use of both refraction and reflection data to invert 1-D (e.g. Braile, 1973), and 2-D structure (e.g. Zelt and Smith, 1992) are well reported.

However, as pointed out by many researchers (e.g. Huang *et al.* 1986), the precise identification of refraction and reflection signals (triplication) is crucial for the success of such inversion schemes. During data processing steps like picking phases, artifacts can be introduced. Sometimes it is worse when it is necessary to interpolate travel time data in order to avoid several problems associated with data sparseness. All these procedures introduce uncertainties and errors in inversion results. Another imperfection about this inversion algorithm is that it cannot retrieve shear velocity information. Even though signal enhancement techniques such as CDP stacking and migration

were developed in the oil industry, oil companies still need new techniques to improve the image of the subsurface structure. All these factors challenge seismologists to find a better way solving problems.

Waveform inversion seems to be a way to avoid introducing artificial effects and to use more information than travel times. Unfortunately, seismologists find it very difficult to directly invert wide-band seismic waveforms, and a two-step approach is often used (Nowack and Braile, 1993). Therefore in exploration seismology, there are two problems regarding waveform inversion: the first is how to retrieve the background velocity (to match the low-frequency part waveform), and the other is how to match the entire waveform once the background velocity is available. Much research is reported on fitting the entire waveform when a good starting model is available (e.g. Mora, 1987; Pan and Phinney, 1989; and Crase *et al.* 1990). Although the assumption of availability of a good starting model seems suitable because of standard velocity analysis procedures widely-used in the oil industry, there has been little progress in retrieving background velocities using waveform inversion techniques because of its fully nonlinear character.

Recently, two good experiments in retrieving background velocity were performed by Koren *et al.* (1991) and Bunks *et al.* (1995). Koren *et al.* (1991) sought an acceptable velocity model using a Simulated Annealing algorithm. In their experiment, they encountered local minima on the hypersurface of the misfit function caused by a cycle-skipping effect, but were able to compute *a posteriori* probability density. As outlined previously, seismologists know, from experience, it is

not a simple task to match the entire waveform. It seems that at least a two-step approach is needed. Based on this idea, Bunks *et al.* (1995) try to use different low-pass filtered waveform in inversion. They first inverted for a simple 1-D model from the low-frequency signal (0-7 Hz), then inverted for a gross 2-D model using middle-frequency waveforms (0-10 Hz), and finally obtained a detailed structure from inverting high-frequency waveforms (0-15 Hz). The results of the Monte Carlo search and multiscale inversion are encouraging. These experiments show we can obtain good resolution when adequate data are available. As commented by Nowack and Braile (1993), the current goal of wavefield inversion in exploration seismology is to find a best inversion procedure.

1.2.3 The Possible Future Direction of Seismology

We can see that global seismology is currently trying to improve the resolution of tomographic image of the Earth and to estimate focal mechanisms of smaller events by extending Harvard CMT method (Ekstrom, 1996). In exploration seismology, high resolution images of subsurface structure can be obtained, but only for shallow depths. So there is an existing gap between the two scales. Since both global seismology and exploration seismology are well developed, we believe that future attention will focus on systematically studying regional structures.

Theoretically, we should directly model waveforms for 3-D structures, but practically, it is impossible because of our current limited knowledge about the complicated structures and our sparse data coverage. So far, there is no report on successful modeling waveform for 3-D, even 2-D structure. Attempts, such as that of Vidale and Helmburger (1992), for matching the complicated waveforms using 2-D finite-difference method have been unsuccessful. Due to present limited computing ability of seismograms for realistic earth models, two directions should be considered for separated source inversion and structure inversion regarding extracting more information in a simplified 1-D model. The first is inversion using broadband waveform data; the second is inversion using as many different types of data as possible. The reason for this is that while broadband waveform data place better constraints than any single data type, additional constraints can be obtained from other data such as $pP - P$ providing constraints on source depth. Once seismologists develop all these tools, the final stage is to build a system which will automatically locate earthquakes, analyze source mechanisms, and indicate "anomalous" earthquakes for further study. All of these will greatly contribute to other branches of geoscience researches such as delineating the tectonic processes, and even monitoring the failure stress change in a fault system (Stein *et al.* 1992). In the meantime, seismologists should continuously develop forward and inverse algorithms for 2-D and 3-D structures, and a further experiment regarding the iterative source and structure inversion could be tested.

Recently, there has been much research in focal mechanism analysis using regional broadband waveform. This work using different subsets of data such as surface-waves (Thio and Kanamori, 1995), body-wave waveforms (Dreger and Helmberger, 1993), full waveforms (Mao, Panza, and Suhadolc, 1994), and even one single station (Fan and Wallace, 1991). Zhou *et al.* (1994) and Zhu *et al.* (1996) showed one interesting method which uses both high-frequency body-wave waveform and low-frequency full waveform in searching for the best focal mechanism. In this study, we will concentrate on the regional structure inversion problem since earth structure is fundamental to source parameter estimation.

1.2.4 Emphasis of This Study

To model regional broadband waveforms, there are two different approaches. The first approach is to match different phases of body-wave such as P_{nl} and S_{nl} . Zhao and Helmberger (1991) proposed one strategy to model waveforms. First, they model long-period data (P_n and S_n) assuming a single crustal layer model and get the average crustal and upper mantle P , S velocities, and crustal thickness. Next, they model the fundamental mode Rayleigh wave by adding some layers in the crust to the previous simple model. Third, they model those short-period waveforms riding on P_n and S_n by adding some layers in upper mantle structure. Finally, they adjust their model by trial and error. This strategy utilizes many body-wave phases with clear

physical meanings, but it requires an experienced seismologist. The second approach requires matching the surface-wave waveform. One example for this approach is the linear inversion method developed by Gomberg and Masters (1988). They use modal superposition to create synthetic seismograms and perturb them with respect to layer parameters (such as S -velocity). Using these partial derivatives, they formulate a linear inverse problem for the differential seismogram between observed and synthetic ground motions. In this study, we will develop other inversion methods for surface-wave waveforms because this approach has the potential to be a fully automatic process. In most regions, sparse data coverage does not support directly modeling waveforms for 2-D, or 3-D structures. Therefore, the synthetic seismograms used in this study will be generated for a 1-D model using the mode summation method (Wang, 1981).

Using a cross-correlation technique, Lerner-Lam and Jordan (1983) formulated an inversion algorithm to obtain earth structure from long-period teleseismic surface-wave waveforms. A successful application was presented by the same group (Lerner-Lam and Jordan 1987) on investigating the continental thickness of Eurasia. Using a similar idea, Cara and Leveque (1987) showed a slightly different way to extract the "secondary observations" and formulated an algorithm to invert them. They used teleseismic seismograms which have well-separated fundamental and higher modes to ensure their success. However, regional seismograms show more complicated mode interference effects and their approach becomes difficult.

Gee and Jordan (1992) introduced Generalized Seismological Data Functionals theory (GSDF) to deal with surface-wave modal interference effects. In this study, an algorithm based on the GSDF theory is proposed and will be tested using an earthquake that occurred in west Texas and was well recorded throughout North America. The comparison between the GSDF method and linear inversion (Gomberg and Masters 1988) will also be addressed.

Using linearized inversion, a good starting model is necessary to guarantee the success of final convergence. It is necessary to use a global search method to ease the dependence on *a priori* information. A second algorithm is also considered. To use Genetic Algorithms (GA) in searching models which produce good surface-wave waveform fits. Hopefully, these two algorithms will provide more insight in how to build a more intelligent and robust inversion algorithm.

CHAPTER 2

THE WEST-TEXAS EARTHQUAKE OF APRIL 14 1995

In this study, the different algorithms will be tested using data from the April 14, 1995 western Texas earthquake. This earthquake was well recorded by broadband seismometers throughout North America. The observations were collected from IRIS (Incorporated Research Institutions for Seismology), CNSN (Canadian National Seismological Network), USGS (United States Geological Survey), UNAM, and PASSCAL experiments. The station distribution is shown in Figure 2.1. For each station, Table 2.1 lists its location, its azimuth from the epicenter, its hypocenter distance from the event, the polarity of P wave first arrival, takeoff angle, and whether or not the dispersion data used in searching Rayleigh or Love wave radiation pattern are shown in Table 2.1.

Using these data, the different algorithms for modeling surface-waveforms will be tested. Before this stage, the source parameters will be reestimated, i.e. source depth and focal mechanism. Table 2.2 lists three different source parameters which include Harvard CMT solution, USGS Sipkin's solution, and the reestimated source parameters used in this study.

Table 2.1 The station informations

Station	Longitude (°)	Latitude (°)	Azimuth (°)	Distance (km)	P	R	L	IH-P (°)
ALE	-62.35	82.50	6.1	6036.3	-1	0	0	29.0
ANMO	-106.46	34.95	331.3	596.8	-3	1	1	69.0
ARC	-124.08	40.88	307.8	2210.4	0	1	0	46.8
BAR	-116.67	32.68	285.4	1295.3	0	0	1	63.7
BBB	-128.11	52.18	327.3	3169.0	0	1	1	36.5
BINY	-75.99	42.20	54.0	2774.7	0	1	1	39.3
BKS	-122.24	37.88	301.0	1934.1	-3	1	0	56.3
BMN	-117.22	40.43	315.6	1689.8	-1	1	1	59.4
CAIG	-100.27	17.05	167.3	1496.1	0	1	1	60.9
CALB	-118.63	34.14	290.1	1503.7	-5	1	0	60.8
CBKS	-99.74	38.81	18.2	1004.2	0	1	0	67.2
CCM	-91.24	38.06	48.9	1408.2	0	1	1	61.9
CEH	-79.09	35.89	68.1	2340.5	-3	0	0	43.1
CMB	-120.39	38.04	303.3	1789.9	-1	1	1	58.9
COL	-147.79	64.90	334.6	4911.3	-1	0	0	32.3
COR	-123.30	45.59	317.7	2365.9	0	1	1	41.4
CUIG	-99.18	19.33	160.0	1281.2	0	1	1	63.9
CYF	-109.87	37.55	325.0	1009.4	-1	1	1	67.2
DAWY	-139.43	64.05	336.6	4525.6	0	0	0	33.2
DGR	-117.01	33.65	289.7	1345.7	3	1	1	62.8
DLBC	-130.03	58.44	334.7	3733.1	0	1	1	35.1
DRLN	-57.50	49.26	47.9	4368.4	0	0	0	33.5
DUG	-112.81	40.20	324.6	1398.3	0	1	1	62.0
EDM	-113.35	53.22	345.1	2677.0	-1	1	1	39.7
EYMN	-91.50	47.95	23.9	2208.2	-1	1	1	46.9
FCC	-94.09	58.76	9.9	3244.3	-1	1	1	36.1
FFC	-101.98	54.74	1.9	2719.7	-1	0	0	39.5
FRB	-68.55	63.75	23.2	4453.6	-1	0	0	33.3
GAC	-75.48	45.70	46.9	2962.4	0	1	0	38.1
GAR	-114.10	38.88	317.0	1373.5	-1	1	1	62.4
GOL	-105.37	39.70	350.5	1063.6	-5	0	0	66.8
GSC	-116.81	35.30	297.4	1397.6	0	1	1	62.3
HOPS	-123.07	38.99	303.5	2047.2	0	0	0	53.0
HRV	-71.56	42.51	55.5	3133.0	0	1	1	36.7
INK	-133.52	68.31	343.8	4663.0	-1	0	0	32.9
ISA	-118.47	35.66	296.9	1535.4	0	0	0	60.5
JFWS	-90.25	42.91	36.1	1823.4	0	1	1	58.4
JRSC	-122.24	37.40	299.4	1916.7	0	0	0	56.7
LBNH	-71.93	44.24	51.9	3160.7	0	1	1	36.6
LMN	-64.81	45.85	51.6	3749.1	0	1	1	35.0
LMP	-111.20	37.98	321.8	1121.5	-1	1	1	66.2
LMQ	-70.33	47.55	46.4	3406.2	0	1	1	35.8
LSCT	-73.22	41.68	56.6	2975.7	0	1	1	38.0
MBC	-119.36	76.24	354.8	5187.3	0	0	0	31.6
MDW	-112.36	38.89	321.6	1264.8	-3	1	1	64.2
MHC	-121.64	37.34	299.8	1864.7	-1	0	0	57.8
MIAR	-93.57	34.55	60.1	1032.6	5	1	0	67.0
MIN	-121.61	40.35	309.0	1997.4	-1	1	0	54.6
MLAC	-118.83	37.63	303.9	1647.0	-3	1	1	59.6
MLC	-116.77	38.99	311.8	1564.3	-1	1	1	60.2
MNV	-118.15	38.43	307.6	1634.5	-1	0	0	59.7
NEE	-114.60	34.82	298.5	1172.2	0	1	1	65.6

NEW	-117.12	48.26	333.4	2318.1	-1	1	1	43.6
NWC	-113.56	37.63	313.6	1248.7	0	0	0	64.5
ORV	-121.50	39.56	306.8	1949.1	-1	1	1	55.9
OXIG	-96.72	17.08	153.8	1606.6	0	0	0	59.9
PAS	-118.17	34.15	191.0	1462.9	0	1	1	61.2
PFO	-116.46	33.61	290.0	1294.6	0	0	0	63.7
PGC	-123.45	48.65	325.8	2660.3	0	1	1	39.8
PH2	-114.98	37.66	310.5	1352.8	-3	1	1	62.7
PKD1	-120.42	35.89	295.9	1711.2	-1	1	0	59.3
PLIG	-99.50	18.39	162.8	1370.8	1	1	1	62.4
PMB	-123.08	50.52	329.4	2786.9	-1	1	1	39.2
PNIG	-98.13	16.40	159.8	1624.5	0	1	1	59.8
PNT	-119.62	49.32	331.6	2522.8	0	1	0	40.3
RCC	-110.59	40.52	331.9	1313.9	-1	1	1	63.3
RES	-94.90	74.69	317.4	4965.5	-1	0	0	32.2
RPV	-118.40	33.74	289.1	1474.4	-3	1	1	61.1
RTS	-115.79	39.67	316.0	1541.4	-3	1	0	60.4
SADO	-79.14	44.77	46.0	2659.2	-1	1	1	39.8
SAO	-121.45	36.77	298.0	1827.5	-3	0	0	58.4
SCHQ	-66.83	54.83	36.1	3975.3	-3	1	1	34.1
SMTC	-115.72	32.95	287.4	1212.4	0	1	0	65.0
SRS	-110.60	38.91	327.2	1168.0	-1	1	1	65.6
SSPA	-77.89	40.64	56.4	2567.4	-1	0	0	40.0
TUC	-110.78	32.31	289.6	745.3	-2	1	1	67.9
ULM	-95.88	50.25	13.6	2305.5	-2	1	1	43.9
USC	-118.29	34.02	290.3	1470.1	0	1	1	61.1
VTV	-117.33	34.57	293.6	1399.8	0	1	0	62.0
WALA	-113.91	49.06	339.7	2271.0	-1	1	1	44.9
WCP	-114.17	40.52	322.2	1503.0	-1	1	1	60.8
WDC	-122.54	40.58	308.6	2079.7	-3	1	1	51.9
WHY	-134.99	60.67	334.6	4102.5	-1	1	1	33.9
WMOK	-98.78	34.74	39.5	655.1	3	1	0	68.4
WMT	-111.84	40.11	327.0	1338.3	0	1	1	62.9
WVOR	-118.64	42.44	318.8	1921.1	-1	0	0	56.6
YBH	-122.72	41.73	311.5	2154.3	0	1	1	49.0
YKW3	-114.61	62.56	350.5	3681.7	-1	1	0	35.3
ZIIG	-101.47	17.61	171.9	1414.2	0	0	0	61.8

Comparing USGS and Harvard CMT solutions, they both have good agreement in hypocenter location and origin time. However, the focal mechanism is different for the two solutions. From experiences, the published source depths for shallow events usually have huge uncertainty. Therefore, we simply use USGS's hypocenter location and origin time and will reestimate the focal mechanism and depth.

From stations which have source-receiver distances greater than 3600 km, it is very common to see a 9 second time difference between P and sP phases (Figure 2.2). At such distance, the observed first

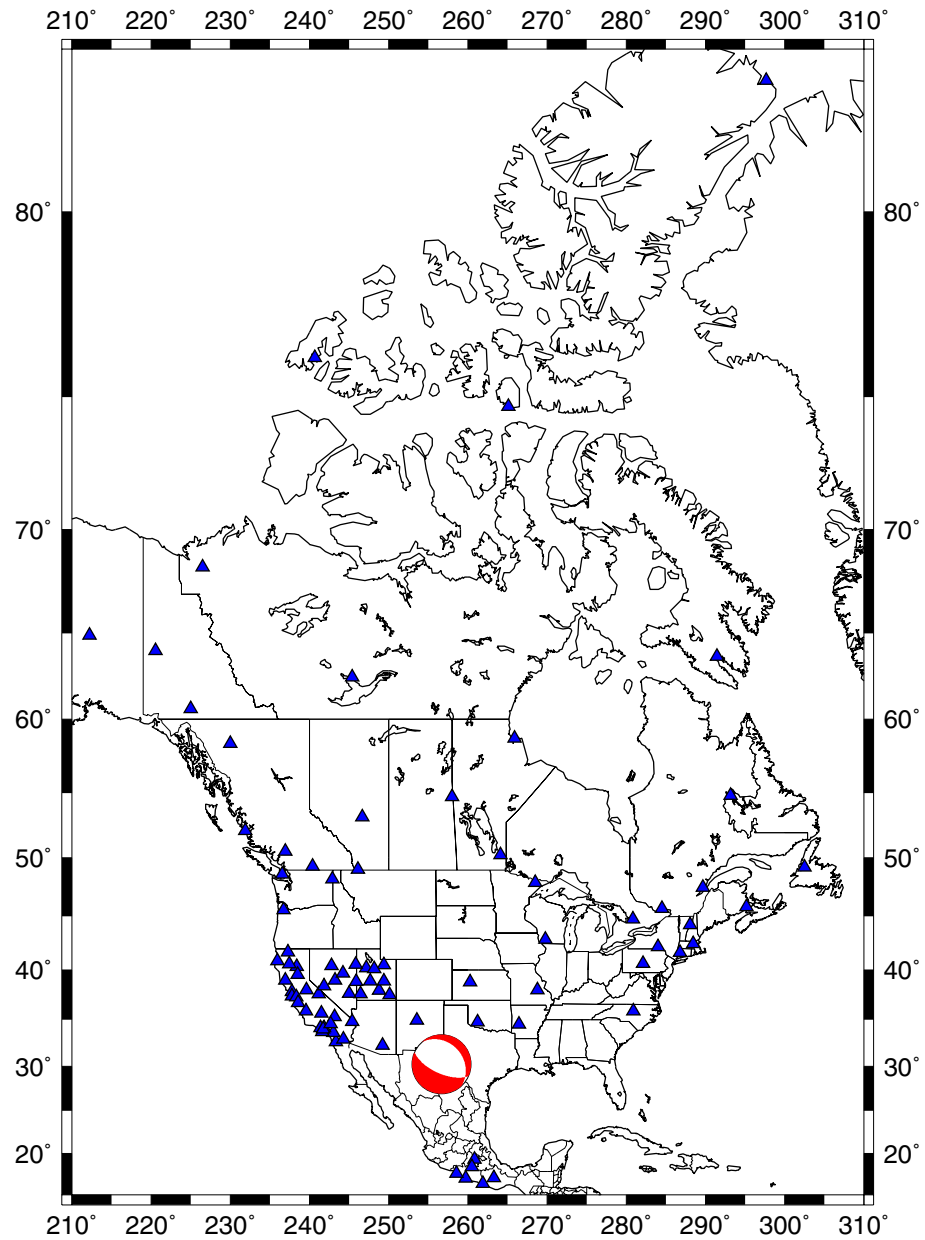


Fig. 2.1. Station distribution map. The stations are shown as triangles. The focal mechanism used in this study is shown as the beach ball. This map is generated using GMT (Wessel and Smith, 1991)

Table 2.2 Source parameters for different solutions

	Longitude (°)	Latitude (°)	Depth (km)	Origin Time	Strike	Dip	Rake	moment (dyne-cm)
HARVARD	-103.32	30.24	15.0	00:32:54.2	117	53	-87	3.82E24
USGS	-103.327	30.261	13.0	00:32:55.04	136	60	-86	4.00E24
this study	-103.327	30.261	20.0	00:32:55.04	114	64	-101	3.00E24

arrival is beyond the upper-mantle P triplication zone which is caused by upper-mantle discontinuities. Therefore, the P waveform and its coda keep the waveform characters that generated in the source. This indicates that source depth is not as shallow as suggested by Harvard and USGS solutions. For a simple crustal model, such a $sP - P$ difference will correspond to an earthquake deeper than 20 kilometers. Using CUS model, synthetics are generated for different depths: 13, 15, 17, 19, 21, 23, and 25 km. From the comparison of observed and synthetic seismograms, the preferred depth would be 20 km. Figure 2.3 shows the comparison for the station DAWY.

The source mechanism used in this study is based on the grid search for Love- and Rayleigh-wave radiation patterns (Herrmann, 1974) using observed spectrum amplitude of fundamental mode group velocities at different frequencies. Based on a grid search for a focal mechanism at different source depths, the optimum result is a point source at 20 km depth, with a strike of 114° , a dip of 64° , a rake of -101° , and with seismic moment $3.0E24$ dyne-cm.

From the station distribution (figure 2.1), we can see that most broadband stations are in the western United States. The second best

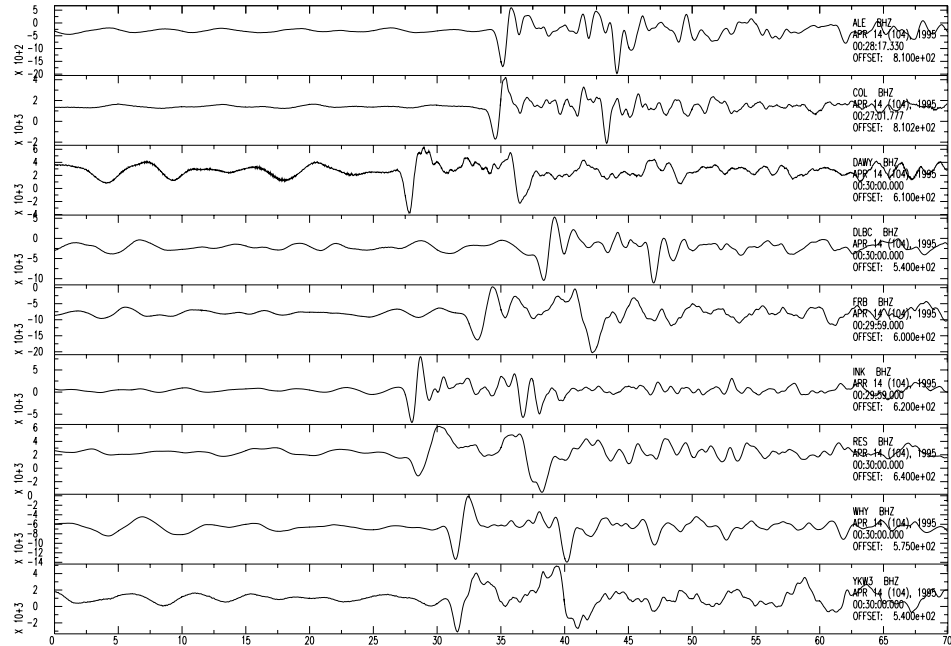


Fig. 2.2. For teleseismic records, a general 9 seconds travel time difference for sP - P is observable.

coverage occurs in the northeastern United States. The fundamental-mode Rayleigh and Love wave spectral amplitudes used in the radiation pattern search also have more dense data points in these two regions. The observed spectral amplitudes delineate a clear nodal plane for the Love wave radiation pattern. All three solutions can provide good Love wave radiation patterns to match the observed data. But from Rayleigh wave radiation patterns, the reestimated focal mechanism is optima. For comparison, figure 2.4, 2.5, and 2.6 show the Love wave radiation patterns at nine periods for the mechanism

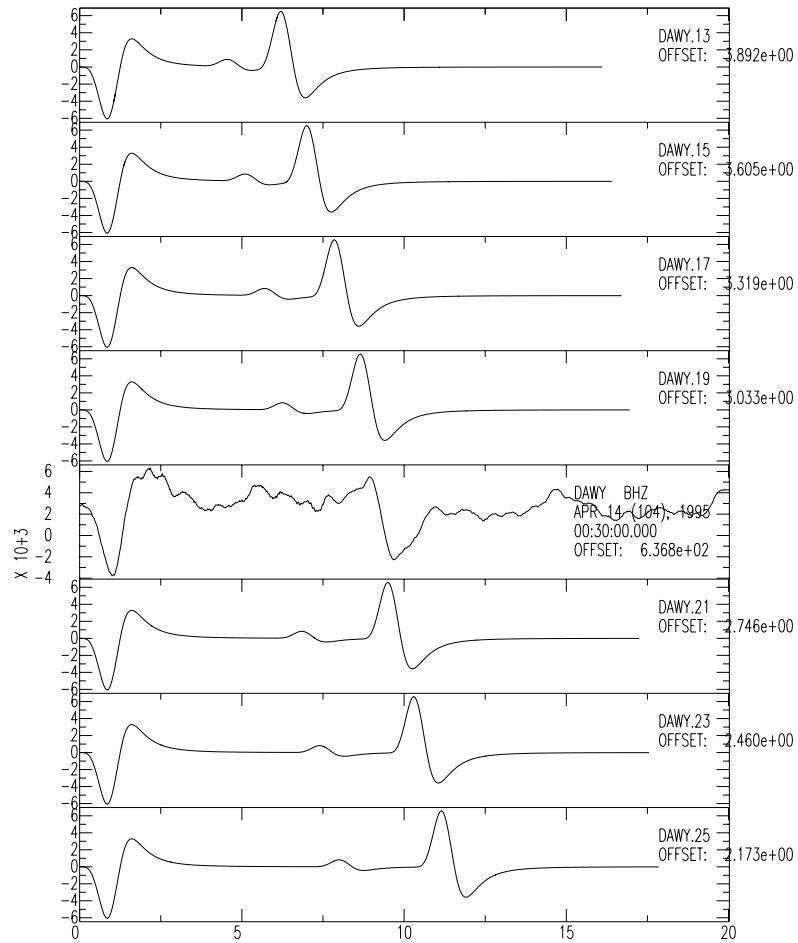


Fig. 2.3. Compare the observed teleseismic P seismogram at DAWY with synthetics, the preferred source depth is 20 km. The synthetics are generated using CUS model for different depths; 13, 15, 17, 19, 21, 23, and 25 km. The used focal mechanism is the reestimated one in this study.

used in this study, for the Harvard CMT solution, and for the USGS Sipkin's solution. Figure 2.7, 2.8, and 2.9 will similarly display the

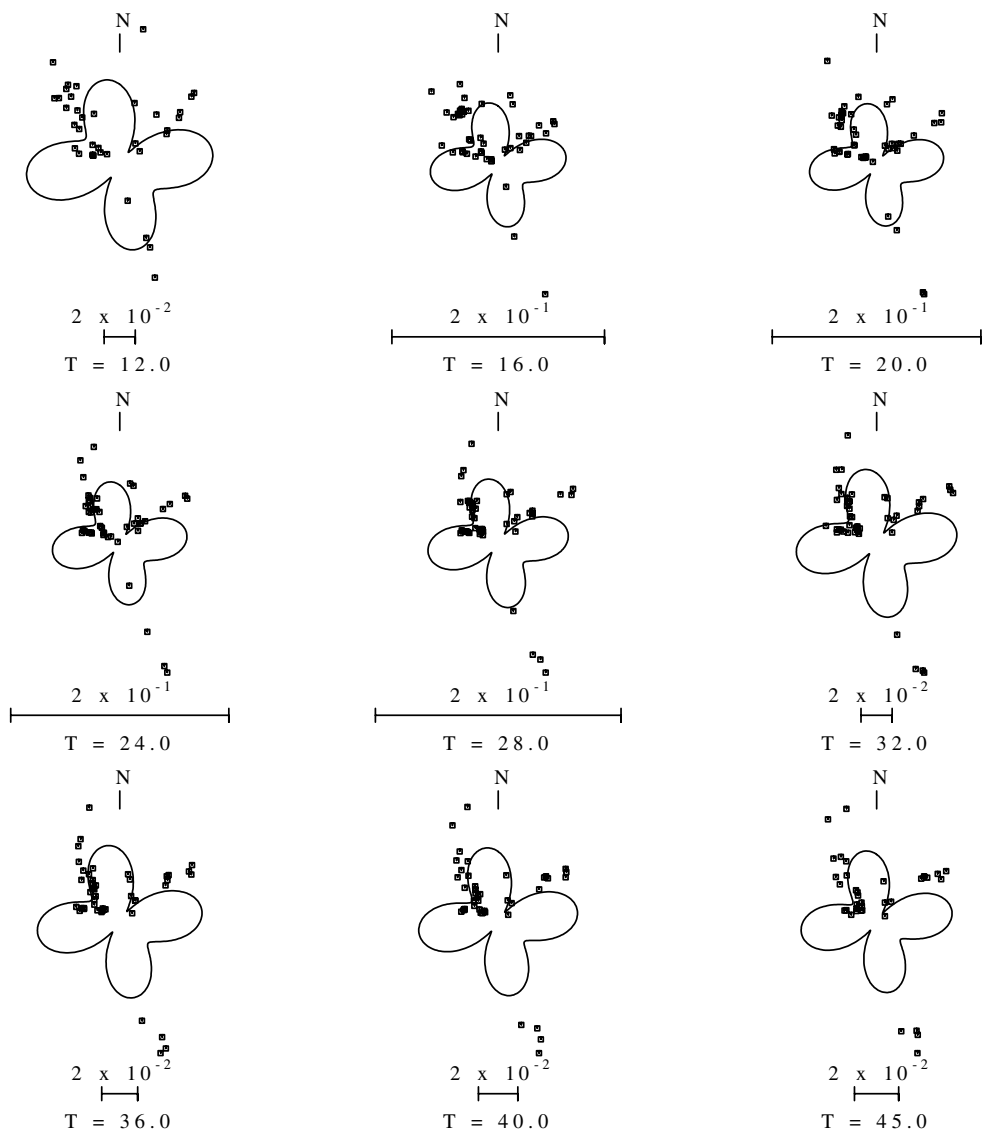


Fig. 2.4. The Love wave radiation patterns for the preferred focal mechanism at 20 km depth. The bars indicate attenuation corrected spectral amplitudes in cm-sec normalized for geometrical spreading to 1000 km.

Rayleigh wave radiation patterns.

P-wave polarities provide a check of focal mechanisms. The P-wave polarity reading is shown in table 2.1. A negative number

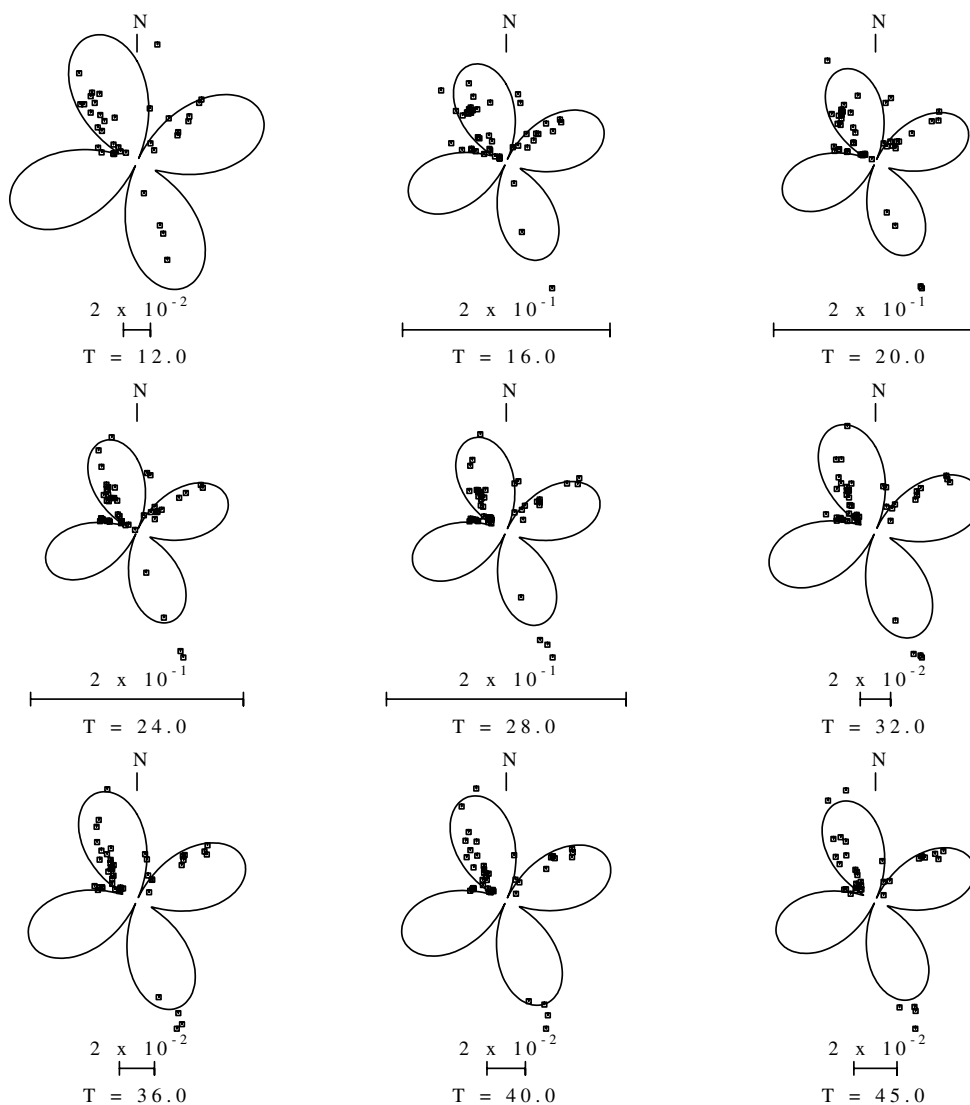


Fig. 2.5. The Love wave radiation patterns for Harvard CMT solution at 15 km depth.

indicates downward movement, and the positive number indicates upward movement. The number 1 indicates a impulsive P-wave arrival; the larger numbers indicate emergent arrivals in which we are less confident. P-wave polarities for these three focal mechanisms are shown as figure 2.10, 2.11, and 2.12. In these figures, the circles

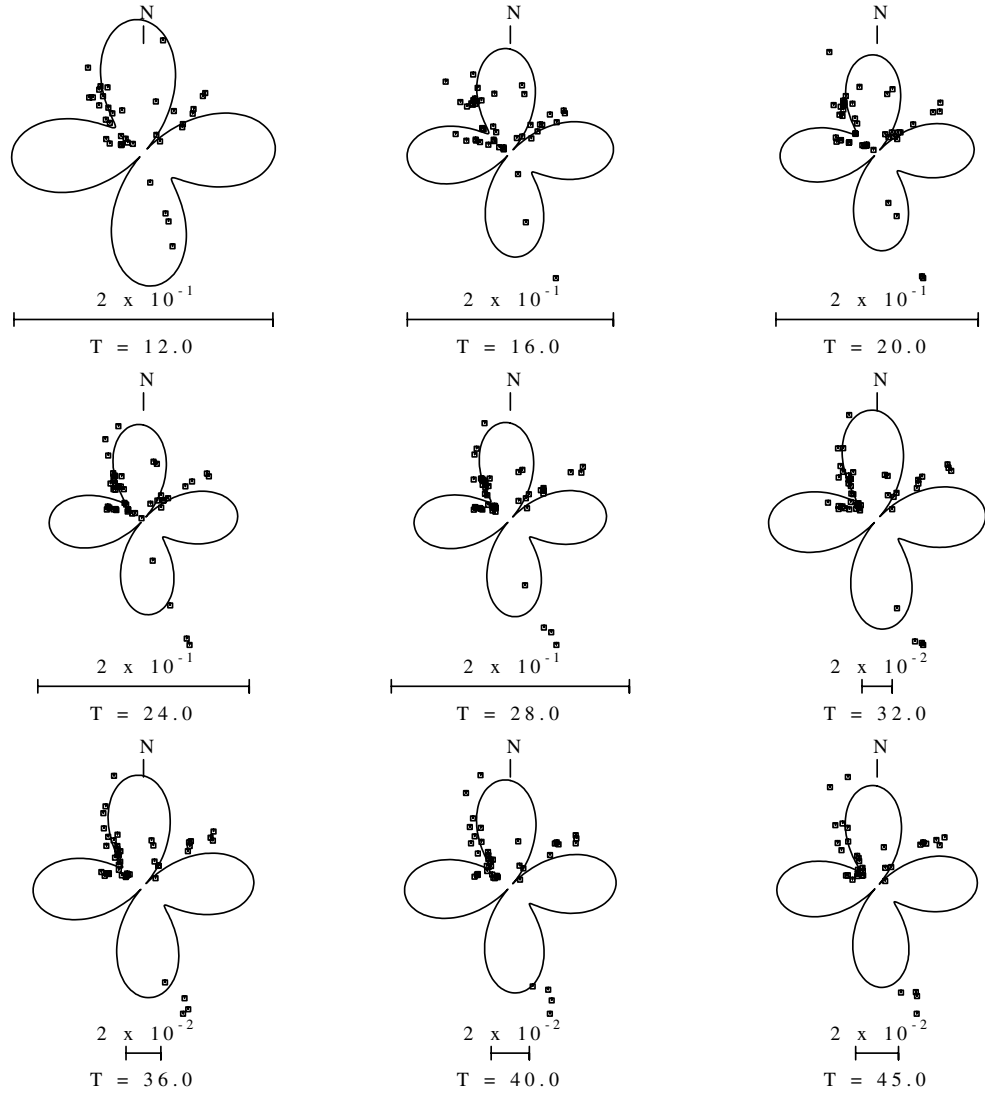


Fig. 2.6. The Love wave radiation patterns for Sipkin's USGS solution at 13 km depth.

represent impulsive upward P arrivals while the plus signs represent emergent upward P arrivals; in a similar way, triangles represent impulsive downward P arrivals and the minus signs are for emergent downward P arrivals. The reestimated focal mechanism which have only one inconsistent station is better than the other two solutions.

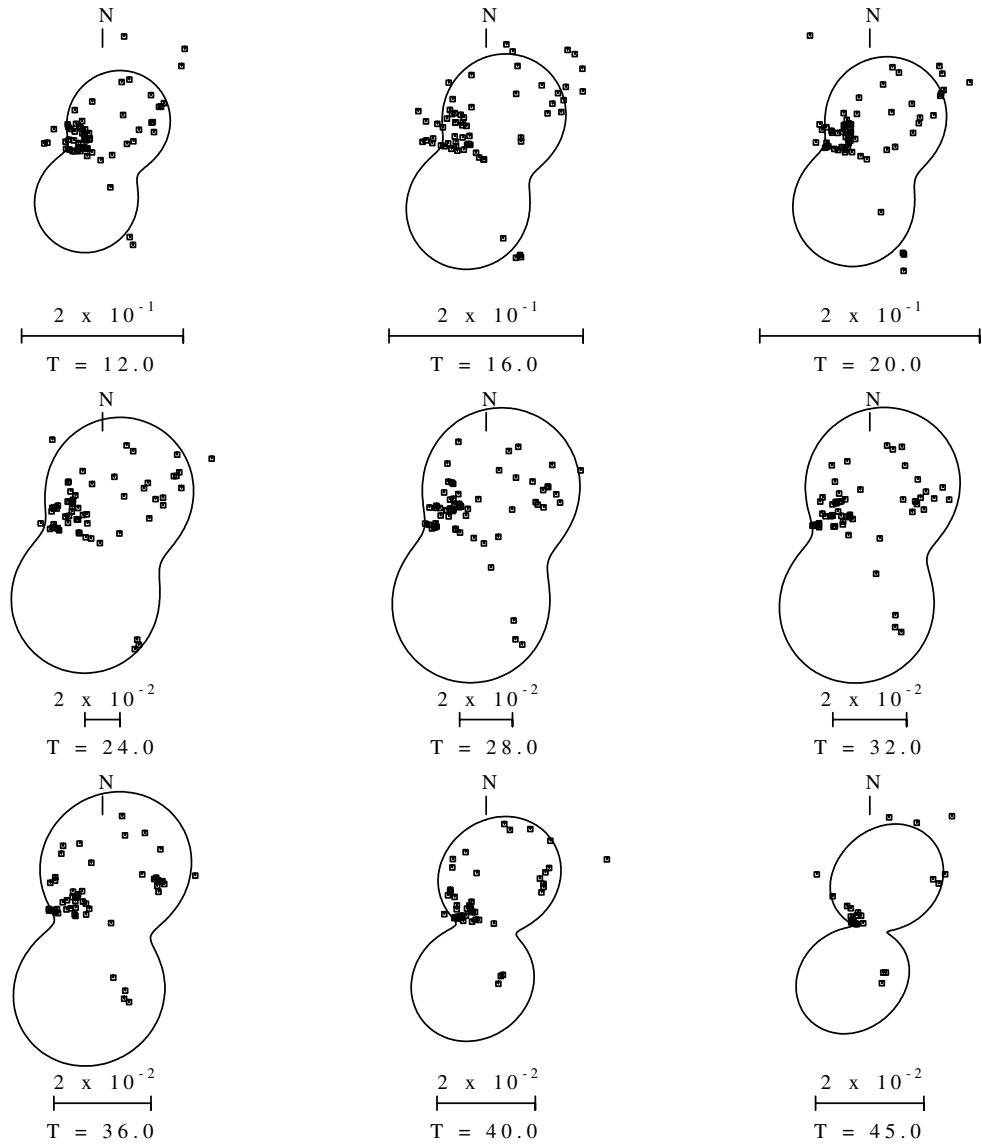


Fig. 2.7. The Rayleigh wave radiation patterns for the preferred focal mechanism at 20 km depth.

From these comparisons, the depth phases, Rayleigh and Love wave radiation patterns, and the first arrival P wave polarities, we are confident that the reestimated focal mechanism is better than the others.

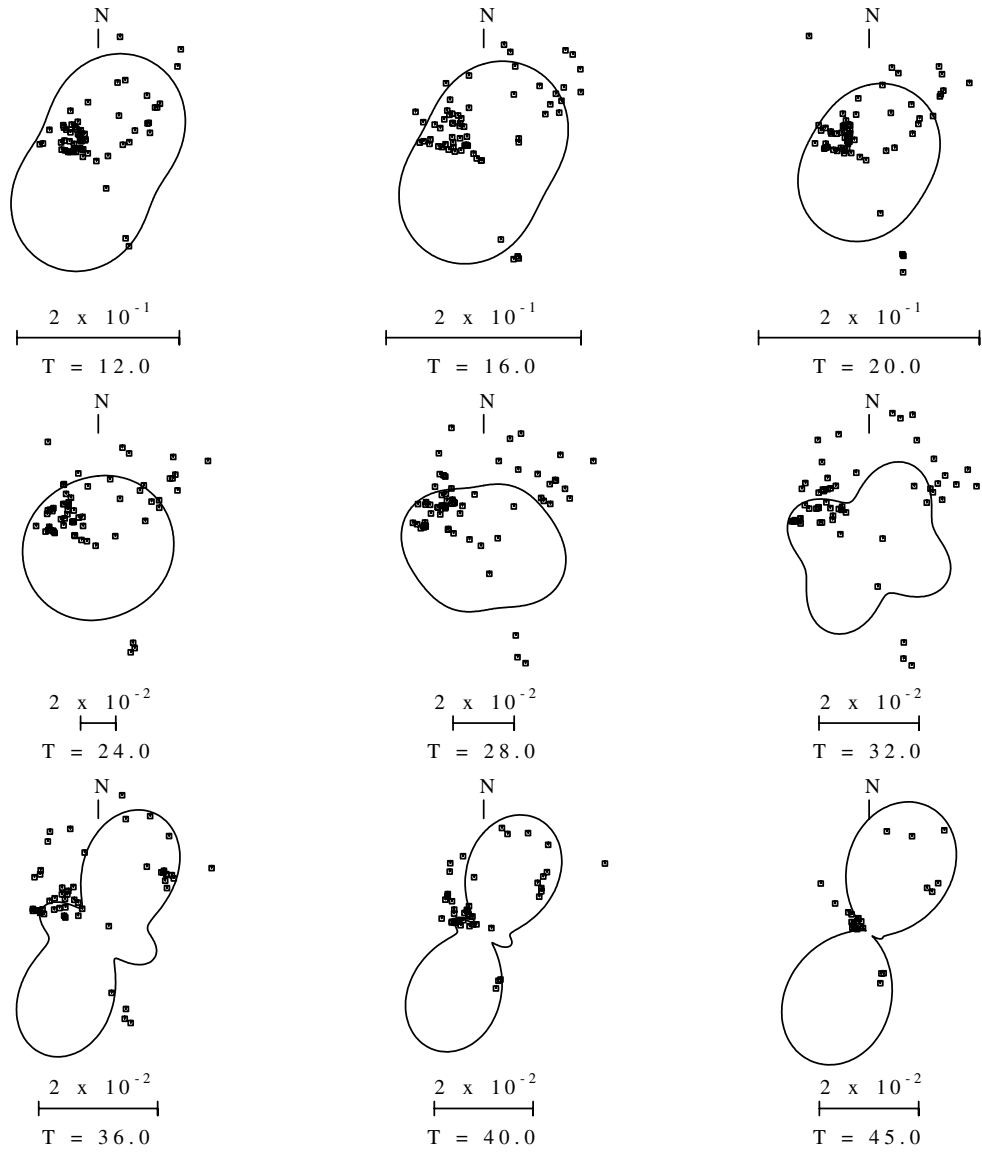


Fig. 2.8. The Rayleigh wave radiation patterns for Harvard CMT solution at 15 km depth.

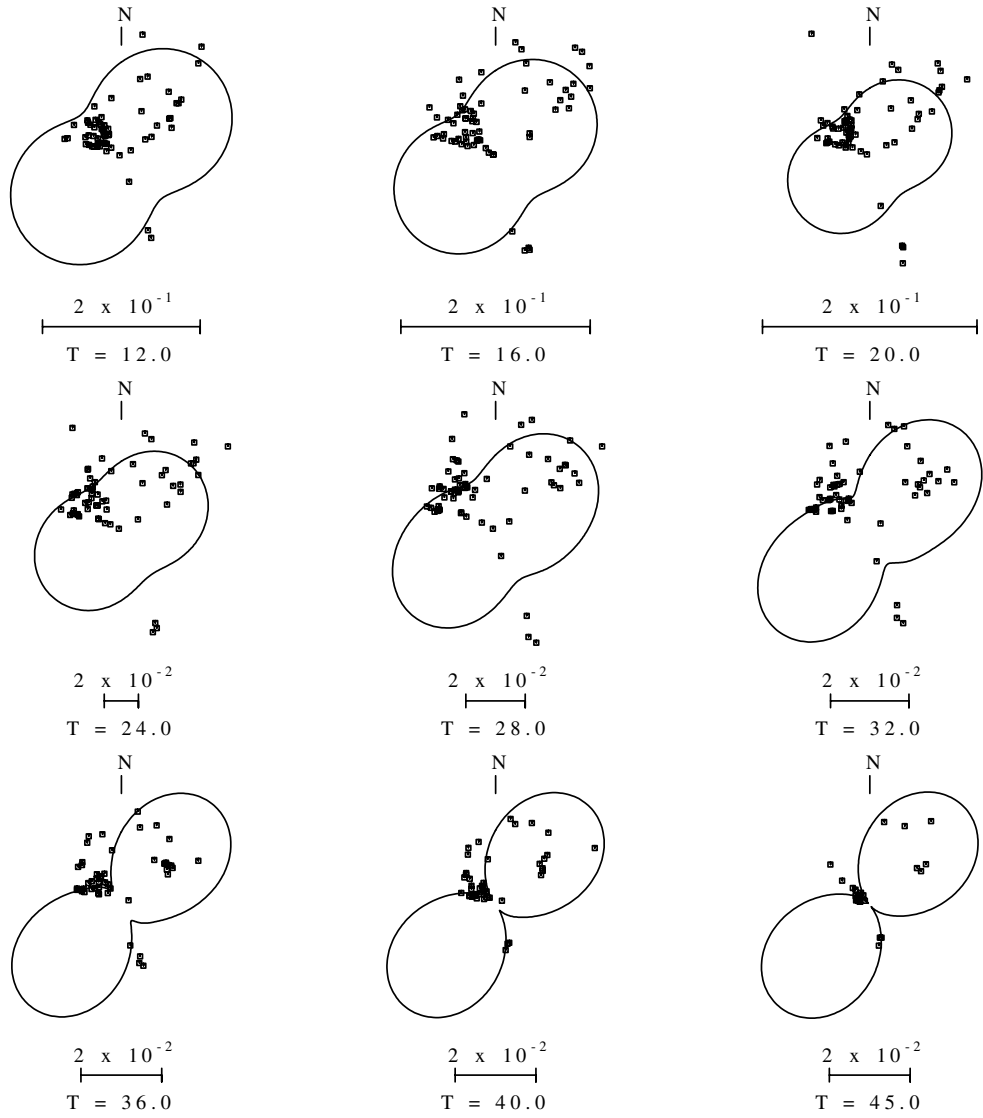


Fig. 2.9. The Rayleigh wave radiation patterns for Sipkin's USGS solution at 13 km depth.

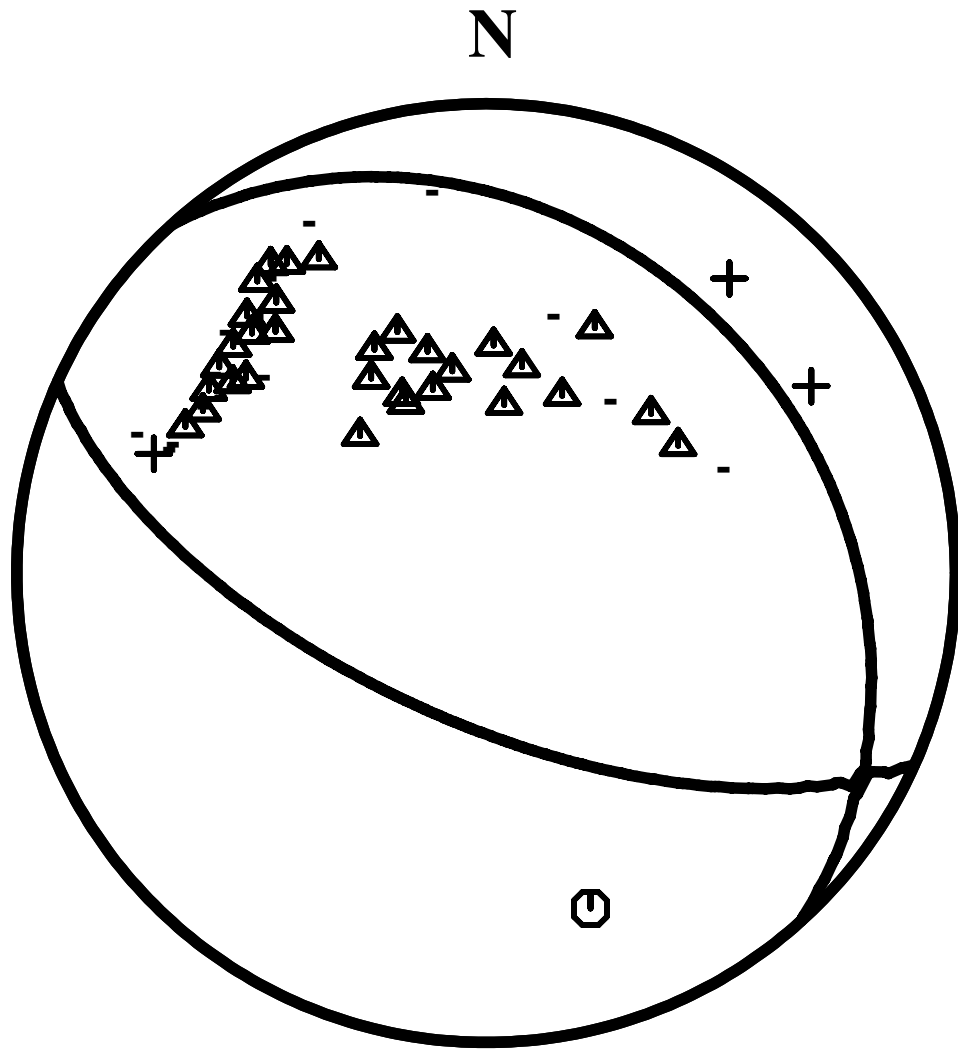


Fig. 2.10. This figure shows the observed P-wave polarities and the reestimated focal mechanism which will be used for testing several surface-waveform modeling algorithms.

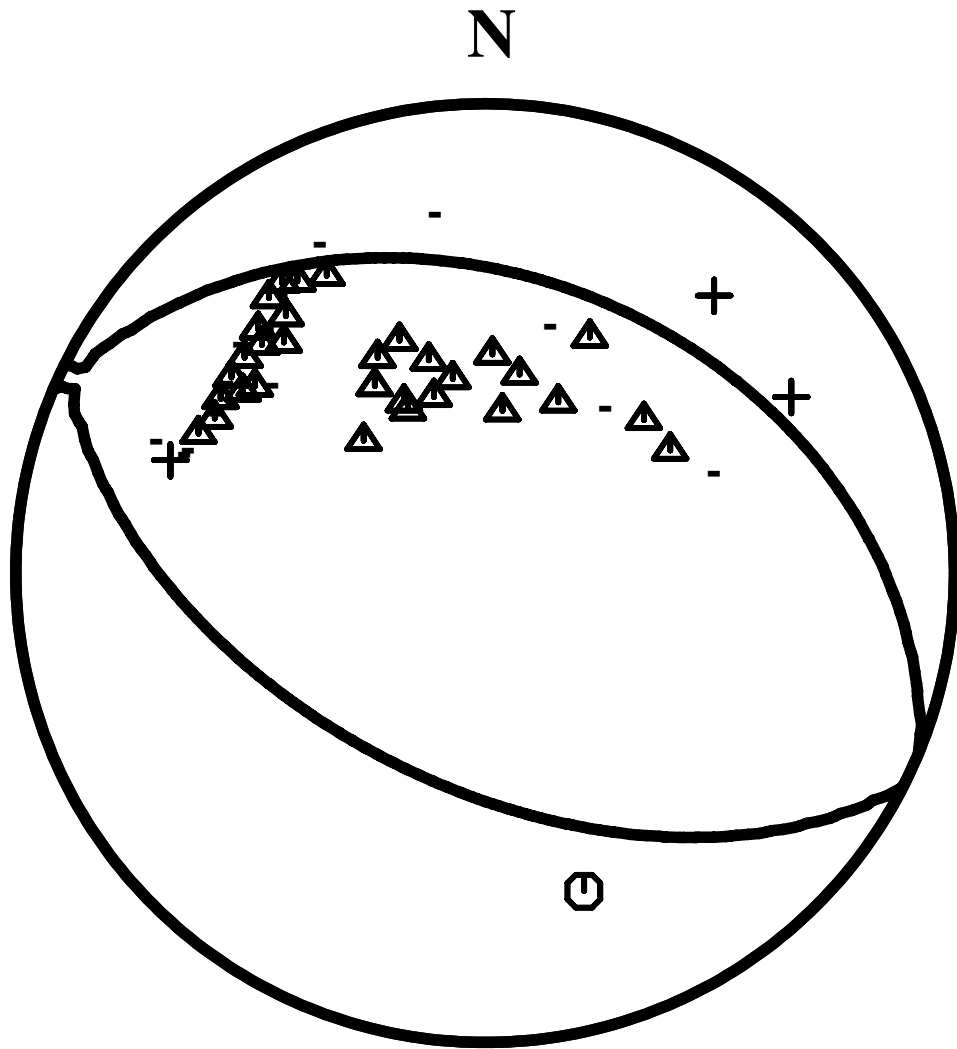


Fig. 2.11. This figure shows the focal mechanism of Harvard CMT solution and the observed P-wave polarities.

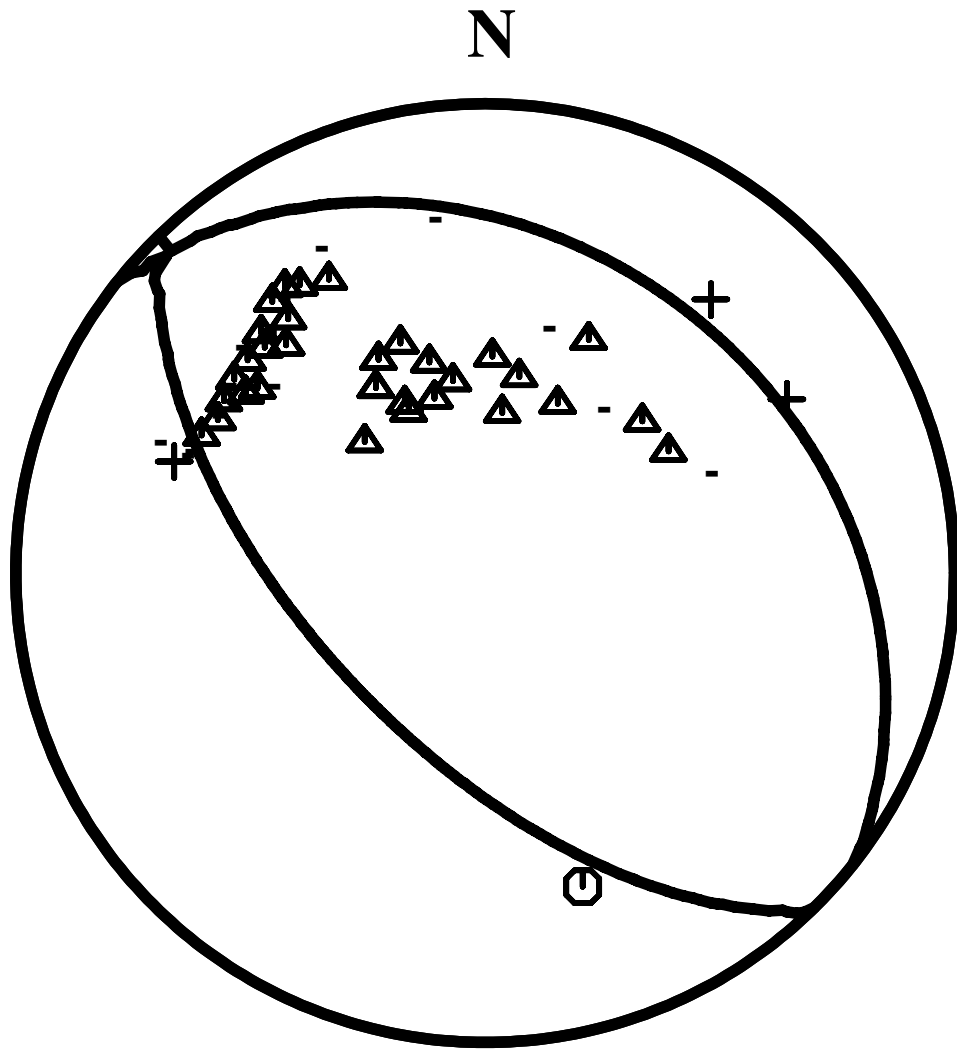


Fig. 2.12. This figure shows the focal mechanism of Sipkin's USGS solution and the observed P-wave polarities.

CHAPTER 3

REVIEW OF GSDF THEORY AND FORMULATION OF THE INVERSION ALGORITHM USING GSDF

3.1 Introduction

Based on their success in observing the apparent anisotropy of the Eurasian upper mantle (Gee and Jordan, 1988), Gee and Jordan (1992) introduced the theory of Generalized Seismological Data Functionals (GSDF) which deals with the interference effects of different surface wave modes at a certain frequency. This theory allows seismologists to precisely measure the group and phase delays between observed and synthetic seismograms at different frequencies even when the modal interference cannot be ignored. Applications have been reported by Gaherty *et al.* (1995, 1996) who used this method to invert for the upper-mantle velocity structure and anisotropy. In this study, we extend the Generalized Seismological Data Functionals (GSDF) theory to the inversion of broadband waveforms modeled as a superposition of surface-wave modes (Wang, 1981). We demonstrate the utility of this new inversion algorithm by conducting a simple synthetic test, and then apply the algorithm to observations from the 1995 west Texas

earthquake to discern what new knowledge about earth structure can be obtained from it.

3.2 Theory of Generalized Seismological Data Functionals

To use the GSDF approach, we must construct a synthetic seismogram (\tilde{s}), an isolation function (\tilde{f}) and single-mode seismograms. An isolation function is a sum of single-mode seismograms which may represent the dominant part of the observed seismogram (s). Using a cross-correlation technique, we can quantify the similarity between observed and synthetic seismograms. For a model that does not significantly deviate from actual earth structure, the peak of the cross-correlograms will be located near zero lag-time for all frequency bands and for all windowed segments of the seismograms. The cross-correlograms reflect the degree that the model used to create synthetic seismogram, isolation function and single-mode seismograms differs from the actual earth. To utilize this information, we have to extract information in different frequency ranges and interpret it in terms of differences in earth structure.

Gee and Jordan (1992) call the extracted information Generalized Seismological Data Functionals (GSDF). In the following, we give a brief review of how the GSDF is defined, how the GSDF is related to familiar physical quantities, and how we extend this theory to invert for Earth structure. Equations directly adapted from Gee and Jordan

(1992) will be cited as (GJ.#), where # indicates the original equation number in their paper.

First, we review the definition and computation of a GSDF. We use a Gaussian wavelet to approximate the filtered and windowed cross-correlagrams at a specified frequency. The windowed, filtered cross-correlagram of an isolation function with a seismogram (either observed or synthetic) is modeled using a five-parameter Gaussian wavelet:

$$\mathbf{F}_i \mathbf{W} \mathbf{C}_{f_s}(t) \approx g(t) \equiv A \text{Ga}[\sigma_s(t - t_g)] \cos[\omega_s(t - t_p)] \quad (\text{GJ.5})$$

$$\mathbf{F}_i \mathbf{W} \tilde{\mathbf{C}}_{f_s}(t) \approx \tilde{g}(t) \equiv \tilde{A} \text{Ga}[\tilde{\sigma}_s(t - \tilde{t}_g)] \cos[\tilde{\omega}_s(t - \tilde{t}_p)] \quad (\text{GJ.8})$$

$$\mathbf{F}_i \mathbf{W} \tilde{\mathbf{C}}_{ff}(t) \equiv \text{Ga}[\tilde{\sigma}_f t] \cos[\tilde{\omega}_f t]$$

where

\mathbf{F}_i is a Gaussian frequency content filter with center frequency ω_i and half-bandwidth σ_i ,

$\mathbf{W} = \text{Ga}[\sigma_w(t - t_w)] \left\{ 1 + 0.01[\sigma_w(t - t_w)]^4 - \dots \right\}$ is a temporal window

with half-bandwidth σ_w and centered at t_w ; usually $t_w = t_c$, where t_c is the lag-time of the peak of $\mathbf{F}_i \mathbf{W} \tilde{\mathbf{C}}_{ff}$,

$\mathbf{C}_{f_s}(t) \equiv \tilde{f}(t) \otimes s(t)$ is the cross-correlation of the observed time history, $s(t)$, with the isolation filter, $\tilde{f}(t)$, where \otimes represents cross-correlation,

$\tilde{\mathbf{C}}_{f_s}(t) \equiv \tilde{f}(t) \otimes \tilde{s}(t)$, is the cross-correlation with the synthetic time history,

$\text{Ga}[x] \equiv \exp(-\frac{x^2}{2})$, Ga is the Gaussian function,

A is the amplitude of Gaussian envelope,

σ is the half-bandwidth of envelope spectrum,

ω is the angular frequency of the oscillating wavelet,

t_g is the envelope group delay from zero lag-time,

t_p is the wavelet phase delay from zero lag-time,

the subscript s denotes the observed seismogram, the subscript s combined with \sim denotes the synthetic seismogram, and the subscript f with \sim denotes the isolation filter.

From (GJ.5) and (GJ.8), Gee and Jordan define four data functionals to characterize the agreement between observed and predicted time histories:

$$\delta t_p = t_p - \tilde{t}_p \quad (\text{GJ.9})$$

$$\delta t_g = t_g - \tilde{t}_g \quad (\text{GJ.10})$$

$$\delta t_q = -\frac{1}{\tilde{\omega}_s} [\ln A - \ln \tilde{A}] \quad (\text{GJ.11})$$

$$\delta t_a = -\frac{1}{\tilde{\sigma}_s^2} [\omega_s - \tilde{\omega}_s] \quad (\text{GJ.12})$$

These four data functionals are related to differential phase delay, differential group delay, differences in logarithmic amplitudes and the differences in center frequencies. These four data functionals are defined from two filtered, windowed cross-correlograms, and can be transformed into more familiar quantities such as phase velocity,

group velocity, and attenuation corrections.

We will briefly describe this transformation. We note that all filtered and windowed cross-correlograms will be normalized by scaling $\mathbf{F}_i \mathbf{W} \tilde{\mathbf{C}}_{ff}$ to unit amplitude. Also, if the observed and synthetic seismograms are composed only of a single mode, then the GSDF are easily interpreted in terms of differences in modeled and actual phase velocity, group velocity and Q. For multi-mode time histories the interpretation is much more difficult.

Before relating GSDF to physical quantities, we must know the roles these quantities play in wave propagation. For a known instrument response $I(\omega)$ and source $S(\omega)$, the difference between the spectrum of an isolation filter $\tilde{f}(\omega) = I(\omega)\tilde{P}(\omega)S(\omega)$ and its corresponding component of the observed seismograms $f(\omega) = I(\omega)P(\omega)S(\omega)$ is called "differential propagation". They are related by the equation

$$\begin{aligned} f(\omega) &= \frac{P(\omega)}{\tilde{P}(\omega)} \tilde{f}(\omega) \\ &= D(\omega) \tilde{f}(\omega) \\ &= e^{i\delta k(\omega)R} \tilde{f}(\omega) = e^{i[k(\omega) - \tilde{k}(\omega)]R} \tilde{f}(\omega) \end{aligned} \tag{GJ.42}$$

where R is source-receiver distance. To a first-order approximation, the differential propagation is as

$$\begin{aligned} D(\omega) &\approx \exp\left(-\omega_j \delta \tau_q(\omega_j) - (\omega - \omega_j) \delta \tau_a(\omega_j)\right) \\ &\quad + \exp\left(i \left[\omega_j \delta \tau_p(\omega_j) + (\omega - \omega_j) \delta \tau_q(\omega_j) \right]\right) \end{aligned} \tag{GJ.44}$$

The propagation effects of the isolation filter $\tilde{f}(t)$ and the corresponding waveform $f(t)$ on the observed seismogram are defined in four equations which are related familiar physical quantities such as total phase delay, total group delay, and attenuation factor.

$$\delta\tau_p(\omega_j) \equiv \tau_p(\omega_j) - \tilde{\tau}_p(\omega_j) \quad (\text{GJ.45})$$

$$\delta\tau_g(\omega_j) \equiv \tau_g(\omega_j) - \tilde{\tau}_g(\omega_j) \quad (\text{GJ.46})$$

$$\delta\tau_q(\omega_j) \equiv \frac{1}{2} \tilde{\tau}_p(\omega_j)[Q^{-1} - \tilde{Q}^{-1}] \quad (\text{GJ.47})$$

$$\delta\tau_a(\omega_j) \equiv \frac{1}{2} \tilde{\tau}_g(\omega_j)[Q^{-1} - \tilde{Q}^{-1}] \quad (\text{GJ.48})$$

where

$\tau_p(\omega_j)$ is total phase delay of $f(t)$ at an arbitrary frequency ω_j with respect to the original time,

$\tilde{\tau}_p(\omega_j)$ is total phase delay of $\tilde{f}(t)$ at ω_j ,

$\tau_g(\omega_j)$ is total group delay of $f(t)$ at ω_j ,

$\tilde{\tau}_g(\omega_j)$ is total group delay of $\tilde{f}(t)$ at ω_j ,

Q^{-1} is attenuation factor of $f(t)$,

\tilde{Q}^{-1} is attenuation factor of $\tilde{f}(t)$.

This means that whenever we are able to measure four differential quantities $\delta\tau_x$ from observed and synthetic seismograms at a certain frequency ω_j , we can approximate to first-order the true waveform spectral behavior $f(\omega)$ at any arbitrary frequency ω .

The GSDF δt_x based on the filtered, windowed cross-correlation, and the $\delta \tau_x$ are related through the time domain windowing function. Their relationships are given by

$$\delta t_g \approx \delta \tau_g(\tilde{\omega}_f) + (1 - \xi_1^2)[t_c - \delta \tau_g(\tilde{\omega}_f)] \quad (\text{GJ.56})$$

$$\delta t_p \approx \delta \tau_p(\tilde{\omega}_f) + (1 - \xi_1^2)\left(\frac{\tilde{\omega}_f - \tilde{\omega}_c}{\tilde{\omega}_f}\right)[t_c - \delta \tau_g(\tilde{\omega}_f)] \quad (\text{GJ.57})$$

$$\delta t_a \approx \xi_1^2 \delta \tau_a(\tilde{\omega}_f) \quad (\text{GJ.58})$$

$$\delta t_q \approx \delta \tau_q(\tilde{\omega}_f) - (1 - \xi_1^2)\left(\frac{\tilde{\omega}_f - \tilde{\omega}_c}{\tilde{\omega}_f}\right) \delta \tau_a(\tilde{\omega}_f) \quad (\text{GJ.59})$$

where

$\tilde{\omega}_c$ is the frequency from $\tilde{\mathbf{C}}_{ff}$,

ξ_1 is a window width factor,

t_c is the lag-time of the peak of cross-correlogram $\mathbf{F}_i \mathbf{W} \mathbf{C}_{ff}$.

There is an additional assumption that must be stated. Due to the difficulty in relating the isolation filter's corresponding feature in the observed seismogram, it is not easy to evaluate $\mathbf{F}_i \mathbf{W} \mathbf{C}_{ff}$. However, if the windowing procedure is effective in isolating $f(t)$ from other phases on the seismograms, then $\mathbf{F}_i \mathbf{W} \mathbf{C}_{fs} \approx \mathbf{F}_i \mathbf{W} \mathbf{C}_{ff}$.

We can estimate t_c from an isolated waveform. For non-isolated waveforms, the \mathbf{C}_{ff} cannot be simply replaced by \mathbf{C}_{fs} , but the Gaussian wavelet can be represented as a sum of interference effects of N different modes.

$$\mathbf{F}_i \mathbf{W} \tilde{\mathbf{C}}_{fs}(t) = \sum_{m=1}^N \sum_{n=1}^N \mathbf{F}_i \mathbf{W} \tilde{\mathbf{C}}_{mn}(t) \quad (\text{GJ.63})$$

$$\mathbf{F}_i \mathbf{W} \mathbf{C}_{f_s}(t) = \sum_{m=1}^N \sum_{n=1}^N \mathbf{F}_i \mathbf{W} \mathbf{C}_{mn}(t)$$

where

$$\mathbf{C}_{mn}(t) \equiv [\text{mode } m \text{ of } \tilde{f}(t)] \otimes [\text{mode } n \text{ of } f(t)],$$

$$\tilde{\mathbf{C}}_{mn}(t) \equiv [\text{mode } m \text{ of } \tilde{f}(t)] \otimes [\text{mode } n \text{ of } \tilde{f}(t)].$$

We now characterize these by the relation

$$\mathbf{F}_i \mathbf{W} \tilde{\mathbf{C}}_{mn}(t) \approx \tilde{A}_{mn} \text{Ga}[\tilde{\sigma}_f(t - \tilde{t}_g^{mn})] \cos[\tilde{\omega}_{mn}(t - \tilde{t}_p^{mn})] \quad (\text{GJ.68})$$

where

$$\tilde{A}_{mn} \equiv \exp(-\tilde{\omega}_f \tilde{t}_q^{mn}),$$

$$\tilde{\omega}_{mn} \equiv \tilde{\omega}_f - \tilde{\sigma}_f \tilde{t}_a^{mn}.$$

In this case, we need to know four time shifts that describe the deviations of $\mathbf{F}_i \mathbf{W} \tilde{\mathbf{C}}_{f_s}$ from $\mathbf{F}_i \mathbf{W} \tilde{\mathbf{C}}_{ff}$. Assume that the windowing and filtering effectively suppress the bandwidth variations, so that $\tilde{\sigma}_s \approx \tilde{\sigma}_f$. The four time shifts are the phase delay \tilde{t}_p , a group delay \tilde{t}_g , and two amplitude parameters

$$\tilde{t}_q = -\frac{1}{\tilde{\omega}_f} \ln \tilde{A} \quad (\text{GJ.60})$$

$$\tilde{t}_a = -\frac{1}{\tilde{\sigma}_f^2} [\tilde{\omega}_s - \tilde{\omega}_f] \quad (\text{GJ.61})$$

By defining the following notation,

$$B_{mn} = \frac{1}{(2\pi)^{1/2}} \exp[-\tilde{\omega}_f(\tilde{t}_q^{mn} - \tilde{t}_q)] \text{Ga}[\tilde{\sigma}_f(\tilde{t}_g^{mn} - \tilde{t}_g)] \quad (\text{GJ.73})$$

$$\phi_{mn} = (\tilde{\omega}_f - \tilde{\sigma}_f^2 \tilde{t}_a^{mn})(\tilde{t}_p^{mn} - \tilde{t}_p) - \tilde{\sigma}_f^2(\tilde{t}_a^{mn} - \tilde{t}_a)(\tilde{t}_p - \tilde{t}_g) \quad (\text{GJ.74})$$

the perturbation expansions can be simplified by using a set $N \times N$ matrices

$$(\mathbf{C})_{mn} = B_{mn} \cos \phi_{mn} \quad (\text{GJ.75})$$

$$(\mathbf{S})_{mn} = B_{mn} \sin \phi_{mn} \quad (\text{GJ.76})$$

$$(\mathbf{C}_{\mathbf{x}})_{mn} = B_{mn} \tilde{\omega}_f(\tilde{t}_x^{mn} - \tilde{t}_x) \cos \phi_{mn} \quad (\text{GJ.77})$$

$$(\mathbf{S}_{\mathbf{x}})_{mn} = B_{mn} \tilde{\omega}_f(\tilde{t}_x^{mn} - \tilde{t}_x) \sin \phi_{mn} \quad (\text{GJ.78})$$

Gee and Jordan (1992) gave the following linearized relationships between the GSDFs and computable quantities from individual mode branches.

$$\delta t_q = \mathbf{1} \cdot \mathbf{C} \cdot \delta \mathbf{t}_q + \mathbf{1} \cdot \mathbf{S} \cdot \delta \mathbf{t}_p \quad (\text{GJ.84})$$

$$\delta t_p = -\mathbf{1} \cdot \mathbf{S} \cdot \delta \mathbf{t}_q + \mathbf{1} \cdot \mathbf{C} \cdot \delta \mathbf{t}_p \quad (\text{GJ.85})$$

$$\delta t_a = -\mathbf{1} \cdot (\mathbf{C}_a + \mathbf{S}_g) \cdot \delta \mathbf{t}_q + \mathbf{1} \cdot (\mathbf{C}_g - \mathbf{S}_a) \cdot \delta \mathbf{t}_p \quad (\text{GJ.86})$$

$$+ \mathbf{1} \cdot \mathbf{C} \cdot \delta \mathbf{t}_a + \mathbf{1} \cdot \mathbf{S} \cdot \delta \mathbf{t}_g$$

$$\delta t_g = -\mathbf{1} \cdot (\mathbf{C}_g - \mathbf{S}_a) \cdot \delta \mathbf{t}_q - \mathbf{1} \cdot (\mathbf{C}_a + \mathbf{S}_g) \cdot \delta \mathbf{t}_p \quad (\text{GJ.87})$$

$$- \mathbf{1} \cdot \mathbf{S} \cdot \delta \mathbf{t}_a + \mathbf{1} \cdot \mathbf{C} \cdot \delta \mathbf{t}_g$$

The $\mathbf{1}$ is a N -dimension vector, each element of which equals one. The $\delta \mathbf{t}_{\mathbf{x}}$ is a N -vector whose n 'th component is δt_x^n , the perturbation corresponding to the quantity x of the n 'th mode. In the following section, we will translate this $\delta \mathbf{t}_{\mathbf{x}}$ into $\delta \boldsymbol{\tau}_{\mathbf{x}}$ which directly relates to the seismogram and has clear physical meaning.

3.3 Structure Inversion

To apply GSDF theory in structure inversion, we must construct the inversion kernel, \mathbf{G} for our inversion. The inverse problem can be simply expressed in the form :

$$\delta \boldsymbol{\tau}_{\mathbf{x}} = \mathbf{G}_{\mathbf{x}} \cdot \delta \mathbf{m}$$

where

\mathbf{x} indicates one of $\{\mathbf{p}, \mathbf{g}, \mathbf{q}, \mathbf{a}\}$.

$\delta \boldsymbol{\tau}_{\mathbf{x}}$ is an N -vector for corresponding to N modes,

$\mathbf{G}_{\mathbf{x}}$ is an $N \times k$ Frechet kernel matrix for structural inverse problem,

$\delta \mathbf{m}$ is a model correction vector for k unknowns.

$\delta \tau_x$ is not measurable but fortunately GSDF theory provides a way to compute these nonmeasurable quantities using the mode interference relationship. Thus, in an application of GSDF theory, we must relate $\delta \boldsymbol{\tau}_{\mathbf{x}}$ to $\delta \mathbf{t}_{\mathbf{x}}$ to create the kernel $\mathbf{G}_{\mathbf{x}}$.

From (GJ.56-59), we can transform $\delta \boldsymbol{\tau}_{\mathbf{x}}$ to $\delta \mathbf{t}_{\mathbf{x}}$ as

$$\delta \mathbf{t}_{\mathbf{g}} = \delta \boldsymbol{\tau}_{\mathbf{g}}(\tilde{\omega}_f) + (1 - \xi_1^2)[t_c \mathbf{1} - \delta \boldsymbol{\tau}_{\mathbf{g}}(\tilde{\omega}_f)]$$

$$\delta \mathbf{t}_{\mathbf{p}} = \delta \boldsymbol{\tau}_{\mathbf{p}}(\tilde{\omega}_f) + a[t_c \mathbf{1} - \delta \boldsymbol{\tau}_{\mathbf{g}}(\tilde{\omega}_f)]$$

$$\delta \mathbf{t}_{\mathbf{a}} = \xi_1^2 \delta \boldsymbol{\tau}_{\mathbf{a}}(\tilde{\omega}_f)$$

$$\delta \mathbf{t}_{\mathbf{q}} = \delta \boldsymbol{\tau}_{\mathbf{q}}(\tilde{\omega}_f) - a \delta \boldsymbol{\tau}_{\mathbf{a}}(\tilde{\omega}_f)$$

where $a = (1 - \xi_1^2) \left(\frac{\tilde{\omega}_f - \tilde{\omega}_c}{\tilde{\omega}_f} \right)$. Substituting these into (GJ.84-87) gives

the following equations which relate the four GSDFs to the inversion kernels \mathbf{G}_x .

$$\begin{aligned}
\delta t_p &= \mathbf{1} \cdot \mathbf{C} \cdot \mathbf{1} a t_c + \mathbf{1} \cdot \left[\mathbf{C}(\mathbf{G}_p - a\mathbf{G}_g) - \mathbf{S}(\mathbf{G}_q - a\mathbf{G}_a) \right] \cdot \delta \mathbf{m} \\
\delta t_q &= \mathbf{1} \cdot \mathbf{S} \cdot \mathbf{1} a t_c + \mathbf{1} \cdot \left[\mathbf{C}(\mathbf{G}_q - a\mathbf{G}_a) + \mathbf{S}(\mathbf{G}_p - a\mathbf{G}_g) \right] \cdot \delta \mathbf{m} \\
\delta t_a &= \mathbf{1} \cdot (\mathbf{C}_g - \mathbf{S}_a) \cdot \mathbf{1} a t_c + \mathbf{1} \cdot \mathbf{S} \cdot \mathbf{1} (1 - \xi_1^2) t_c \\
&\quad + \mathbf{1} \cdot \left[-(\mathbf{C}_a + \mathbf{S}_g)(\mathbf{G}_q - a\mathbf{G}_a) + (\mathbf{C}_g - \mathbf{S}_a)(\mathbf{G}_p - a\mathbf{G}_g) \right] \cdot \delta \mathbf{m} \\
&\quad + \mathbf{1} \cdot \left[\xi_1^2 \mathbf{C} \mathbf{G}_a + \xi_1^2 \mathbf{S} \mathbf{G}_g \right] \cdot \delta \mathbf{m} \\
\delta t_g &= -\mathbf{1} \cdot (\mathbf{C}_a + \mathbf{S}_g) \cdot \mathbf{1} a t_c + \mathbf{1} \cdot \mathbf{C} \cdot \mathbf{1} (1 - \xi_1^2) t_c \\
&\quad + \mathbf{1} \cdot \left[-(\mathbf{C}_g - \mathbf{S}_a)(\mathbf{G}_q - a\mathbf{G}_a) - (\mathbf{C}_a + \mathbf{S}_g)(\mathbf{G}_p - a\mathbf{G}_g) \right] \cdot \delta \mathbf{m} \\
&\quad + \mathbf{1} \cdot \left[-\xi_1^2 \mathbf{S} \mathbf{G}_a + \xi_1^2 \mathbf{C} \mathbf{G}_g \right] \cdot \delta \mathbf{m}
\end{aligned}$$

Now, we have a general form of inversion problem for earth structure in terms of the GSDF's δt_x , kernels \mathbf{G}_x , and the interference effects $\mathbf{C}, \mathbf{S}, \mathbf{C}_x, \mathbf{S}_x$.

At this point, it is possible to outline this structure inversion problem. At a particular frequency, according to GSDF theory, using a cross-correlation we can obtain four "observations" (GJ.9-12) and evaluate the mode interference, which we will use with \mathbf{G}_x to form inversion kernels. Therefore, we perform this measurement procedure at several frequencies, we then have the "data vector" and "kernel

matrix" ready for inversion. In the following sections, we will show how we create the kernels (\mathbf{G}_x).

Kernel \mathbf{G}_p

Kernel \mathbf{G}_p relates phase velocity changes to model perturbations.

$$\delta\tau_p = \mathbf{G}_p \cdot \delta\mathbf{m}$$

The n 'th component in the differential phase velocity vector $\delta\tau_p$ is defined as

$$\begin{aligned} \delta\tau_{p_n} &= \frac{R}{c_{n_{obs}}} - \frac{R}{c_{n_{syn}}} \\ &= \frac{R}{c_n + \delta c_n} - \frac{R}{c_n} = \frac{R}{c_n} \left[-1 + \left(1 - \frac{\delta c_n}{c_n} + \left(\frac{\delta c_n}{c_n} \right)^2 \dots \right) \right] \\ &= \frac{R}{c_n} \left[-\frac{\delta c_n}{c_n} + \left(\frac{\delta c_n}{c_n} \right)^2 \dots \right] \\ &\approx -\frac{R}{c_n^2} \delta c_n = \left[-\frac{R}{c_n^2} \frac{\partial c_n}{\partial \mathbf{m}} \right] \cdot \delta\mathbf{m} \end{aligned}$$

where

R is the source-receiver distance, and

c_n is phase velocity for the n 'th mode of the synthetic seismogram.

In matrix form, we can see that $\delta\tau_{p_1}$ is the total phase delay for *mode 1* when model \mathbf{m} changes into $\mathbf{m} + \delta\mathbf{m}$.

$$\begin{bmatrix} \delta\tau_{p_1} \\ \delta\tau_{p_2} \\ \vdots \\ \delta\tau_{p_N} \end{bmatrix}_{N \times 1} = - \begin{bmatrix} \frac{R}{c_1^2} \frac{\partial c_1}{\partial m_1} & \frac{R}{c_1^2} \frac{\partial c_1}{\partial m_2} & \frac{R}{c_1^2} \frac{\partial c_1}{\partial m_3} & \cdots & (\#1 \text{ mode}) \\ \frac{R}{c_2^2} \frac{\partial c_2}{\partial m_1} & \frac{R}{c_2^2} \frac{\partial c_2}{\partial m_2} & \frac{R}{c_2^2} \frac{\partial c_2}{\partial m_3} & \cdots & (\#2 \text{ mode}) \\ \cdots & \cdots & \cdots & \cdots & \cdots \\ \frac{R}{c_N^2} \frac{\partial c_N}{\partial m_1} & \frac{R}{c_N^2} \frac{\partial c_N}{\partial m_2} & \frac{R}{c_N^2} \frac{\partial c_N}{\partial m_3} & \cdots & (\#N \text{ mode}) \end{bmatrix}_{N \times k} \begin{bmatrix} \delta m_1 \\ \delta m_2 \\ \delta m_3 \\ \vdots \\ \delta m_k \end{bmatrix}_{k \times 1}$$

Kernel \mathbf{G}_g

To construct the kernel \mathbf{G}_g which relates group velocity variation to model perturbations,

$$\delta\tau_g = \mathbf{G}_g \cdot \delta\mathbf{m}$$

the n 'th component in the differential group velocity vector $\delta\tau_g$, $\delta\tau_{g_n}$ is defined as

$$\begin{aligned} \delta\tau_{g_n} &= \frac{R}{U_{n_{obs}}} - \frac{R}{U_{n_{syn}}} \\ &= \frac{R}{U_n + \delta U_n} - \frac{R}{U_n} = \frac{R}{U_n} \left[-1 + \left(1 - \frac{\delta U_n}{U_n} + \left(\frac{\delta U_n}{U_n}\right)^2 \cdots \right) \right] \\ &= \frac{R}{U_n} \left[-\frac{\delta U_n}{U_n} + \left(\frac{\delta U_n}{U_n}\right)^2 \cdots \right] \\ &\approx -\frac{R}{U_n^2} \delta U_n = \left[-\frac{R}{U_n^2} \frac{\partial U_n}{\partial \mathbf{m}} \right] \cdot \delta\mathbf{m} \end{aligned}$$

where

U_n is group velocity of n 'th mode synthetic seismogram.

In matrix form

$$\begin{bmatrix} \delta\tau_{g_1} \\ \delta\tau_{g_2} \\ \vdots \\ \delta\tau_{g_N} \end{bmatrix}_{N \times 1} = - \begin{bmatrix} \frac{R}{U_1^2} \frac{\partial U_1}{\partial m_1} & \frac{R}{U_1^2} \frac{\partial U_1}{\partial m_2} & \frac{R}{U_1^2} \frac{\partial U_1}{\partial m_3} & \cdots & (\#1 \text{ mode}) \\ \frac{R}{U_2^2} \frac{\partial U_2}{\partial m_1} & \frac{R}{U_2^2} \frac{\partial U_2}{\partial m_2} & \frac{R}{U_2^2} \frac{\partial U_2}{\partial m_3} & \cdots & (\#2 \text{ mode}) \\ \cdots & \cdots & \cdots & \cdots & \cdots \\ \frac{R}{U_N^2} \frac{\partial U_N}{\partial m_1} & \frac{R}{U_N^2} \frac{\partial U_N}{\partial m_2} & \frac{R}{U_N^2} \frac{\partial U_N}{\partial m_3} & \cdots & (\#N \text{ mode}) \end{bmatrix}_{N \times k} \begin{bmatrix} \delta m_1 \\ \delta m_2 \\ \delta m_3 \\ \vdots \\ \delta m_k \end{bmatrix}_{k \times 1}$$

Kernel \mathbf{G}_q

To create kernel \mathbf{G}_q which relates attenuation to model perturbations,

$$\delta\tau_q = \mathbf{G}_q \cdot \delta\mathbf{m}$$

we write (GJ.47) in a general matrix form and reformulate the above equation to yield

$$\begin{aligned} \delta\tau_q &= \frac{1}{2} \tilde{\tau}_p(\omega) [Q^{-1} - \tilde{Q}^{-1}] \\ &= \frac{1}{2} \left[\tilde{\tau}_p(\omega) \frac{\partial Q^{-1}}{\partial \mathbf{m}} \right] \delta\mathbf{m} \\ &= \mathbf{G}_q \cdot \delta\mathbf{m} \end{aligned}$$

Using the relationship between γ and Q , the partial derivative of γ with respect to model perturbations can be calculated.

$$\gamma_n = \frac{\omega}{2c_{0_n}} \mathbf{Q}_n^{-1}$$

$$\frac{\partial \gamma_n}{\partial \mathbf{m}} = \frac{\omega}{2c_{0_n}} \frac{\partial \mathbf{Q}_n^{-1}}{\partial \mathbf{m}} - \mathbf{Q}_n^{-1} \frac{\omega}{2c_{0_n}^2} \frac{\partial c_{0_n}}{\partial \mathbf{m}}$$

Therefore, the partial derivative of \mathbf{Q}_{RL}^{-1} can be rewritten as

$$\frac{\partial \mathbf{Q}_n^{-1}}{\partial \mathbf{m}} = \left[\frac{\partial \gamma_n}{\partial \mathbf{m}} + \mathbf{Q}_n^{-1} \frac{\omega}{2c_{0_n}} \frac{\partial c_{0_n}}{\partial \mathbf{m}} \right] \frac{2c_{0_n}}{\omega}$$

The n 'th row (# n mode) of kernel \mathbf{G}_q is

$$(\mathbf{G}_q)_n = \tilde{\tau}_{p_n}(\omega) \left\{ \frac{c_{0_n}}{\omega} \frac{\partial \gamma_n}{\partial \mathbf{m}} + \frac{\mathbf{Q}_n^{-1}}{2c_{0_n}} \frac{\partial c_{0_n}}{\partial \mathbf{m}} \right\}$$

\mathbf{G}_q in matrix form is

$$\begin{bmatrix} \tilde{\tau}_{p_1} \left(\frac{c_{0_1}}{\omega} \frac{\partial \gamma_1}{\partial m_1} + \frac{\mathbf{Q}_1^{-1}}{2c_{0_1}} \frac{\partial c_{0_1}}{\partial m_1} \right) & \tilde{\tau}_{p_1} \left(\frac{c_{0_1}}{\omega} \frac{\partial \gamma_1}{\partial m_2} + \frac{\mathbf{Q}_1^{-1}}{2c_{0_1}} \frac{\partial c_{0_1}}{\partial m_2} \right) & \cdots & (\#1 \text{ mode}) \\ \tilde{\tau}_{p_2} \left(\frac{c_{0_2}}{\omega} \frac{\partial \gamma_2}{\partial m_1} + \frac{\mathbf{Q}_2^{-1}}{2c_{0_2}} \frac{\partial c_{0_2}}{\partial m_1} \right) & \tilde{\tau}_{p_2} \left(\frac{c_{0_2}}{\omega} \frac{\partial \gamma_2}{\partial m_2} + \frac{\mathbf{Q}_2^{-1}}{2c_{0_2}} \frac{\partial c_{0_2}}{\partial m_2} \right) & \cdots & (\#2 \text{ mode}) \\ \cdots & \cdots & \cdots & \cdots \\ \tilde{\tau}_{p_N} \left(\frac{c_{0_N}}{\omega} \frac{\partial \gamma_N}{\partial m_1} + \frac{\mathbf{Q}_N^{-1}}{2c_{0_N}} \frac{\partial c_{0_N}}{\partial m_1} \right) & \tilde{\tau}_{p_N} \left(\frac{c_{0_N}}{\omega} \frac{\partial \gamma_N}{\partial m_2} + \frac{\mathbf{Q}_N^{-1}}{2c_{0_N}} \frac{\partial c_{0_N}}{\partial m_2} \right) & \cdots & (\#N \text{ mode}) \end{bmatrix}_{(N \times k)}$$

Kernel \mathbf{G}_a

The last kernel is \mathbf{G}_a . From (GJ.48), we have the relationship between \mathbf{G}_a and \mathbf{Q} .

$$\delta \boldsymbol{\tau}_a = \frac{1}{2} \tilde{\tau}_g(\omega) [\mathbf{Q}^{-1} - \tilde{\mathbf{Q}}^{-1}] = \mathbf{G}_a \cdot \delta \mathbf{m}$$

In a manner similar to that for deriving \mathbf{G}_q , we can use the Q and γ relation and the partial derivatives of γ to obtain the kernel \mathbf{G}_a as

$$\begin{aligned} (\mathbf{G}_a)_n &= \frac{\tilde{\tau}_{g_n}(\omega)}{2} \frac{\partial Q_n^{-1}}{\partial \mathbf{m}} \\ &= \tilde{\tau}_{g_n}(\omega) \left\{ \frac{c_{0_n}}{\omega} \frac{\partial \gamma}{\partial \mathbf{m}} + \frac{Q_n^{-1}}{2} \frac{\partial c_{0_n}}{\partial \mathbf{m}} \right\} \end{aligned}$$

\mathbf{G}_a in matrix form is

$$\left[\begin{array}{ccc} \tilde{\tau}_{g_1} \left(\frac{c_{0_1}}{\omega} \frac{\partial \gamma_1}{\partial m_1} + \frac{Q_1^{-1}}{2c_{0_1}} \frac{\partial c_{0_1}}{\partial m_1} \right) & \tilde{\tau}_{g_1} \left(\frac{c_{0_1}}{\omega} \frac{\partial \gamma_1}{\partial m_2} + \frac{Q_1^{-1}}{2c_{0_1}} \frac{\partial c_{0_1}}{\partial m_2} \right) & \cdots \quad (\#1 \text{ mode}) \\ \tilde{\tau}_{g_2} \left(\frac{c_{0_2}}{\omega} \frac{\partial \gamma_2}{\partial m_1} + \frac{Q_2^{-1}}{2c_{0_2}} \frac{\partial c_{0_2}}{\partial m_1} \right) & \tilde{\tau}_{g_2} \left(\frac{c_{0_2}}{\omega} \frac{\partial \gamma_2}{\partial m_2} + \frac{Q_2^{-1}}{2c_{0_2}} \frac{\partial c_{0_2}}{\partial m_2} \right) & \cdots \quad (\#2 \text{ mode}) \\ \cdots & \cdots & \cdots \quad \cdots \\ \tilde{\tau}_{g_N} \left(\frac{c_{0_N}}{\omega} \frac{\partial \gamma_N}{\partial m_1} + \frac{Q_N^{-1}}{2c_{0_N}} \frac{\partial c_{0_N}}{\partial m_1} \right) & \tilde{\tau}_{g_N} \left(\frac{c_{0_N}}{\omega} \frac{\partial \gamma_N}{\partial m_2} + \frac{Q_N^{-1}}{2c_{0_N}} \frac{\partial c_{0_N}}{\partial m_2} \right) & \cdots \quad (\#N \text{ mode}) \end{array} \right]_{(N \times k)}$$

Partial Derivatives of c , U , and γ

All four kernels \mathbf{G}_p , \mathbf{G}_g , \mathbf{G}_q , and \mathbf{G}_a are derived in terms of partial derivatives of phase velocity c , group velocity U , and attenuation γ . In this section, We will give all partial derivatives which will be used in creating kernels.

Perturbation theory is used to obtain phase velocity partials with respect to medium parameters, and a numerical method introduced by Rodi *et al.* (1975) is used to calculate surface-wave group-velocity partial derivatives. The following equations apply to a single mode at a

certain frequency, therefore we omit the subscript n for the n 'th mode. The subscript 0 is used to denote the value before introducing causal Q. The velocity subscript v can be replaced by P -wave velocity α or S -wave velocity β . ρ is layer density. h is layer thickness. ω_r is a reference angular frequency used for introducing causal Q.

Rayleigh Waves

The equation for phase velocity, c , attenuation, γ , group velocity, U , and various partial derivatives with respect to these quantities are given as follows:

$$c = c_0 + \frac{1}{\pi} \ln\left(\frac{\omega}{\omega_r}\right) \Sigma \left[\frac{\partial c_0}{\partial \beta} \beta \mathbf{Q}_\beta^{-1} + \frac{\partial c_0}{\partial \alpha} \alpha \mathbf{Q}_\alpha^{-1} \right]$$

$$\gamma = \frac{\omega}{2c_0^2} \Sigma \left[\frac{\partial c_0}{\partial \beta} \beta \mathbf{Q}_\beta^{-1} + \frac{\partial c_0}{\partial \alpha} \alpha \mathbf{Q}_\alpha^{-1} \right]$$

$$U = U_0 \left[1 + \left(2 - \frac{U_0}{c_0}\right) \left(\frac{c - c_0}{c_0}\right) + \frac{2\gamma U_0}{\pi \omega} \right]$$

$$\frac{\partial c}{\partial v} = \frac{\partial c_0}{\partial v} \left[1 + \frac{1}{\pi \mathbf{Q}_v} \ln\left(\frac{\omega}{\omega_r}\right) \right]$$

$$\frac{\partial c}{\partial \rho} = \frac{\partial c_0}{\partial \rho} + \frac{1}{\pi} \ln\left(\frac{\omega}{\omega_r}\right) \left[\frac{\partial c_0}{\partial \beta} \left(-\frac{\beta}{2\rho}\right) \mathbf{Q}_\beta^{-1} + \frac{\partial c_0}{\partial \alpha} \left(-\frac{\alpha}{2\rho}\right) \mathbf{Q}_\alpha^{-1} \right]$$

$$\frac{\partial c}{\partial h} = \frac{\partial c_0}{\partial h}$$

$$\frac{\partial c}{\partial Q_v^{-1}} = \frac{1}{\pi} \ln\left(\frac{\omega}{\omega_r}\right) \frac{\partial c_0}{\partial v} v$$

$$\frac{\partial \gamma}{\partial v} = \frac{\omega}{2c_0^2} \frac{\partial c_0}{\partial v} Q_v^{-1} - \frac{2\gamma}{c_0} \frac{\partial c_0}{\partial v}$$

$$\frac{\partial \gamma}{\partial \rho} = \frac{\omega}{2c_0^2} \left[\frac{\partial c_0}{\partial \beta} \left(-\frac{\beta}{2\rho}\right) Q_\beta^{-1} + \frac{\partial c_0}{\partial \alpha} \left(-\frac{\alpha}{2\rho}\right) Q_\alpha^{-1} \right] - \frac{2\gamma}{c_0} \frac{\partial c_0}{\partial \rho}$$

$$\frac{\partial \gamma}{\partial h} = -\frac{2\gamma}{c_0} \frac{\partial c_0}{\partial h}$$

$$\frac{\partial \gamma}{\partial Q_v^{-1}} = \frac{\omega}{2c_0^2} \frac{\partial c_0}{\partial v} v$$

$$\frac{\partial U}{\partial v} = \frac{\partial U_0}{\partial v} \left[\frac{U}{U_0} - \frac{U_0}{c_0} \left(\frac{c-c_0}{c_0}\right) + \frac{2\gamma U_0}{\pi\omega} \right] + \frac{\partial c_0}{\partial v} \left(\frac{U_0}{c_0}\right)^2 \left[2\frac{c}{c_0} - 2\frac{c}{U_0} - 1 \right]$$

$$+ \frac{\partial c}{\partial v} \frac{U_0}{c_0} \left(2 - \frac{U_0}{c_0}\right) + \frac{\partial \gamma}{\partial v} \frac{2U_0^2}{\pi\omega}$$

$$\frac{\partial U}{\partial \rho} = \frac{\partial U_0}{\partial \rho} \left[\frac{U}{U_0} - \frac{U_0}{c_0} \left(\frac{c-c_0}{c_0}\right) + \frac{2\gamma U_0}{\pi\omega} \right] + \frac{\partial c_0}{\partial \rho} \left(\frac{U_0}{c_0}\right)^2 \left[2\frac{c}{c_0} - 2\frac{c}{U_0} - 1 \right]$$

$$+ \frac{\partial c}{\partial \rho} \frac{U_0}{c_0} \left(2 - \frac{U_0}{c_0}\right) + \frac{\partial \gamma}{\partial \rho} \frac{2U_0^2}{\pi\omega}$$

$$\frac{\partial U}{\partial h} = \frac{\partial U_0}{\partial h} \left[\frac{U}{U_0} - \frac{U_0}{c_0} \left(\frac{c-c_0}{c_0}\right) + \frac{2\gamma U_0}{\pi\omega} \right] + \frac{\partial c_0}{\partial h} \left(\frac{U_0}{c_0}\right)^2 \left[2\frac{c}{c_0} - 2\frac{c}{U_0} - 1 \right]$$

$$+ \frac{\partial c}{\partial h} \frac{U_0}{c_0} \left(2 - \frac{U_0}{c_0}\right) + \frac{\partial \gamma}{\partial h} \frac{2U_0^2}{\pi\omega}$$

$$\frac{\partial U}{\partial Q_v^{-1}} = \frac{U_0}{c_0} \left(2 - \frac{U_0}{c_0}\right) \frac{\partial c}{\partial Q_v^{-1}} + \frac{2U_0^2}{\pi\omega} \frac{\partial \gamma}{\partial Q_v^{-1}}$$

Love Wave

The corresponding quantities and partial derivatives for Love waves are as follows:

$$c = c_0 + \frac{1}{\pi} \ln\left(\frac{\omega}{\omega_r}\right) \sum \frac{\partial c_0}{\partial \beta} \beta Q_\beta^{-1}$$

$$\gamma = \frac{\omega}{2c_0^2} \sum \frac{\partial c_0}{\partial \beta} \beta Q_\beta^{-1}$$

$$U = U_0 \left[1 + \left(2 - \frac{U_0}{c_0}\right) \left(\frac{c - c_0}{c_0}\right) + \frac{2\gamma U_0}{\pi\omega} \right]$$

$$\frac{\partial c}{\partial \beta} = \frac{\partial c_0}{\partial \beta} \left[1 + \frac{1}{\pi Q_v} \ln\left(\frac{\omega}{\omega_r}\right) \right]$$

$$\frac{\partial c}{\partial \rho} = \frac{\partial c_0}{\partial \rho} + \frac{1}{\pi} \ln\left(\frac{\omega}{\omega_r}\right) \left[\frac{\partial c_0}{\partial \beta} \left(-\frac{\beta}{2\rho}\right) Q_\beta^{-1} \right]$$

$$\frac{\partial c}{\partial h} = \frac{\partial c_0}{\partial h}$$

$$\frac{\partial c}{\partial Q_\beta} = \frac{1}{\pi} \ln\left(\frac{\omega}{\omega_r}\right) \frac{\partial c_0}{\partial \beta} \beta$$

$$\frac{\partial \gamma}{\partial \beta} = \frac{\omega}{2c_0^2} \frac{\partial c_0}{\partial \beta} Q_\beta^{-1} - \frac{2\gamma}{c_0} \frac{\partial c_0}{\partial \beta}$$

$$\frac{\partial \gamma}{\partial \rho} = \frac{\omega}{2c_0^2} \left[\frac{\partial c_0}{\partial \beta} \left(-\frac{\beta}{2\rho} \right) Q_\beta^{-1} - \frac{2\gamma}{c_0} \frac{\partial c_0}{\partial \rho} \right]$$

$$\frac{\partial \gamma}{\partial h} = -\frac{2\gamma}{c_0} \frac{\partial c_0}{\partial h}$$

$$\frac{\partial \gamma}{\partial Q_\beta^{-1}} = \frac{\omega}{2c_0^2} \frac{\partial c_0}{\partial \beta} \beta$$

$$\begin{aligned} \frac{\partial U}{\partial \beta} &= \frac{\partial U_0}{\partial \beta} \left[\frac{U}{U_0} - \frac{U_0}{c_0} \left(\frac{c-c_0}{c_0} \right) + \frac{2\gamma U_0}{\pi \omega} \right] + \frac{\partial c_0}{\partial \beta} \left(\frac{U_0}{c_0} \right)^2 \left[2 \frac{c}{c_0} - 2 \frac{c}{U_0} - 1 \right] \\ &\quad + \frac{\partial c}{\partial \beta} \frac{U_0}{c_0} \left(2 - \frac{U_0}{c_0} \right) + \frac{\partial \gamma}{\partial \beta} \frac{2U_0^2}{\pi \omega} \end{aligned}$$

$$\begin{aligned} \frac{\partial U}{\partial \rho} &= \frac{\partial U_0}{\partial \rho} \left[\frac{U}{U_0} - \frac{U_0}{c_0} \left(\frac{c-c_0}{c_0} \right) + \frac{2\gamma U_0}{\pi \omega} \right] + \frac{\partial c_0}{\partial \rho} \left(\frac{U_0}{c_0} \right)^2 \left[2 \frac{c}{c_0} - 2 \frac{c}{U_0} - 1 \right] \\ &\quad + \frac{\partial c}{\partial \rho} \frac{U_0}{c_0} \left(2 - \frac{U_0}{c_0} \right) + \frac{\partial \gamma}{\partial \rho} \frac{2U_0^2}{\pi \omega} \end{aligned}$$

$$\begin{aligned} \frac{\partial U}{\partial h} &= \frac{\partial U_0}{\partial h} \left[\frac{U}{U_0} - \frac{U_0}{c_0} \left(\frac{c-c_0}{c_0} \right) + \frac{2\gamma U_0}{\pi \omega} \right] + \frac{\partial c_0}{\partial h} \left(\frac{U_0}{c_0} \right)^2 \left[2 \frac{c}{c_0} - 2 \frac{c}{U_0} - 1 \right] \\ &\quad + \frac{\partial c}{\partial h} \frac{U_0}{c_0} \left(2 - \frac{U_0}{c_0} \right) + \frac{\partial \gamma}{\partial h} \frac{2U_0^2}{\pi \omega} \end{aligned}$$

$$\frac{\partial U}{\partial Q_\beta^{-1}} = \frac{U_0}{c_0} \left(2 - \frac{U_0}{c_0} \right) \frac{\partial c}{\partial Q_\beta^{-1}} + \frac{2U_0^2}{\pi \omega} \frac{\partial \gamma}{\partial Q_\beta^{-1}}$$

3.4 Forming Inversion Kernel

As shown above, we calculate partial derivatives with respect to all parameters (α , β , ρ , Q_α , Q_β , h) instead of computing partial derivatives for shear velocity only. The intention is that we try to provide all the possible tools to interpret the seismograms as completely as possible, and as automatically as possible. Therefore, it is the user's responsibility to choose those specific model parameters to invert for; and only the chosen part will be used to assemble the inversion kernel.

To stabilize the inversion, all information for different frequencies inside the inversion kernel are weighted according to their frequency amplitudes. This weighting procedure greatly improves the inversion stability.

When inverting teleseismic surface-wave waveforms, sometimes the body waves (e.g. *SS*, *SSS*) or some unwanted surface waves due to improper rotation will adversely affect the cross-correlation between the isolation function and the observed seismogram, and resulting in signal misalignment. To avoid this problem, a window is applied to the seismograms before cross-correlation, and this may successfully isolate the surface-waves from body waves. Although a pre-windowing procedure is applied, the same trouble may still happen occasionally. In such a situation, the information at that frequency must be rejected when forming the inversion kernel, otherwise it will plague the inversion for its strongly misaligned "phase delay" or "group delay." Figure 3.1 shows an example of this problem. Because of improper rotation,

the unwanted Love-wave waveform appears on the radial component seismogram prior to the Rayleigh wave wavetrain. This unwanted Love wave signal causes two problems, misidentification of a Gaussian wavelet (Figure 3.1a) and signal misalignment (Figure 3.1b), which can not be incorporated in inversion.

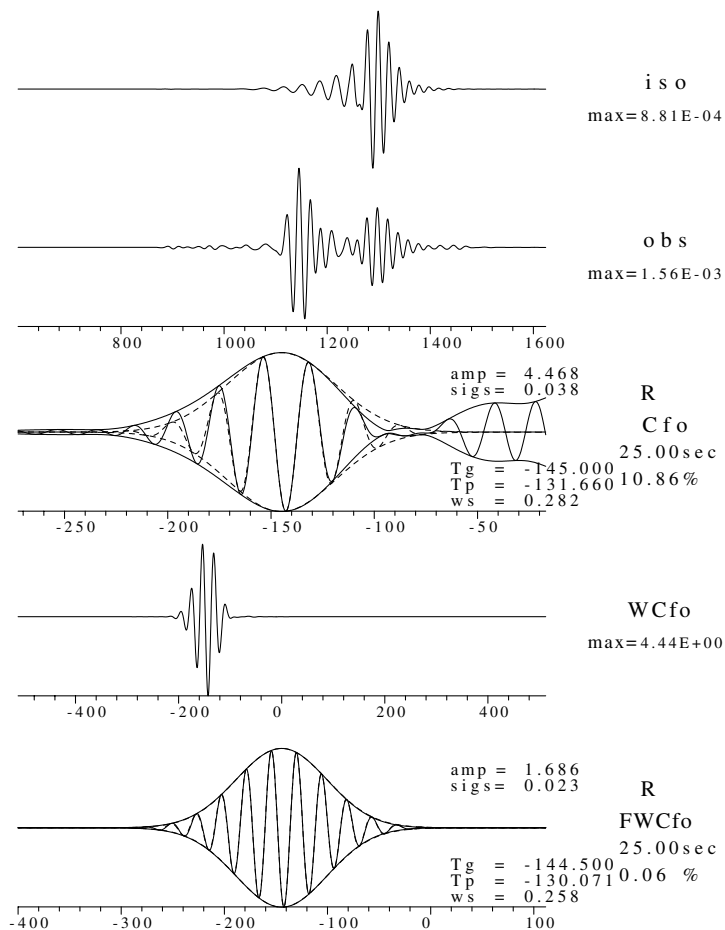


Fig. 3.1b. (cont'd). (b) Misalignment of signals which produces significant bias phase and group delay. This arises because a period of 25 seconds is considered compared to 20 seconds in Fig. 3.1a.

We have mentioned that users have the power to decide what parameters will be inverted for during the inversion. An aspect which

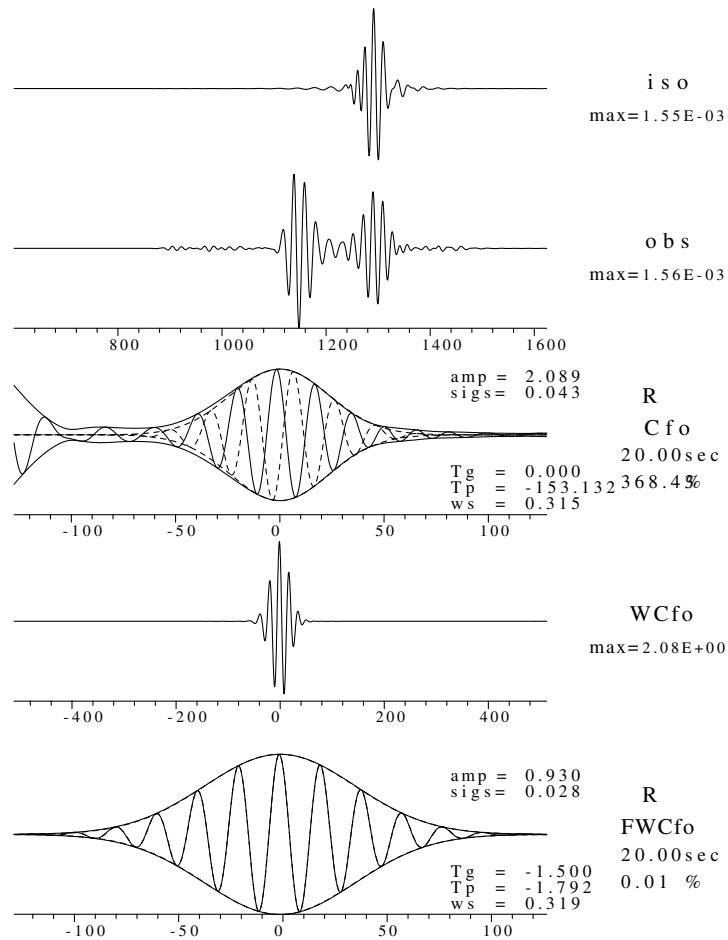


Fig. 3.1a. This is an example showing how unexpected signal interference affects the extracting procedure in GSDF theory. There are five traces presented to show the different processing stages. The top two traces are the prefiltered isolation filter and observed seismogram, respectively, The third trace shows the Gaussian filtered cross-correlation at a target period of 20.0 seconds. The five extracted parameters are shown. The dashed curve inside the envelope is from the synthetics and the solid curve is from the observed data. The fourth trace is the windowed cross-correlagram from the third trace. The bottom trace is the filtered windowed cross-correlagram and its five Gaussian wavelet parameters which are to be used in further processing. Due to improper rotation, the Love wave appears on radial component before the Rayleigh wave arrival. The Love wave wavetrain may causes error (a) wrong determination of Gaussian wavelet parameters, and

is strongly related to this decision is the phrase "using what kind

information." During each iteration in the inversion, we have calculated partial derivatives with respect to parameters for each layer at several appointed frequencies, and all this information is rearranged to form four kinds of delay at each frequency. After manually rejecting miscalculated cross-correlations at some frequencies, users have to decide which combinations of δt_p , δt_g , δt_a , δt_q they will use to invert for a particular combination of model parameters (α , β , ρ , Q_α , Q_β , h). From our experience, we found that when we invert for velocity structure the phase delay (δt_p) and the group delay (δt_g) play major roles in inversion, and the other two delays (δt_a , δt_q) are better in inverting for attenuation factors. We also found that when the initial model is far from the final result, using group delay information in the inversion can easily pull the model close enough to the final model so that phase delays can be used. It only at the final stage when the synthetic is very close to the observed seismograms that the phase delay information can be used for a powerful fine tuning of the model since there is no "cycle skipping" problem.

3.5 Synthetic Test

A simple source with strike, dip, rake angles of 45° , 45° , 45° , respectively, at a 20 km depth was used in this synthetic test. The receiver is located 1000 km away along a line with an azimuth of 10° . The "observed" seismograms were created for a two layered crust with an upper mantle deviating slightly from the PREM model (Figure 3.2).

Here, we only try to invert for shear velocity structure, so all the other parameters related to the source and earth model are assumed to be known. The starting model is a two-layered crustal model overlying a PREM mantle. Figure 3.3 shows that the starting synthetic seismograms after greatly slow "observed" seismograms.

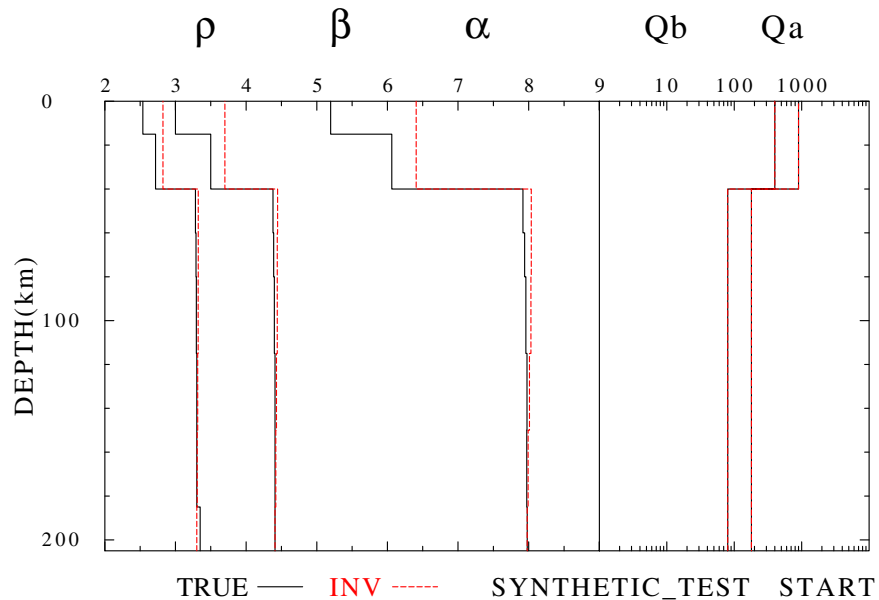


Fig. 3.2. The starting model (dashed line) used in synthetic test of the GSDF inversion algorithm and the 'true' model (solid line) used to create the 'observed data'.

After 12 iterations, the synthetic seismograms are almost the same as the "observed" seismograms (Figure 3.4). Checking the model differences between the "true" model and the final model (Figure 3.5), we can see that the structure almost matches the "true" model, except in the upper mantle where the surface waves do not provide enough resolving power, causing the "zig-zag" pattern. The differences in Q models are not significant at these frequencies and this distance.

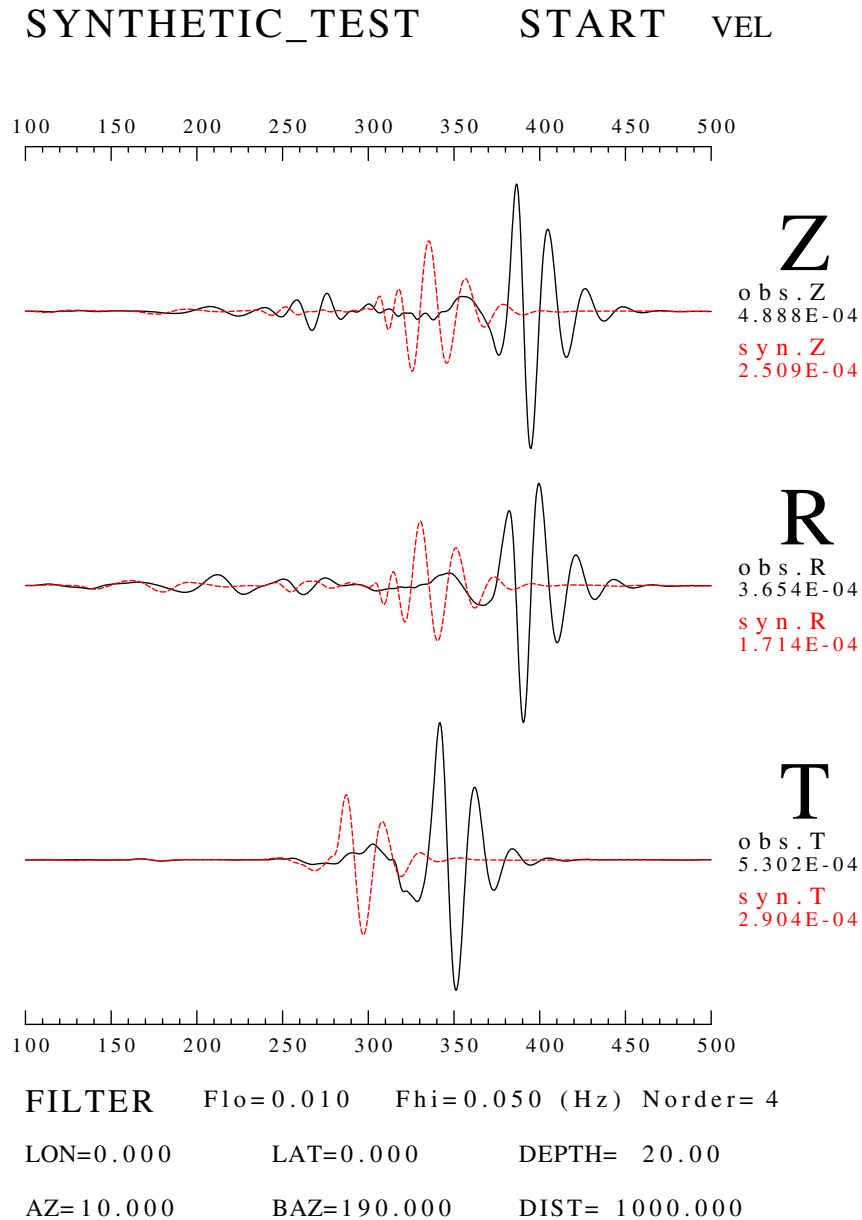


Fig. 3.3. The velocity time histories of 'observed seismograms' (solid line) and the those from the starting model (dashed line) are both filtered in the frequency band 0.01-0.05 Hz by using a Butterworth filter with four poles. The plotted seismograms are normalized according the maximum amplitude of each component in the current frequency band. It is clear that the starting model is not close to the 'true' model and this may test the ability of the inversion programs to resolve structure.

3.6 Real Data Test

After the successful synthetic test, we wish to test this technique on real data. The April 14, 1995 Texas earthquake provides useful data for this purpose. According to the USGS solution, the epicenter of the Texas earthquake is at 30.261°N 103.33°W and the origin time is 00:32:55UT. The current collected data set consists of 89 broadband records from IRIS, Canadian National Seismological Center (CNSDC), USGS, UNAM, and PASSCAL instruments (Figure 2.1).

Some source parameters were refined on the basis of fitting surface-wave amplitude spectra (Table 2.2). The redetermined source depth is 20 km deep, with strike, dip, rake angles of 114° , 64° , -101° , respectively and $M_w = 5.6$.

3.7 Inversion Procedure

We have tried three different inversion runs, the first two had major problems in matching the waveform or in the reasonableness of the resulting model, so the third one was adopted for inverting structure. In performing the inversions, we use an earth flattening approximation to use plane-layered surface-wave theory to generate synthetics.

The first run consisted of a joint inversion of both Rayleigh and Love wave seismograms for shear velocity structure. The result was that that the synthetic seismograms tended to fit the largest surface

SYNTHETIC_TEST FINAL VEL

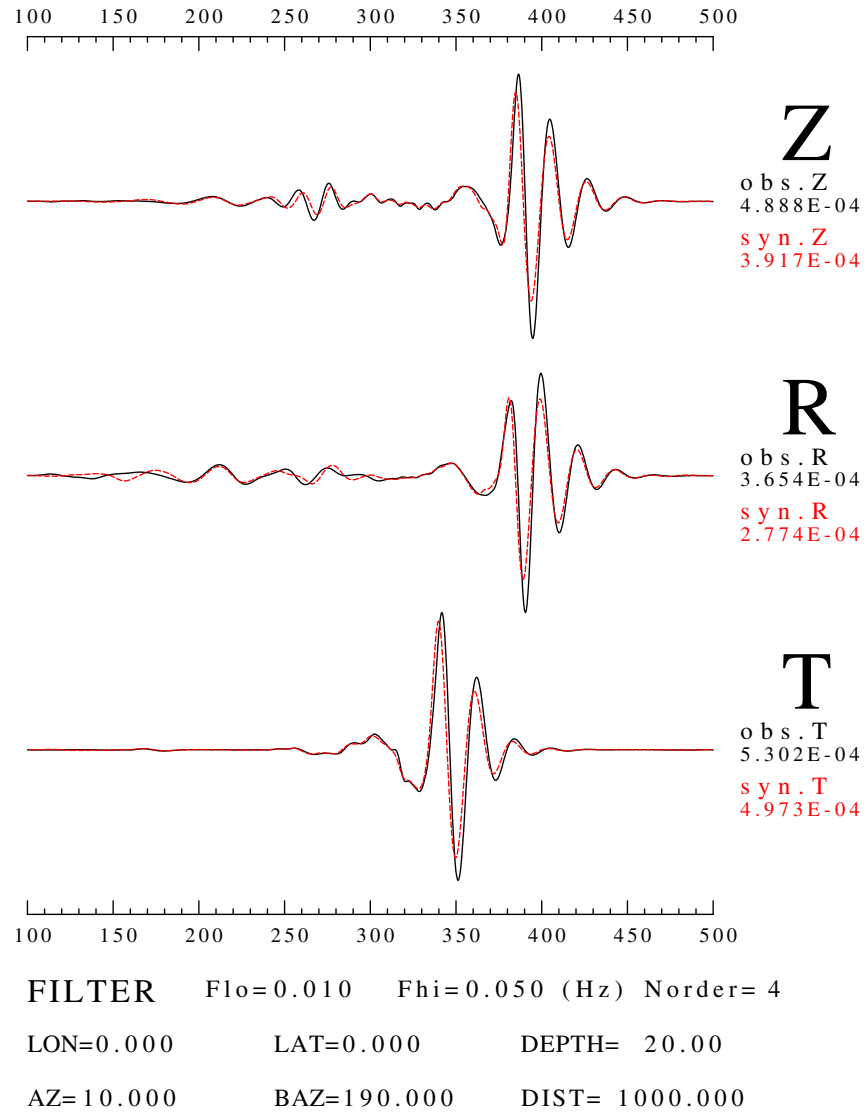


Fig. 3.4. After 12 iterations, the final inversion result shows a predicted waveforms that closely agree with 'observed seismograms'.

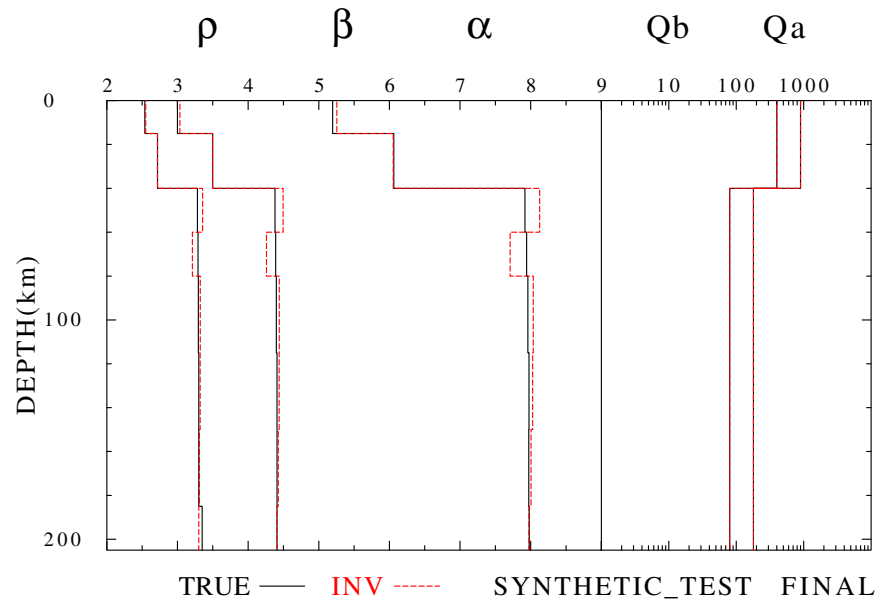


Fig. 3.5. The comparison between the final model and the 'true model'. We can see that the 2-layer crust is very close to the 'true' model, but that in the upper mantle the model fluctuates around the 'true model'.

wave amplitude, and ignored the small amplitude wavefields. This arose because of the amplitude level weighting used to stabilize the inversion. Therefore, separate inversions for Rayleigh wave and Love wave were necessary.

The second inversion sequence consisted of inverting for the shear velocity structure from the Love wave, and then using this structure as an *a priori* shear velocity structure so the the Rayleigh wave provided information on the compressional velocity structure. This procedure can match both Rayleigh wave and Love wave waveforms very well, but we found it is impossible to find a reasonable explanation for the anomalous Poisson's ratios in the inverted model. It is well known that the lower mode Rayleigh wave are insensitive to compressional

wave velocity structure, so the only conclusion for this is that the shear velocity structure inverted from Love wave is not adequate for explaining Rayleigh wave. An unaccounted anisotropy effect may cause the overcorrection in compressional velocity structure. Figure 3.6 compares waveforms and Figure 3.7 shows the model resulting from the second inversion procedure. Although the synthetic waveform does not perfectly fit the Rayleigh wave (Figure 3.6), we can see the general features are matched using a single model for both Love and Rayleigh waves. In Figure 3.7 we see that the P-wave velocity structure has lower values to compensate for the high shear velocity, and vice versa. This results in some unexplainable Poisson's ratios such as 0.135 for the middle crust and 0.328 for the lower crust.

Since our forward synthetic seismogram algorithm does not include anisotropy effects, we modify our inversion procedure as follows: we invert for $V_{\beta_{SH}}$ from Love waves, and use another separate inversion to get $V_{\beta_{PSV}}$ from the Rayleigh wave on the vertical component. We fixed the Poisson's ratio when we invert for $V_{\beta_{PSV}}$. The fixed Poisson's ratios are kept the same as the original input model. In this study, we set the Poisson's ratio at 0.25 for the crust, 0.28 for the layers between 40 km and 220 km, and adopt the values from PREM model for those layers deeper than 220 km.

When we invert for the shear-wave velocity structures, the attenuation factors can be determined simultaneously either by joint inversion of V_{β} and Q or by a subsequent Q inversion. The Q determination is not definitive, since we have many uncertainties in our source and

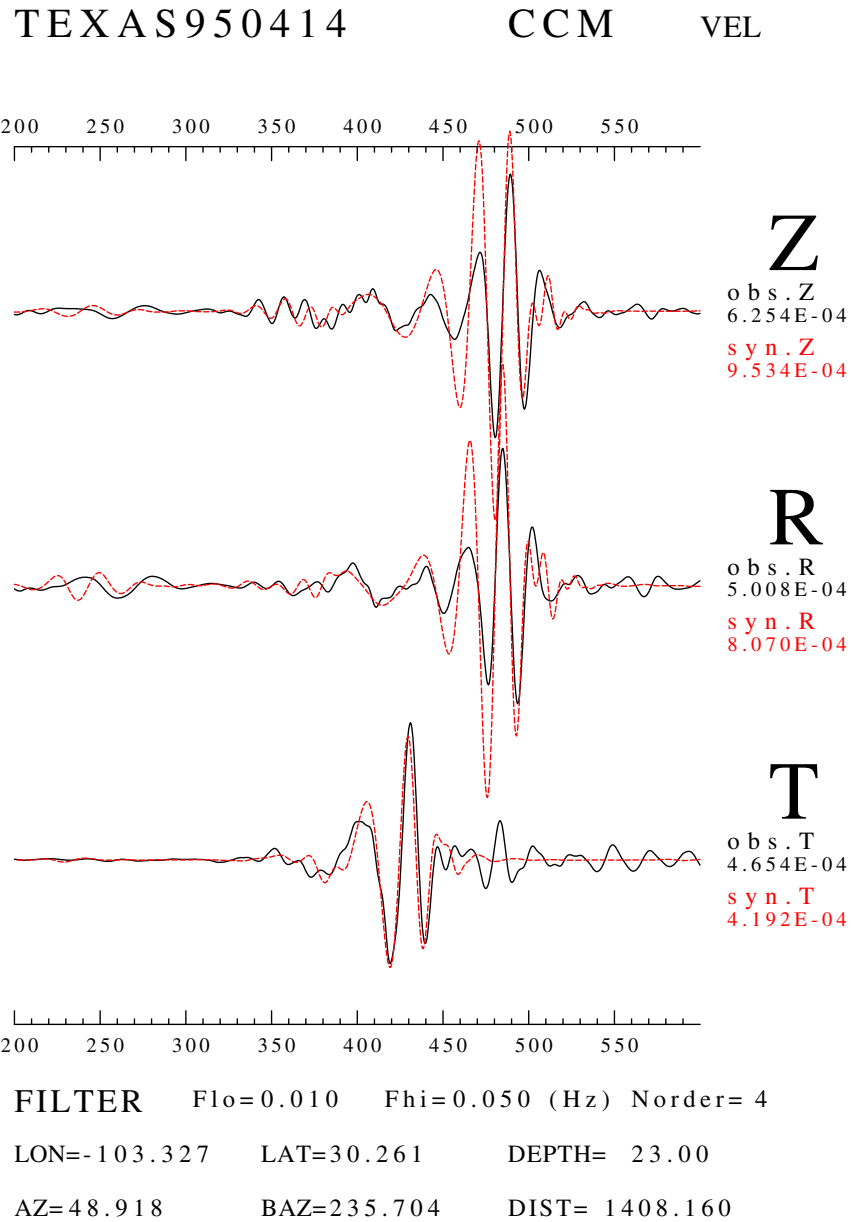


Fig. 3.6. The result of inversion using the second procedure. This inversion procedure first obtains the S wave velocity from the Love wave and then inverts for the P wave velocity from Rayleigh wave by assuming no anisotropy effect. This shows a acceptable waveform match in phase, but not in envelope.

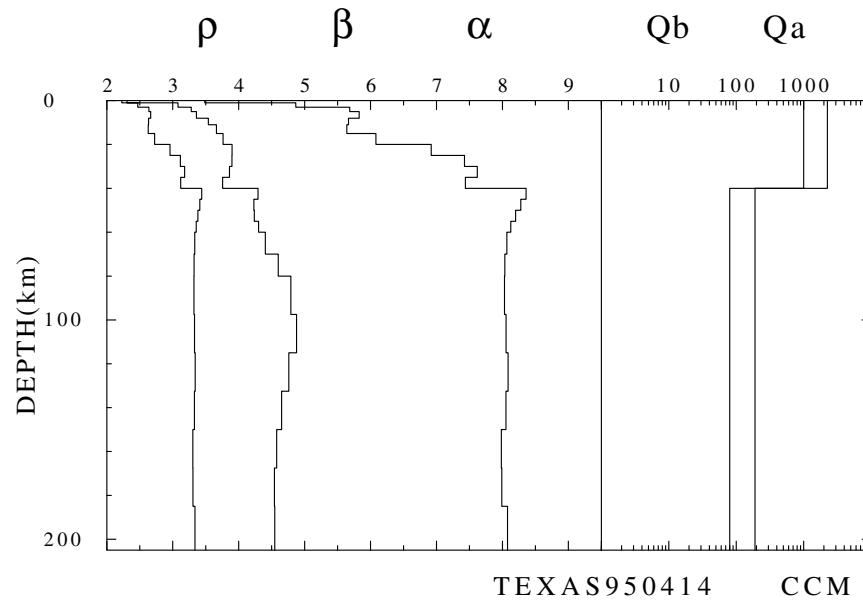


Fig. 3.7. The model inverted by the second inversion procedure.

velocity structures in our inversion, so the only objective criterion for determining Q is the envelope shape of the surface waves. As shown on Figure 3.8, the Rayleigh wave signal at large distance is well dispersed with a strong Airy phase. This Airy phase is affected by crustal wave propagation; therefore, the envelope amplitude of the Airy phase is controlled by the crustal attenuation factors. So the Q structure determined is sensitive to the crust and uppermost mantle.

3.8 Inversion Results

Data from 43 of 89 broadband stations were inverted. In this report, three representative stations were selected to present the inversion results. The waveform fitting success will be shown in

several different frequency bands.

Station ALE, which is located in Arctic Canada is the farthest station used in this study. There are some interesting features in the inverted results. Looking at the waveform fit in the low frequency range (0.005-0.03 Hz bandpass; shown as Figure 3.8a), it is clear to see that the synthetic seismograms successfully match the observed surface wave. Two velocity models, PSV and SH are obtained respectively from Rayleigh wave and Love wave.

For ALE, the attenuation factor was fixed during inversion (Figure 3.9). A high Q structure ($Q_S = 1000$) is used for crust, a low Q ($Q_S = 100$) was adopted for structure between 40 km and 500 km, and $Q_S = 143$ for those depths greater than 500 km. And from Figures 3.8a,b, the synthetic Rayleigh wave and Love wave amplitudes only show small deviations from observed seismograms; therefore the Q model is considered adequate. We also note that the sharp Q contrast between the crust and mantle is a common feature for those stations located inside the North America craton.

The second station is FCC which located on the west shoreline of Hudson Bay and is in the center of the North American craton. The inverted models (Figure 3.10) show high shear velocity for upper mantle but not as high as SNA model (Grand and Helmberger, 1984). The current inversion result shows 4.5% anisotropy between 70 km and 140 km. The synthetics fit data well at low frequency (Figure 3.11a) and can fit the fundamental mode as high as 0.1 Hz (Figure 3.11), but have difficulty in producing some higher mode arrivals between 800

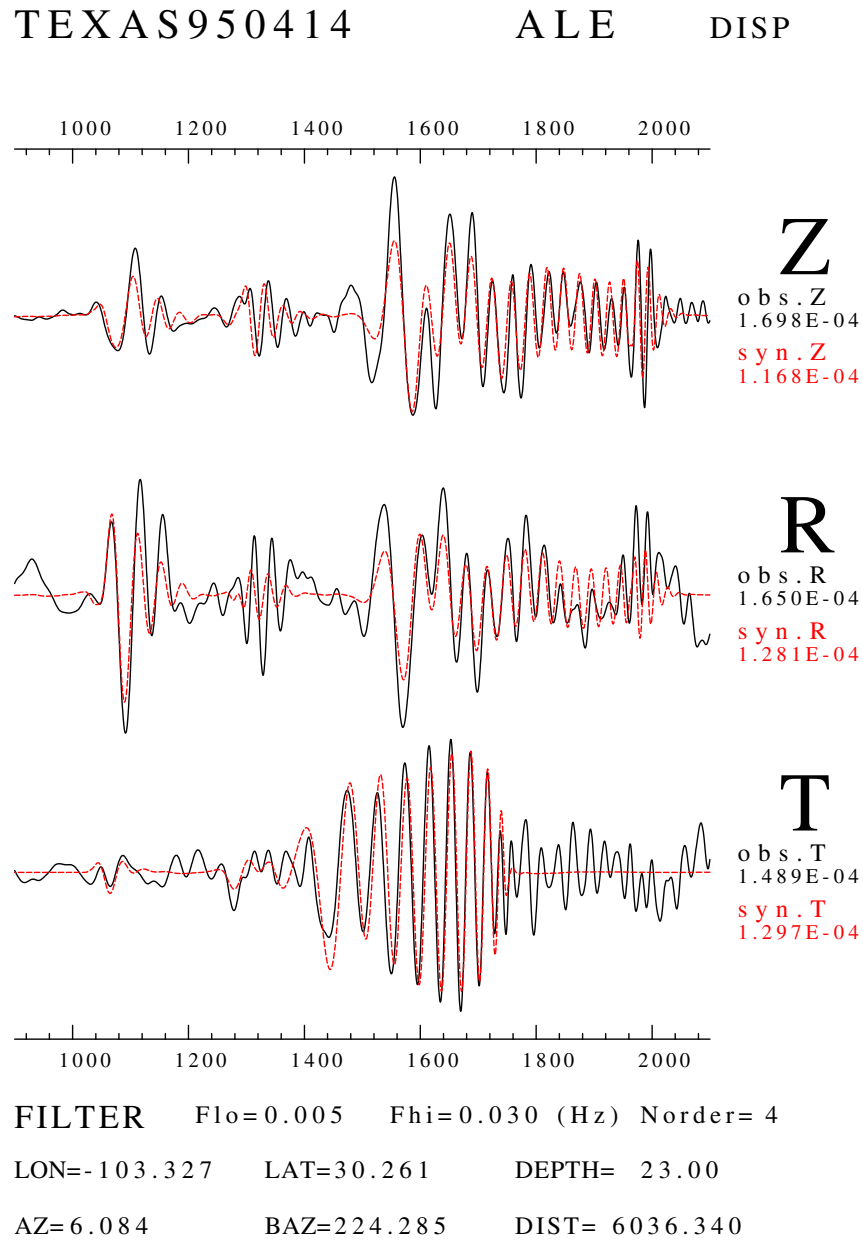


Fig. 3.8a. Waveform fit of the final inverted model for ALE in the frequency band of 0.005-0.03 Hz. The signal which arrives at 1020 seconds and around 1300 seconds are the S and SS phases, respectively. From the S phase waveform, we can say that the source time function used in this inversion is a little short but is close enough.

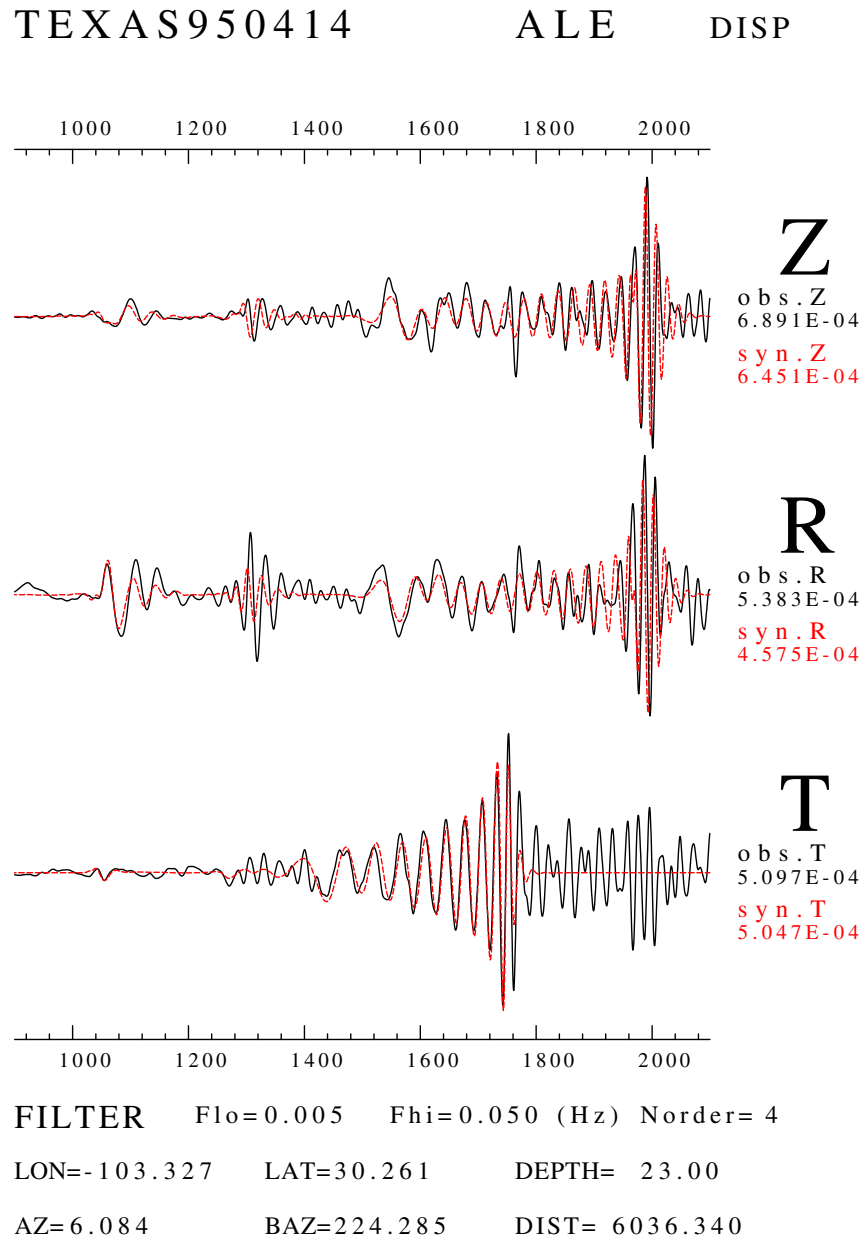


Fig. 3.8b. (Cont'd). Waveform fit in the 0.005-0.05 Hz frequency band.

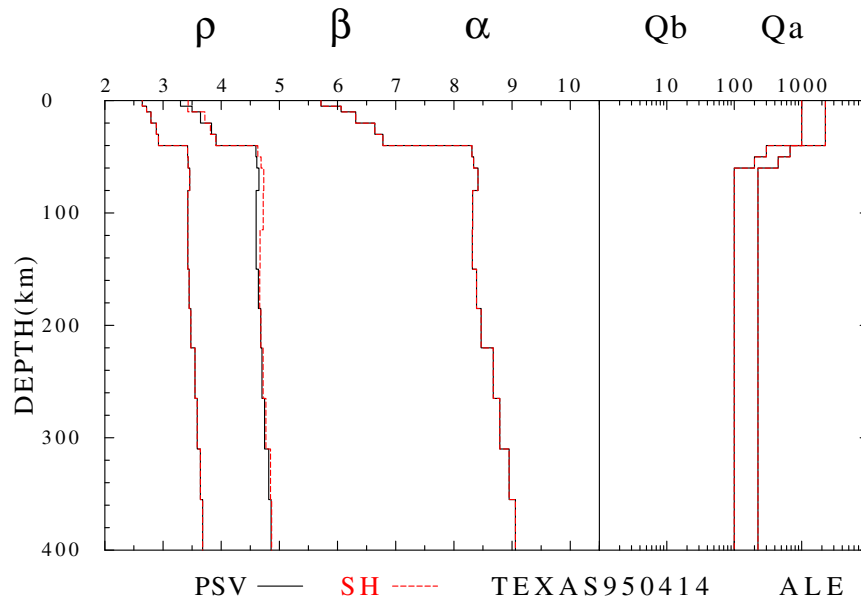


Fig. 3.9. The inverted models for ALE. Two models (PSV and SH) were obtained from the Love wave and Rayleigh Wave. Comparing these two models, there is one slight anisotropic zone above 200 km.

and 940 seconds.

The final station is PAS. The wave propagates through the southern Basin and Range. The inverted model (Figure 3.12) does not require anisotropy and the shear velocity model is very close to the TNA model (Grand and Helmberger, 1984). The synthetics fit the S phase which arrives at 350 seconds and the surface wave very well (Figures 3.13abc). The model suggests that a velocity discontinuity at 220 km which cannot be seen in the TNA model. Q is very low, with the average Q for crust of lower than 200. However we found one interesting feature about the Q behavior. The Q values between 40 and 220 km are slightly higher than those for the PREM model, i.e., a low Q crust overlying a slightly higher Q upper mantle with respect to

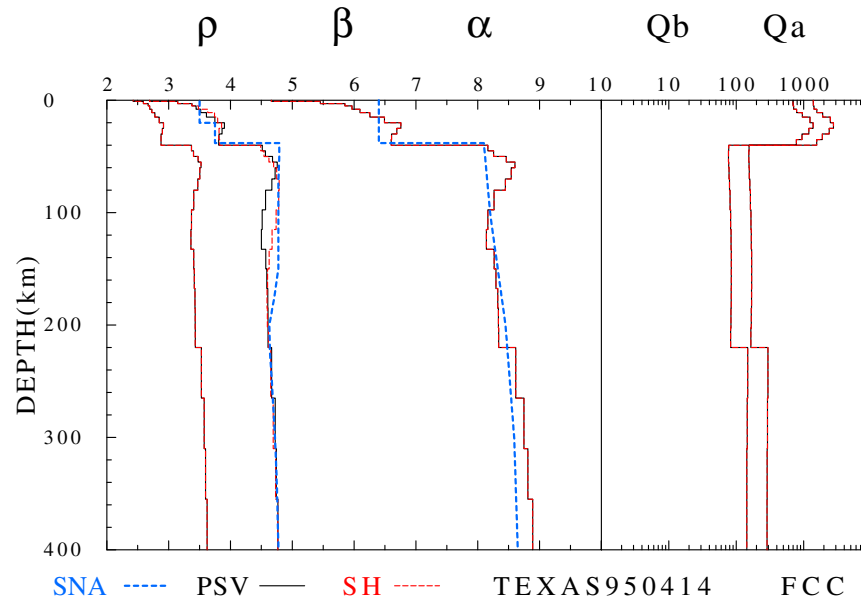


Fig. 3.10. The final inverted model for FCC. There is 4.5% anisotropy effect exists between 70 and 140 km.

the reference model.

3.9 Conclusion

We implemented the Generalized Seismological Data Functionals technique of Gee and Jordan (1992) in a surface-wave waveform inversion algorithm. A simple synthetic test shows its robust inversion ability. After a successful synthetic test, we used this inversion algorithm on real data to further test its ability. The Texas earthquake (30.26 °N 103.33°W, 00:32:55UT, April 14, 1995) is a very good earthquake for this purpose because it was well recorded, its source depth is well constrained, the focal mechanism is fairly well determined, and

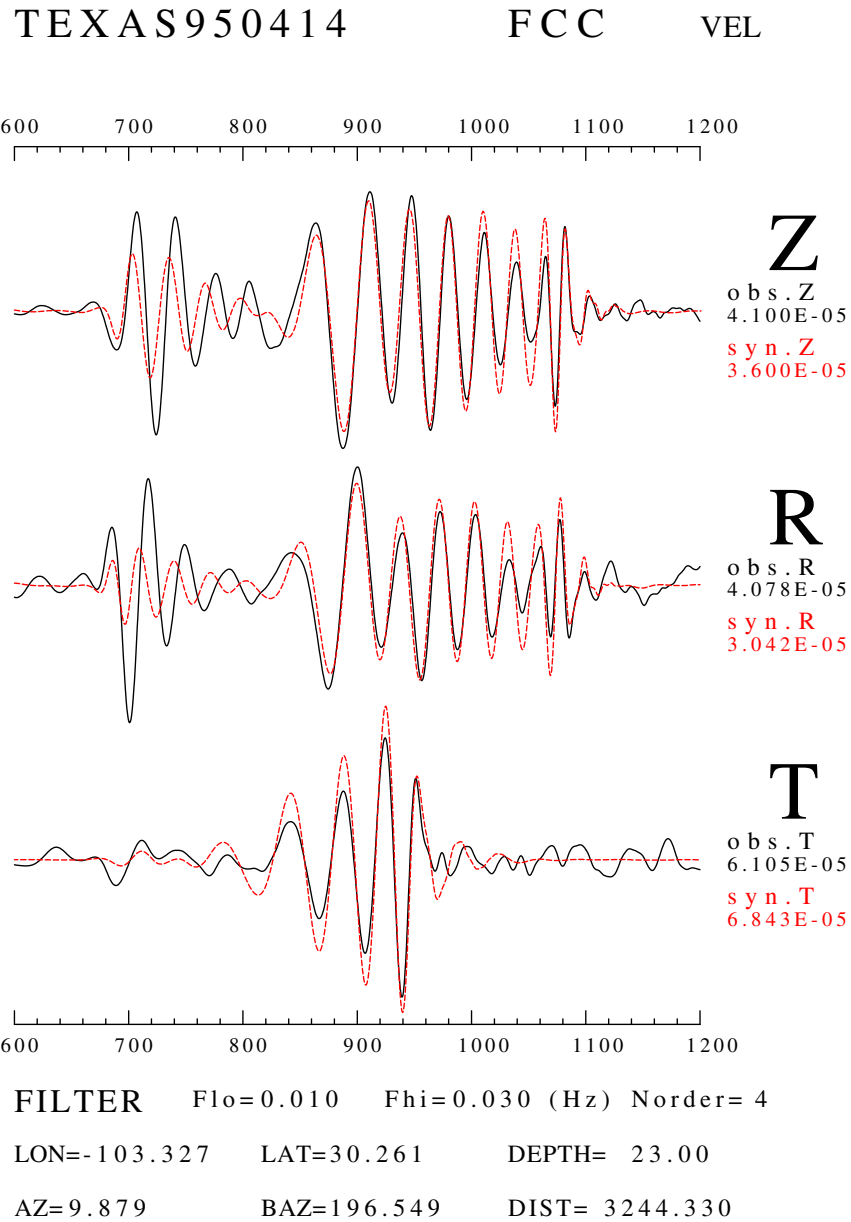


Fig. 3.11a. The waveform fit for the final model for FCC is shown at three frequency bands : (a) 0.01-0.03 (b) 0.01-0.05 (c) 0.01-0.1 Hz. The SS phase arrives at 660 seconds. The inverted model can fit fundamental mode Love wave and Rayleigh wave waveforms as high as 0.1 Hz, but it lacks the ability to simulate the high frequency higher modes.

TEXAS950414

FCC

VEL

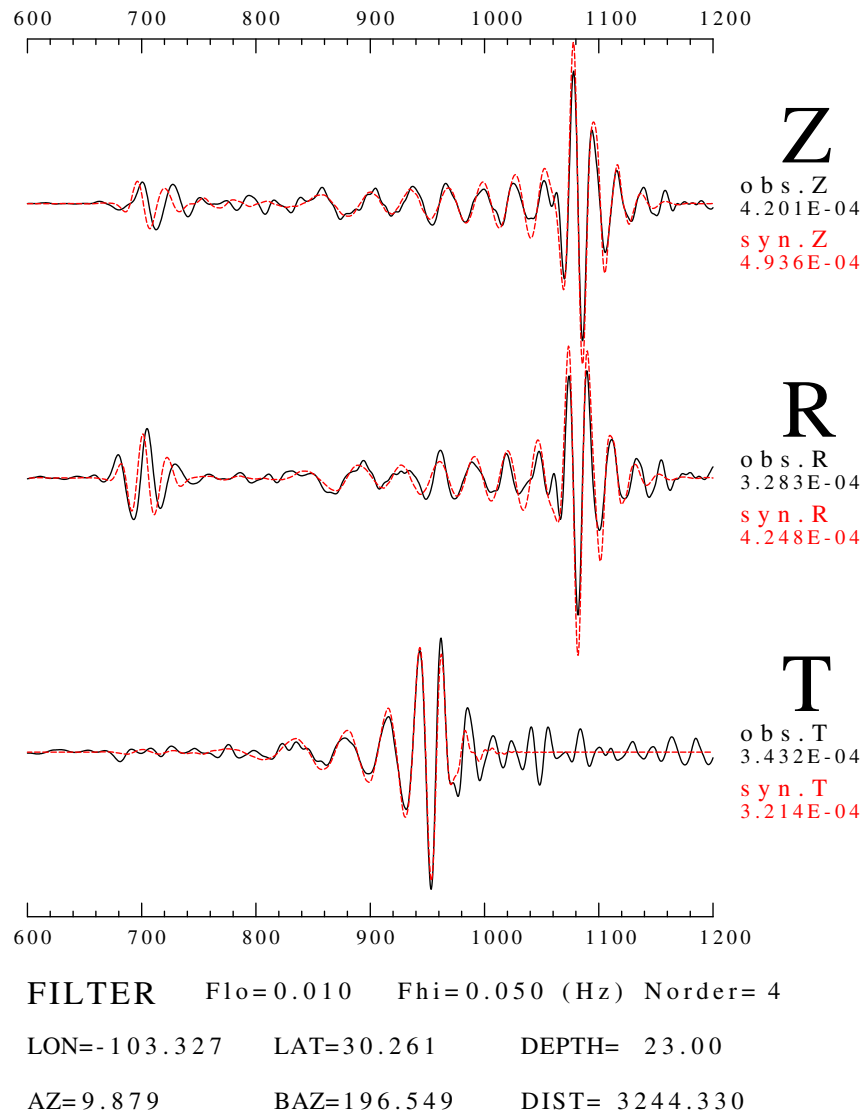


Fig. 3.11b. (Cont'd). (b) 0.01-0.05 Hz.

TEXAS950414

FCC

VEL

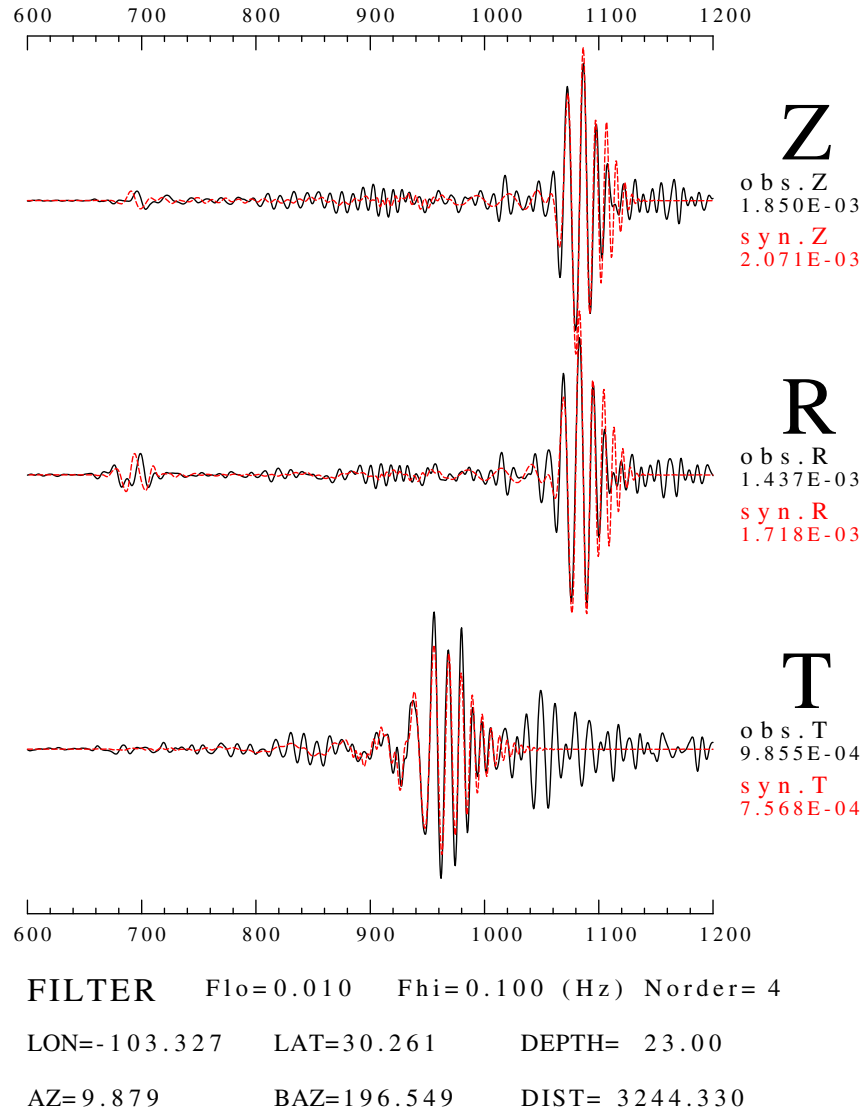


Fig. 3.11c. (Cont'd). (c) 0.01-0.1 Hz. The SS phase arrives at 660 seconds. The inverted model can fit fundamental mode Love wave and Rayleigh wave waveforms as high as 0.1 Hz, but it lacks the ability to simulate the higher modes.

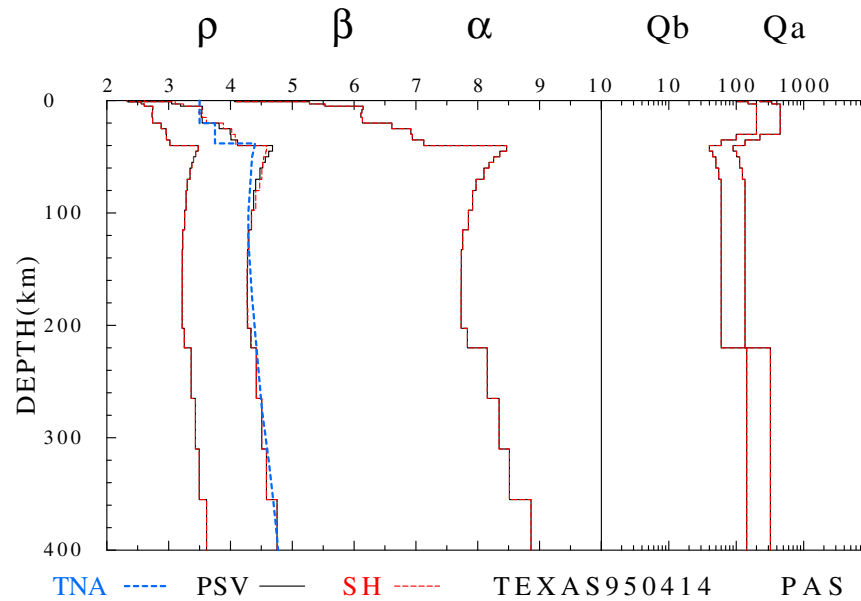


Fig. 3.12. The inverted models for PAS. There are no clear anisotropy effects. The crustal Q is very low.

the seismic moment is constrained by long-period surface waves. The inversion results are excellent and show some interesting features that agree with results of other studies. For the craton there is some evidence for anisotropy and crustal Q is high. For the mountain region, although the inverted model shows a shear velocity structure similar to the TNA model, but the model prefers a velocity discontinuity at 220 km. More effort is required to define the confidence on these features.

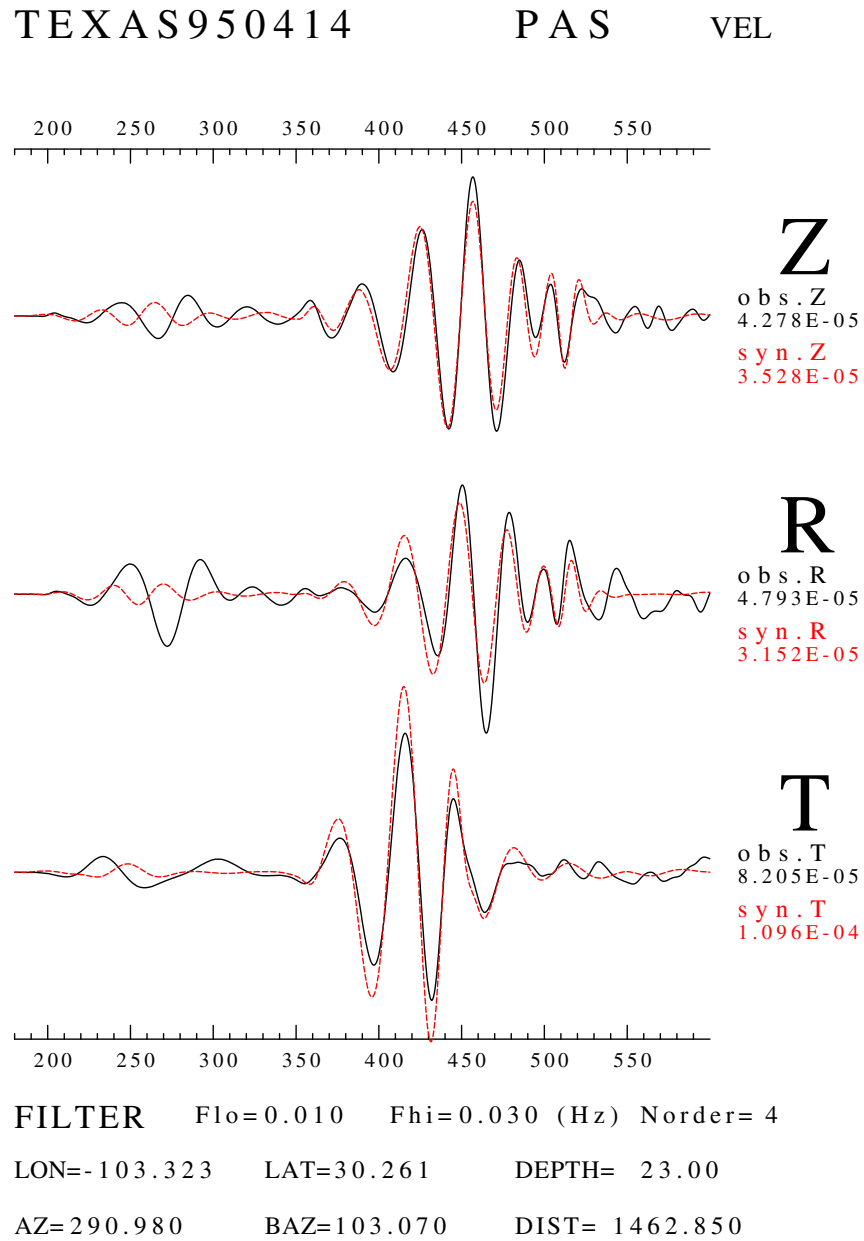
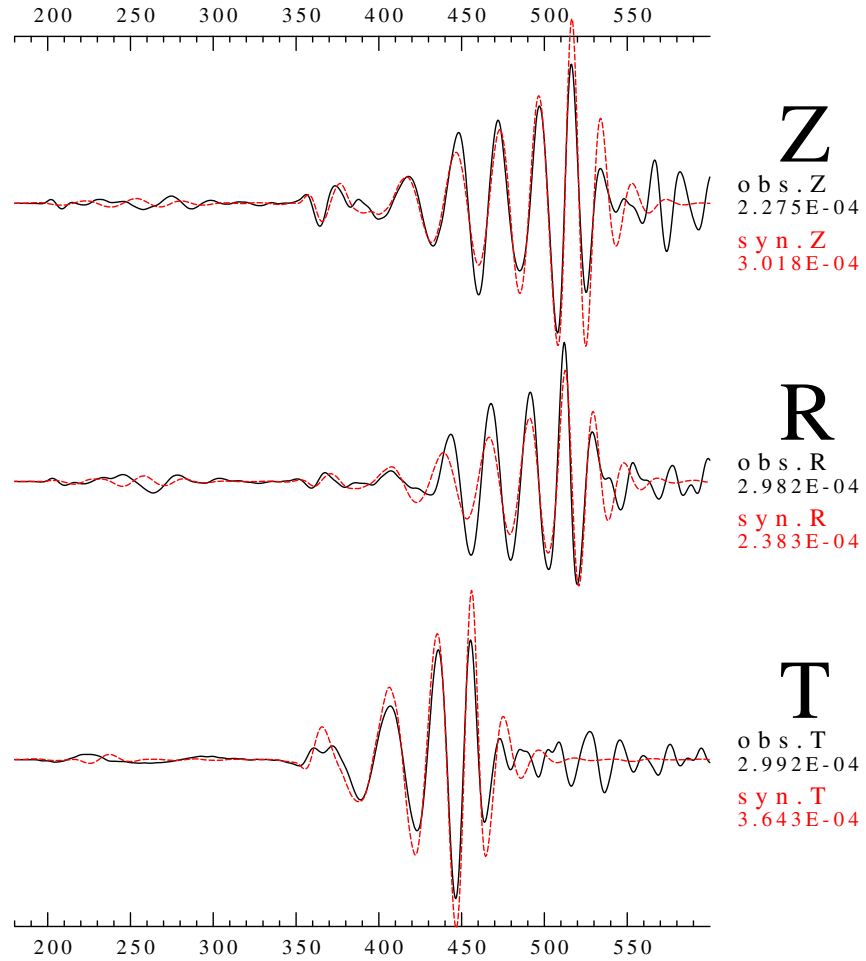


Fig. 3.13a. Waveform fitting is shown on three frequency bands: (a) 0.01-0.03 (b) 0.01-0.05 and (c) 0.01-0.1 Hz. The S wave signal arrives at 350 seconds.

TEXAS950414 P A S V E L



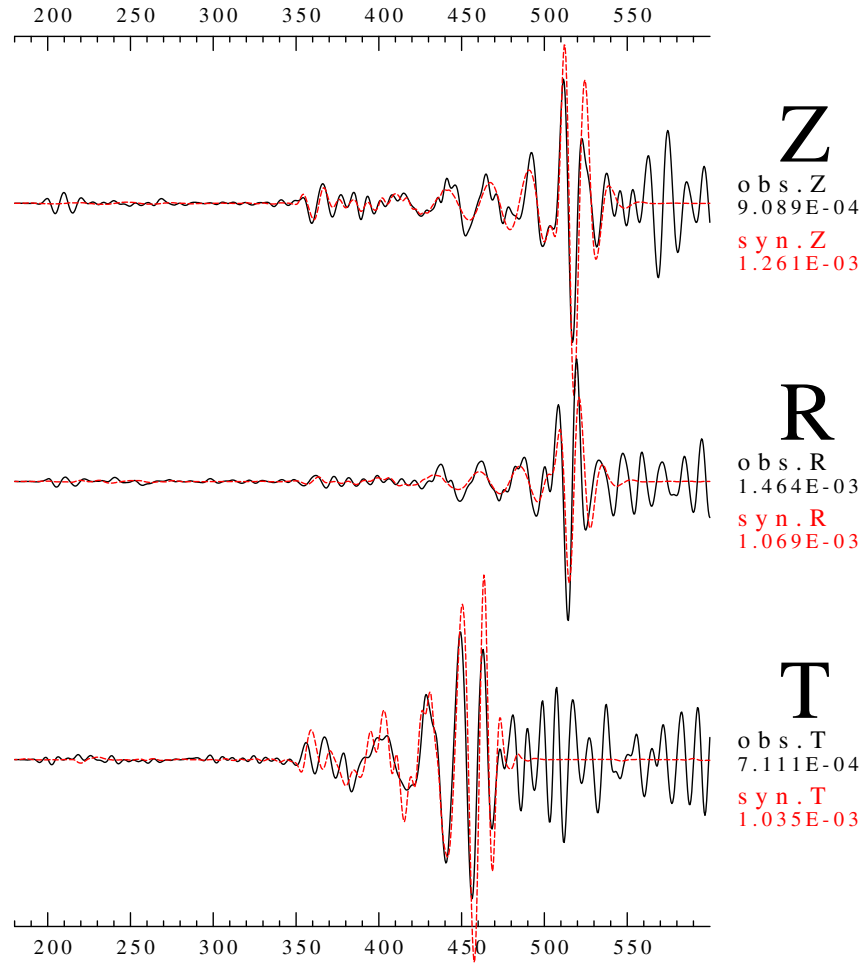
FILTER Flo=0.010 Fhi=0.050 (Hz) Norder= 4

LON=-103.323 LAT=30.261 DEPTH= 23.00

AZ=290.980 BAZ=103.070 DIST= 1462.850

Fig. 3.13b. (Cont'd). (b) 0.01-0.05 Hz.

TEXAS950414 PAS VEL



FILTER Flo=0.010 Fhi=0.100 (Hz) Norder= 4

LON=-103.323 LAT=30.261 DEPTH= 23.00

AZ=290.980 BAZ=103.070 DIST= 1462.850

Fig. 3.13c. (Cont'd). (c) 0.01-0.1 Hz.

CHAPTER 4

GENETIC ALGORITHMS

Most seismological inverse problems are nonlinear. The techniques used to solve such nonlinear problems can be placed into two groups. The strategy of the first group is to linearize nonlinear problems, then use iterative processes to seek a better solution by using the gradient information of the misfit function. The strategy of the second group is to directly search the model space, and find the acceptable models.

Methods such as least squares, steepest descents, and conjugate gradient belong to the first group. Although these methods are widely used in seismology, the requirement of a good starting model is a well-known disadvantage. For studying large scale large wavelength features or deep features beneath the lithosphere, this would not be a real problem because the research of the past half century already provide some good starting models such as PREM, IASPEI91 (Kennett and Engdahl, 1991). On the other hand, for studying the crustal or lithospheric structures, a good starting model may not be available because the crust or lithosphere is the most structurally heterogeneous region in the Earth. Studying the lithosphere is important because

the evolution history of the lithosphere is hidden in its structure. We have to investigate the structure of the crust and lithosphere all over the world to study evolutionary history, to understand the tectonic processes, to better predict seismic activity, and to lower the damage of earthquake hazards.

Based on such a situation, we need to find a way to investigate many possible models, i.e. to search the whole model space and to select the acceptable models of structure and their variations. The Monte Carlo, simulated annealing (SA), and genetic algorithms (GA) search methods are belong to this group. The Monte Carlo method is a random search method which has been used in seismology for a long time (e.g. Keilis-Borok and Yanovskaja, 1967; Press, 1968). Press (1968) showed a successful experiment which used the Monte Carlo method to search for the model that can produce correct body-wave travel-times, surface-wave dispersion, the earth's free oscillation periods, mass, and moment of inertia. Six models were found from about five million randomly generated models. As pointed out by Press (1968), the reason for using the Monte Carlo method is that it offers the advantage of exploring the range of possible solutions and indicates the degree of uniqueness achievable with currently available geophysical data. Examining these six models, we can find that the structures for the lower mantle are consistent, but that large variations occur in the upper mantle. However, the Monte Carlo method has its own disadvantages. As pointed out by Keilis-Borok and Yanovskaja (1967), the Monte Carlo method does not use information obtained

from previous trials in the next trial.

Recently, simulated annealing and genetic algorithms methods have become very popular in seismology. The simulated annealing method mimics the crystalizing process observed in chemistry. The genetic algorithm is inspired by the evolution process observed in biological science. These two algorithms are better search methods to determine a global best fit than the Monte Carlo method because they use information obtained in previous trials. The seismological applications have been the estimation of residual statics (Rothman, 1985, 1986), waveform inversion of reflection data (Sen and Stoffa, 1992; Stoffa and Sen, 1991; Sambridge and Drijkoningen, 1992), earthquake hypocenter location determination (Sambridge and Gallagher, 1993), and receiver function inversion (Shibutani, Sambridge, and Kennett, 1996). There is one thing in common for all these applications; they all deal with nonlinear problems.

For example, in receiver function inversion, Ammon *et al.* (1990) showed that the final models were dependent on the initial models. Shibutani *et al.* (1996) showed that use of the genetic algorithm can estimate an average model which is more stable and less dependent on the starting assumptions.

We can see that both simulated annealing (SA) and genetic algorithms (GA) are good ways to perform the uncertainty assessment in a complicated nonlinear problem. As stated by Sambridge and Drijkoningen (1992) on SA and GA methods: "any problem feasible by one could also be tackled by the other". To choose which of the two

methods (GA or SA) is better for the surface-waveform modeling problem, we need to understand both algorithms and the purpose of our application. As is well known, generating multi-mode surface wave synthetics is computationally intensive. So the computation time will be a crucial factor for selection of the algorithm.

4.1 Workflow of Simulated Annealing Method

The computation procedures of simulated annealing consists of the following step:

- start from an arbitrary model
- temperature-loop : at temperature $T = T_0 - k \cdot \delta T$
 - parameter-loop : for model parameter $S_i, i = 1, \dots, m$
 - fix all other parameter value except S_i
 - for the parameter S_i , there are n possible values.
 - possible-value-loop : $S_{ij}, j = 1, \dots, n$
 - calculate the energy function $E(S_{ij})$ such as the normalized cross-correlation of observed and synthetic seismogram.
 - end of possible-value-loop
 - end of parameter-loop
 - compute the probability distribution

$$P(S_{ij}) = \frac{\exp\left[-\frac{E(S_{ij})}{T}\right]}{\sum_{j=1}^m \exp\left[-\frac{E(S_{ij})}{T}\right]}$$

- end of temperature-loop

We can see that for each temperature, it is necessary to perform $(m \cdot n)$ forward computations of synthetics. If there are k steps in lowering temperature to reach the global minimum, the total forward computation will be $(k \cdot m \cdot n)$. The problem is that there is no rule for choosing the starting temperature T_0 and increment of temperature difference δT . Basu and Frazer (1990) designed a sequence of test runs to find the critical temperature. In spite of this, it is still too time consuming for surface-waveform modeling.

4.2 Workflow of the Genetic Algorithm

For an m member society evolving through n generation, the computation sequence of the genetic algorithm is as follows:

- Randomly generate m individual models as first generation.
- Generation-loop : for $generation = 1, \dots, n$
 - Compute m synthetic seismograms (individuals)
 - Evaluate each individual's performance; i.e. calculate the goodness-of-fit.
 - population-loop : for $child = 1, \dots, m$
 - Based on the individuals' performance (probability) select them as parents;
 - change parents' DNA; and
 - apply possible mutation on their children.
 - end of population-loop

- end of generation-loop

We can see it is possible to perform GA on a small population. This will be more computational efficient than SA in the surface-waveform modeling problem. However, performing GA on a small population society has its own risk, as pointed out by Sambridge and Drijkoningen (1992). The society's members are not close to the global solution, the few relatively good individuals in the society will multiply themselves and dominate the population (i.e. trapped in local minimum). This problem can be solved by increasing the population size. However, our purpose for using GA in surface-waveform modeling is not to rely on the GA to reach the global minimum. Instead, we prefer to have several runs to see the possible uncertainty, get the rough idea about the structure, and find some good initial models for other inversion techniques. In our test, a GA run will take 1 to 3 hours of CPU time in SUN ULTRA 1 (167MHz) workstation. It is affordable to have several reruns if we find it trapped in a local minimum. We note that the goodness of fit criteria is user defined, and can combine a variety of different criteria. We thus choose the genetic algorithm for modeling surface-waveform. In the following sections, we will address several technical issues in applying GA in surface-waveform modeling.

4.3 Smoothing Mechanism

Since GA is just one type of a random search method, there is no strong constraint between parameters (layer S-velocity in this case).

Usually, there will be a strong zig-zag pattern in the velocity model; this is undesirable for the purpose in seismology if the emphasis is on determining the simplest acceptable model. To reduce this pattern in velocity model, we smooth the layer velocity by considering the adjacent velocity contrast without changing the vertical travel times. As shown in Figure 4.1, the original model (solid line) has a strong zig-zag pattern but the smoothing mechanism reduces the contrast between layer shear velocities (dashed line represents the after smoothed model). We thus attempt to find the smoothest model consistent with data.

Introducing this smoothing mechanism can be viewed as a heavy mutation case in GA. Of course, the best model may not survive under such mutation. But, we can find it from the record of models of each generation. This may help to us escape from some local minimum in some cases and provide a driving force for evolution.

4.4 Generation Number and Population Size

Although GA is a global search method which can potentially find the global minimum, we did not set that as our goal in this study. Due to the intensive computational load of generating multi-mode surface-wave synthetics, we limited our computations to a small population size and only propagated it through finite generations. We hoped, by using GA search method, to get some starting models for other inversion algorithms. To understand what generation number is sufficient

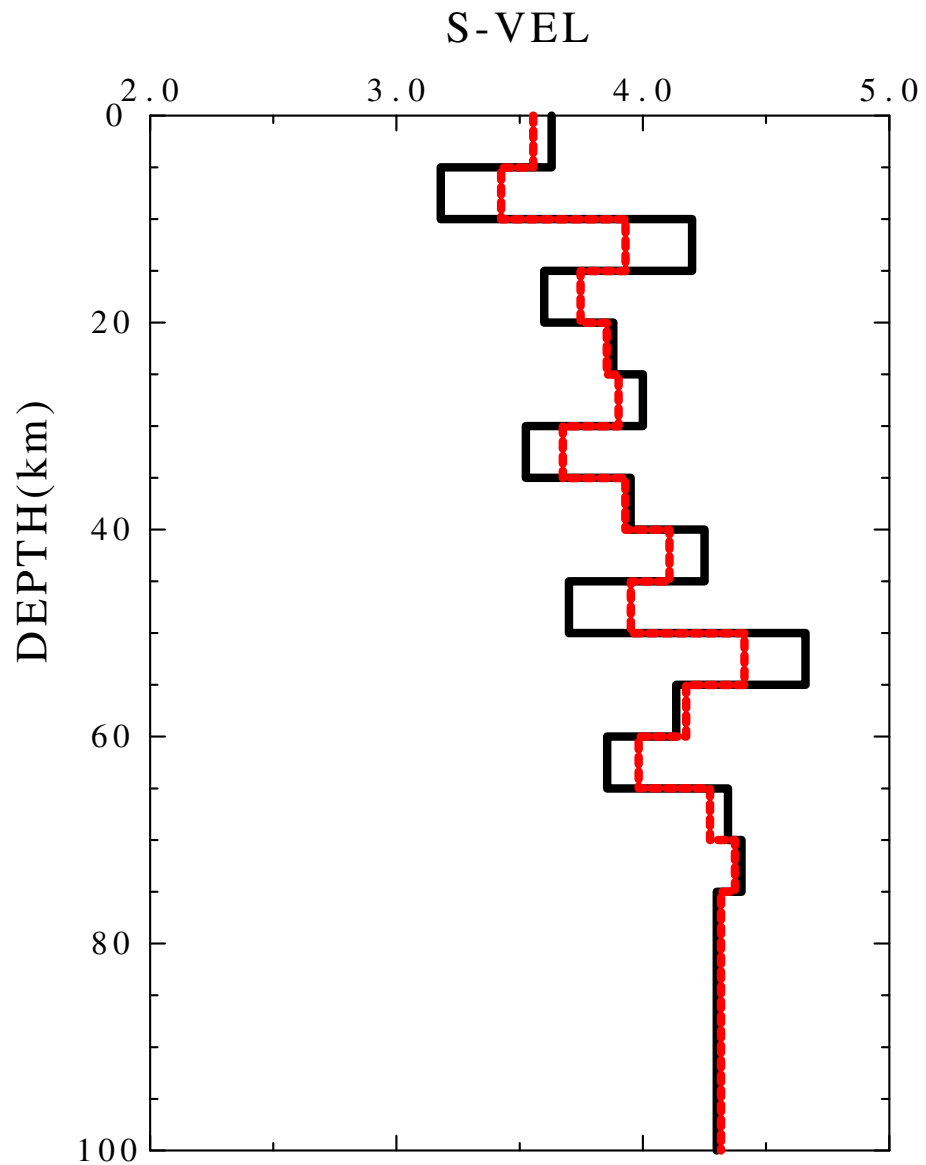


Fig. 4.1. In GA, models are randomly generated, so there always will be some 'ZIG-ZAG' patterns. To obtaining a smooth background velocity model, a smoothing mechanism is introduced. Without changing the vertical shear wave travel time, the smoothed model (dashed line) has less 'ZIG-ZAG' pattern than the original model (solid line).

for our purpose, we have tested the consequences of a large generation number. In this test, with results shown in Figure 4.2, we propagated 500 generations and find that after 50 generations model improvement is less rapid, indicating a degree of convergence. Therefore, in the subsequent tests, we will only use 50 generations for a small population (i.e. 20). This will only consume 1 to 3 hours of CPU time in SUN ULTRA 1 workstation.

In some cases, we find the GA trapped in a local minimum. Usually, this situation is associated with other difficulties such as cycle-skipping problems for teleseismic waveforms. This will be discussed later.

4.5 Criteria of Goodness-of-Fit

A surface-wave signal has a longer duration and a more complicated waveform behavior than any single, pulse-like body-wave phase. To model such long-duration complicated waveforms, there is a cycle-skipping problem which may produce an unreasonably low or high velocity model. In addition when processing surface-wave data, we cannot shift the synthetic seismogram to match the observed arrival time, a well adapted technique in processing body wave data such as receiver function inversion. Due to this effect, an L2 norm, such as used by Gomberg and Masters (1988), may not be suitable for quantifying surface-waveform goodness-of-fit. Instead we choose a cross-correlation as our criteria of goodness-of-fit to circumvent the oscillatory

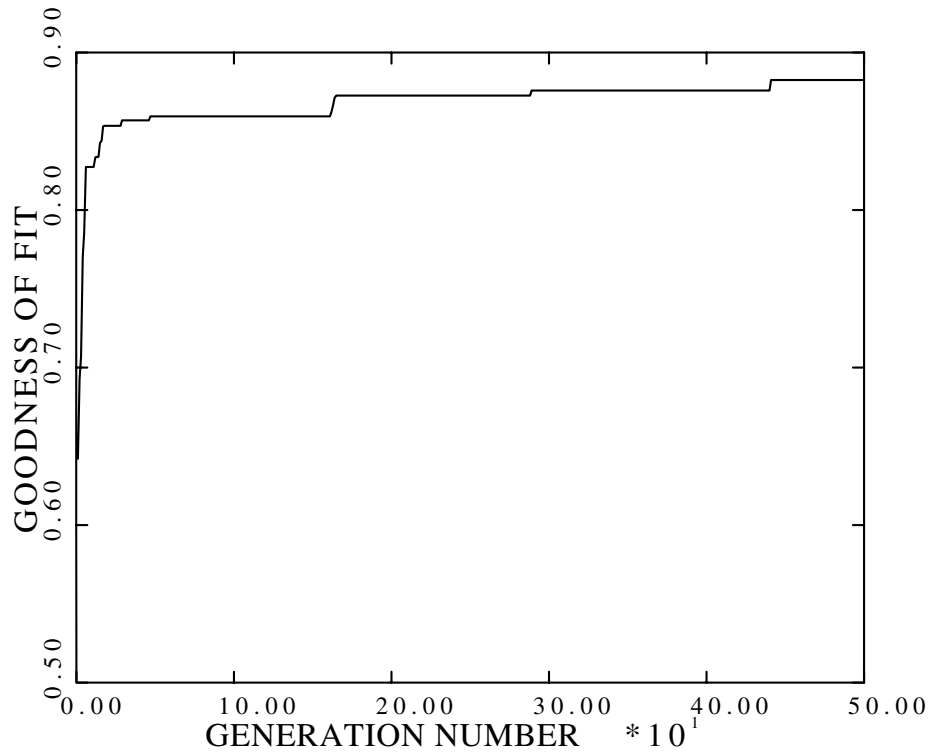


Fig. 4.2. To know how many generations is necessary for surface-waveform modeling, an experiment with large generation number (500) is tested. The result shows that GA can find a fairly good model within 50 generations. After that, the model improvement is less rapidly.

signal character, and to focus on agreement of waveform shapes.

Surface-waves usually have a broad frequency content, which means that a single cross-correlation measurement only represents the fit of the largest amplitudes, which are typically high-frequency for crustal earthquakes. This will only resolve the very shallow part of structure but leave the deeper structure uncertain with high variation. To overcome this problem, we divide the frequency range of interest

into several subranges and evaluate the normalized cross-correlation of narrow band-filtered observed and synthetic seismograms for each subrange. An averaged cross-correlation value of these subrange cross-correlations is used as our goodness-of-fit. For example, for ANMO, we divided the period range (10-50 sec) into 4 intervals : (10-20 sec), (20-30 sec), (30-40 sec), (40-50 sec). Using these period intervals as the ranges for bandpass filtering observed and synthetic seismograms, a cross-correlation value is computed for each interval and an average cross-correlation is used as our goodness-of-fit.

4.6 Test on the Western Texas Earthquake

We apply this GA search method to the April 14, 1995 Texas earthquake (30.26 °N 103.33°W, 00:32:55UT). The source depth of the Texas event is 20 km, with strike, dip, rake angles of 114°, 64°, -101°, respectively with $M_w = 5.6$.

Three stations (ANMO, TUC, WMOK) are selected to show the capability of the GA search method. For each station, three plots of final good models, waveform fitting, and cross-correlation of different period ranges of the best result are shown. The first plot shows the search bounds (thickest dashed line), the good models (thin dashed line) which have goodness-of-fit greater than a certain value, and the best model (black solid line). The second plot shows the waveform fit of the best model. The observed seismogram is drawn as a black line and the synthetics as a thin dashed line. The third plot shows the

cross-correlation measurements of the best searched model in the different period ranges which gives us an idea of how good can this model fits the data. We also can see the reason for using averaged cross-correlation as our criteria of goodness-of-fit because the broadband (e.g. 10-50 sec) waveform with top row is dominated by a high frequency signal such as is the waveform on the second row (e.g. 10-20 sec).

Examining the results for ANMO (Figures 4.3, 4.4, 4.5), we found that our best final model for the Rayleigh wave has an unreasonably low velocities for layers deeper than 50 km. Also on the cross-correlation diagram, we can see that at the 40-50 second period, the envelope's maximum of the Z component is off central position. This is the flaw of currently used criteria which can not overcome the cycle-skipping problem. Combining the correlation coefficient at zero lag with the lag shift of the maximum correlation may be another goodness of fit criterion to use in the future. However, comparing two best models obtaining from the separate GA searches for Love and Rayleigh waves, we see these two models show a very similar model for the upper 50 km.

For TUC (Figures 4.6, 4.7, 4.8, and 4.9), we tested this search scheme on three cases: using Rayleigh wave only, using Love wave only, and using both Rayleigh and Love wave. The final results show that waveform fitting from the separated search are better than those from the joint search. But in the macroscopic view, they all have a very similar velocity gradient in the crust. This may illustrate that the crustal structure is well resolved as indicated by the relative

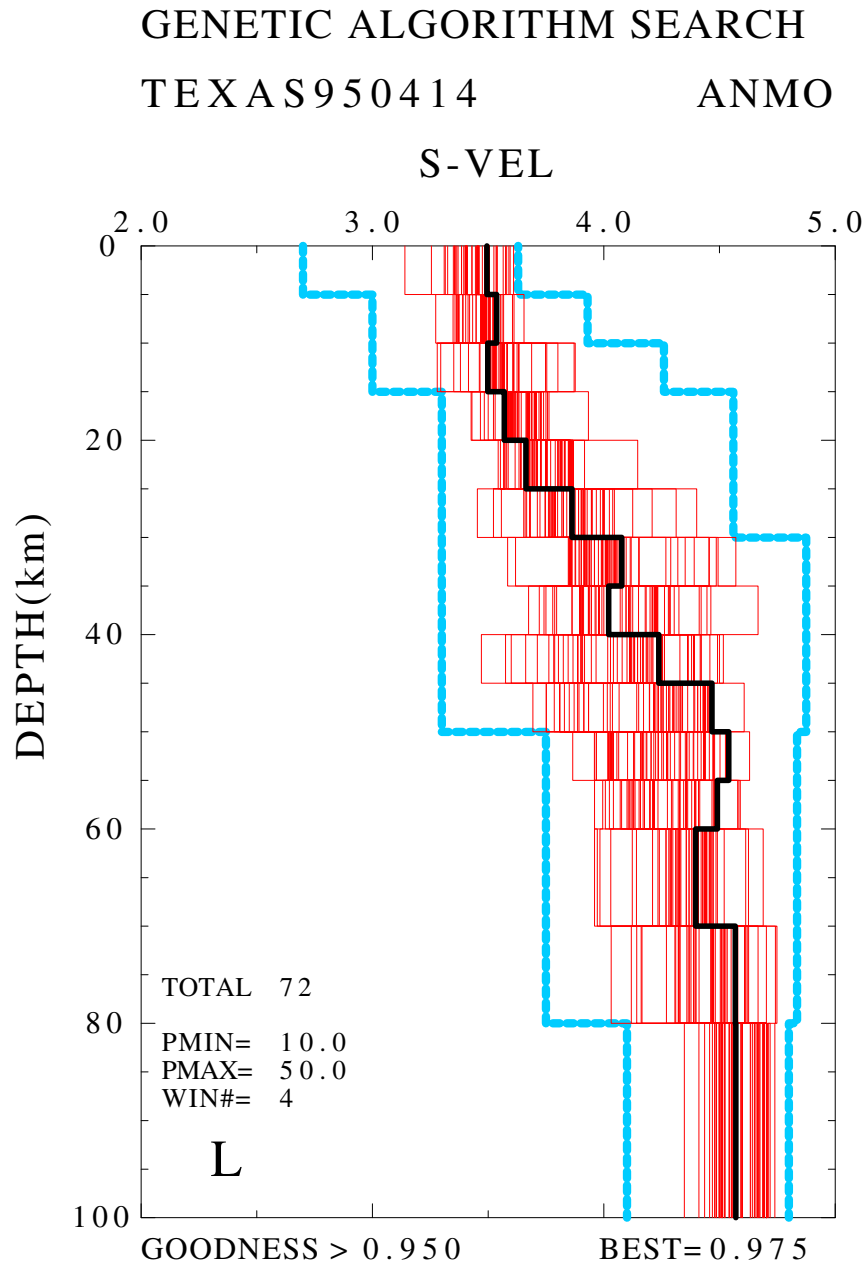


Fig. 4.3a. Using GA to model the surface-waveform of station ANMO. In this test, separate GA runs were conducted for Love and Rayleigh wave respectively. The searched models are shown in these figures, the heavy lines are the search bounds, the thin lines are models which have goodness-of-fit greater than a certain value shown at the left bottom, and the best model is plotted as thick black line. (a) Models for Love wave.

GENETIC ALGORITHM SEARCH

TEXAS950414

ANMO

S-VEL

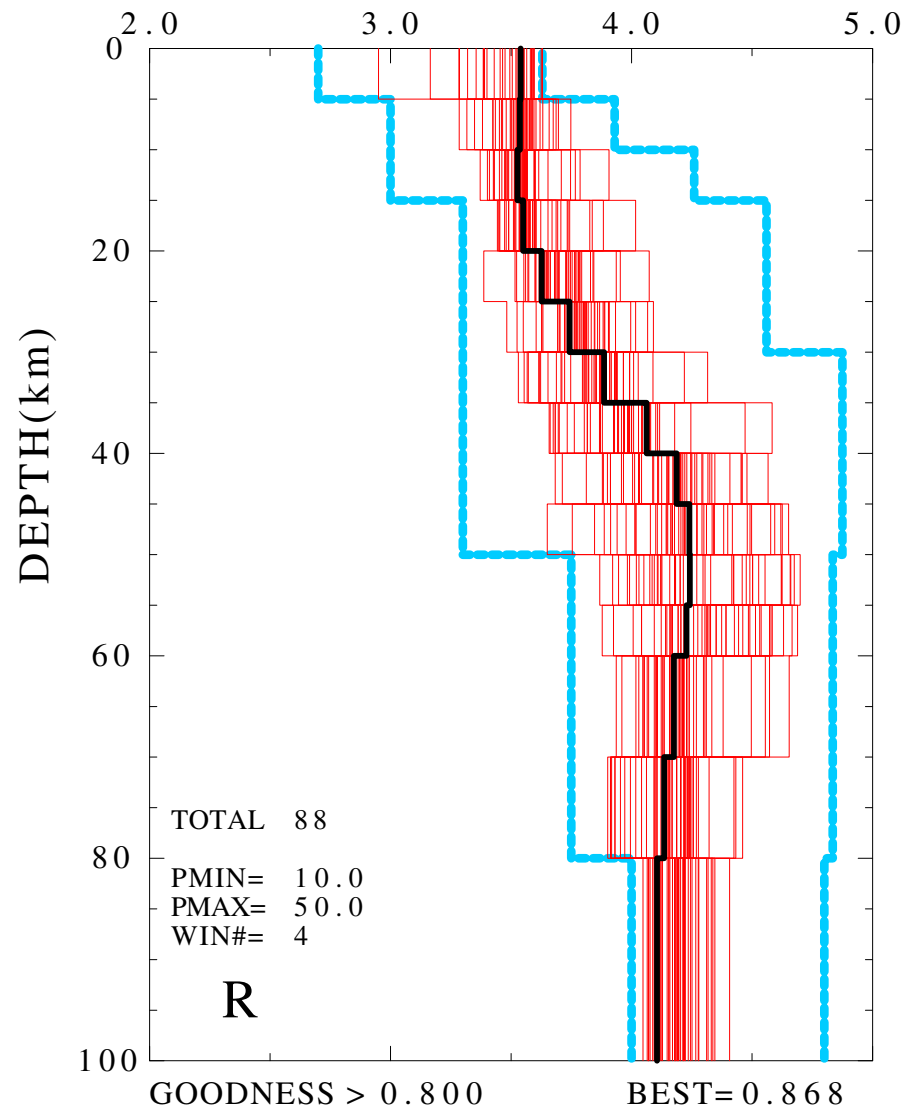


Fig. 4.3b. (cont'd). (b) Models for Rayleigh wave.

TEXAS950414

ANMO VEL

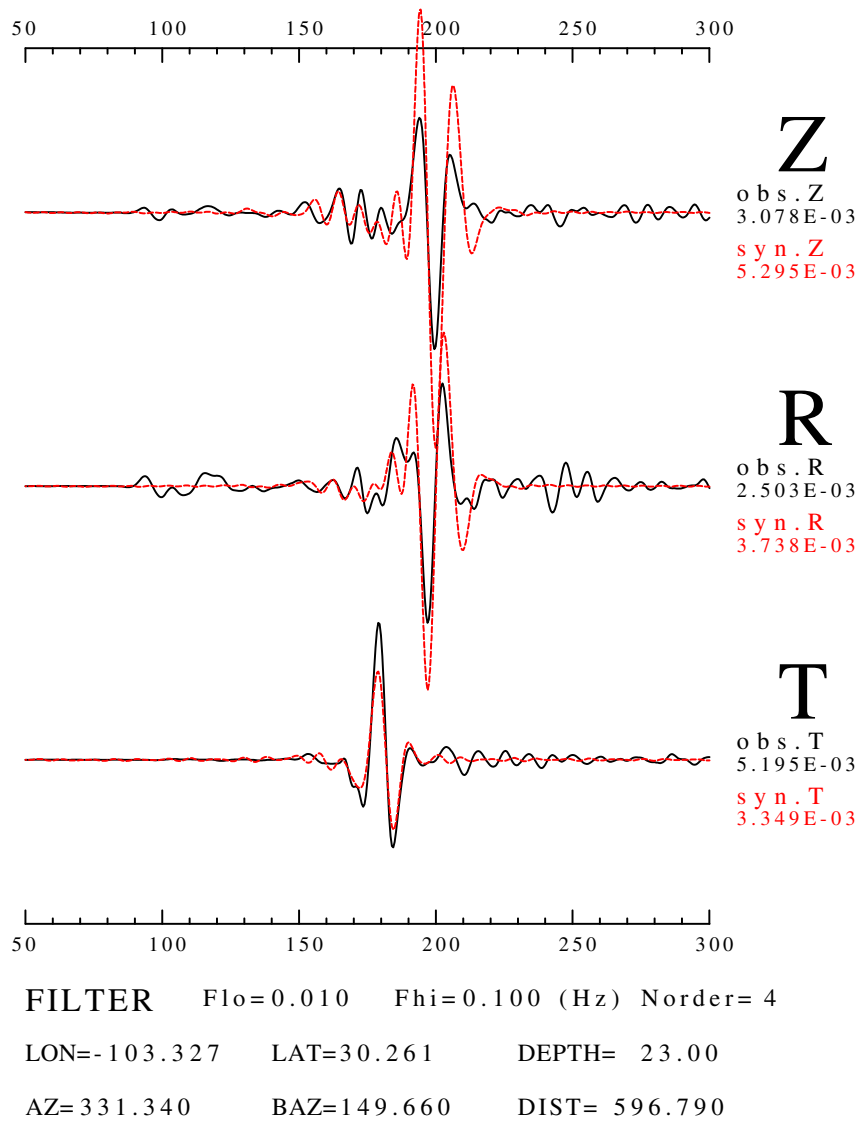


Fig. 4.4. For ANMO, the observed waveforms (solid line) and predicted waveforms (dashed line) which generated for the best searched models for Love and Rayleigh wave at frequency range 0.01 to 0.1 Hz.

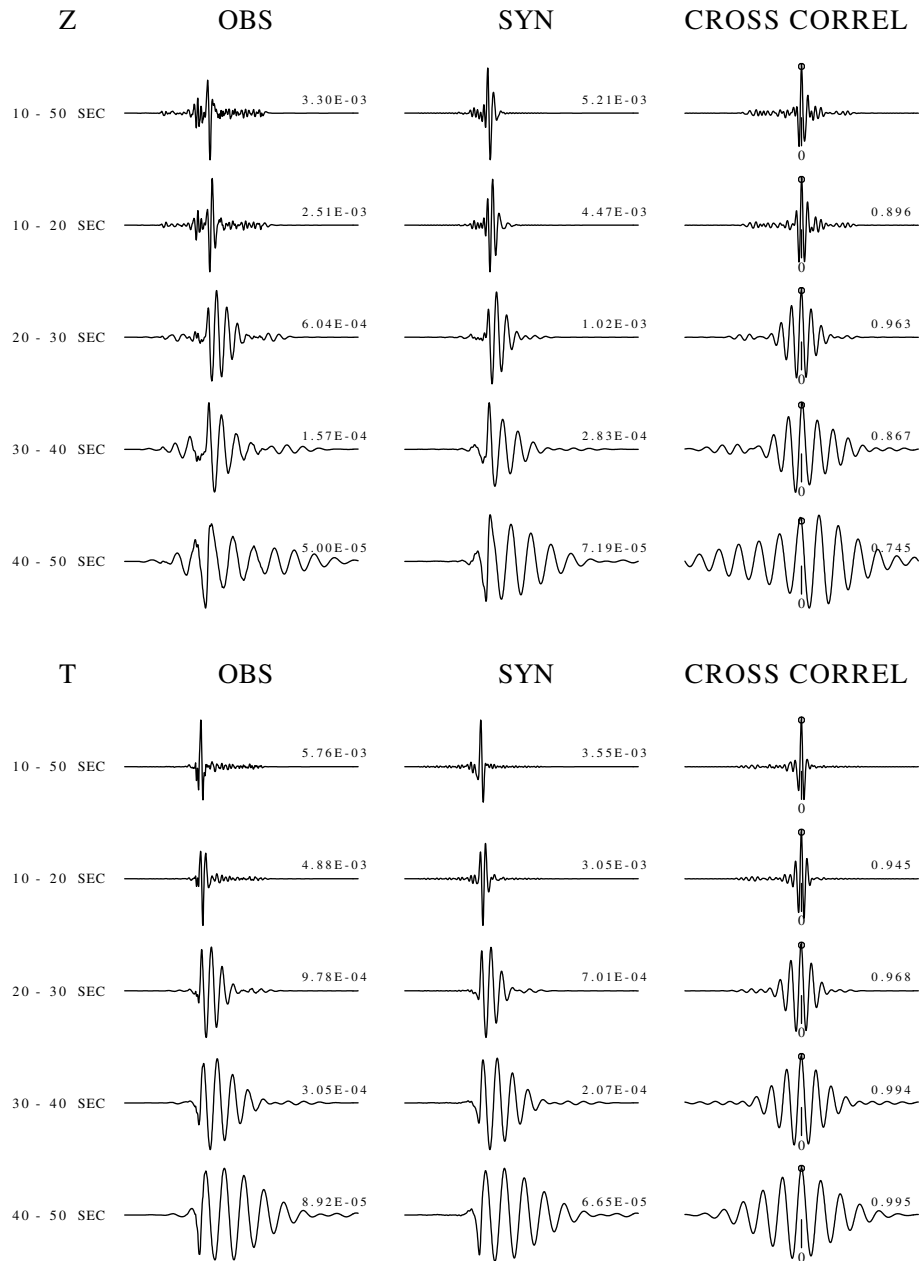


Fig. 4.5. For ANMO, the filtered cross-correlations of observed and synthetic waveforms at different frequency bands. The number at the right of cross-correlation traces is the cross-correlation value at zero-lag which is used to construct the value of goodness-of-fit.

narrow width of acceptable velocities at shallow depths. In the uppermost mantle, Figure 4.6(a) shows that a fixed half-space beneath 80 km may not be appropriate and may cause the model between 60 to 80 km to have lower their values to compensate this high velocity half-space. However, from Figure 4.6(b), the Rayleigh wave seems prefer this high velocity half-space. So we need to conduct more tests to see if there exists an apparent anisotropy zone beneath the propagation path.

For WMOK (Figures 4.10, 4.11, and 4.12), the waveform of the best model fits the observed seismogram very well, not only for the fundamental mode but also for the first higher mode Rayleigh wave. The propagation path through the west Texas region is only 655 km. This region is a uniform platform between Rocky mountain and Ouachita orogenic belt. From the final model, we can see the existence of a transitional crust-mantle-boundary between 35 and 50 km, which is all that can be resolved using these low frequency filtered data.

4.7 Test for Teleseismic Traces

In our test, we found that our implementation of GA only works for recordings at short epicentral distance. For the teleseismic records, this algorithm doesn't work simply because the cycle-skipping problem. However, surface waves at teleseismic distance samples the upper mantle, and is very important to provide information and constraints on the upper mantle. We need to find a way to apply GA

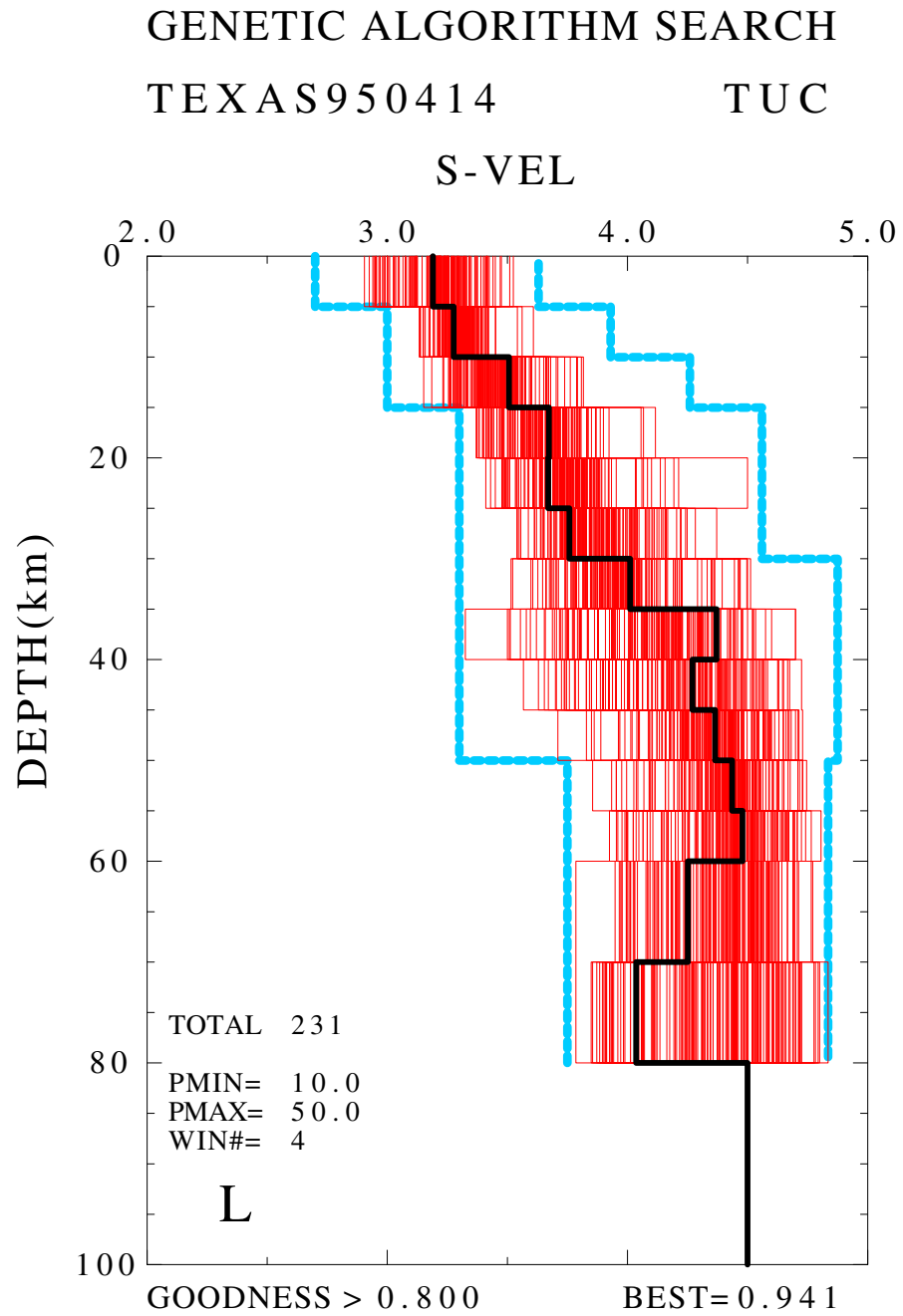


Fig. 4.6a. Separate GA search results for Love and Rayleigh wave recorded at TUC.
(a) Love-wave model.

GENETIC ALGORITHM SEARCH

TEXAS950414

TUC

S-VEL

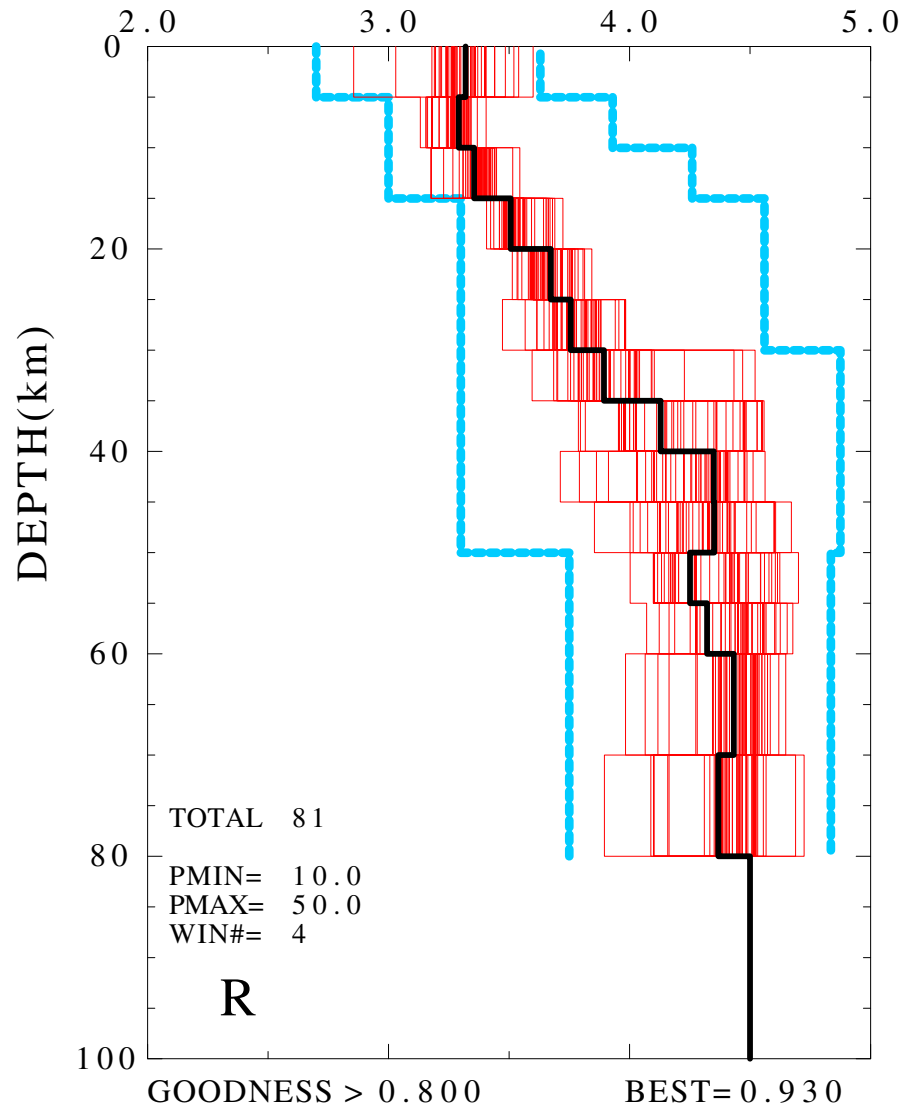


Fig. 4.6b. (cont'd). (b) Rayleigh-wave model.

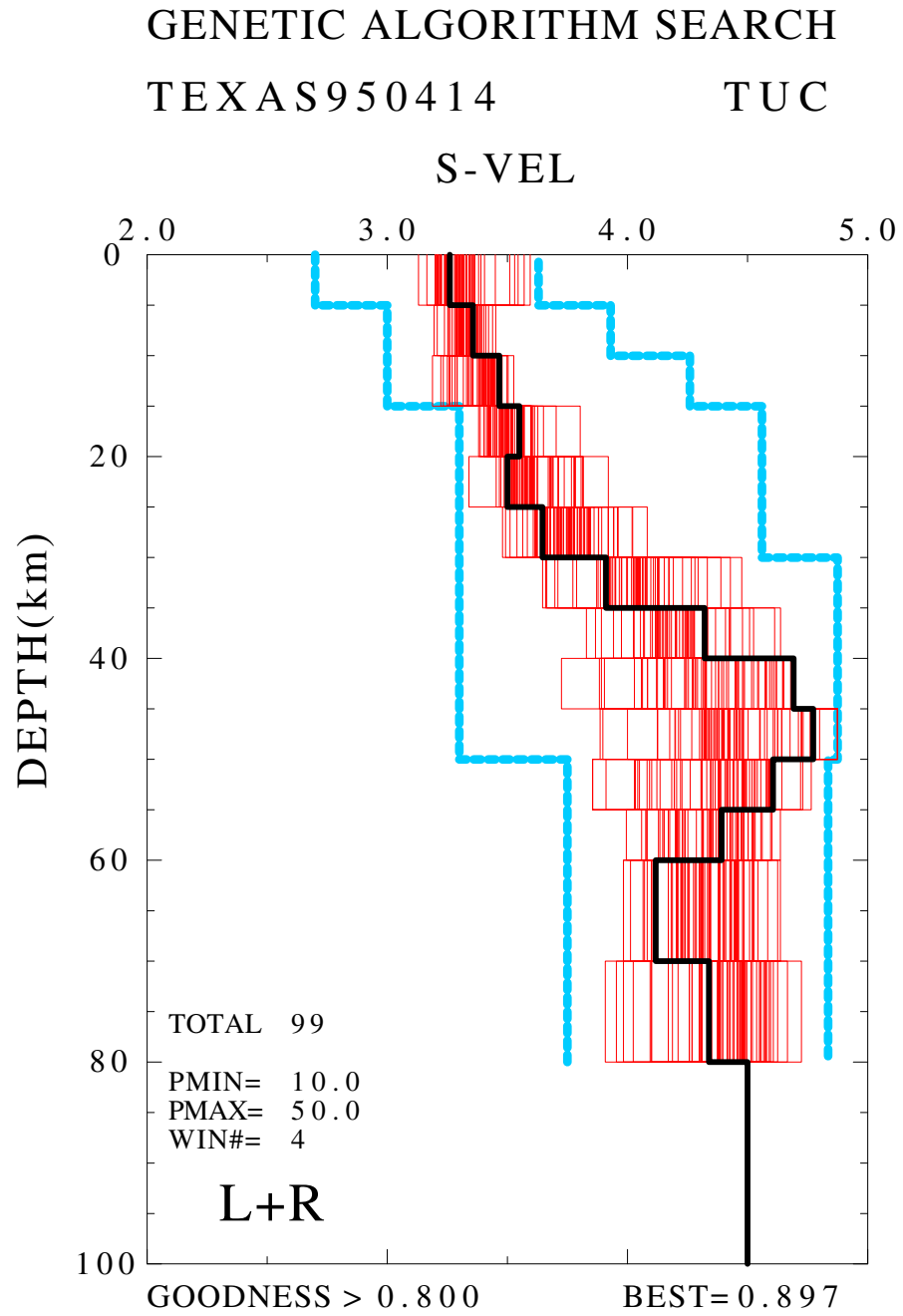


Fig. 4.7. A joint GA search using both Love and Rayleigh waveforms at TUC.

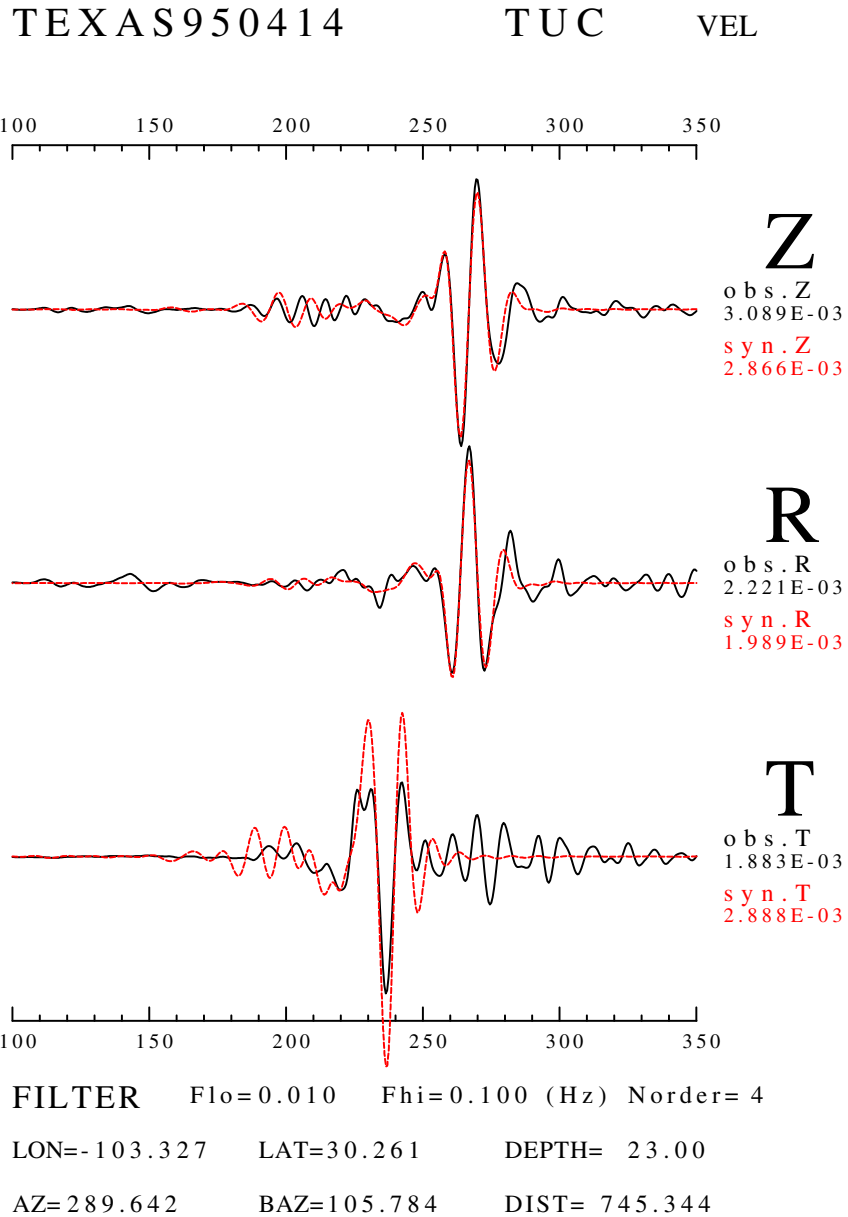


Fig. 4.8a. For TUC, filtered waveforms at frequency range 0.01 to 0.1 Hz for observed and predicted seismograms. (a) The predicted seismograms were generated using the best models from individual searches for Love and Rayleigh wave (Figures 4.6ab).

TEXAS950414

TUC

VEL

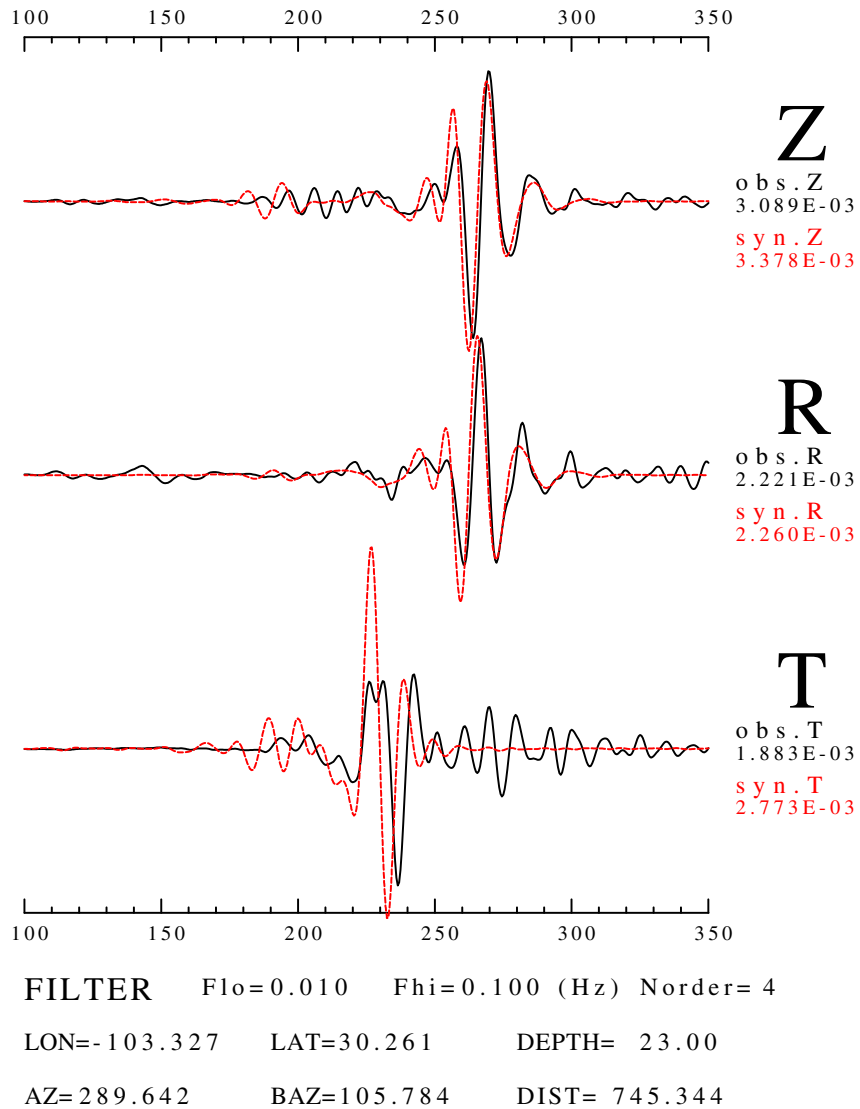


Fig. 4.8b. (cont'd). (b) The predicted seismograms were generated using the best model from a joint searches for both Love and Rayleigh wave (Figure 4.7).

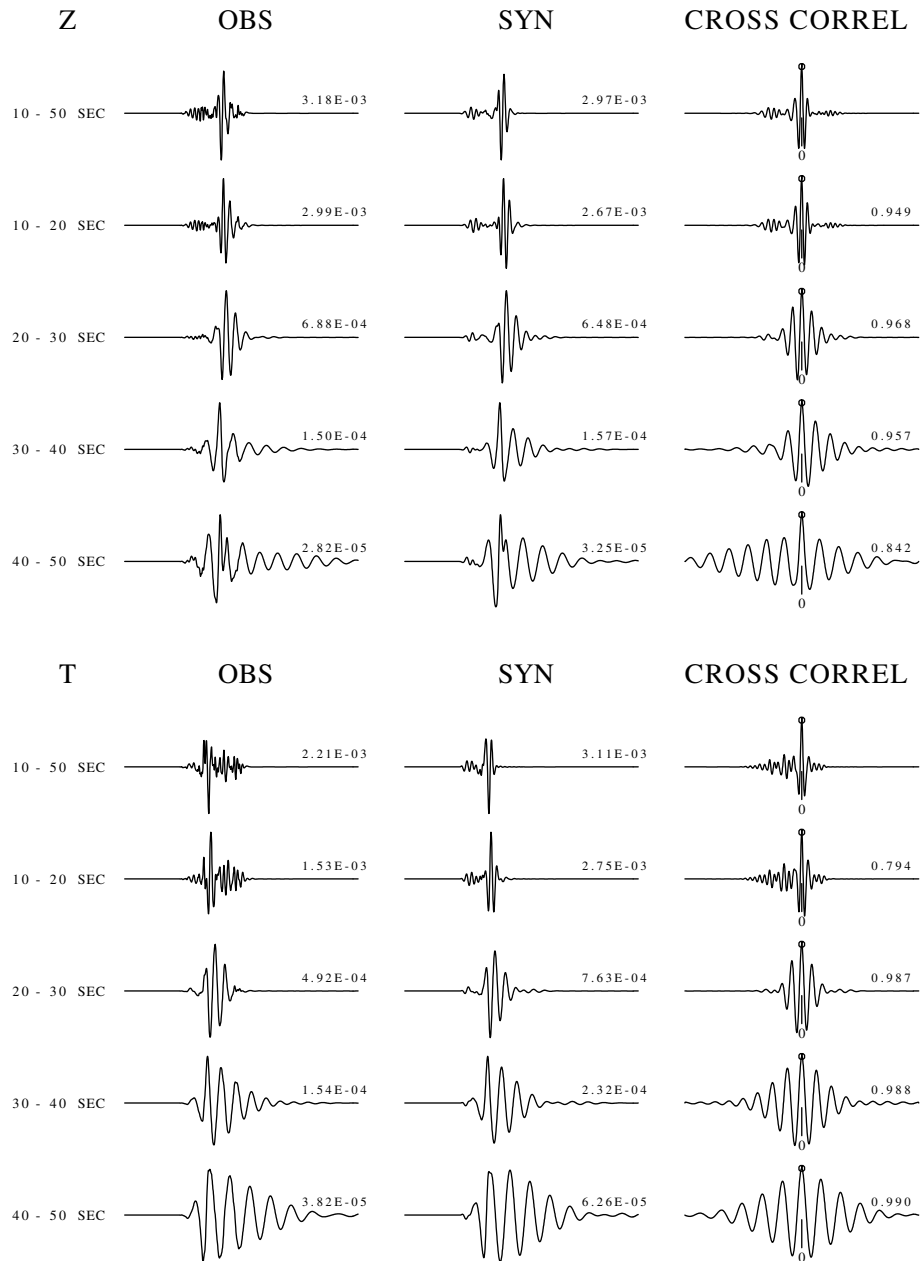


Fig. 4.9a. For TUC, the cross-correlations for the observed and synthetic seismograms which were generated using GA searched models. (a) The synthetics were computed using the best models from the separate search models for Love and Rayleigh wave (Figures 4.6ab).

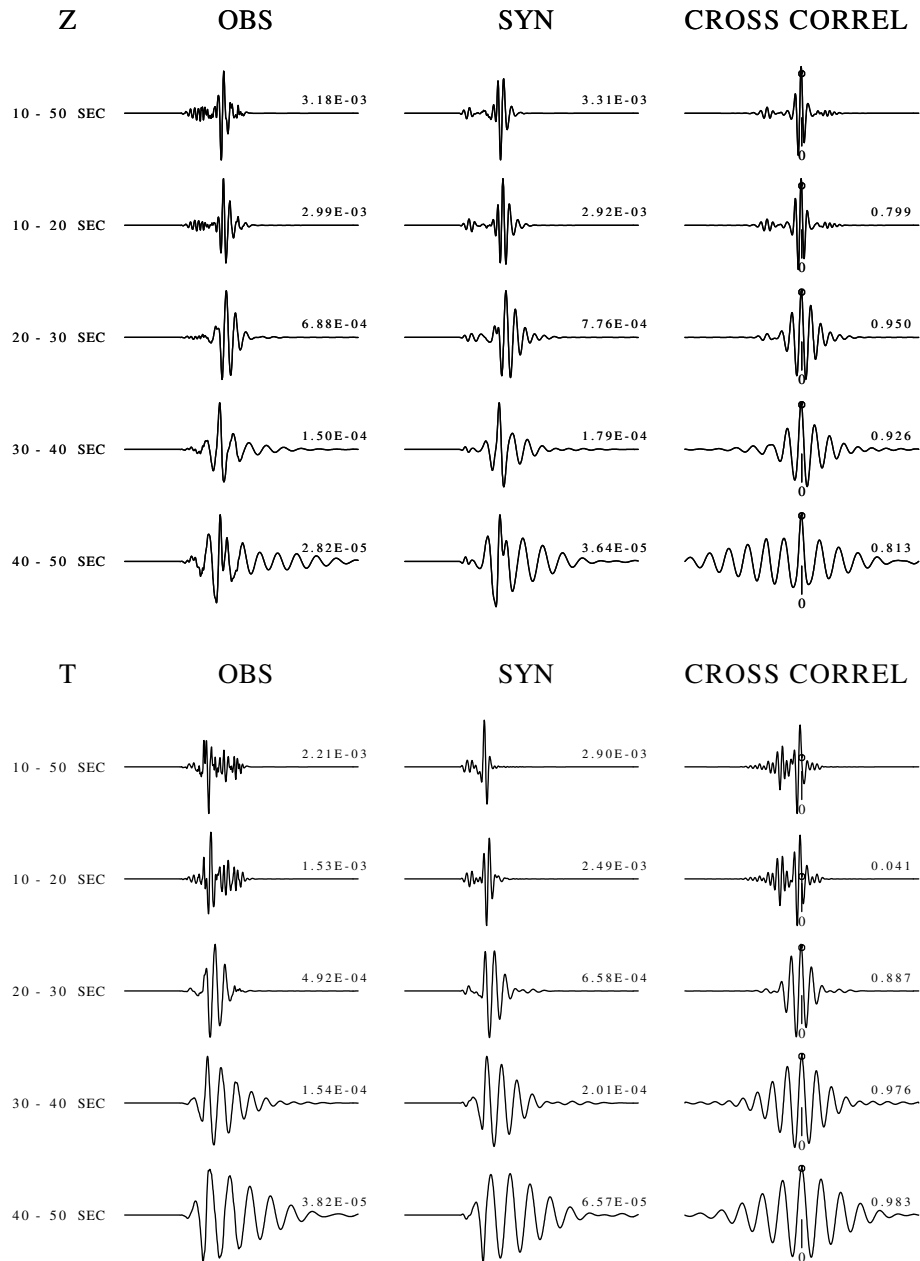


Fig. 4.9b. (cont'd). (b) The synthetics were computed using the best model from a joint search for both Love and Rayleigh wave (Figure 4.7).

search technique to teleseismic records.

To apply GA search technique to teleseismic seismograms, we change the parameterization of the model. We use three 20 km thick layers over a half-space, which corresponding to the upper crust, lower crust, uppermost mantle, and the upper mantle. From the reports on the structure of the lithosphere, we notice that the average velocity for the uppermost mantle (40-60 km) is greater than the lower crust (20-40 km), and the lower crust velocity is higher than upper crust (0-20 km). In the upper mantle (half-space in this parameterization), the average velocity should not deviate too much from the uppermost mantle. So we place these observational constraints on our GA searched models, i.e. the velocities of the first three layers should increase monotonically and the difference between the uppermost mantle and upper mantle should not be greater than 0.2 km/sec.

The test results show a good improvement in the searched model, it overcomes the cycle-skipping problem. Results at three stations (HRV, FRB, LMN) show the successful GA search results. However, this strategy has its own weakness. We will use the GA searched results for INK to illustrate the weaknesses.

For HRV (Figures 4.13, 4.14), the best GA searched model can predict the waveform very well in the frequency range of 0.01 to 0.05 Hz. The models show a fairly small uncertainty and the best model is consistent with the velocity structure of stable continents. For FRB (Figures 4.15, 4.16), the GA search show its ability to find the models to predict the well dispersed fundamental mode waveform. We also

GENETIC ALGORITHM SEARCH
TEXAS950414 WMOK
S-VEL

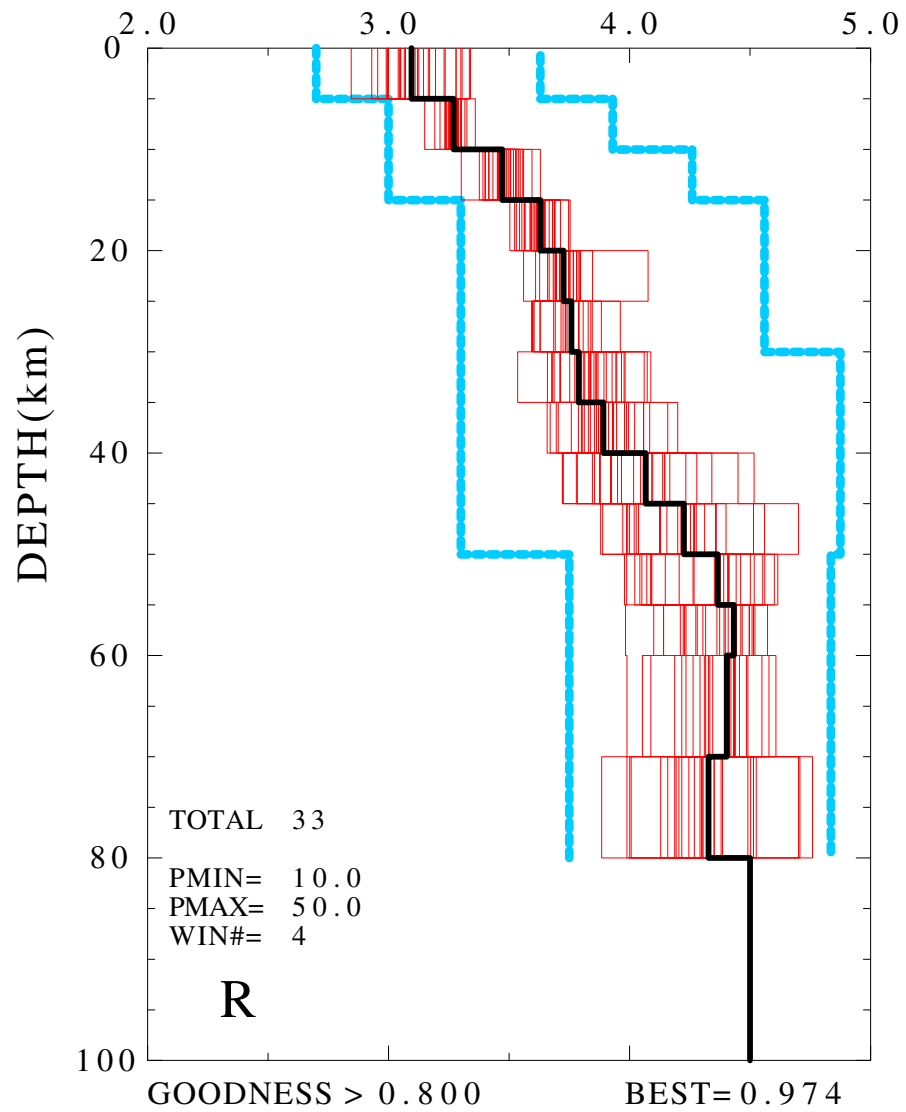
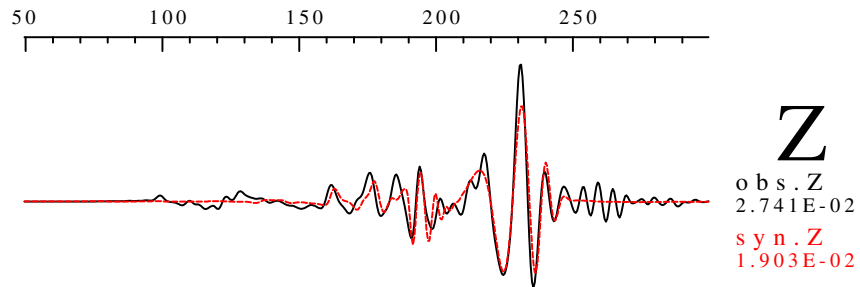


Fig. 4.10. The models from GA search for Rayleigh wave recorded at WMOK.

TEXAS950414

WMOK DISP



R

T

50 100 150 200 250
 FILTER Flo=0.010 Fhi=0.200 (Hz) Norder= 4
 LON=-103.327 LAT=30.261 DEPTH= 23.00
 AZ= 39.529 BAZ=221.965 DIST= 655.074

Fig. 4.11. The waveform comparison of observed and synthetic seismograms for WMOK (Figure 4.10).

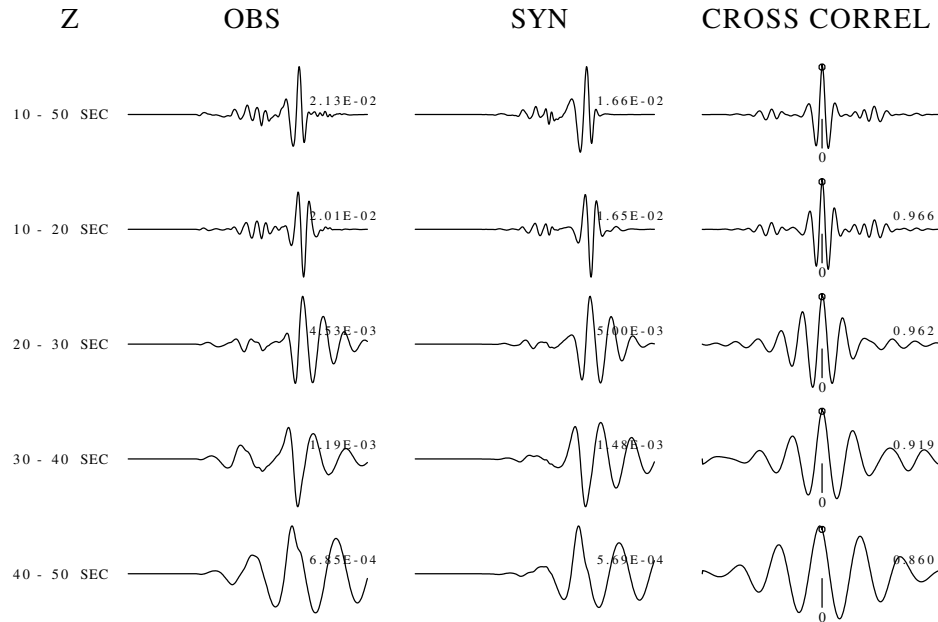


Fig. 4.12. The cross-correlation of the best GA searched model for WMOK (Figure 4.10).

notice the envelope of synthetics is shorter than the observed seismograms which may reflect that the model is not good enough to produce correct amplitude. From Figure 4.16, we see that lower crust velocity may be too low and uppermost mantle velocity may be a little high. For LMN (Figures 4.17, 4.18), the waveform fit is acceptable and its model looks reasonable, but we can see the synthetics do not match the observed Airy phase. This may be caused by the criteria of goodness-of-fit used. In applying GA search technique to teleseismic seismograms, we divided the period range 10-70 seconds into 6 subranges. The period content of wave traveling through crust is mainly shorter than 30 seconds, therefore the criteria of goodness-of-fit has more weighting for low-frequency signals and may not properly represent

the crustal wave. The problem is more clear for INK (Figures 4.19, 4.20). We can see that due to the lack of proper representation of crustal signals, the GA search technique fails in its search for good model for the noisy traces such as INK which suffer from multipathing problem.

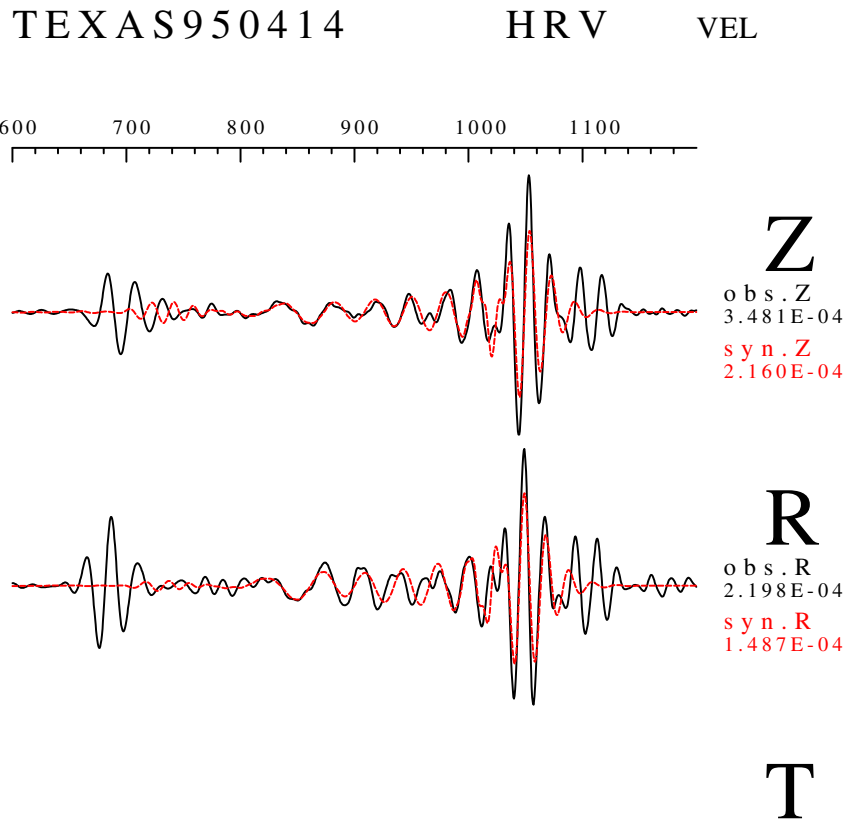
4.8 Discussion

From this experiment, we found that the GA search method works well for regional seismograms ($\Delta < 1000$ km) but not as well for teleseismic traces ($\Delta > 2500$ km). The reasons for this are as follow:

- First, the regional seismograms have a more concentrated energy envelope instead of a well-dispersed wavetrain seen in teleseismic surface waves. Therefore, the cycle-skipping problem is less severe in this case.
- Second, the goodness-of-fit criteria may be too simple. The criteria investigated here only utilizes the amplitude information of the cross-correlation but ignore the time-shift information.

A different model parameterization designed for teleseismic seismograms works well for some high S/N ratios with strong Airy phase traces.

Another important result of genetic algorithms is that they provide a suite of possible models. The distribution of possible solutions at a given depth qualitatively indicates the sensitivity of the data to the velocity model. For example, for the ANMO transverse component,



600 700 800 900 1000 1100

FILTER Flo=0.010 Fhi=0.050 (Hz) Norder= 4

LON=-103.327 LAT=30.261 DEPTH= 23.00

AZ=55.535 BAZ=254.724 DIST= 3132.950

Fig. 4.13. The waveform fit of the best GA searched model for HRV.

GENETIC ALGORITHM SEARCH

TEXAS950414

HRV

S-VEL

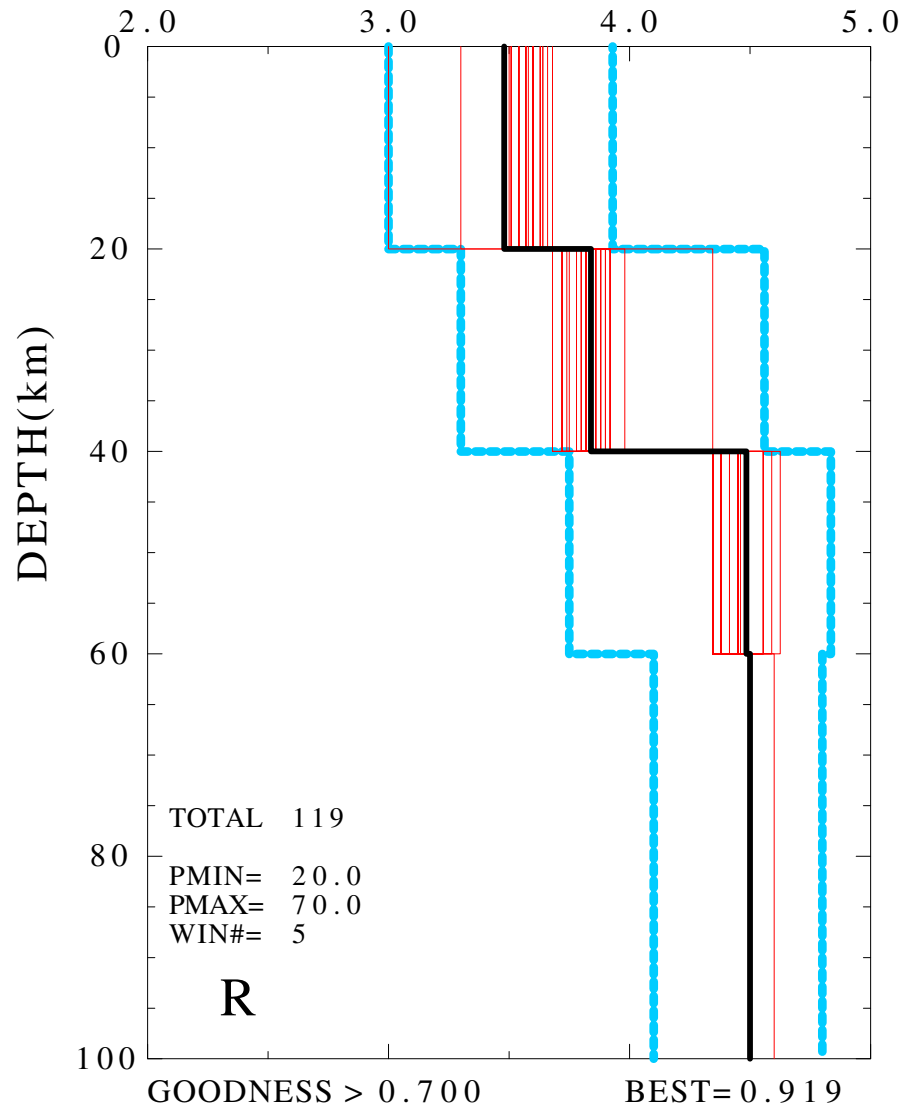


Fig. 4.14. The GA searched models for HRV.

TEXAS950414 F R B VEL

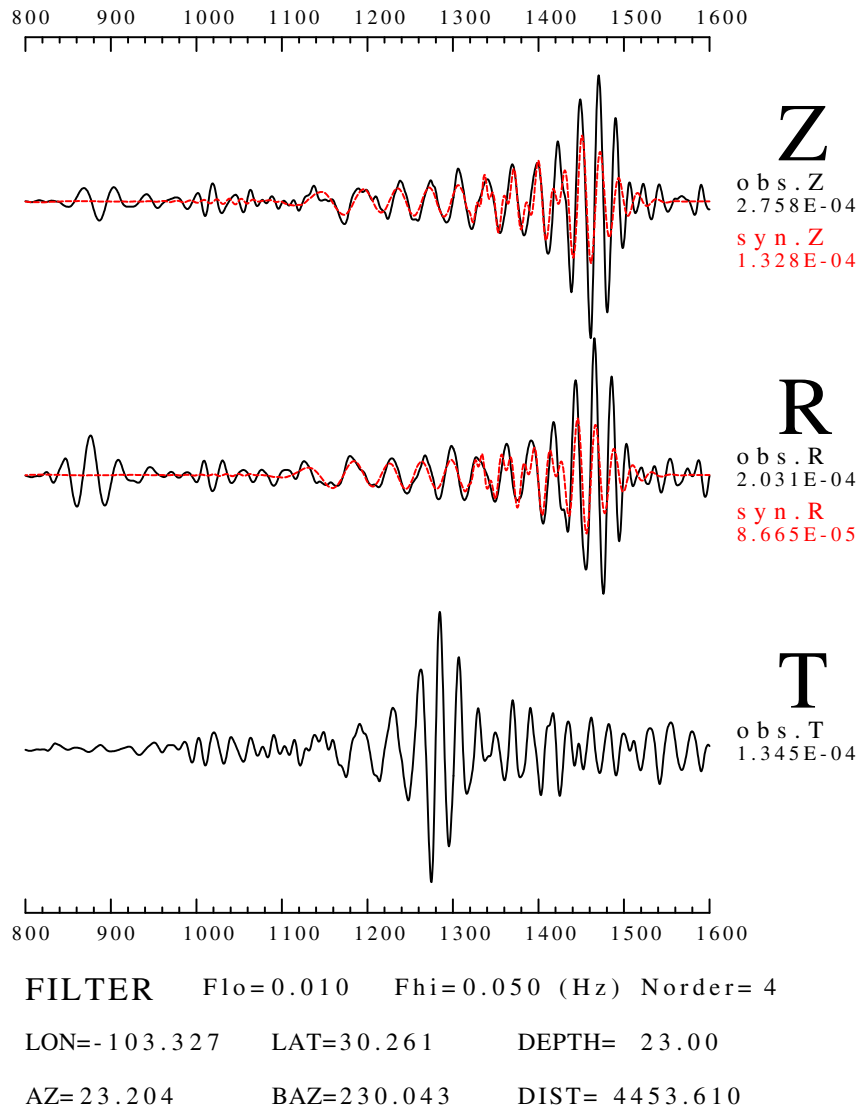


Fig. 4.15. The waveform fit of the best GA searched model for FRB.

GENETIC ALGORITHM SEARCH

TEXAS950414

FRB

S-VEL

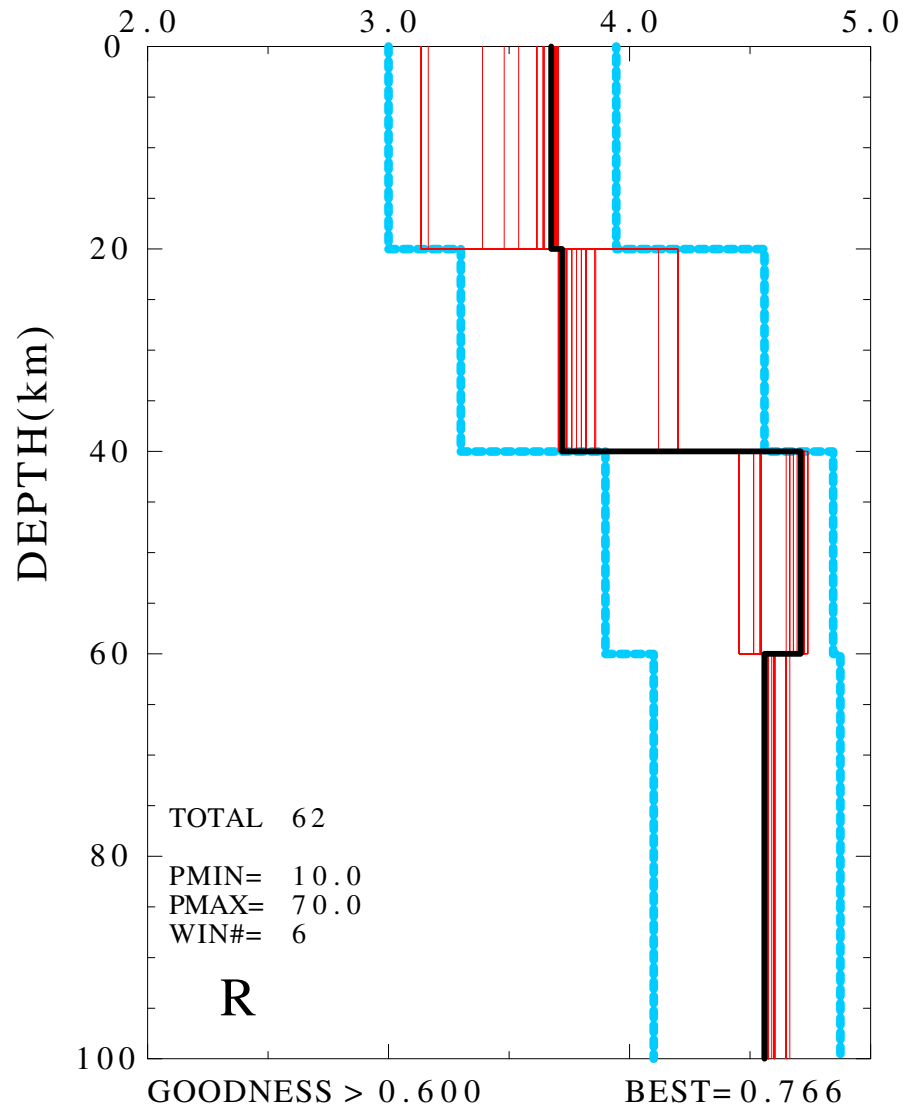
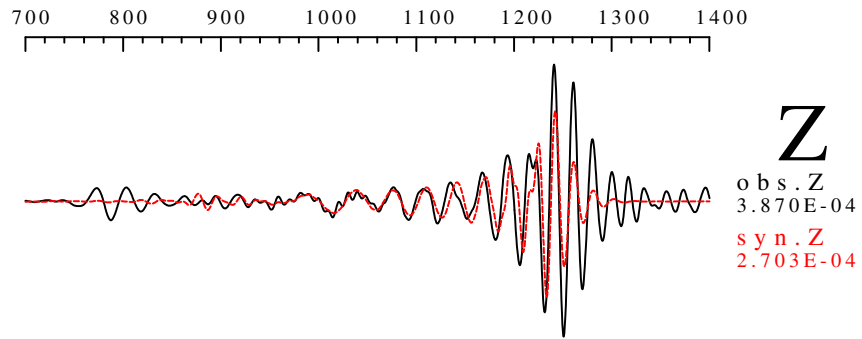


Fig. 4.16. The GA search models for FRB.

TEXAS950414 LMN VEL



R

T

700 800 900 1000 1100 1200 1300 1400

FILTER Flo=0.010 Fhi=0.050 (Hz) Norder= 4

LON=-103.327 LAT=30.261 DEPTH= 23.00

AZ= 51.632 BAZ=256.067 DIST= 3749.110

Fig. 4.17. The waveform fit of the best GA searched model for LMN.

GENETIC ALGORITHM SEARCH

TEXAS950414

LMN

S-VEL

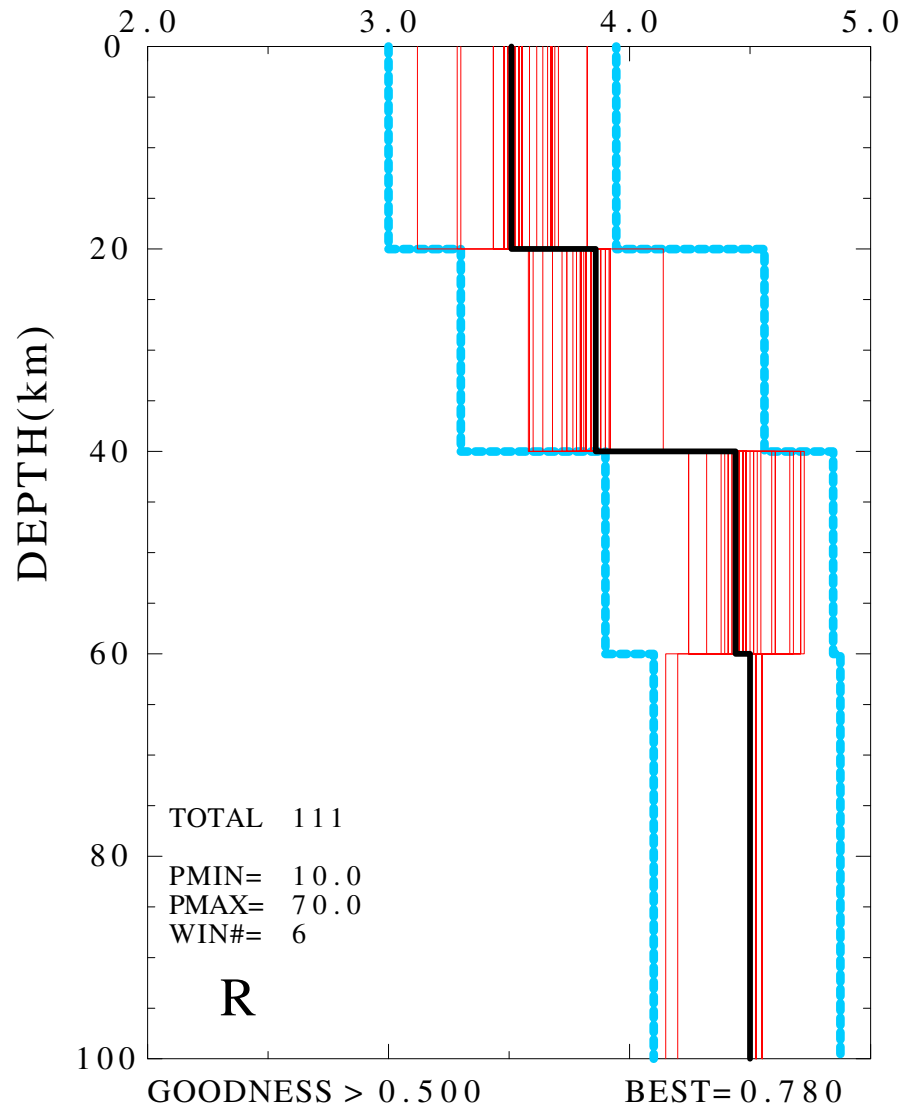


Fig. 4.18. The GA search models for LMN.

TEXAS950414 I N K DISP

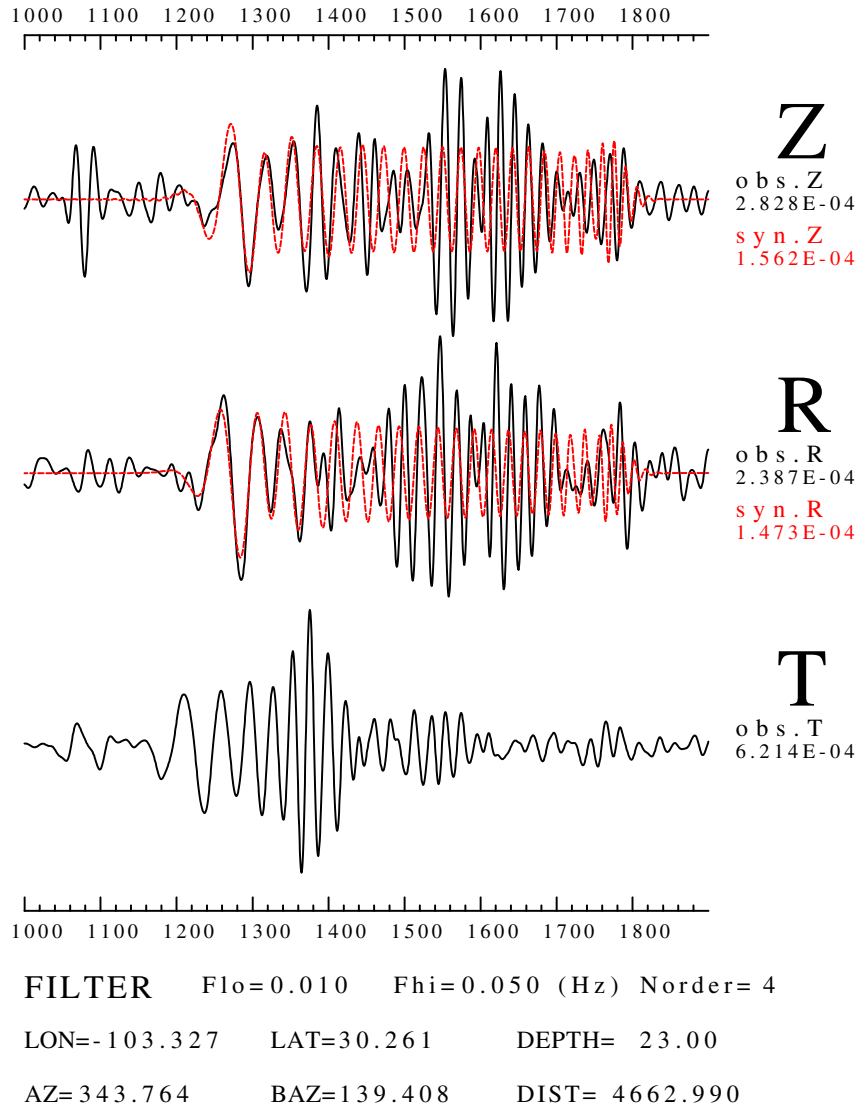


Fig. 4.19. The waveform fit for INK. INK is located in the most northwest of Canada. From the Rayleigh wave trace, we can see the wavetrain due to the multipathing effect arrives after the 1600 seconds. The currently used criteria of goodness-of-fit can not properly represent the crustal wave and may cause an overly extended synthetic trace.

GENETIC ALGORITHM SEARCH

TEXAS950414

INK

S-VEL

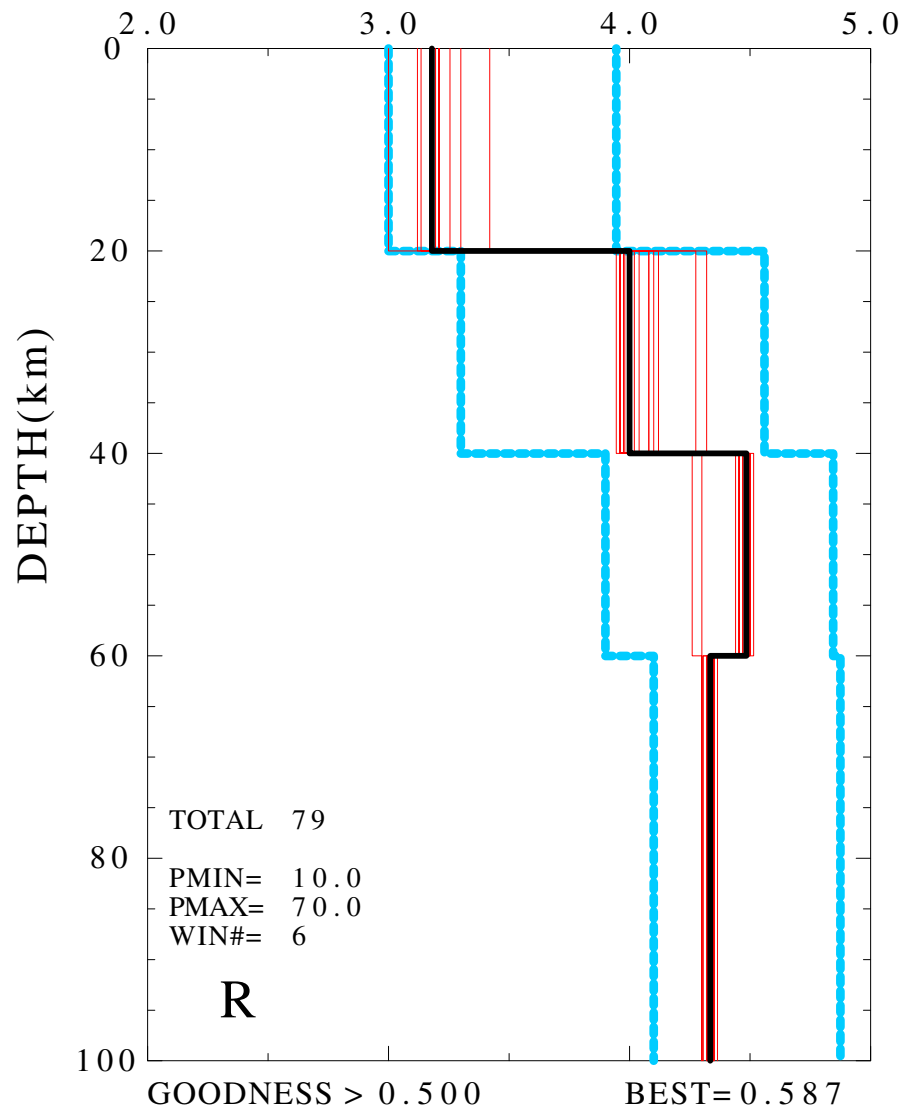


Fig. 4.20. The GA search models for INK. The unreasonable low crustal velocity value is due to the criteria of goodness-of-fit which can not properly represent the crust wave.

the crustal velocities are better defined than upper mantle velocities, which is as expected for a signal recorded only 600 km away from a crustal event.

Our results can be used to build a more intelligent algorithm for modeling surface-wave waveform in the future. This future algorithm should use both amplitude and time-shift information as its criteria of goodness-of-fit. It could also attempt to match signal amplitudes, e.g. to use group velocity information as well. A better way of parameterization will further improve GA search technique's applicability and believability of its results.

CHAPTER 5

COMPARISON OF TECHNIQUES

In this chapter, four different techniques will be used to model the surface-waveform recorded at CCM (Cathedral Cave, Missouri). The techniques compared are Genetic Algorithm, traditional inversion of dispersion data, linear waveform inversion (Gomberg and Masters, 1988), and GSDF inversion. The comparison of different results will illustrate the strength and weakness of each method. A discussion will address the new knowledge can we learn through the waveform modeling as well as way to judging the reliability of inversion results.

The reason for using CCM data in this test is that we found the CCM waveform very difficult to model. It cannot be fit by any simple model. Through all these waveform modeling tests, we believe that some new knowledge can be learned. All these experiences can be used to improve the algorithms of waveform modeling.

5.1 Genetic Algorithms

In applying GA search method to CCM, two steps were taken. As mentioned in Chapter 4, there is a cycle-skipping problem in applying

many layers GA search to stations at large distances. For this reason, the search was performed using a 4-layer GA search. The best result from this first step search is used to refine the searching bounds for the second step GA search.

Figure 5.1 shows the 4-layer GA search results and search bounds. The best model from first step search can match the low frequency waveform (Figure 5.2). Starting with the first stage model, the second stage GA search bounds were designed. The subsequent GA search results are shown in Figure 5.3. The waveform predicted from the best model can fit the fundamental mode as high as 0.1 Hz, but the higher modes are out of phase (Figure 5.4).

The GA search method provides a very good starting model which has the fundamental mode matched in phase even though the higher modes are out of phases. The most important advantage for GA search method is that it requires no human intervention during the search. The computational time is the least among all methods tested in this study.

5.2 Inversion of Dispersion Data

The traditional surface wave inversion method to get seismic structure use the dispersion data (e.g. Russell, 1987). The Multiple Filter Technique (Dziewonski et. al., 1969; Herrmann, 1973) is often used to extract surface-wave group velocity dispersion curves. However, inversion using only group velocity dispersion data usually

GENETIC ALGORITHM SEARCH

TEXAS950414

CCM

S-VEL

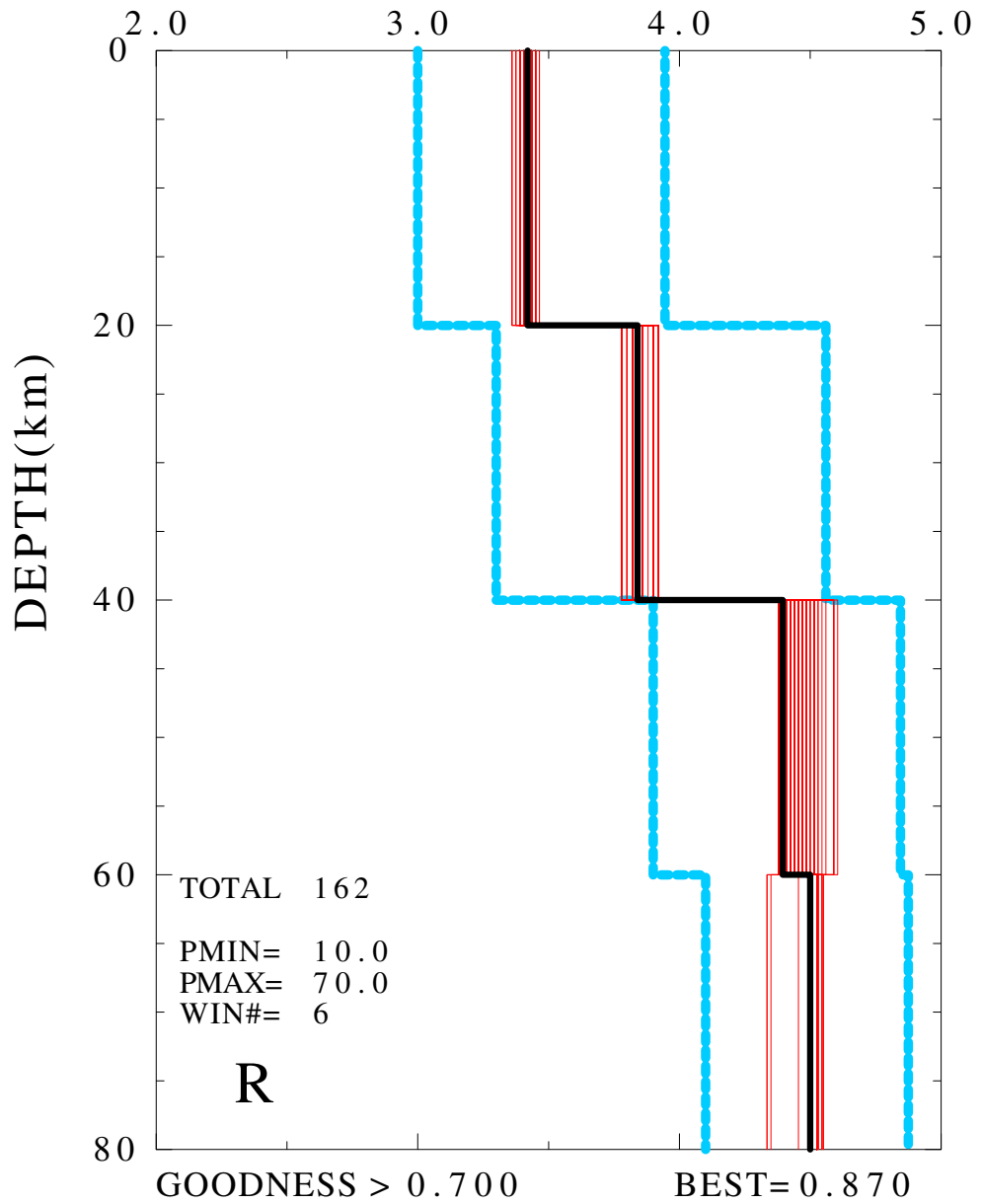
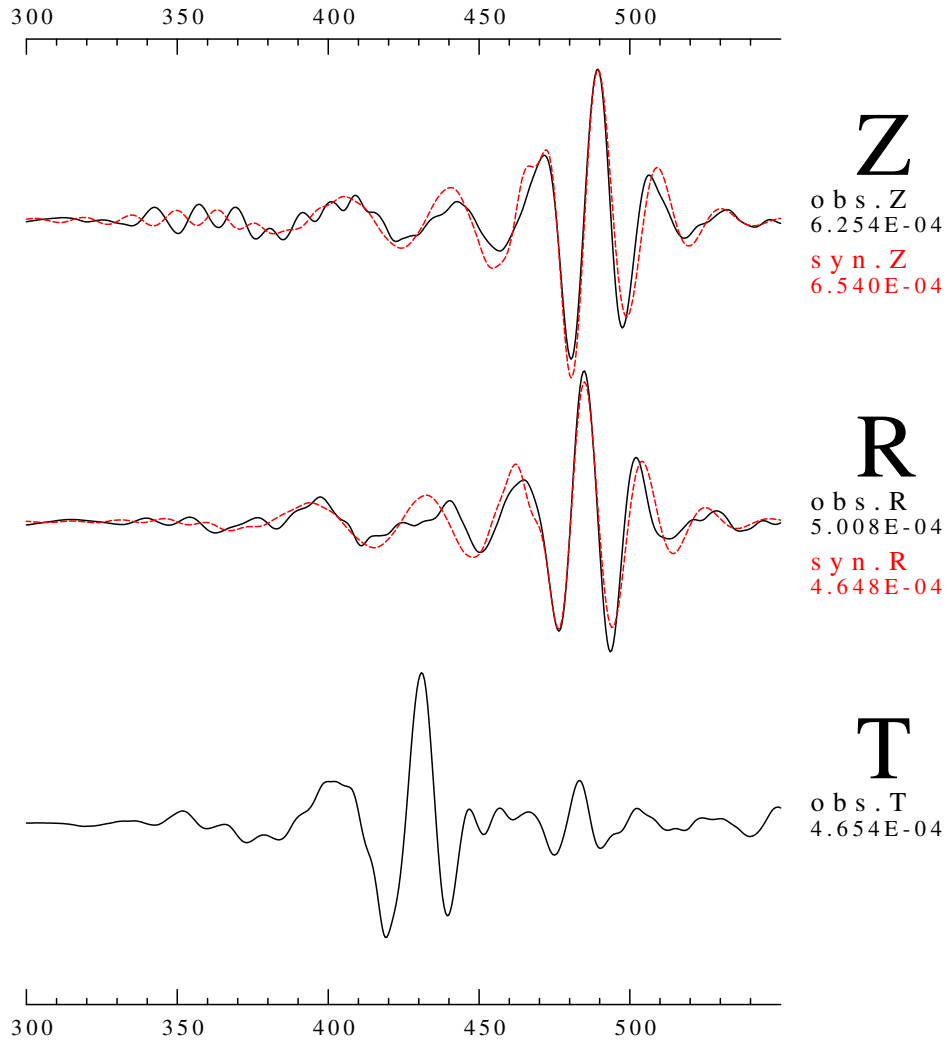


Fig. 5.1. First stage 4-layers GA search result.

TEXAS950414

CCM

VEL



FILTER Flo=0.010 Fhi=0.050 (Hz) Norder= 4

LON=-103.327 LAT=30.261 DEPTH= 23.00

AZ=48.918 BAZ=235.704 DIST= 1408.160

Fig. 5.2. The waveform fit for the best model in first step GA search.

GENETIC ALGORITHM SEARCH

TEXAS950414

CCM

S-VEL

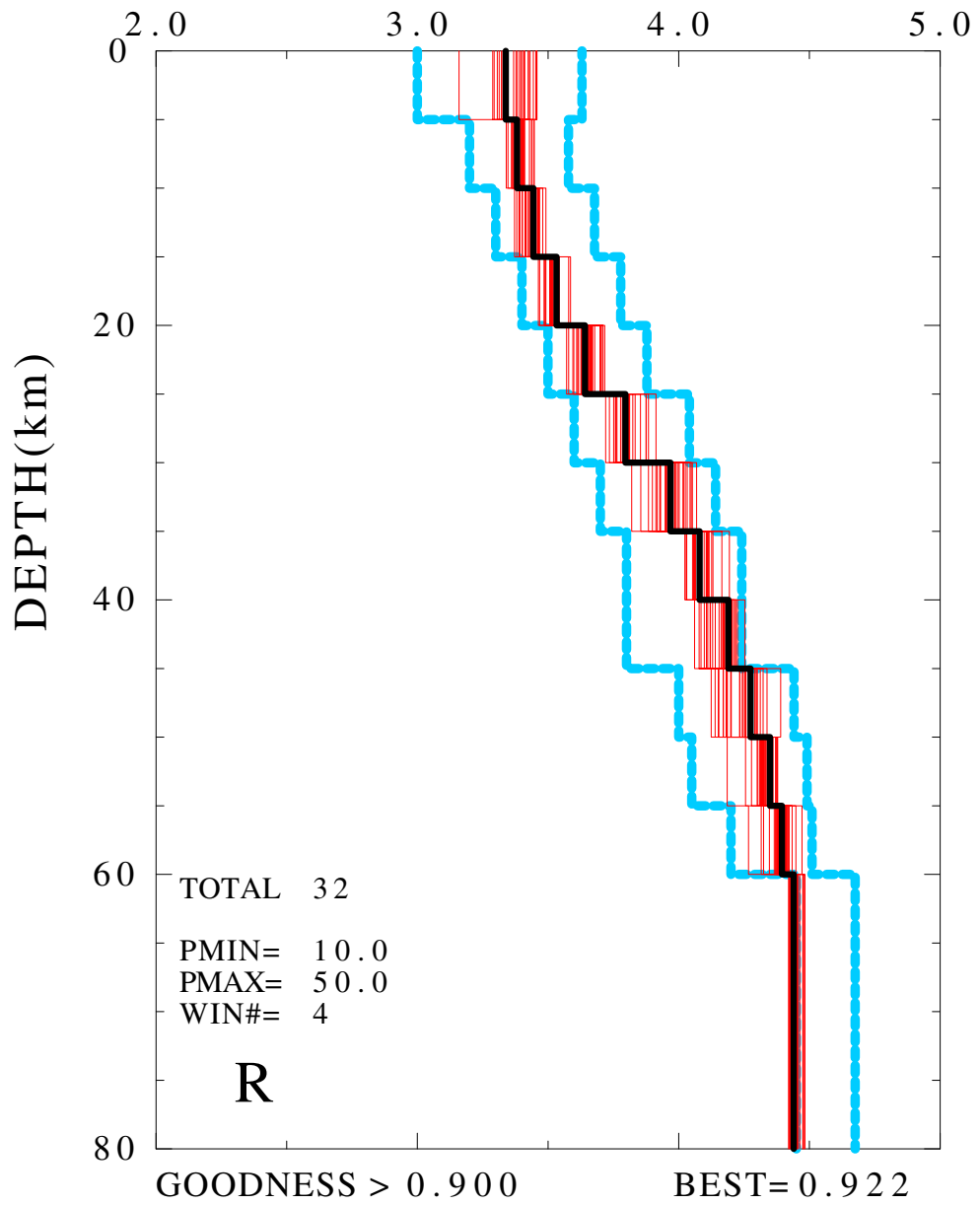
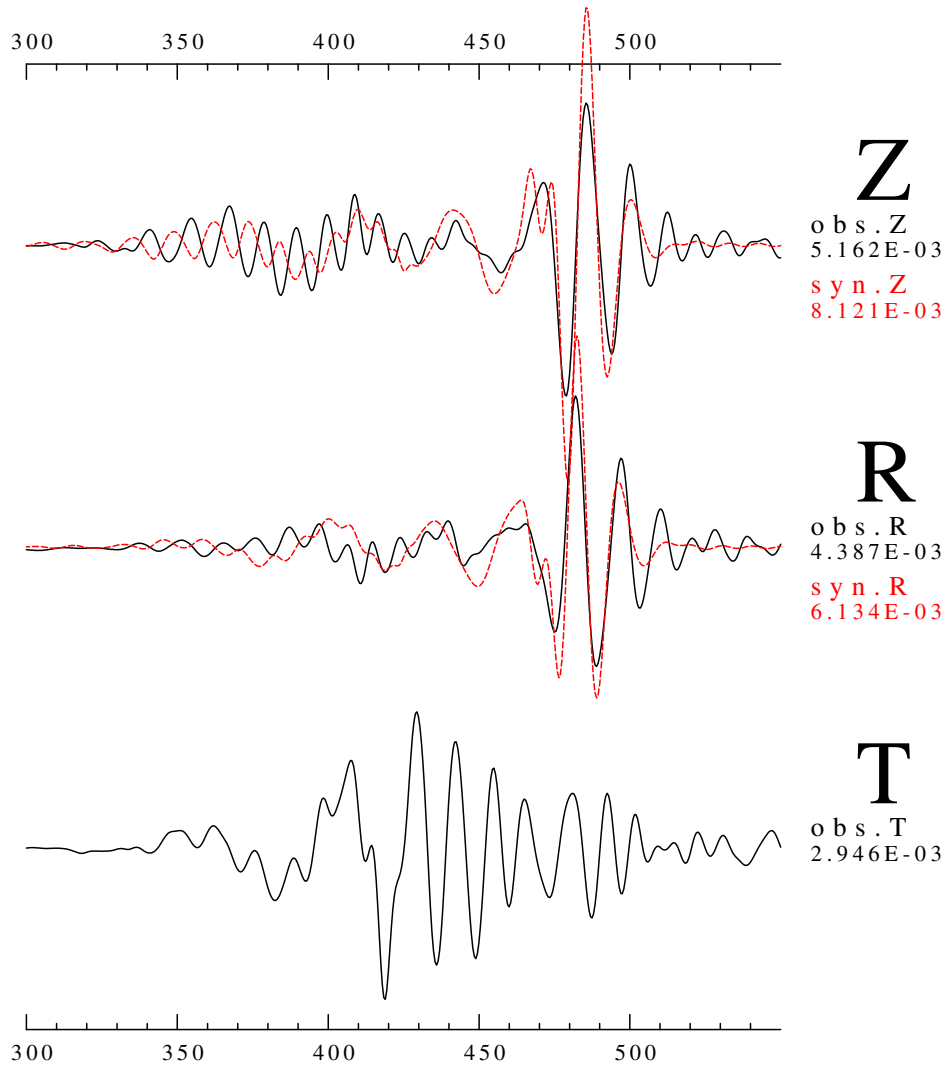


Fig. 5.3. Second stage GA search results.

TEXAS950414

CCM

DISP



FILTER Flo=0.010 Fhi=0.100 (Hz) Norder= 4

LON=-103.327 LAT=30.261 DEPTH= 23.00

AZ=48.918 BAZ=235.704 DIST= 1408.160

Fig. 5.4. The waveform fit of the best model in second step GA search.

suffers nonuniqueness and instability. The better way is to use both group and phase velocity dispersion in the inversion. This requires another procedure to extract surface wave phase velocity dispersion data. Herrin and Goforth (1977) introduced the use of a phase-matched filter to estimate the phase velocity. After these two procedures, we can perform the traditional surface-wave dispersion curve inversion.

On Figure 5.5, we show the multiple filtering result. The bottom figure shows the group velocity dispersion curve. At CCM, the vertical component displacement record shows a very clear fundamental mode and first higher mode Rayleigh wave. At periods longer than 40 seconds, the fundamental mode curve is not as smooth at shorter periods. This character, which is observable for stations in similar geological regions such as that where station CBKS (shown on figure 5.24), may be caused by some structure or may be due to low S/N at long periods. The first higher mode is clearly identified between 6 and 18 seconds. But for periods shorter than 5 seconds, a possible second higher mode arrives to form a strong Lg phase at 3.4 km/sec. We would like to see whether all these features can be modeled through waveform modeling. Figure 5.6 shows the extracted fundamental and first higher mode using phase-matched filter technique. The top trace is the observed and the bottom trace is the residual seismogram after subtracting the extracted fundamental and first higher mode Rayleigh wave. In the residual seismogram, we can see a possible second higher mode signal in the time window 320 to 430 seconds. But there

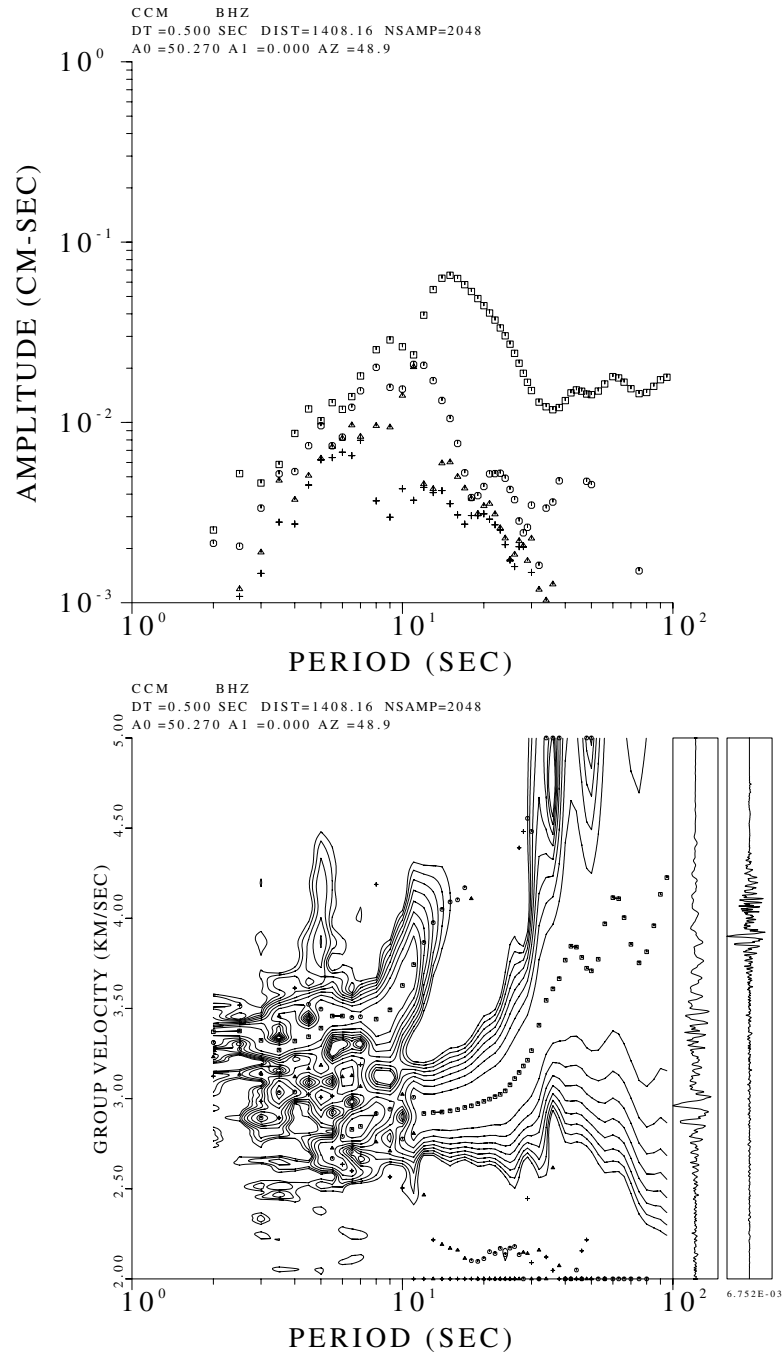


Fig. 5.5. The extracted surface wave dispersion data using multiple filtering techniques. The top plot shows the spectrum amplitudes at different periods. The bottom plot shows the group velocity dispersion curve.

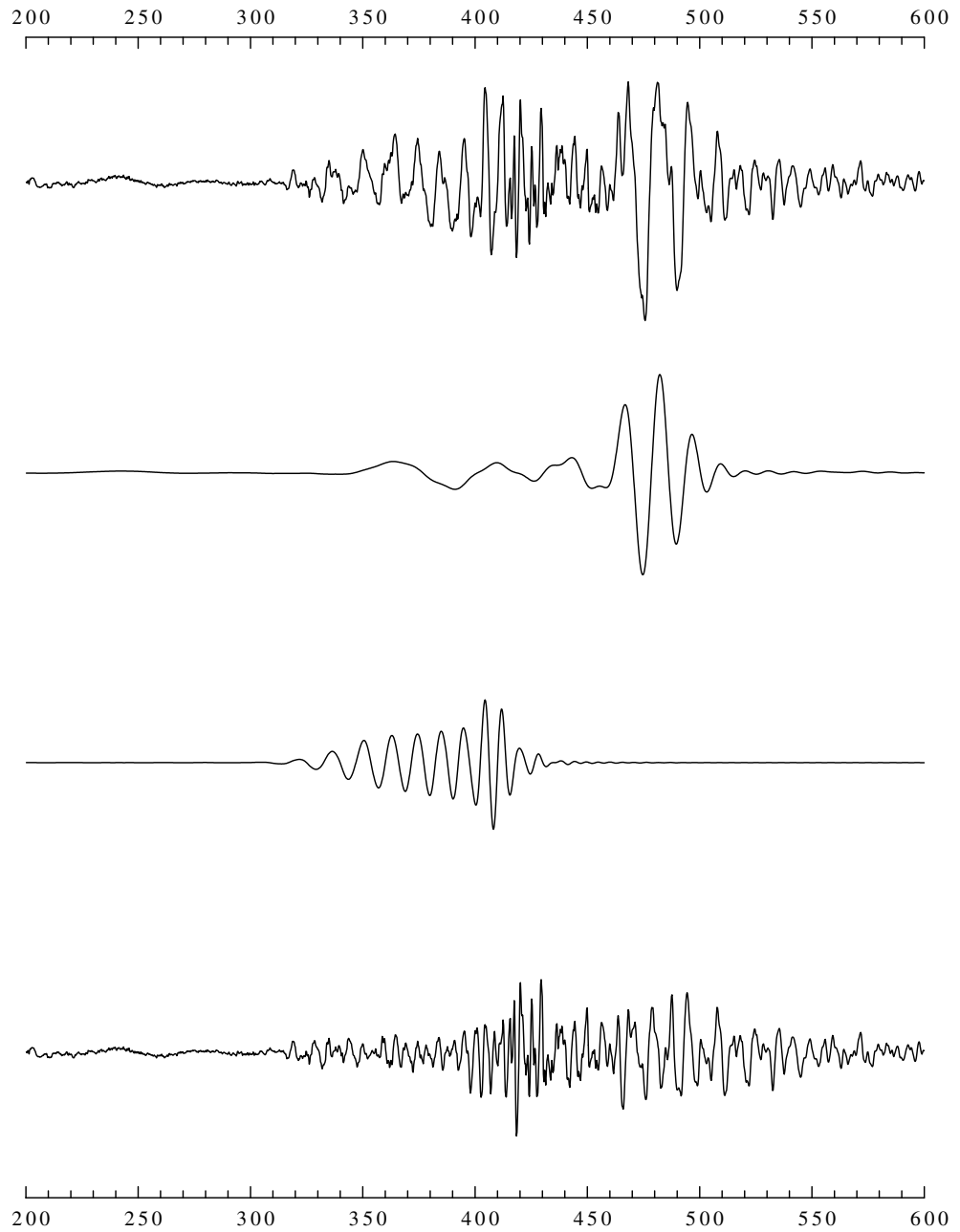


Fig. 5.6. This figure shows the extracted traces using the phase match filter technique. The top trace is the vertical component displacement seismogram of CCM. The second trace is extracted fundamental mode. The third trace is the extracted first higher mode. The bottom trace is the residual.

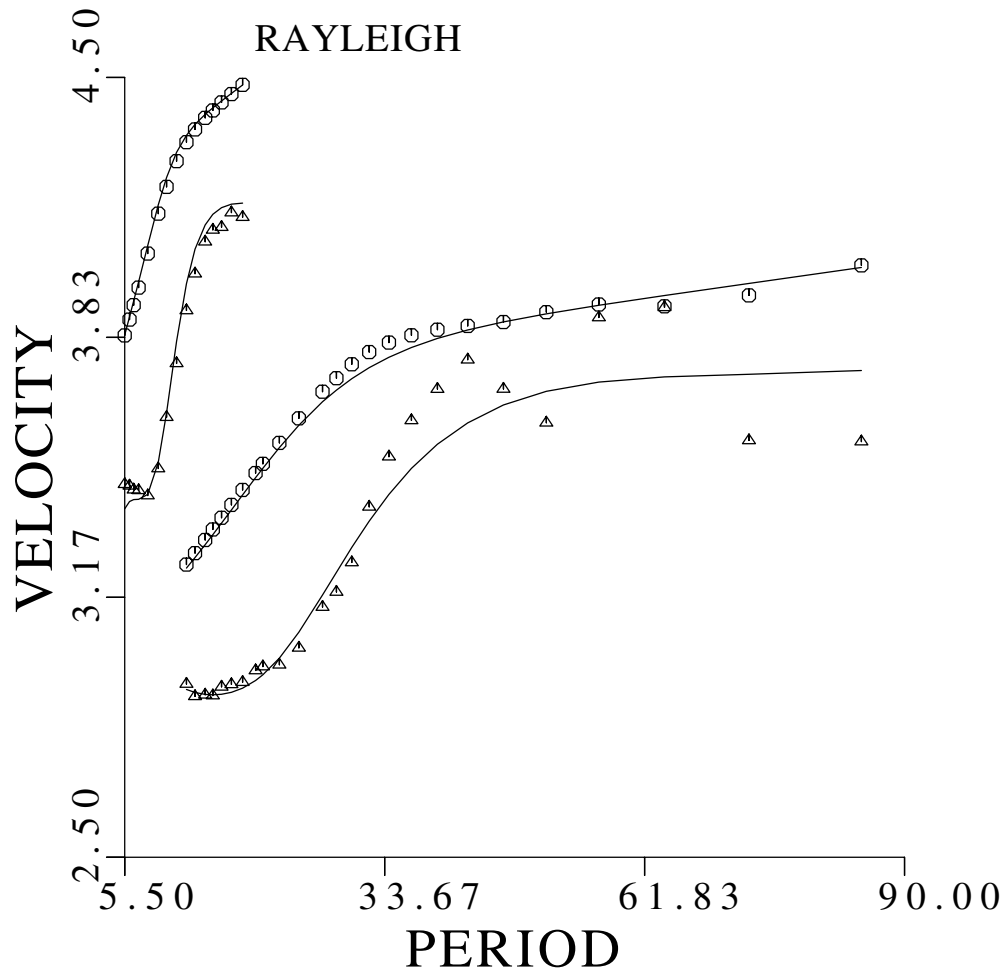


Fig. 5.7. The comparison of observed phase (circle), group velocities (triangle), and predicted (line) from inversion for the fundamental and first higher mode Rayleigh-wave.

remains one question about what kind signal is that which arrives between 440-540 seconds with strong energy.

Using group and phase velocities in the inversion, the results are shown in Figure 5.7 and 5.8. Figure 5.7 shows the used observed and predicted dispersion curves. Figure 5.8 shows the inverted model. The starting model uses the best model obtained in first-stage GA

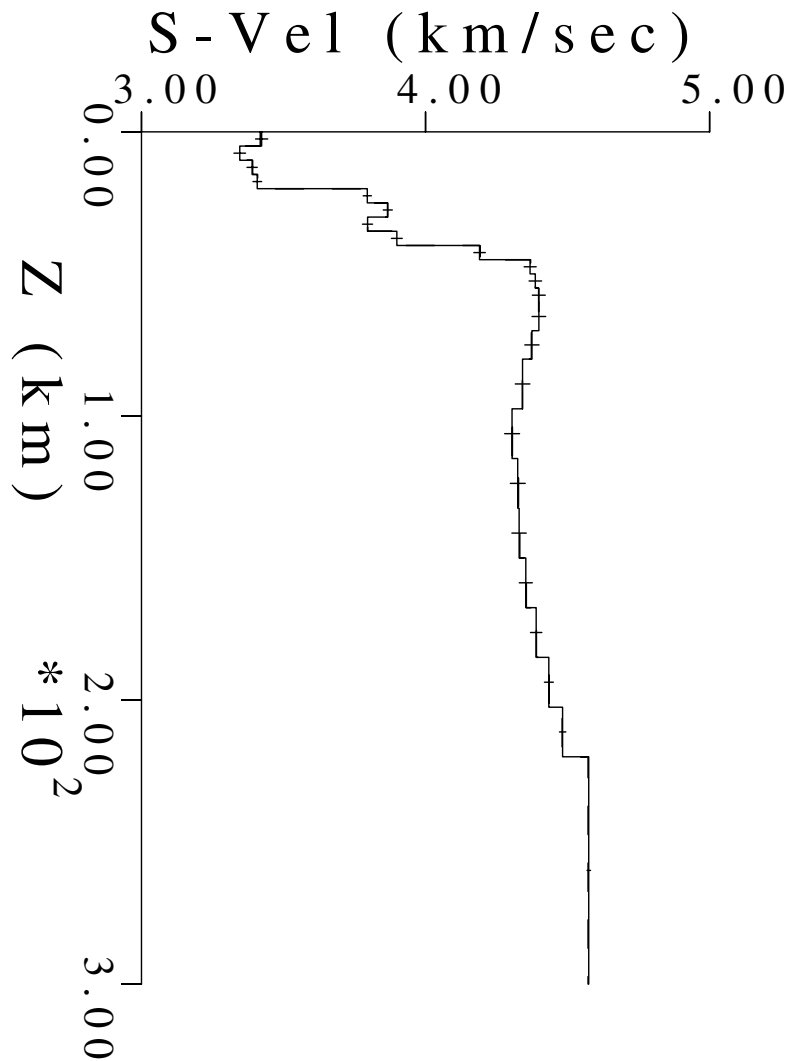


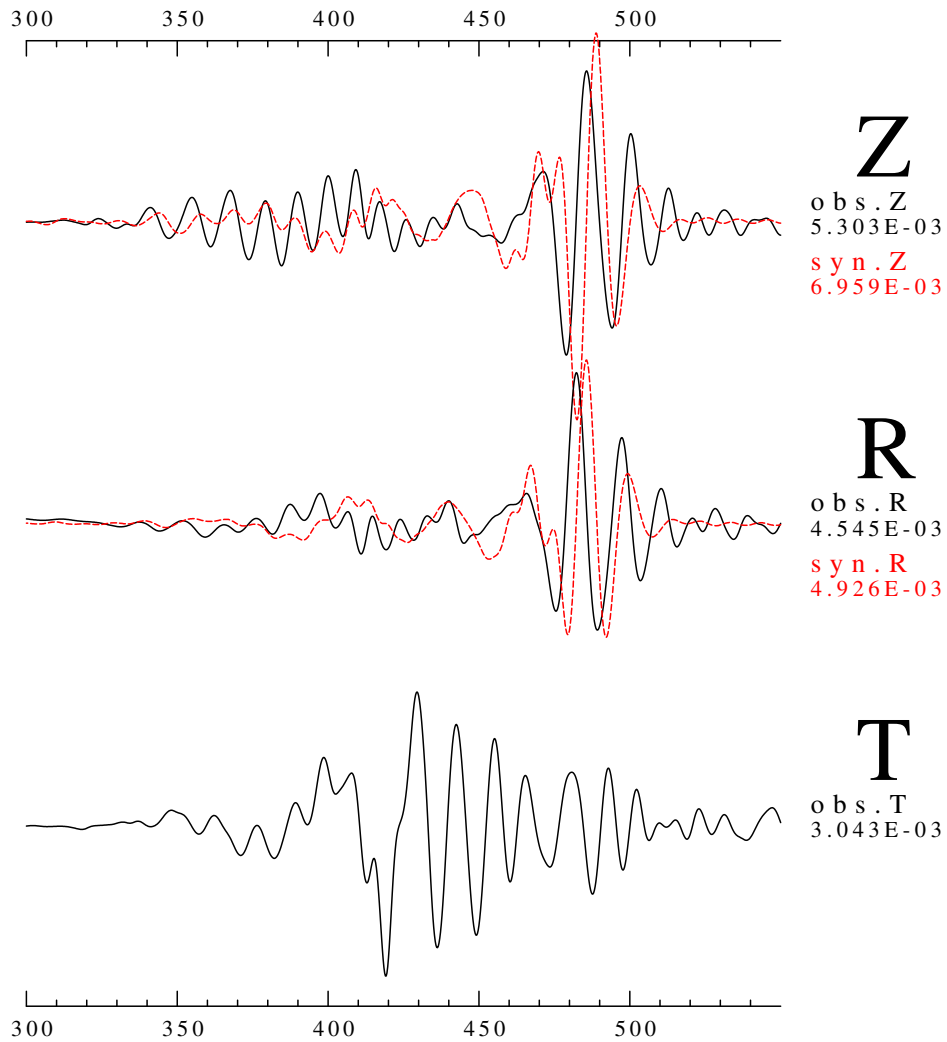
Fig. 5.8. The inversion model.

search shown on figure 5.1. Figure 5.9 shows the waveform fit using the inverted model at two different frequency bands 0.01-0.1 and 0.01-0.5 Hz. There is *a priori* information used in generating the synthetics which is not available from this inversion-the frequency dependent Q model which will be described later in this chapter. From the dispersion curve fit, it is not surprising to see that synthetic

TEXAS950414

CCM

DISP



FILTER Flo=0.010 Fhi=0.100 (Hz) Norder= 4

LON=-103.327 LAT=30.261 DEPTH= 23.00

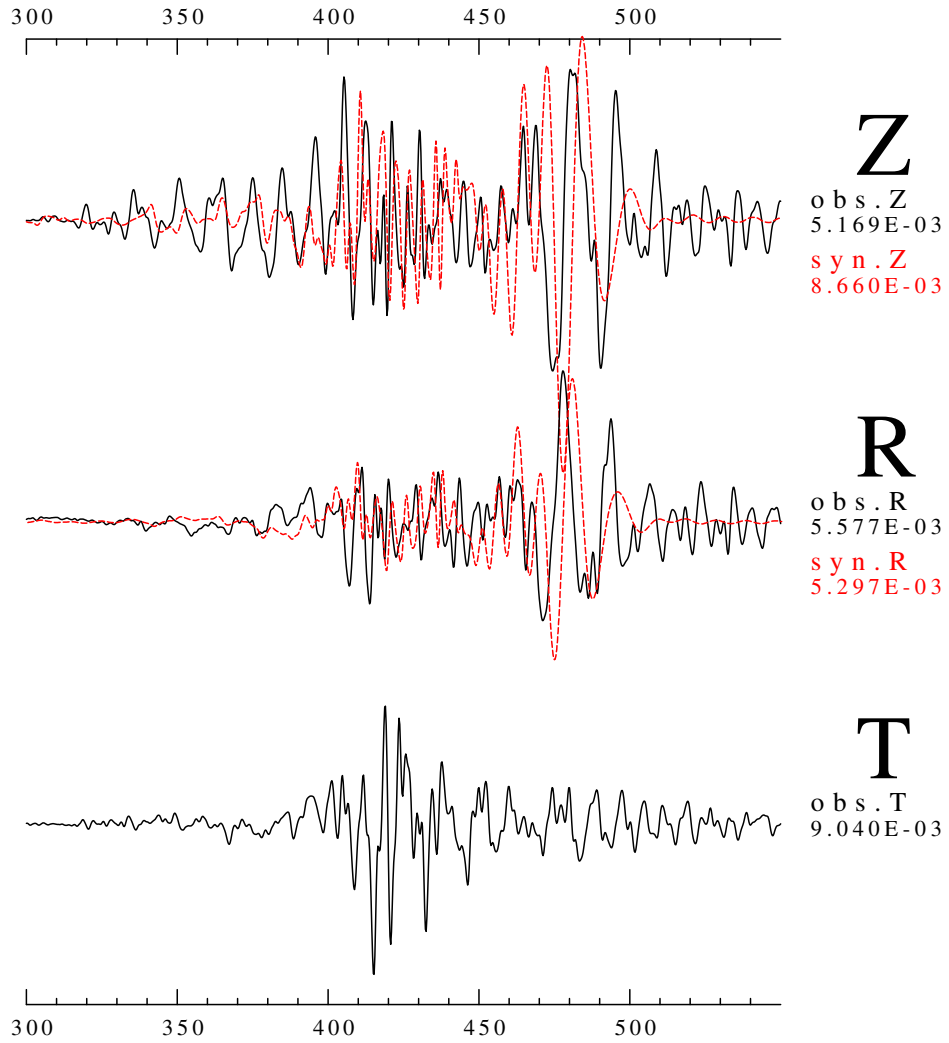
AZ=48.918 BAZ=235.704 DIST= 1408.160

Fig. 5.9a. The waveform fit of observed and predicted seismograms. The model is shown as figure 5.8. (a) Displayed at frequency range 0.01-0.1 Hz.

TEXAS950414

CCM

DISP



FILTER Flo=0.010 Fhi=0.500 (Hz) Norder= 4

LON=-103.327 LAT=30.261 DEPTH= 23.00

AZ=48.918 BAZ=235.704 DIST= 1408.160

Fig. 5.9b. (Cont'd) (b) The waveform fit for the frequency range 0.01-0.5 Hz.

fundamental mode is slightly slower than observed for the crustal wave and the mantle wave is not matched (Figure 5.9a). Also, the first higher mode (Figure 5.9b) should be fit much better than fundamental mode.

This exercise shows that traditional surface-wave inversion can provide a fairly good model from the point of view of waveform modeling. However this method also has its limitations, the inversion is dominated by short-period data which has more data points than the long period data and has no ability to change model to fit the data around 30 seconds in this case. However, this technique is very fast compared to waveform inversion techniques.

5.3 Linear Waveform Inversion

Gomberg and Masters (1988) introduced a linear waveform inversion technique. This technique formulates the residual seismogram of observed and synthetic seismograms in terms of model parameter perturbations. In this section, we will show the inversion results obtained by applying the method to the CCM data. The programs used here were coded by Professor Robert Herrmann, Saint Louis University.

In the original paper (Gomberg and Masters, 1988), the inversions were performed directly using the entire frequency range of interest. However, it was found by Professor Herrmann, that a better way to use this tool is by performing the inversions in different frequency bands. This improved procedure can utilize different information for

low frequency and high frequency to constrain the model in a more stable and robust way. A similar idea was reported by Bunks *et al.* (1995) for studying seismic reflection data.

We started with the best model obtained from first-stage GA search, and performed the linear waveform inversion. Figure 5.10 shows the waveform fit at two frequency ranges. We can see that the phase and amplitude of fundamental mode matches the observed. The first higher mode does not match the observed data because the *a priori* information of frequency dependent Q is not used in this test. The inverted model is not shown because it is used later to do fine adjustment by trial and error to obtain a better waveform fit.

Although all reported applications of linear waveform inversion were for the short distance records, we believe it is possible to apply this technique to longer distance records. The strength of this method is that the inversion will be directed toward reducing the large residual between observed and predicted data. However, the weakness of this method is associated with its strength, i.e. it needs a sophisticated controlling method to avoid the effects that are caused by improper knowledge of earthquake source.

5.4 GSDF Inversion

In this section, we describe our application of the GSDF inversion method to the CCM data. As with the model obtained from linear waveform inversion, the inverted model is not shown here, but an

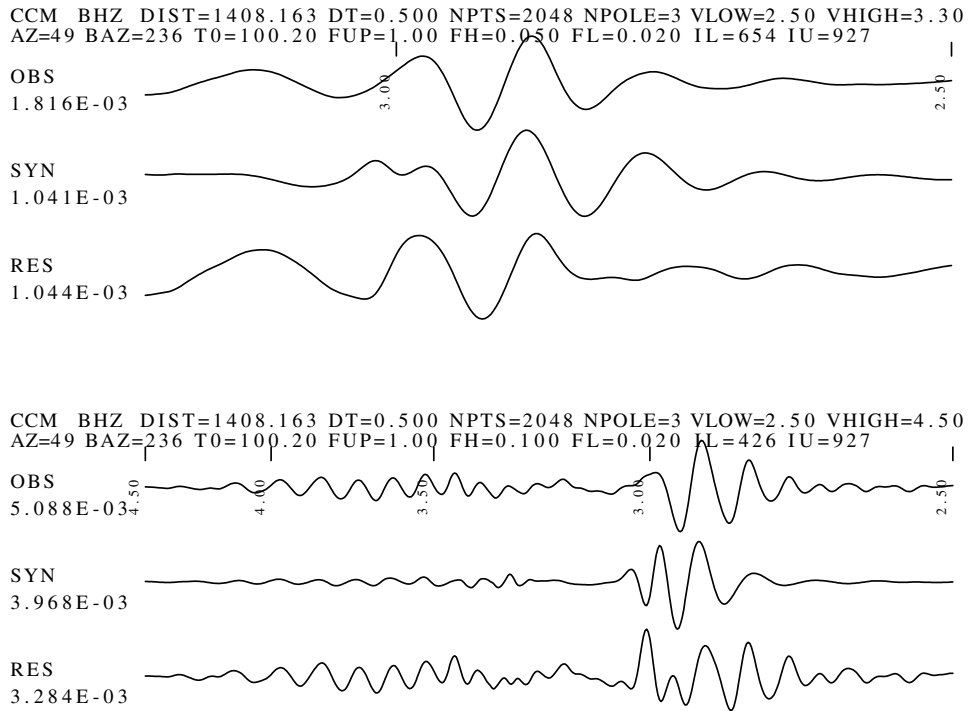


Fig. 5.10. The waveform comparison of observed, synthetic, and the residual seismograms at two different frequency bands. The top panel which corresponds to apparent velocities of 3.3-2.5 km/sec is plotted at 0.02-0.05 Hz. The bottom panel is for a 4.5-2.5 km/sec window and a 0.02-0.1 Hz frequency band.

improved waveform fit, by trial and error adjustment, based on this model will be shown later in this chapter. Figure 5.11 shows the waveform fit of the GSDF inversion result.

5.5 How to Judge the Waveform Fit

What is the criteria to assess the goodness of waveform fit? From the viewpoint of waveform modeling, the synthetics should be able to match the observed data in both phase and amplitude in different

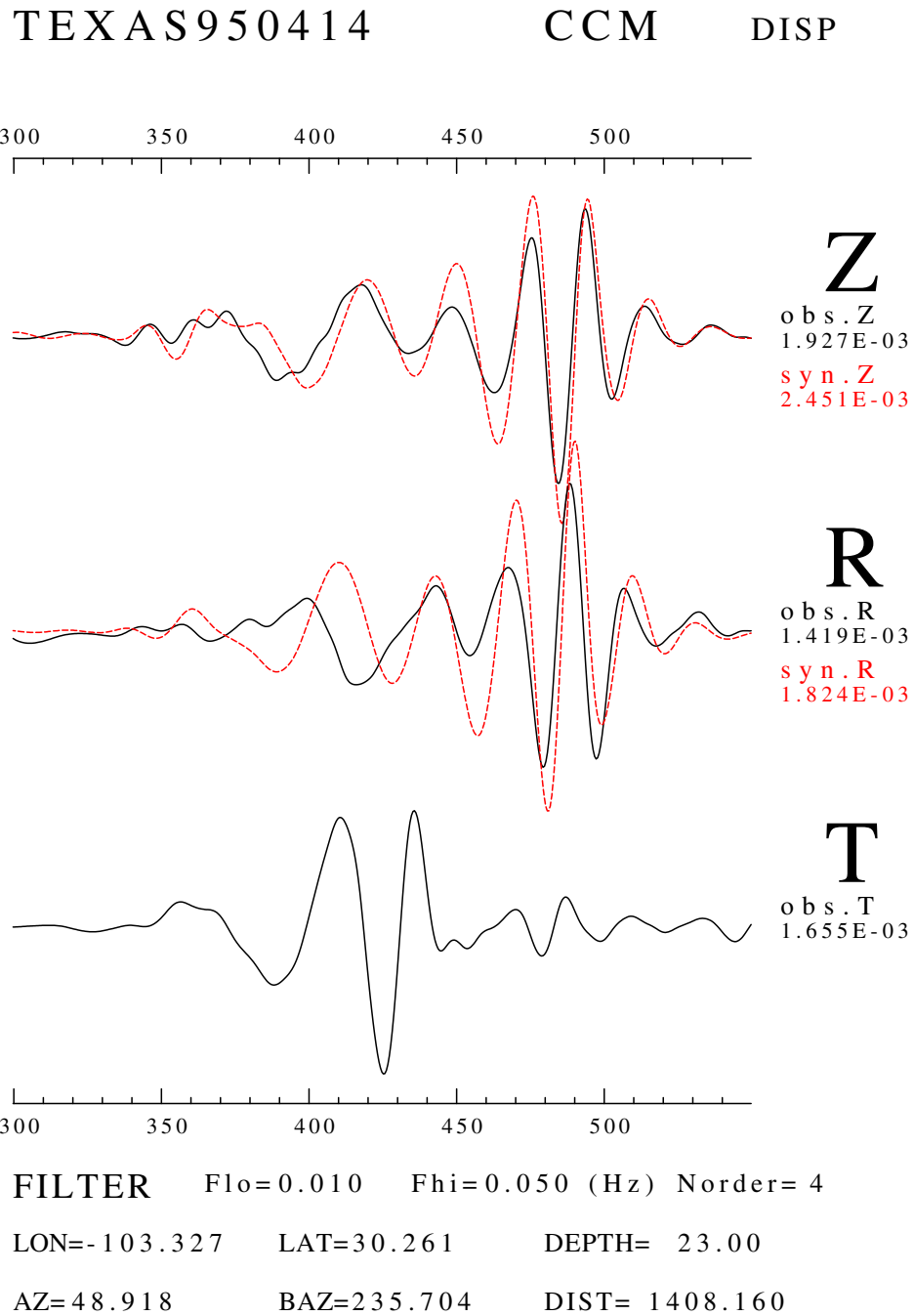
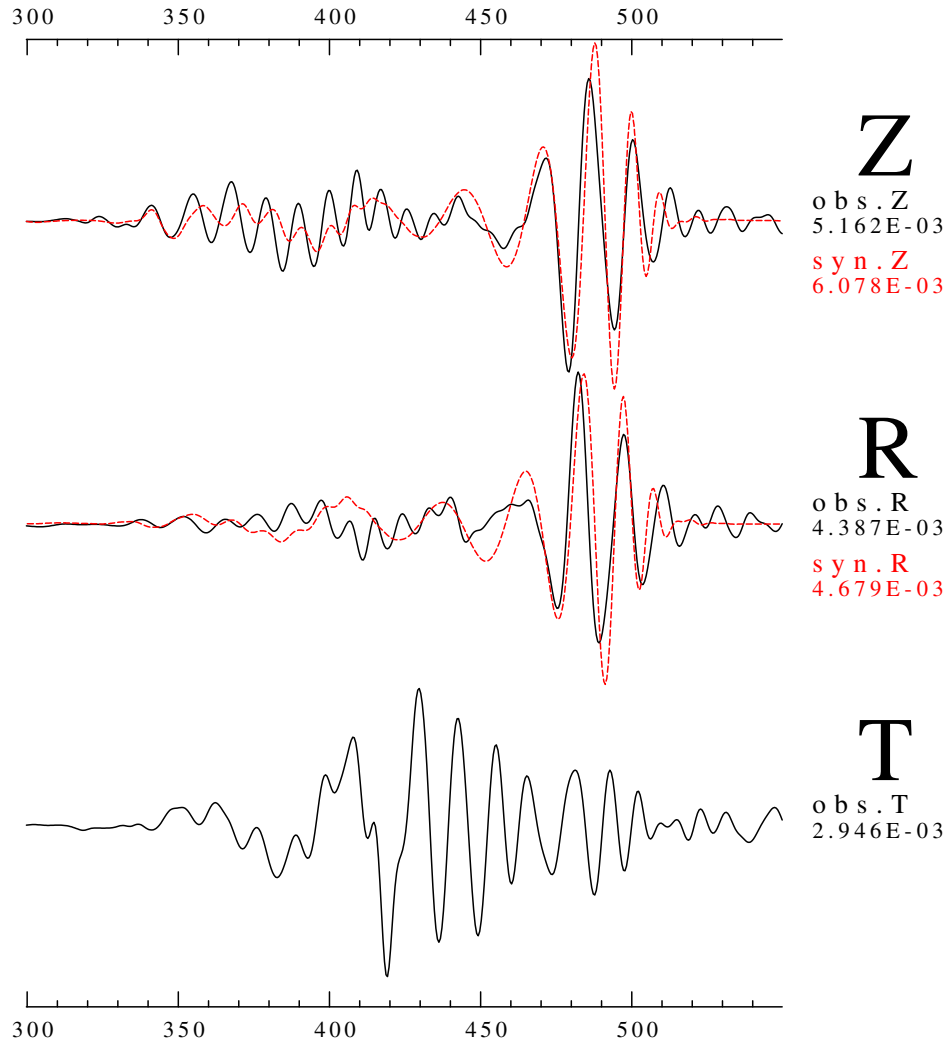


Fig. 5.11a. The waveform fit for the model obtained from GSDF inversion. Three different frequency ranges are shown: (a) for 0.01-0.05 Hz.

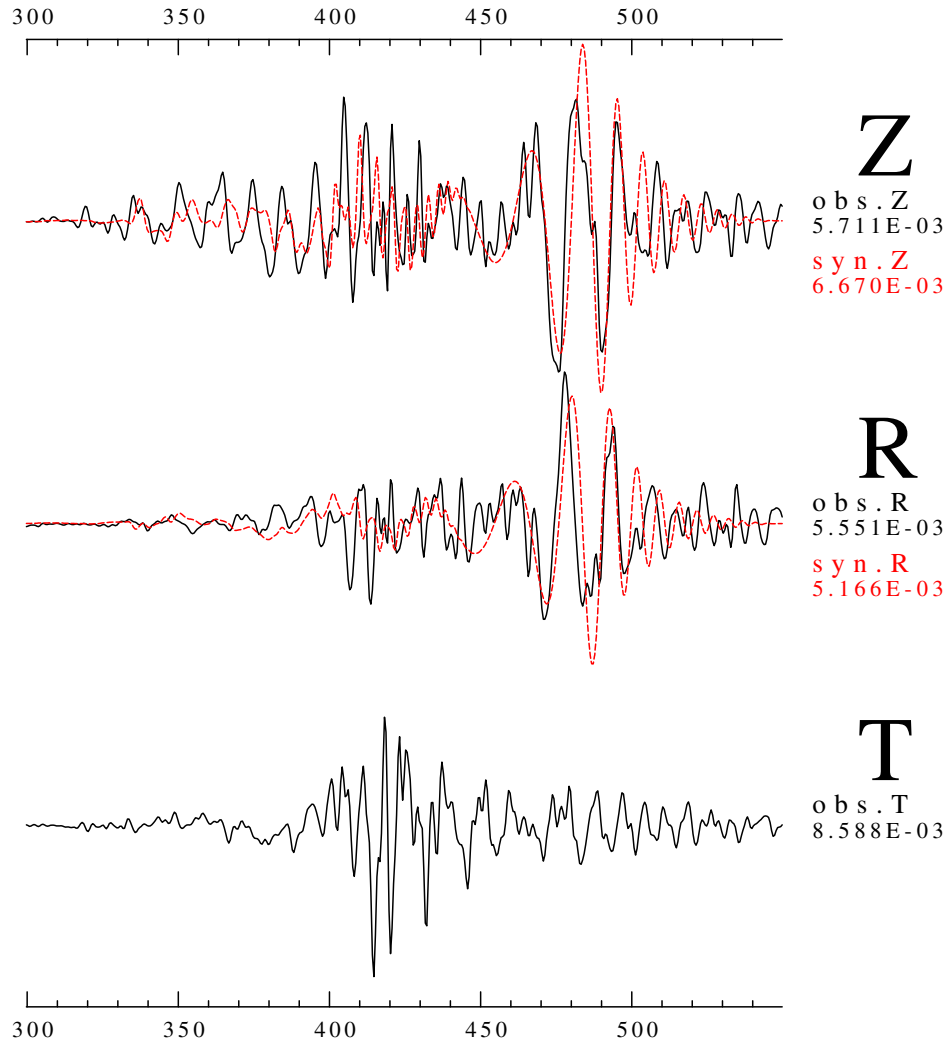
TEXAS950414 CCM DISP



FILTER Flo=0.010 Fhi=0.100 (Hz) Norder= 4
LON=-103.327 LAT=30.261 DEPTH= 23.00
AZ=48.918 BAZ=235.704 DIST= 1408.160

Fig. 5.11b. (Cont'd) (b) for 0.01-0.1 Hz.

TEXAS950414 CCM DISP



FILTER Flo=0.010 Fhi=0.500 (Hz) Norder= 4
LON=-103.327 LAT=30.261 DEPTH= 23.00
AZ=48.918 BAZ=235.704 DIST= 1408.160

Fig. 5.11c. (Cont'd) (c) for 0.01-0.5 Hz.

frequency bands. In this case, first let's see what is observable from recorded seismograms of station CCM. At CCM, we can see a fundamental mode and first higher mode with large amplitude, so the first requirement should be a good match to both fundamental and higher modes signal. If we can find such a model which can predict observed surface waveform, we would like to know whether this model is also good enough to match the body wave, P_{nl} and S in this case. After that, we would like to know if a model can generally meet the first two requirements, then is there a way to quantify the confidence in this model or to indicate any improvement that can be expected in additional modeling.

From above discussion, we can say that all four algorithms can provide fairly good models that can match fundamental mode up to 0.1 Hz. However, those models can not fit the higher modes, therefore the question is how to match the higher mode. Looking at the GSDF inversion result (figure 5.11b), we can see predicted higher mode amplitude is about factor two smaller than observed.

There are two possible ways to increase the higher mode amplitude. Let's examine the partial derivatives created for the GSDF inversion. As shown in Figure 5.12, we see that if we increase the upper mantle Q value, it is possible to increase the higher mode amplitude. Of course, the crustal Q value should decrease to compensate for the change and to maintain the fundamental mode amplitude. The result is shown in Figure 5.13. Indeed, the higher mode amplitude increases, but compared to Figure 5.11 we see that not only higher

mode but also fundamental mode amplitude are increased in amplitude, especially the low frequency part of fundamental mode which corresponding to the wave traveling through the upper mantle. Another problem with from this model, is that we cannot explain the signals in the 420-440 second time window.

The second way to increase the higher mode amplitude is to consider a frequency dependent Q for the high-frequency signal. To preserve the low frequency fundamental mode amplitude, the frequency dependent Q is applied to part of the signal whose frequency content is greater than 0.1 Hz. To avoid the abrupt change in spectrum shape when applying frequency dependent Q , a transition zone is used for 0.1-0.2 Hz. The following two examples are based on trial and error adjustment for the two models from GSDF inversion and linear waveform inversion. The reference period for frequency dependent Q is 0.1 Hz and $\eta = 0.5$. During the trial and error adjustment, the fundamental mode may shift in and out of phase. But the purpose is to understand how to fit the higher mode phase and amplitude, and what process creates such strong Lg wave.

The first example is a fine tuning result for the GSDF inversion result. The model is shown in Figure 5.14 and uses frequency dependent Q . The waveform fit is displayed in Figure 5.15. From the waveform, we can see that low frequency fundamental mode amplitude does not change much. Through the trial and error adjusting, the higher mode phase and amplitude are generally matched. However, the Airy phase amplitude is increases during such an adjustment. The

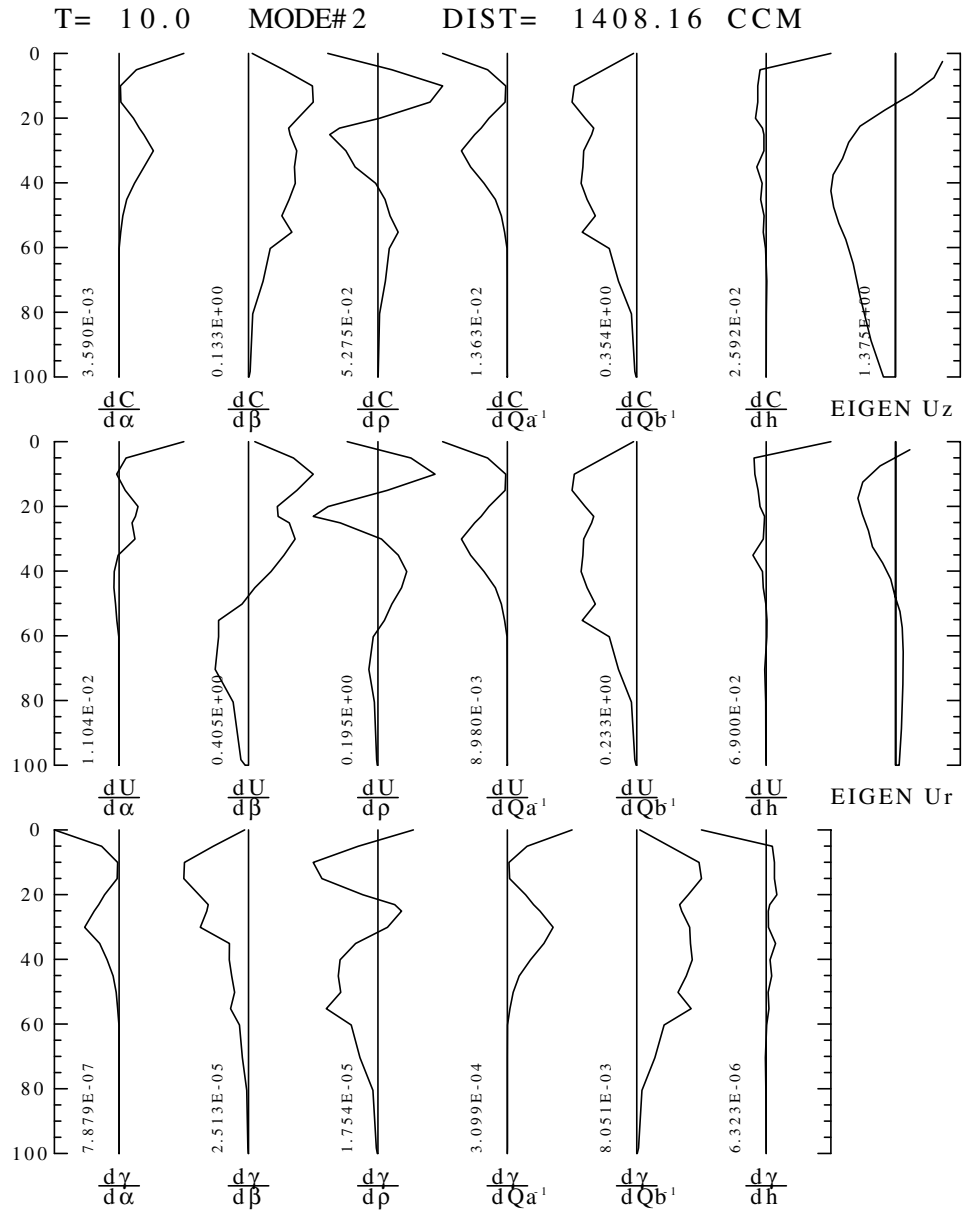
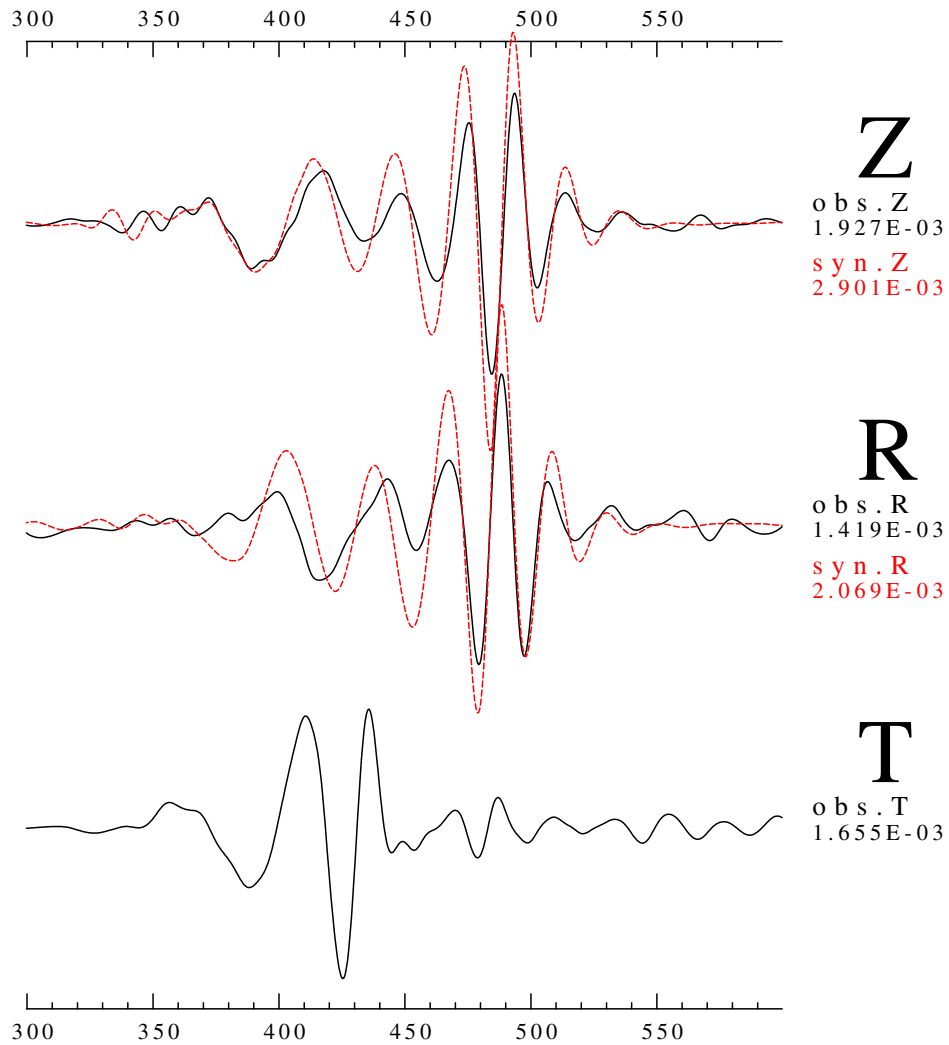


Fig. 5.12. The partial derivatives of first higher mode at 10 seconds which computed for the GSDF inversion.

TEXAS950414 CCM DISP



FILTER Flo=0.010 Fhi=0.050 (Hz) Norder= 4

LON=-103.327 LAT=30.261 DEPTH= 23.00

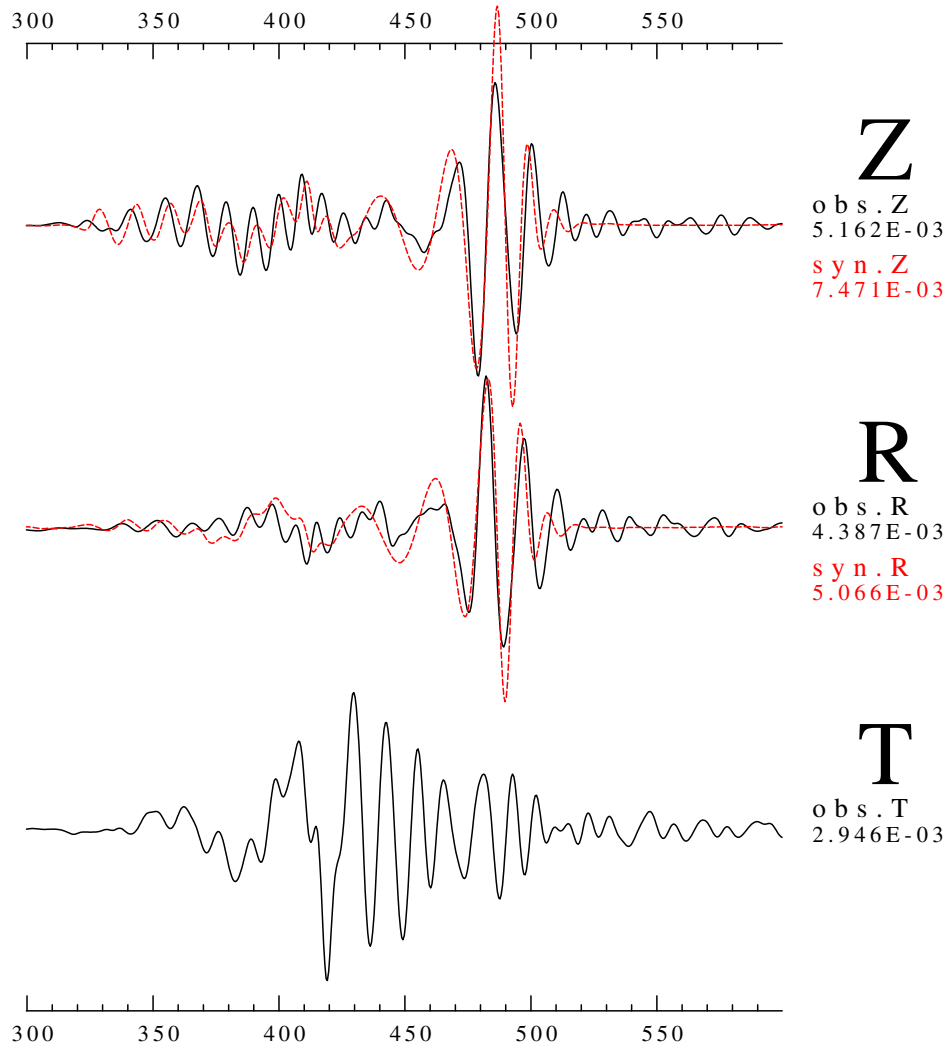
AZ=48.918 BAZ=235.704 DIST= 1408.160

Fig. 5.13a. Waveform fit for the model which increasing the upper mantle Q. Three different frequency ranges are displayed: (a) 0.01-0.05 Hz.

TEXAS950414

CCM

DISP



FILTER Flo=0.010 Fhi=0.100 (Hz) Norder= 4

LON=-103.327 LAT=30.261 DEPTH= 23.00

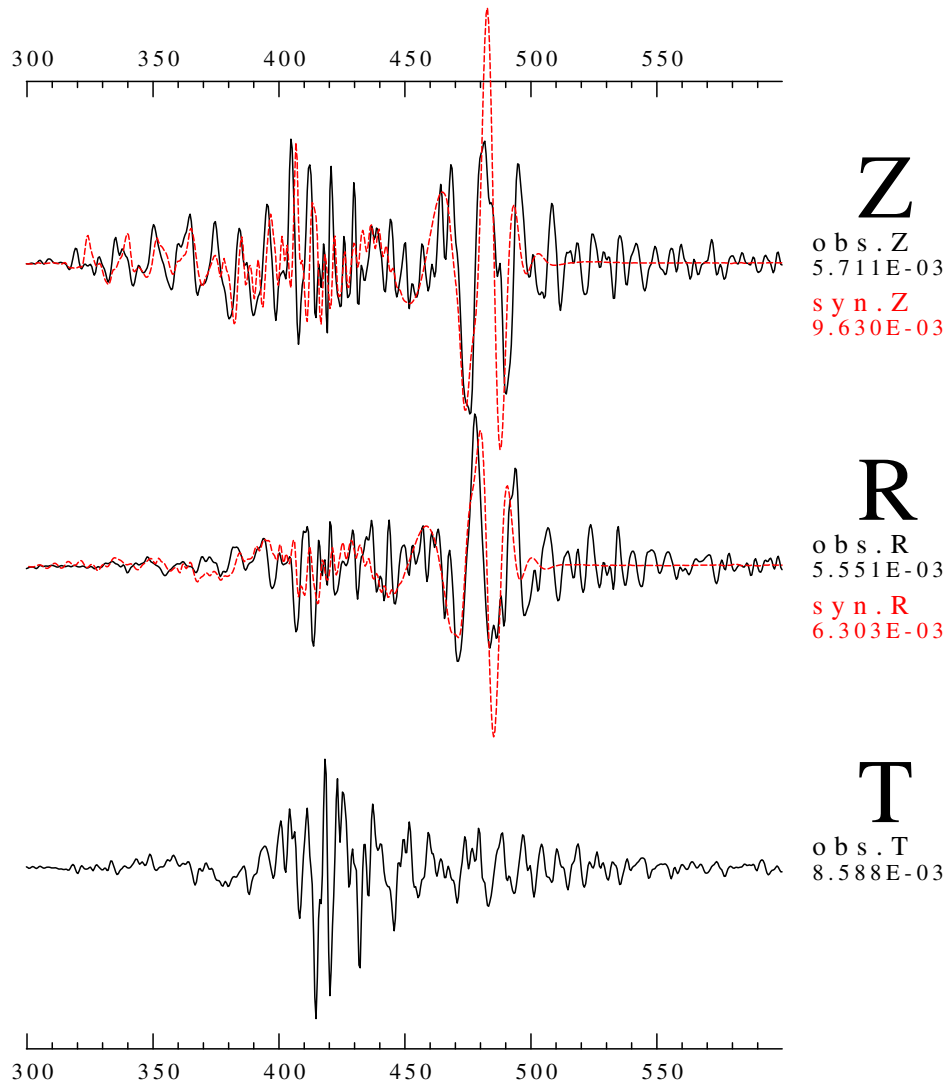
AZ=48.918 BAZ=235.704 DIST= 1408.160

Fig. 5.13b. (Cont'd) (b) 0.01-0.1 Hz.

TEXAS950414

CCM

DISP



FILTER Flo=0.010 Fhi=0.500 (Hz) Norder= 4

LON=-103.327 LAT=30.261 DEPTH= 23.00

AZ=48.918 BAZ=235.704 DIST= 1408.160

Fig. 5.13c. (Cont'd) (c) 0.01-0.5 Hz.

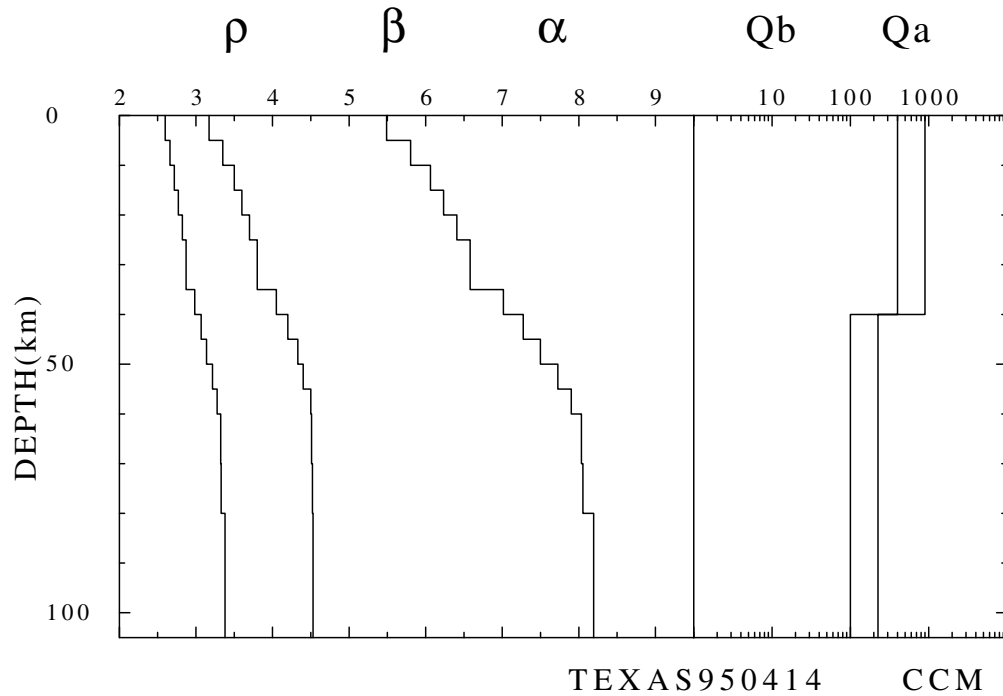


Fig. 5.14. This figure shows a better model which based on GSDF inversion result, and using trial and error to do the fine tuning.

waveform, again, cannot match the signals in the time window 420-440 seconds, and it cannot explain what high frequency signals between 440 and 470 seconds. Looking at the individual mode contributions (Figure 5.16), we see that the higher mode signal are mainly composed of the first two higher modes.

The second example starts with the inversion result of linear waveform inversion. This adjusted model shows good agreement with observed data, so we will use this model as an example to illustrate the reliability of model. In this model, not only the Rayleigh wave but also the Love wave are modeled. Figure 5.17 shows the models for the

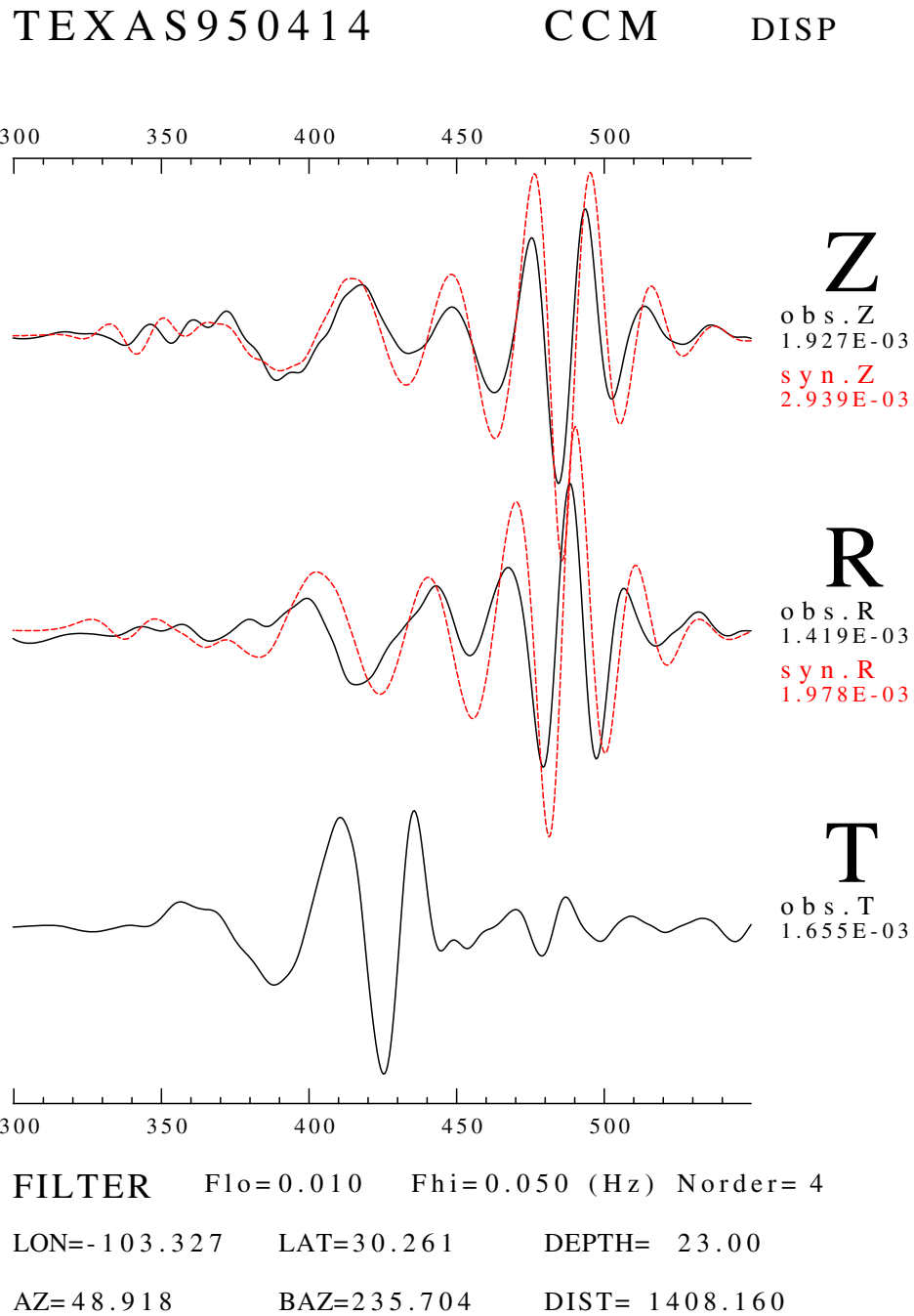
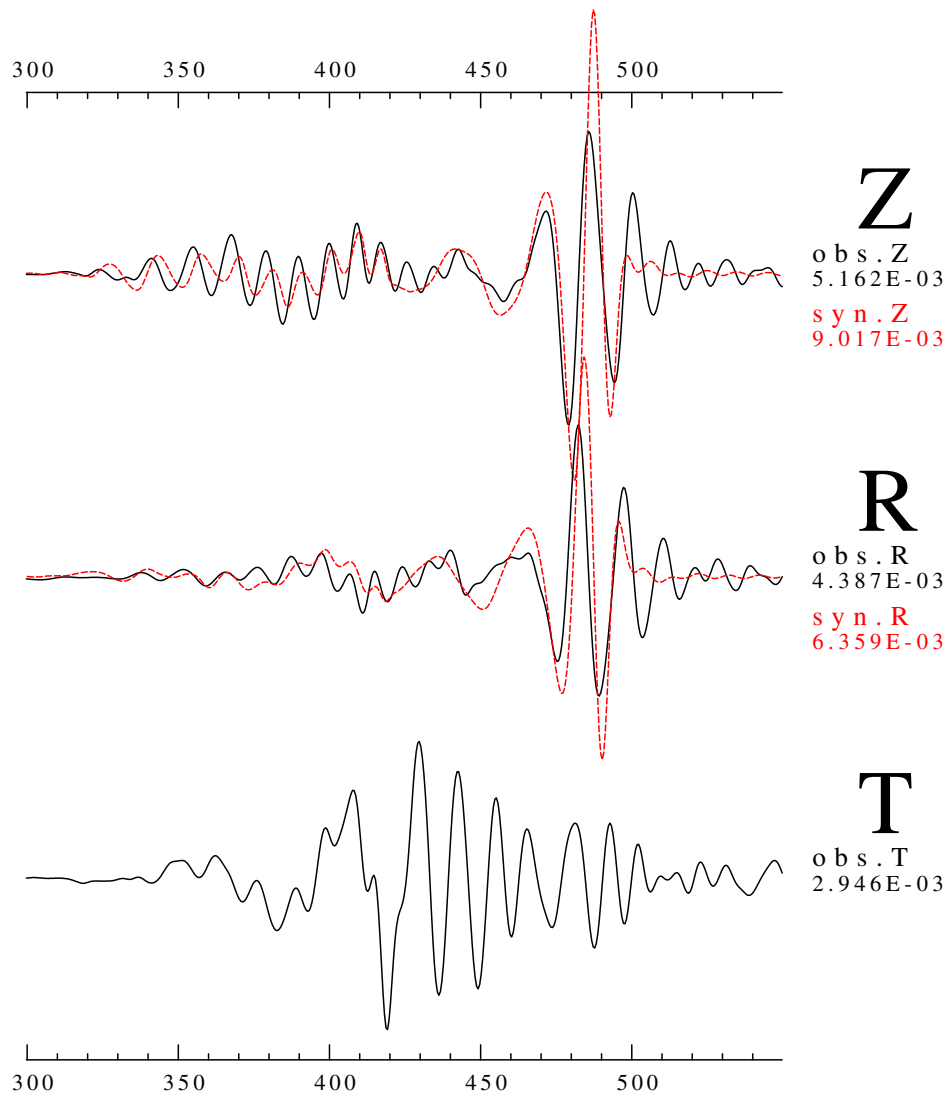


Fig. 5.15a. The waveform fit of the model shown as figure 5.14. Three frequency ranges are displayed: (a) 0.01-0.05 Hz.

TEXAS950414

CCM

DISP



FILTER Flo=0.010 Fhi=0.100 (Hz) Norder= 4

LON=-103.327 LAT=30.261 DEPTH= 23.00

AZ=48.918 BAZ=235.704 DIST= 1408.160

Fig. 5.15b. (Cont'd) (b) 0.01-0.1 Hz.

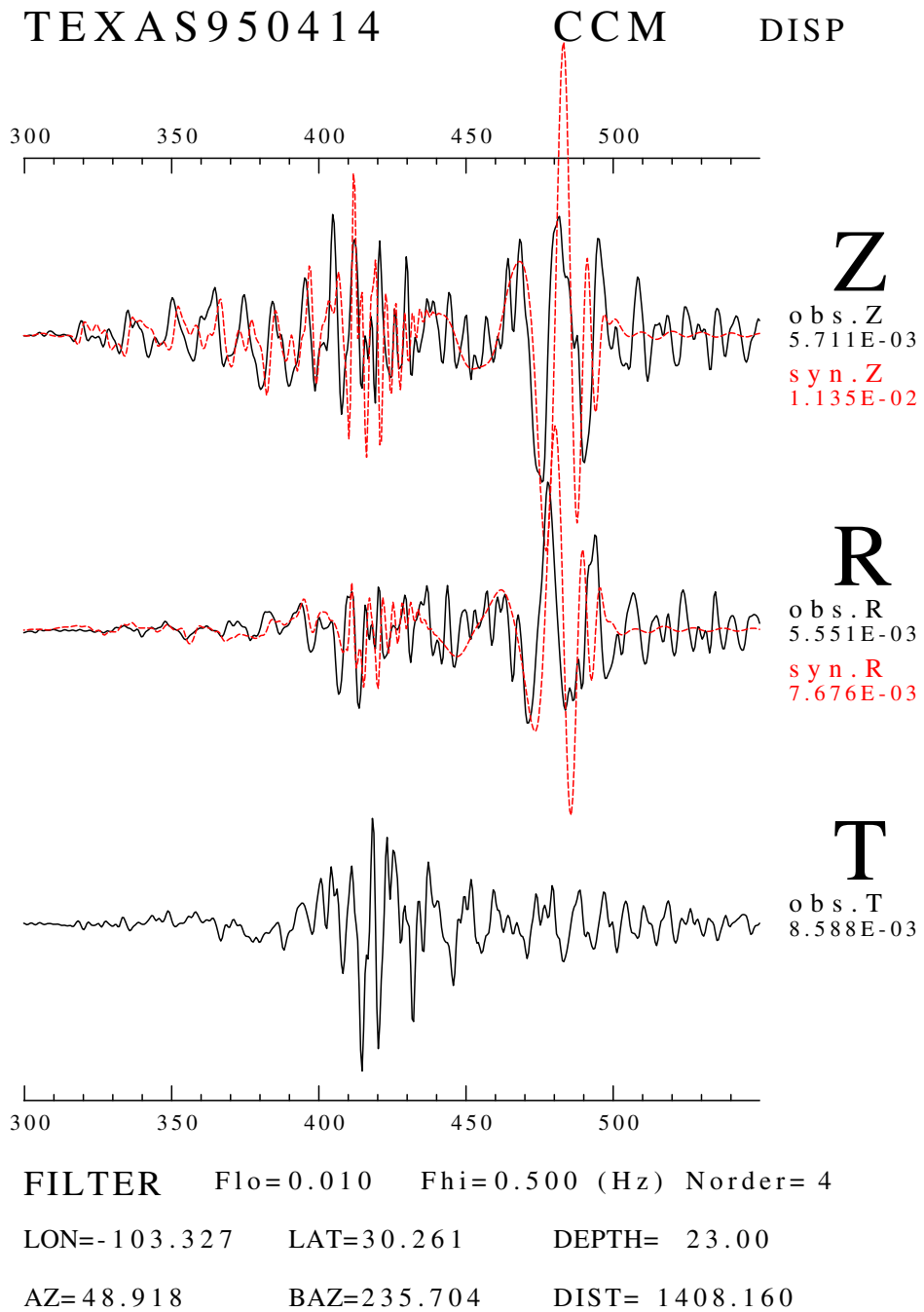
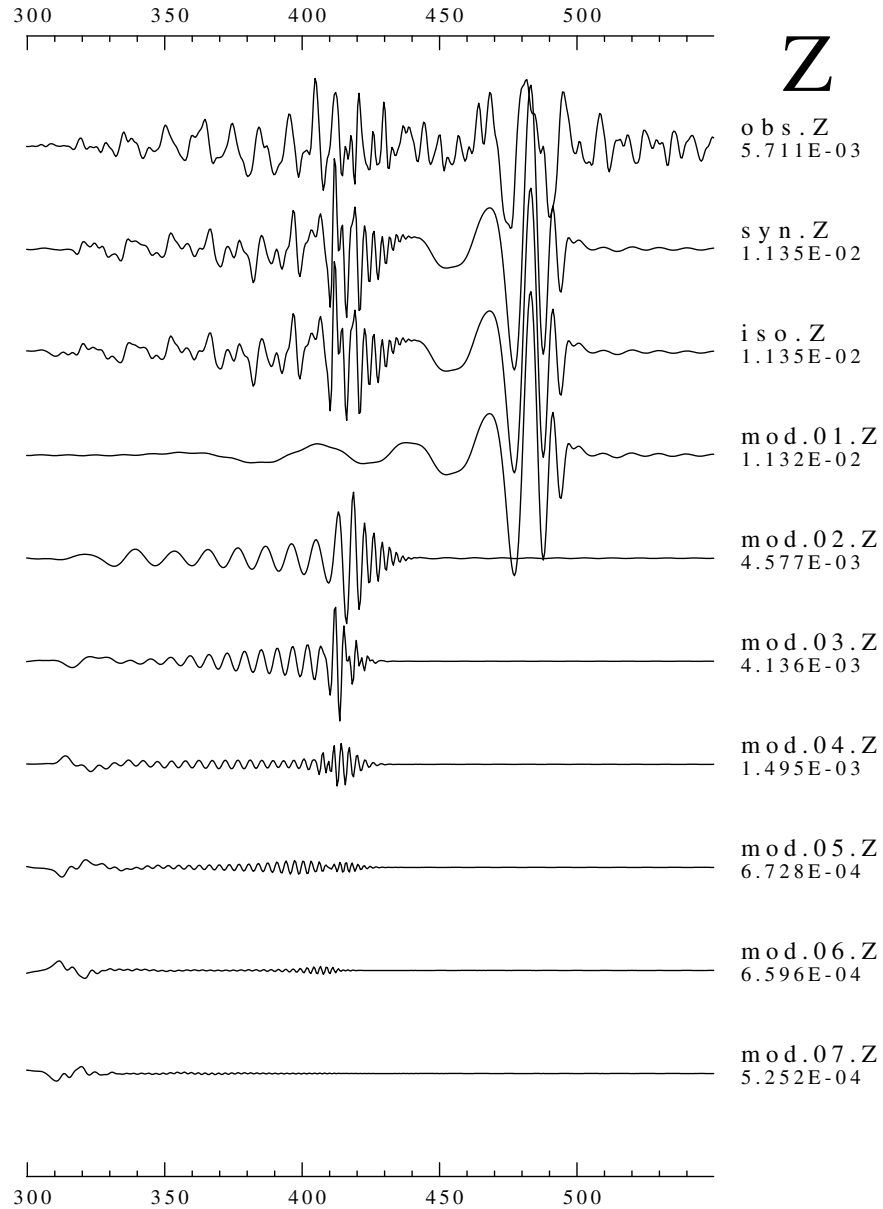


Fig. 5.15c. (Cont'd) (c) 0.01-0.5 Hz.

TEXAS950414 CCM DISP



FILTER Flo=0.010 Fhi=0.500 (Hz) Norder= 4

LON=-103.327 LAT=30.261 DEPTH= 23.00

AZ=48.918 BAZ=235.704 DIST= 1408.160

Fig. 5.16. The observed, synthetic, and seven single-mode seismograms.

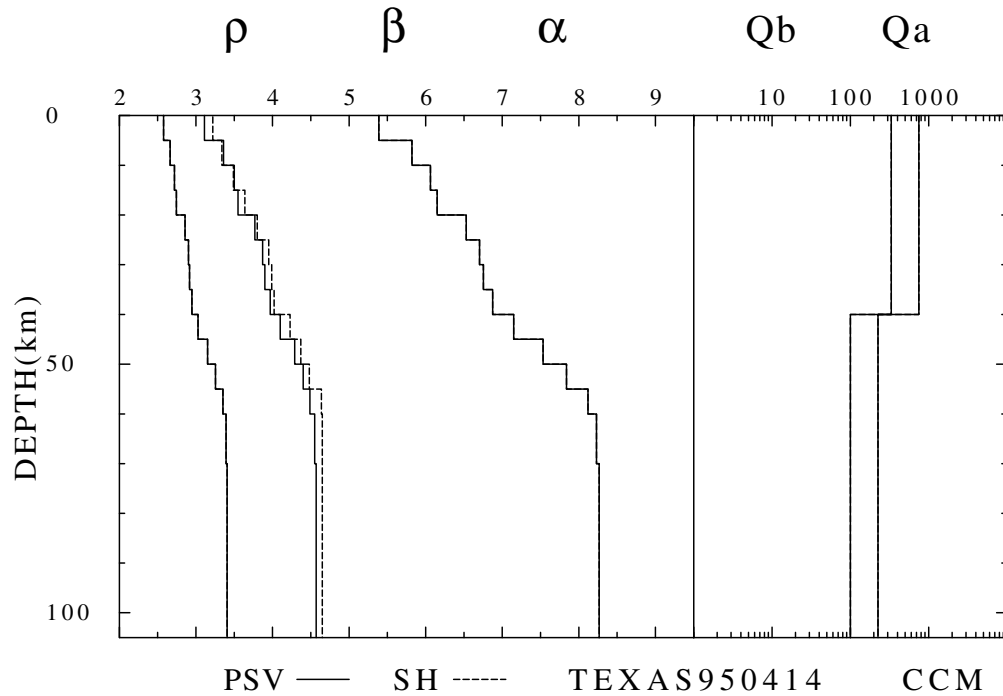


Fig. 5.17. This figure shows a better model which based on linear waveform inversion result, and using trial and error to do the fine tuning.

Rayleigh and Love waves. There are several characteristics worth mentioning. First of all, during the adjusting process, no low velocity zone is allowed in the crust. Second, there is no need to introduce a low velocity zone in the uppermost mantle (40-220 km) which is usually seen in other reported surface wave inversion results. Third, the model shows a gradient zone between 40 and 60 km instead of a sharp crust-mantle boundary. Finally, the lower crust (20-40 km) has a steep velocity gradient. Figure 5.18 shows the waveform fit at three different frequency ranges. From these plots, we see a good fit to the higher mode waveform signal, especially for the signals in the 400-440 time window which are not well modeled by the other models. In Figure

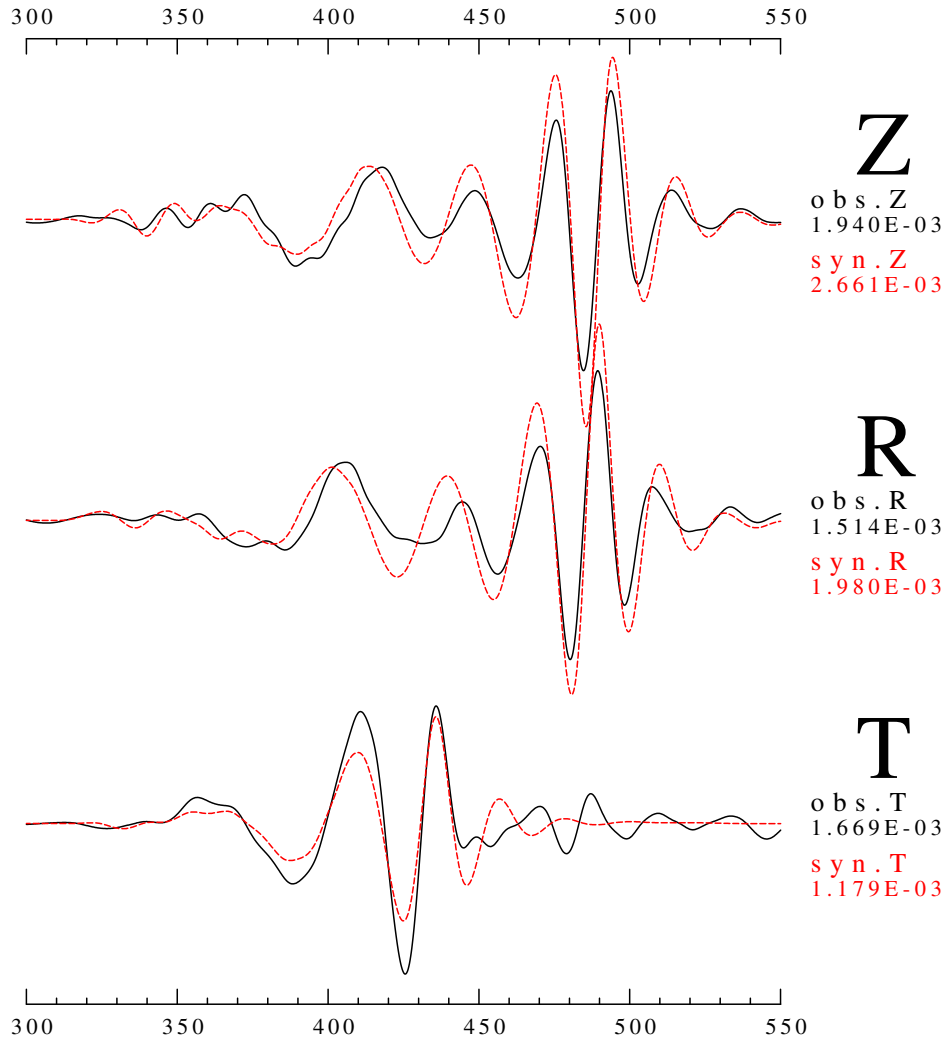
5.20, the single mode display shows a very good first higher mode envelop with a nice tail after 410 seconds. This is consistent with the observed data. It also shows that the amplitude variation is possibly caused by construction and destruction of higher modes. Figure 5.19 shows that the synthetic seismograms generated by the locked mode approximation can match the P_{nl} phase. One important result of waveform modeling shown here is that it demonstrates that a single 1-D model can match both body wave and surface wave waveforms in a regional stable area.

How confident is this model? In this study, the inversions were performed using damped least square method (Marquardt, 1963). The calculation of resolving kernels are straightforward. Figure 5.21 shows the resolving kernels and standard deviation of model parameters. However, the standard deviation bar depends on the damping value used, and does not show any information. On the other hand, the measurements of four GSDFs may provide extra information to indicate the goodness of waveform fit. Figure 5.22 shows the four GSDF measurements for the vertical component Rayleigh wave. The group velocity differential time dTG indicates that predicted Airy phase envelope is 11 seconds slower than observed at a 37 second period. From dTP , it is clear to see that this model may do well in high frequency but the low frequency part is systematically 5 seconds faster than the data. From dTQ , we can see that at a period around 35 seconds, the synthetic seismogram's amplitude is too large. The GSDF measurements are a good indicator of waveform but do not map

TEXAS950414

CCM

DISP



FILTER F_{lo}=0.010 F_{hi}=0.050 (Hz) Norder= 4

LON=-103.327 LAT=30.261 DEPTH= 23.00

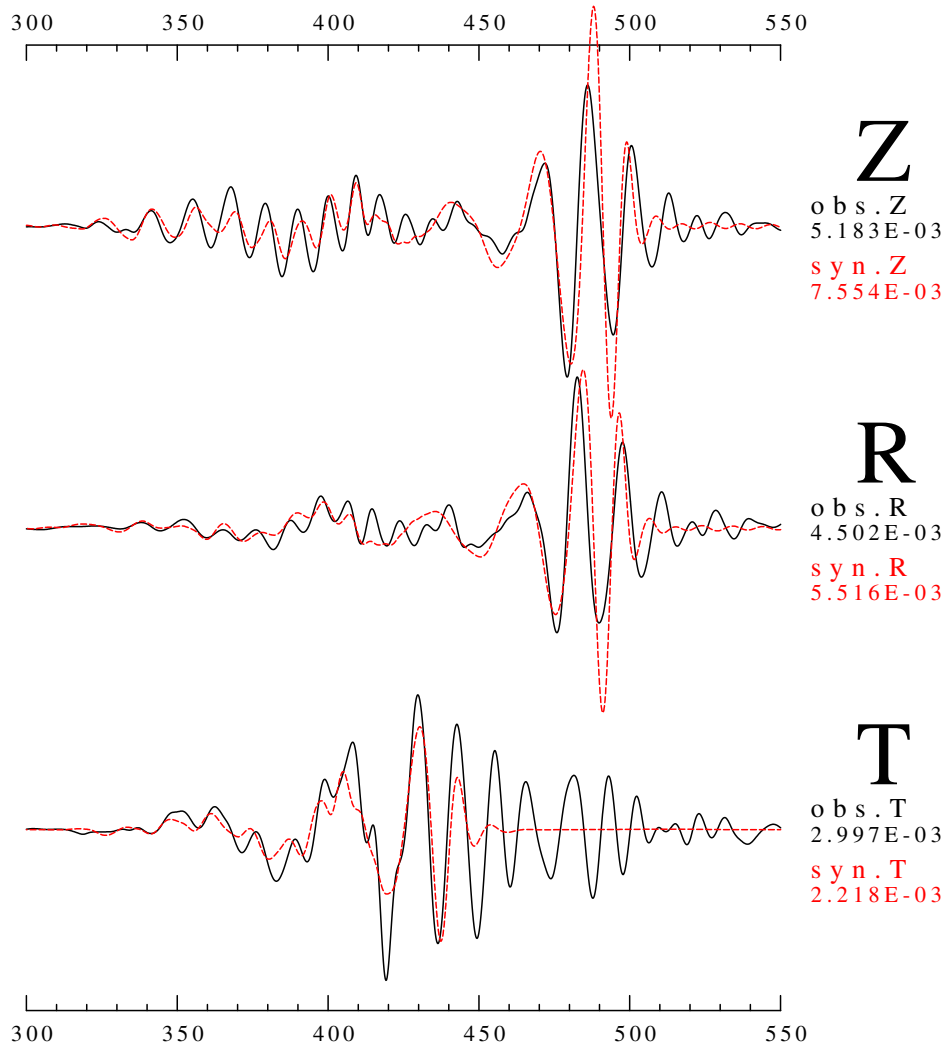
AZ=48.918 BAZ=235.704 DIST= 1408.160

Fig. 5.18a. The waveform fit of the fine-tuning model shown at figure 5.17. Three different frequency ranges are shown: (a) 0.01-0.05 Hz.

TEXAS950414

CCM

DISP



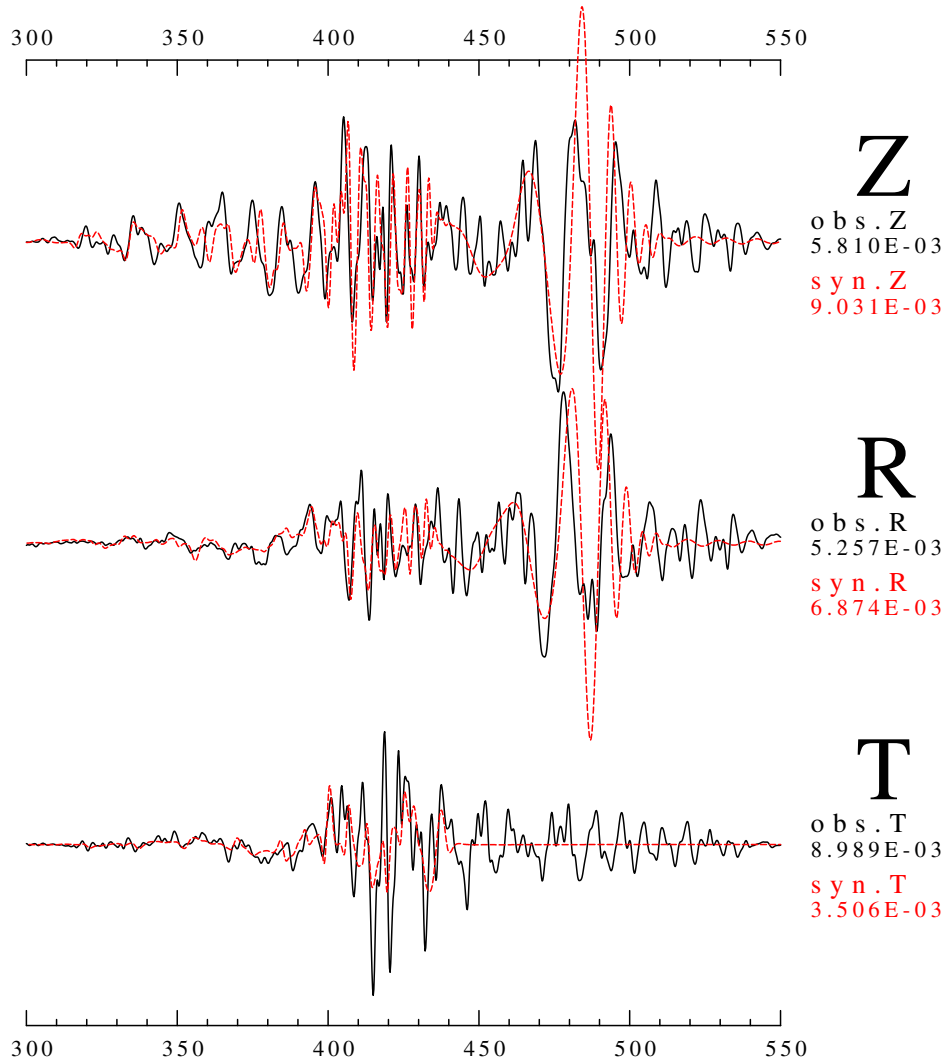
FILTER Flo=0.010 Fhi=0.100 (Hz) Norder= 4

LON=-103.327 LAT=30.261 DEPTH= 23.00

AZ=48.918 BAZ=235.704 DIST= 1408.160

Fig. 5.18b. (Cont'd) (b) 0.01-0.1 Hz.

TEXAS950414 CCM DISP



FILTER Flo=0.010 Fhi=0.500 (Hz) Norder= 4
 LON=-103.327 LAT=30.261 DEPTH= 23.00
 AZ=48.918 BAZ=235.704 DIST= 1408.160

Fig. 5.18c. (Cont'd) (c) 0.01-0.5 Hz.

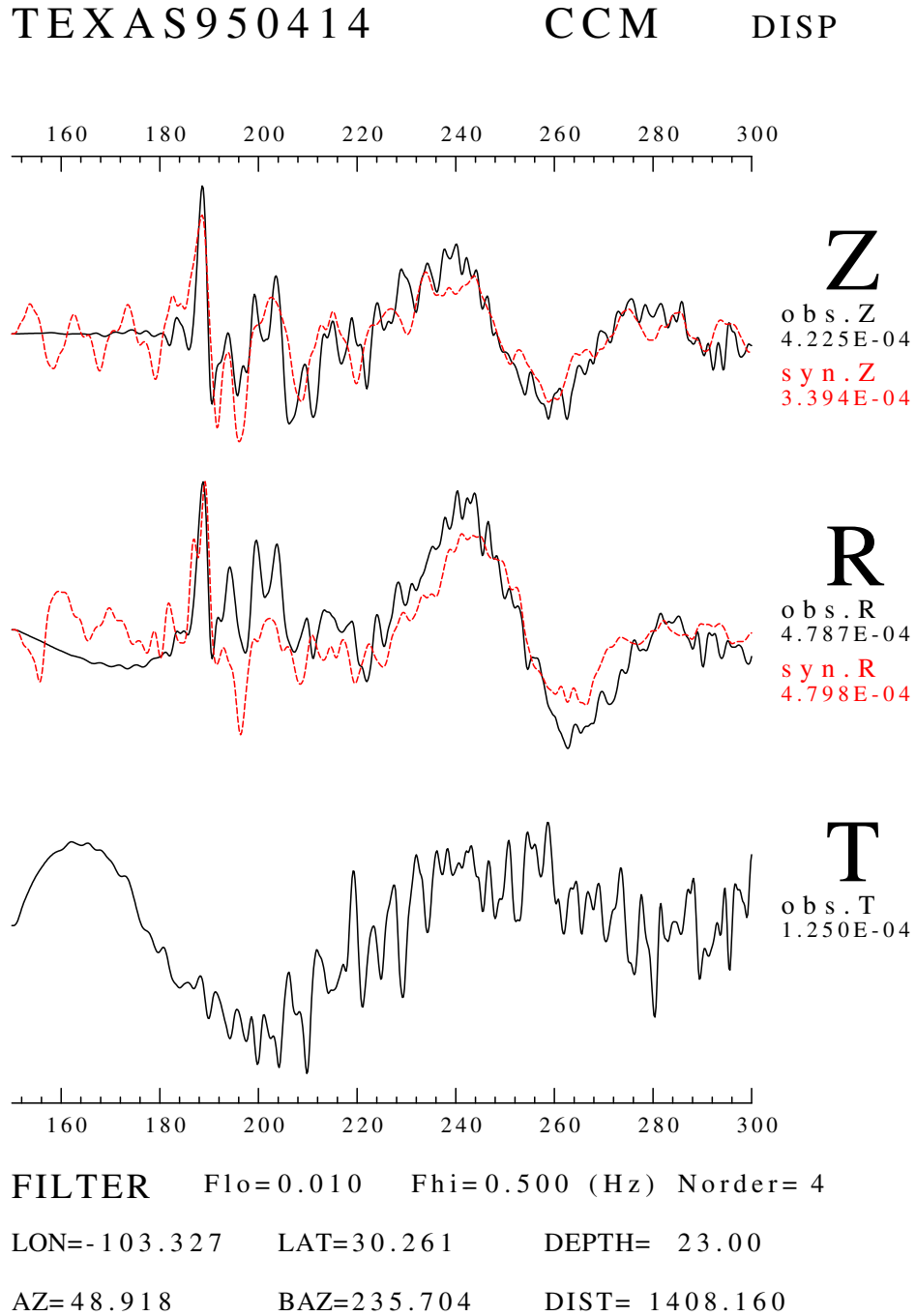
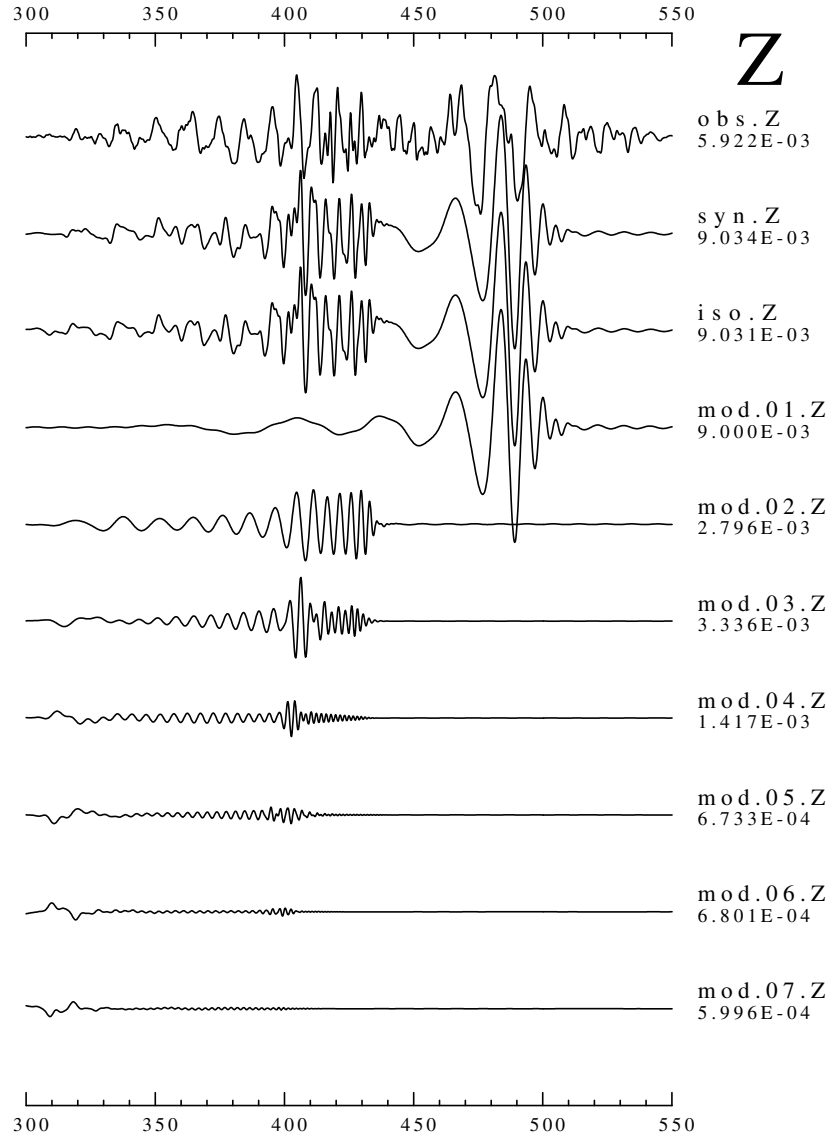


Fig. 5.19. The P_{nl} waveform fit which computed using locked mode approximation for the fine-tuning model shown at figure 5.17.

TEXAS950414

CCM

DISP



FILTER Flo=0.010 Fhi=0.800 (Hz) Norder= 4

LON=-103.327 LAT=30.261 DEPTH= 23.00

AZ=48.918 BAZ=235.704 DIST= 1408.160

Fig. 5.20. The observed, synthetic, and seven single-mode seismograms were shown here.

directly into the velocity-Q model.

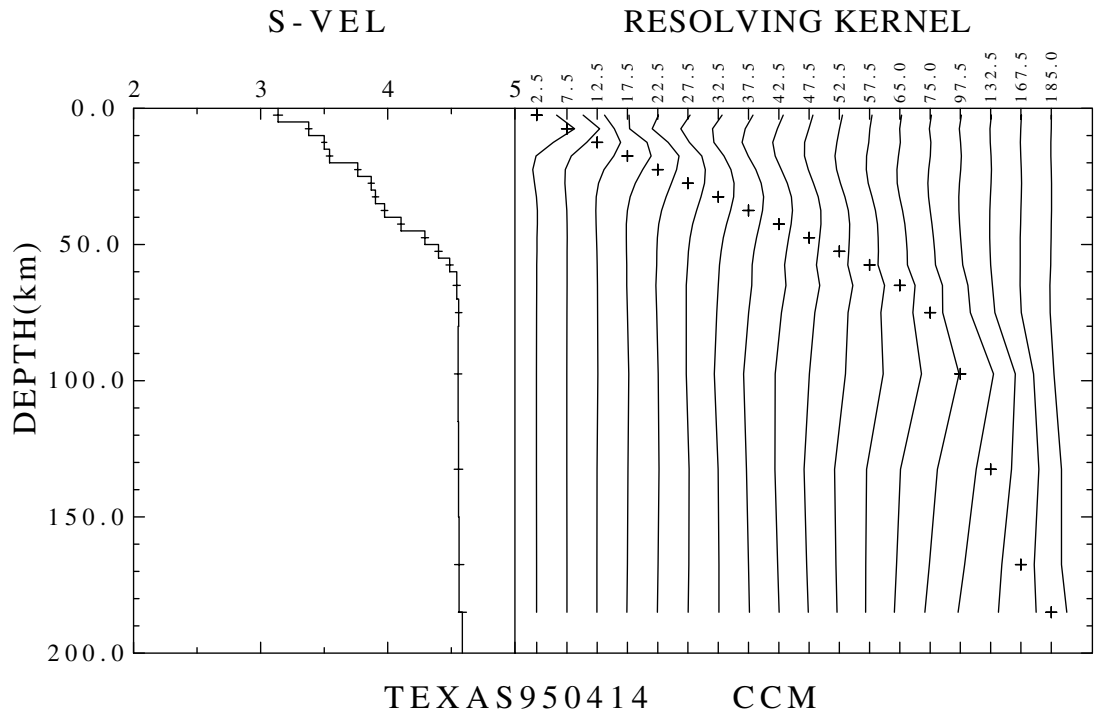


Fig. 5.21. The resolving kernel for the model shown on figure 5.18.

So far, there two hypotheses are proposed to fit the data. The first hypothesis is that a gradient velocity transition zone exists in the uppermost mantle instead of a sharp crust-mantle boundary. The second hypothesis is that the frequency dependent Q for the crust (Mitchell, 1980). We will use another two stations in the same region to search for similar features.

The first station is CBKS. Its group velocity dispersion curve (Figure 5.23) shows almost no interference from noise. The GSDF inversion result is shown in Figure 5.25 and its associated waveform fit is shown in Figure 5.24. The second station used is WMOK. The

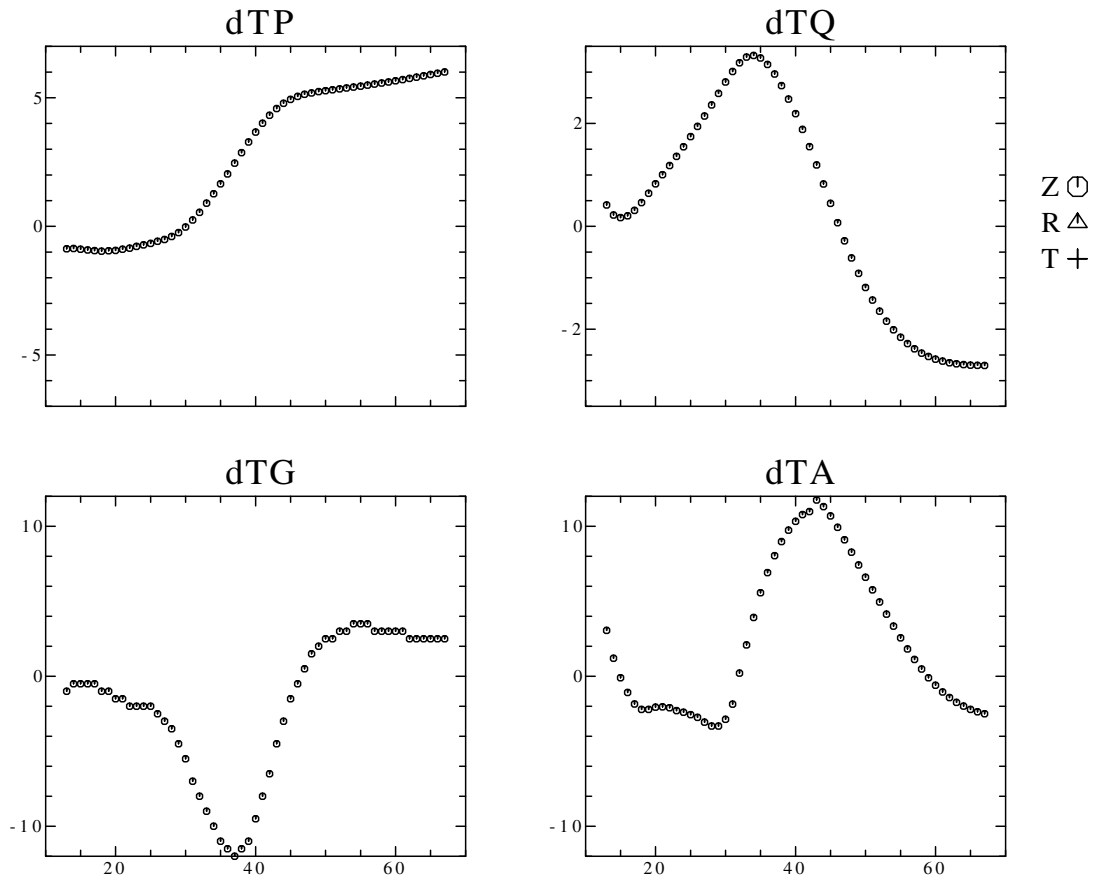


Fig. 5.22. The measurements of four GSDF functionals for the model shown on figure 5.18.

hypocentral distance is very short, only about 650 km. The dispersion curve (Figure 5.26) is not as clean as CBKS, only the 8-30 second fundamental mode can be identified due to a spectral hole near 30 seconds. The waveform fit is shown as Figure 5.27 and the model is shown as Figure 5.28. Although the waveform fits for both CBKS and WMOK are not perfect for higher modes, they do have correct amplitudes. The data do not require frequency dependent Q to fit the amplitudes of both fundamental and higher modes. But compared to CCM,

these two models all have high crustal Q values. There are two possibilities for this:

- (1). The frequency dependent Q behavior is not observable for short distance stations. Also, as noted by Mitchell (1980), frequency dependence of Q could only be observed using higher mode amplitudes at periods less than 4 seconds.
- (2). The observed frequency dependent Q at CCM is an artifact due to improper source radiation pattern which creates large amplitude synthetics and forces the crustal Q to decrease to compensate for this effect and the frequency dependent Q behavior is then required to match the higher mode amplitude.

Although, there is no conclusive answer to this problem, but this question arises when trying to determine fundamental earth structure through waveform modeling.

By comparing models of the crust and upper mantle beneath CCM, CBKS, and WMOK, we see that all three models have a velocity transition zone in the uppermost mantle. Durrheim and Mooney (1994) use seismic and geochemical data to constrain the evolution of Precambrian lithosphere evolution. Their conclusion is that underplating occurs at the Proterozonic, but not at Archean crust-mantle boundaries. The seismic signature of underplating is a basal layer with high P-velocity (7.0-7.6 km/sec). In our study, the source is located between the Proterozonic platform and Rocky mountains, and the stations CCM, CBKS, and WMOK lay inside the Proterozonic platform, therefore the propagation paths sample the relatively uniform

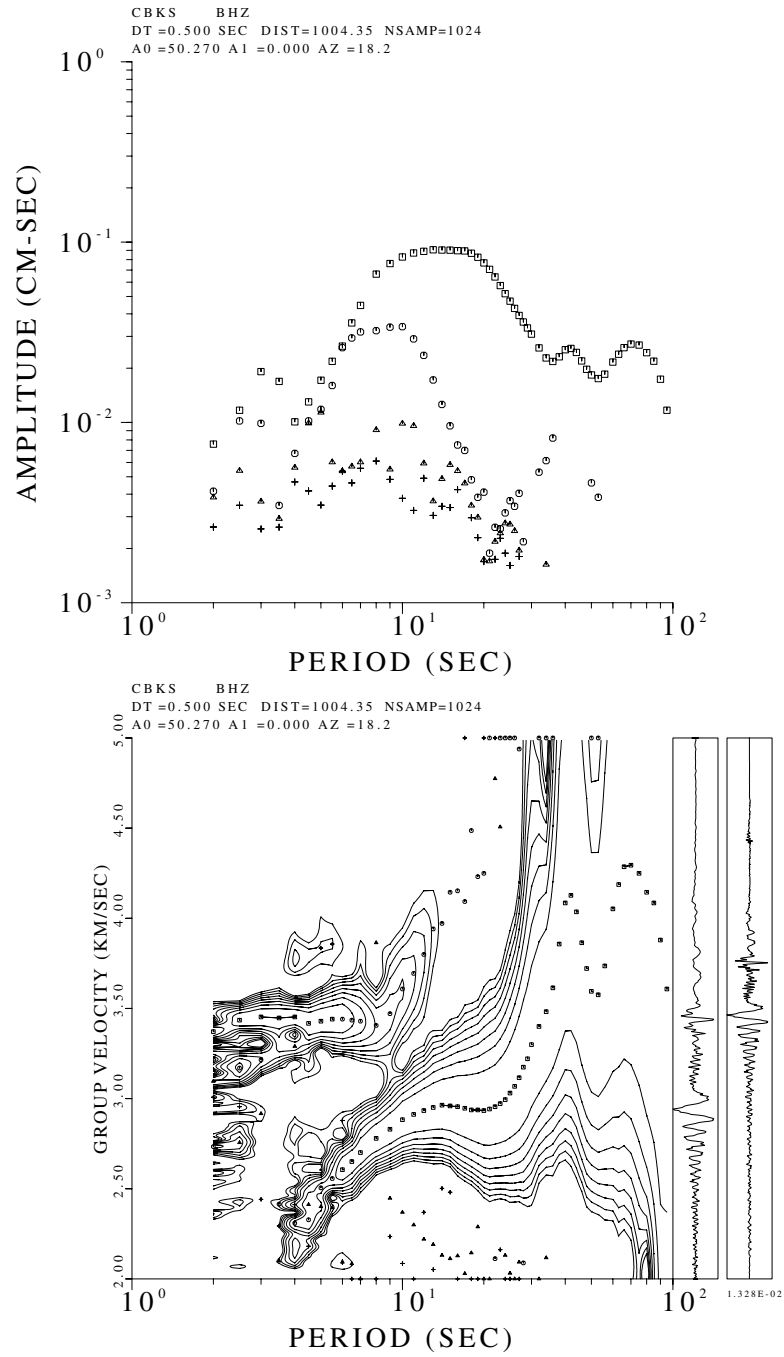
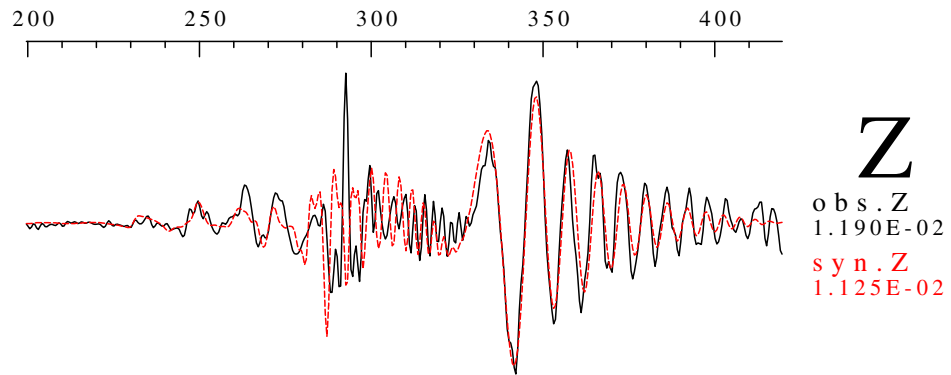


Fig. 5.23. The group velocity dispersion curve and spectrum amplitudes for station CBKS.

TEXAS950414

CBKS

DISP

**R****T**

200 250 300 350 400
FILTER Flo=0.010 Fhi=0.500 (Hz) Norder= 4
 LON=-103.327 LAT=30.261 DEPTH= 23.00
 AZ=18.170 BAZ=200.204 DIST= 1004.352

Fig. 5.24. The waveform fit for station CBKS at frequency band 0.01-0.5 Hz.

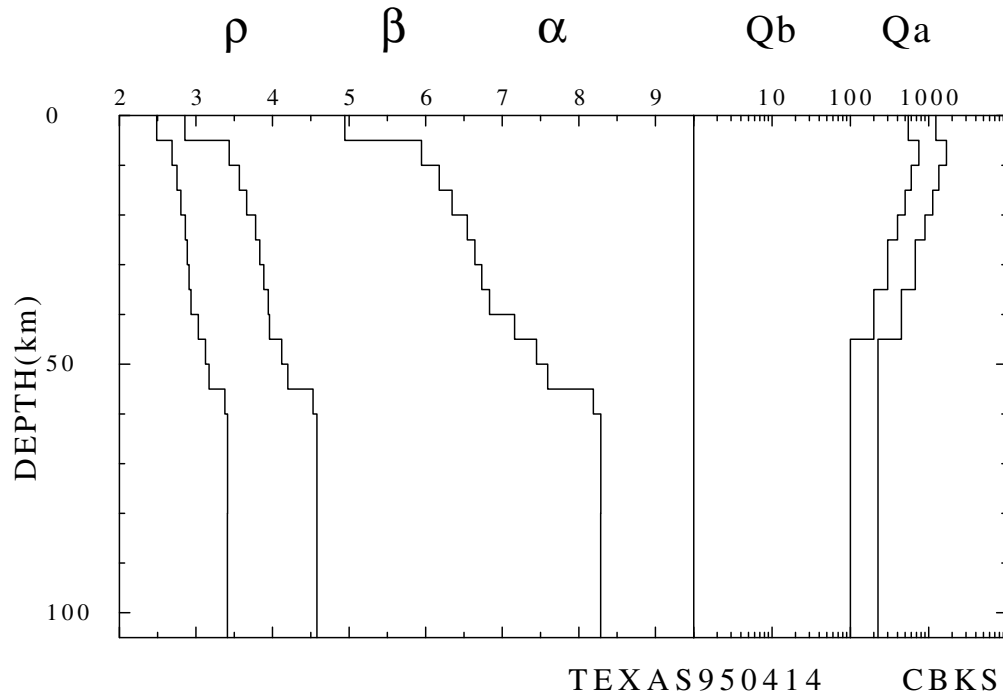


Fig. 5.25. The fine-tuning model for station CBKS which is based on the GSDF inversion result.

platform. With fixed Poisson's ratio in the inversion, the transitional velocity zone between 40 and 60 km shown in each model may be the evidence of an underplating process. It would be interesting to study an Archean region using waveform modeling techniques to see whether a basal layer exists or not.

A question remains unanswered. That is what are those signals that arrive between 430 and 470 seconds on the vertical component CCM data. We have no answer for this. But from Figure 5.9(b), the dispersion curve inversion result, we see a clue.

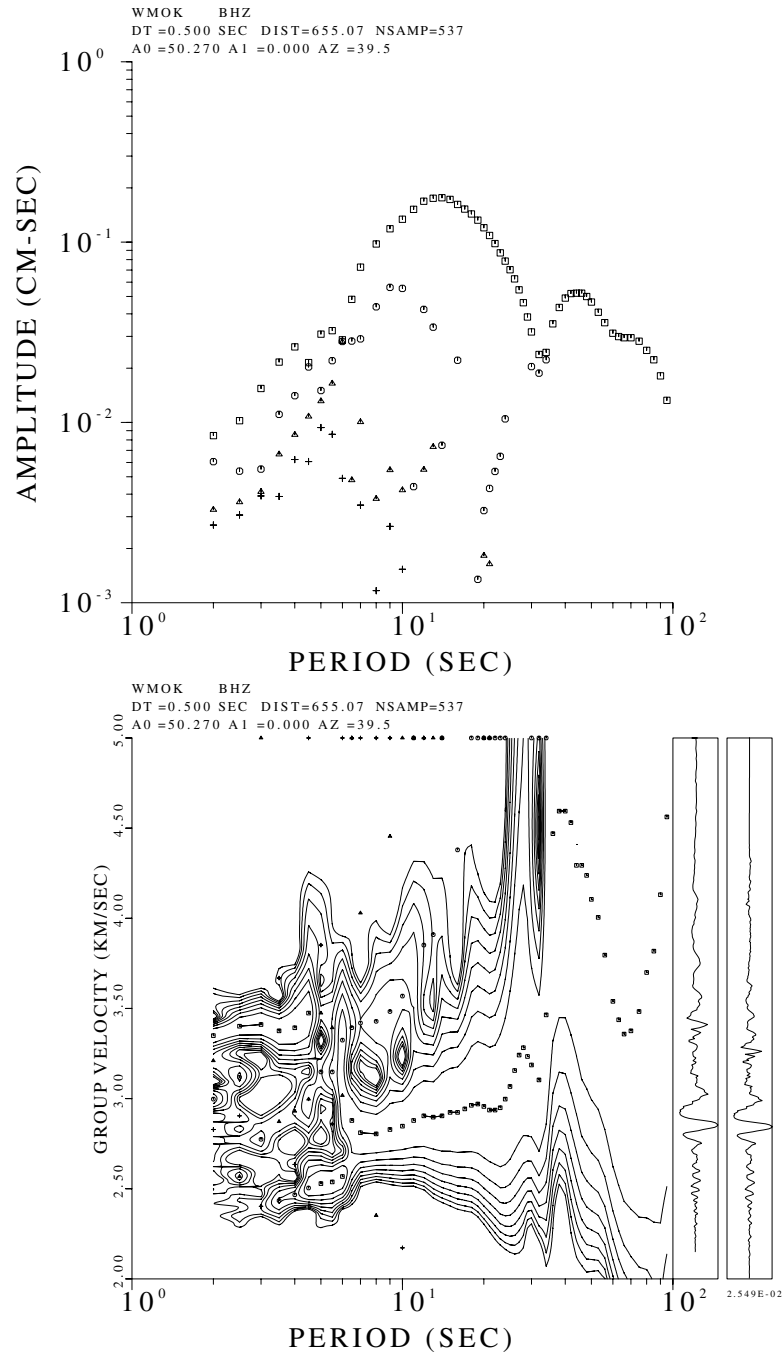


Fig. 5.26. The group velocity dispersion curve and spectral amplitudes for station WMOK.

TEXAS950414

WMOK DISP

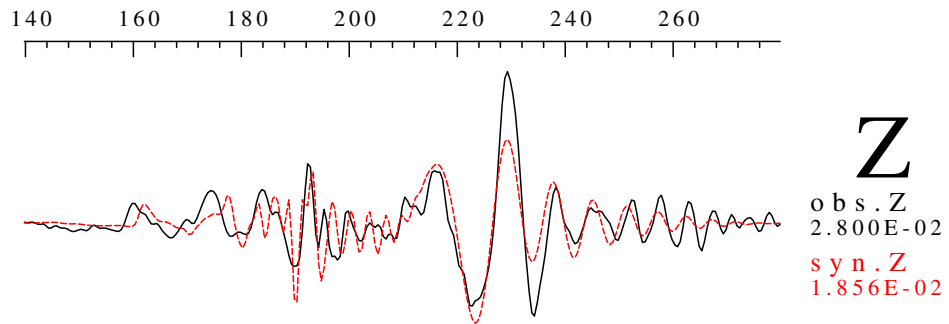
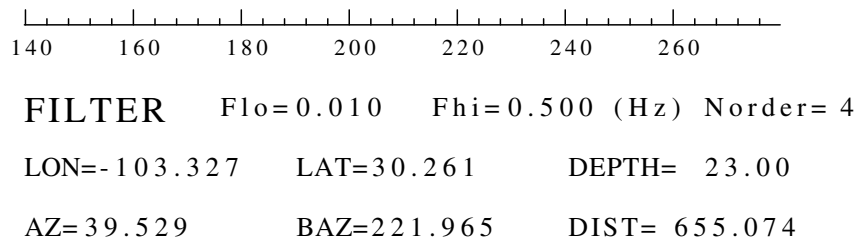
**R****T**

Fig. 5.27. The waveform fit at 0.01-0.5 Hz of station WMOK for the model shown on figure 5.28.

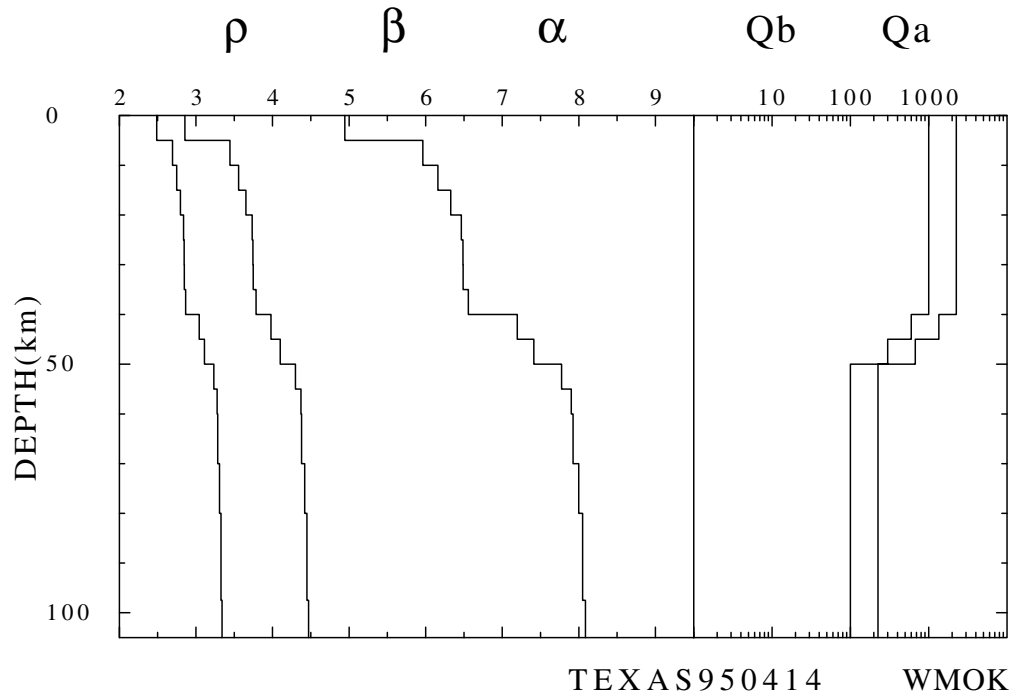


Fig. 5.28. The fine-tuning model for WMOK which based on GSDF inversion result.

From results of reflection and refraction studies of continental lithosphere, it has been observed that a reflective region occurs in the lower crust (e.g. Mooney and Brocher, 1987). Such seismic reflectors can be related to geological interpretations such as thrust stack, duplex, and so on (Hatcher, 1986). Braile and Chiang (1986) conduct numerical experiments to study what kind structure can produce the reflective Moho. Their tests show that a Moho transition zone with many fine layers which have small velocity variations (ZIG-ZAG pattern) is feasible.

During a trial and error modeling process, we manually kept the velocity model as smooth as possible and removed any low velocity

zones. The layer thickness of the model is 5 km for the top 60 km. For such a layer thickness and smooth velocity curve, it will only generate a smooth fundamental mode. Therefore, a fine-layer velocity model with small perturbations is a possible origin for those signals.

5.6 Discussion

In this chapter, we applied four different algorithms to model the surface-wave waveform. The results show that each algorithm can provide different waveform fit result which emphasizes different parts of waveform because of their different criteria and formulations. For example, the GA search algorithm can find models that match the most energetic phase, the fundamental mode in this case, but it lacks the ability to match the other less energetic phases such as higher modes. The reason is simple because of the criteria used. In a similar fashion, the linear waveform inversion is also controlled by the large residuals which might be artifacts caused by improper source description. Using different windows and filters to force the inversion to focus on different part of waveform is a possible solution, but the controlling mechanism will strongly depend on the user's expertise. The traditional dispersion curve inversion also has its own problems such as the accuracy in phase velocity measurements and the data density used in inversion. Like the traditional dispersion curve inversion, GSDF inversion also suffers from a data density problem because both of them utilize the different remeasurements from waveform.

All four algorithms can provide reasonable model with waveform fits as good as up to 0.1 Hz. However, since more structural information is revealed in higher frequency contents, the design of a model refining algorithm will be the task for seismologists. From this study, we believe that a multi-isolation-filters GSDF inversion algorithm may be a possible improvement.

What is a good criterion for waveform modeling? So far, there is no answer to this question. But we know what are not good criteria. To measure a simple pulse, several widely used criteria like cross-correlation and L2-norm can serve the purpose. However, to judge the similarity of a complicated waveform, all these criteria will not give a satisfactory answer. The cross-correlation can only tell the similarity of the most energetic phase. The L2-norm will behave as a oscillatory wavelet, like cross-correlation, when the cycle-skipping problem is involved. Therefore, we believe that the success of waveform inversion algorithms will depend on how the criteria have been designed.

When a good model is obtained, without tectonic interpretation, it is just a model. We would like outline the possible contributions from interpreting waveform modeling results. First we would ask what is the physical process happen that formed the continental lithosphere? So far, evidence from all branches of geoscience is too sparse to provide a complete answer. So we will ask what kind seismic evidence can we provide on this topic?

Jordan (1975) proposed the continental tectosphere hypothesis. The continental tectosphere has a cool thick root (up to 400 km).

Using numerical modeling, the influence of such thick tectosphere on the geodynamic processes of the mantle and on the plate motion has been modeled (e.g. Stoddard and Abbott, 1996). Therefore, the first question is how to determine the thickness of the continental lithosphere?

As described previously, the evolutionary model of Precambrian lithosphere proposed by Durrheim and Mooney (1994) suggests that the Archean lithosphere is thicker than Proterozonic lithosphere. Some mantle processes, such as underplating, only happened on the Proterozonic crust-mantle boundary. Therefore, the second question will be: Can we observe the fundamental difference of these two regions from seismological studies?

Sato *et al.* (1989) suggested that seismic velocity and Q models can be used to estimate the temperature gradient and partial melt fraction in the upper mantle. The temperature gradient can be inferred from waveform modeling results. This could be another indirect constraint besides the heat flow measurements for continental lithosphere evolution.

Anisotropy is a commonly observed phenomenon in the Earth. By observing the SKS and SKKS splitting, Silver and Chan (1991) suggested that the anisotropy is caused by the subcontinental upper mantle deformations during the different tectonic episodes. Therefore, anisotropy can be another indicator to the evolutionary history of the continental lithosphere.

CHAPTER 6

DISCUSSION AND CONCLUSION

In this study, several algorithms have been used to model surface-wave waveforms. Each algorithm has different advantages and weaknesses. One of the most important conclusions is that, through careful waveform modeling, both body waves and surface waves can be modeled using 1-D model. Waveform modeling can also provide more detailed structure information than can be obtained by fitting gross data sets such as surface wave dispersion data.

The differences among tested algorithms are mainly in the "data" preparation for inversion. The linear inversion scheme used requires no *a priori* information (Lawson and Hanson, 1974). Issues associated with incorporating *a priori* information (Tarantola and Valette, 1982), and constrained inversion (Carrion, 1989) have not been tested in this study.

Another issue related to inversion schemes is that of the weighting functions. For linear inversion, each parameter acts acting as a free parameter, and the inversion will become unstable due to the parameterization and data density used in inversion. Russell (1987) introduced a "differential" weighting function to constrain the

inversion. However, when dealing with teleseismic records or a many layers parameterization, this weighting function will not be able to avoid producing some funny low-velocity zones in model. Therefore, a Nolet style weighting function (Nolet, 1990; Snoke *et al.*, 1997) could be tested in the future to see can it stabilize the inversion result.

What can be done in future? For methodology improvement consider the following: First of all, from this study, we notice that the envelope of surface wave is a good indicator for Q structure. We believe formulating an algorithm to invert Q structure from different bandpassed surface wave envelopes will be a useful tool to study upper mantle Q structure. A similar idea has already been reported by Cara *et al.* (1987) and Nolet (1990). Second, a fine tuning algorithm is needed to match the less energetic higher mode waveforms without destroy the fit to the well matched fundamental mode. We believe it can be implemented by constructing a multiple isolation filters in the GSDF inversion scheme which will utilize information from different wavegroups simultaneously. Another alternative will be a multi-windowed linear waveform inversion. Implementation of an inversion for an anisotropic model is required. Finally, invent an inversion technique using both both surface and body waves.

For possible uses of these algorithms consider the following: We strongly feel that waveform inversion techniques can be very powerful tools to study regional events. First, regional events have their energy concentrated in short time windows which may have less influence by multi-pathing effects. The GA search results shown in Chapter 4

support this argument. Second, the propagation path is more likely travel through the same geological region. Although such modeling may only provide information on average crustal structure, but it can be applied to many regions. It would be interesting to apply waveform inversion methods to smaller regions.

With respect to global search techniques: The major thing to be done is to find a better criteria of waveform fit. An additional effort is required to combine GA search and gradient information to speed up the process. This will increase the application of global search technique.

BIBLIOGRAPHY

- Ammon, C. J., G. E. Randall, and G. Zandt (1990). On the nonuniqueness of receiver function inversions, *J. Geophys. Res.*, **95**, 15303-15318.
- Basu, A., and L. N. Frazer (1990). Rapid determination of the critical temperature in simulated annealing inversion, *Science*, **249**, 1409-1412.
- Braile, L. W. (1973). Inversion of crustal seismic refraction and reflection data, *J. Geophys. Res.*, **78**, 7738-7744.
- Braile, L. W., and C. S. Chiang (1986). The continental Mohorovicic discontinuity: results from near-vertical and wide-angle seismic reflection studies, in *Reflection Seismology: A Global Perspective*, (eds. M. Barazangi and L. Brown), Geodynamics Series V. 13, Am. Geophys. Union.
- Bunks, C., F. M. Saleck, S. Zaleski, and G. Chavent (1995). Multiscale seismic waveform inversion, *Geophysics*, **60**, 1457-1473.
- Carrion, P. M. (1989). Generalized non-linear elastic inversion with constraints in model and data spaces, *Geophys. J.*, **96**, 151-162.
- Cara, M., and J. J. Leveque (1987). Waveform inversion using secondary observables, *Geophys. Res. Lett.*, **14**, 1046-1049.
- Cruse, E., A. Pica, M. McDonald, and A. Tarantola (1990). Robust elastic nonlinear waveform inversion: application to real data, *Geophysics*, **55**, 527-538.
- Dreger, D. S., and D. V. Helmberger (1993). Determination of source parameters at regional distances with three-component sparse network data, *J. Geophys. Res.*, **98**, 8107-8125.

- Durrheim, R. J., and W. D. Mooney (1994). Evolution of the Precambrian lithosphere: seismological and geochemical constraints, *J. Geophys. Res.*, **99**, 15359-15374.
- Dziewonski, A. M., S. Bloch, and M. Landisman (1969). A technique for the analysis of transient seismic signals, *Bull. Seis. Soc. Am.*, **59**, 427-444.
- Dziewonski, A. M., and D. L. Anderson (1981). Preliminary reference earth model, *Phys. Earth Planet. Int.*, **25** 297-356.
- Dziewonski, A. M., T-A. Chou, and J. H. Woodhouse (1981). Determination of earthquake source parameters from waveform data for studies of global and regional seismicity, *J. Geophys. Res.*, **86**, 2825-2852.
- Dziewonski, A. M., and J. H. Woodhouse (1983). An experiment in systematic study of global seismicity: centroid-moment tensor solutions for 201 moderate and large earthquakes of 1981, *J. Geophys. Res.*, **88**, 3247-3271.
- Dziewonski, A. (1984). Mapping the lower mantle: determination of lateral heterogeneity in P velocity up to degree and order 6, *J. Geophys. Res.*, **89**, 5929-5952.
- Ekstrom, G (1996). Studying global seismicity, *EOS*, Trans. Am. Geophys. Union, **77**, F47.
- Fan, G. and T. Wallace (1991). The determination of source parameters for small earthquakes from a single, very broadband seismic station, *Geophys. Res. Lett.*, **18**, 1385-1388.
- Gaherty, J. B., and T. H. Jordan (1995). Lehmann discontinuity as the base of an anisotropic mechanical boundary layer beneath continents, *Science*, **268**, 1468-1471.
- Gaherty, J. B., T. H. Jordan, and L. S. Gee (1996). Seismic structure of the upper mantle in a central Pacific corridor, *J. Geophys. Res.*, **101**, 22291-22309.
- Gee, L. S., and Jordan, T. H. (1988). Polarization anisotropy and fine-scale structure of the Eurasian upper mantle, *Geophys. Res. Lett.*, **15**, 824-827.

- Gee, L. S., and Jordan, T. H. (1992). Generalized seismological data functionals, *Geophys. J. Int.*, **111**, 363-390.
- Gomberg, J. S., and T. G. Masters (1988). Waveform modeling using locked-mode synthetic and differential seismograms: application to determination of the structure of Mexico, *Geophys. J.*, **94**, 193-218.
- Grand, S. P., and D. V. Helmberger (1984). Upper mantle shear structure of North America, *Geophys. J. R. astr. Soc.*, **76**, 399-438.
- Hatcher, R. D. (1986). Interpretation of seismic reflection data in complexly deformed terranes: a geologist's perspective, in *Reflection Seismology: The Continental Crust*, (ed. M. Barazangi and L. Brown), Geodynamics Series, V. 14, Am. Geophys. Union.
- Herrin, E., and T. Goforth (1977). Phase-matched filters: application to the study of Rayleigh waves, *Bull. Seis. Soc. Am.*, **67**, 1259-1275.
- Herrmann, R. B. (1973). Some aspects of band-pass filtering of surface waves, *Bull. Seis. Soc. Am.*, **63**, 663-671.
- Herrmann, R. B. (1974). Surface wave generation by central United States earthquakes, Ph.D. Dissertation, Saint Louis University.
- Huang, H., C. Spencer, and A. Green (1986). A method for the inversion of refraction and reflection travel times for laterally varying velocity structures, *Bull. Seis. Soc. Am.*, **76**, 837-846.
- Jordan, T. H. (1975). The continental tectosphere, *Rev. Geophys. Space Phys.*, **13**, 1-12.
- Keilis-Borok, V. I., and T. B. Yanovskaja (1967). Inverse problem of seismology (structural review), *Geophys. J. R. astr. Soc.*, **13**, 223-234.
- Kennett, B. L. N., and E. R. Engdahl (1991). Traveltimes for global earthquake location and phase identification, *Geophys. J. Int.*, **105**, 429-465.
- Koren, Z., K. Mosegaard, E. Landa, P. Thore, and A. Tarantola (1991). Monte Carlo estimation and resolution analysis of seismic background velocities, *J. Geophys. Res.*, **96**, 20289-20299.

- Lawson, C. L. and R. J. Hanson (1974). *Solving least squares problems*, Prentice-Hall Inc., New Jersey.
- Lerner-Lam, A. L. and T. H. Jordan (1983). Earth structure from fundamental and higher-mode waveform analysis, *Geophys. J. R. astr. Soc.*, **75**, 759-797.
- Lerner-Lam, A. L., and T. H. Jordan (1987). How thick are the continents?, *J. Geophys. Res.*, **92**, 14007-14026.
- Mao, W. J., G. F. Panza, and P. Suhadolc (1994). Linearized waveform inversion of local and near-regional events for source mechanism and rupturing processes, *Geophys. J. Int.*, **116**, 784-798.
- Marquardt, D. W. (1963). An algorithm for least-squares estimation of nonlinear parameters, *J. Soc. Indust. Appl. Math.*, **11**, 431-441.
- Masters G., T. H. Jordan, P. G. Silver, and F. Gilbert (1982). Aspherical earth structure from fundamental spheroidal-mode data, *Nature*, **298**, 609-613.
- Mitchell, B. J. (1980). Frequency dependence of shear wave internal friction in the continental crust of eastern North America, *J. Geophys. Res.*, **85**, 5212-5218.
- Mooney, W. D. and T. M. Brocher (1987). Coincident seismic reflection/refraction studies of the continental lithosphere: a global review, *Rev. Geophys.*, **25**, 723-742.
- Mooney, W. D., G. Laske, and G. Masters (1996). Crust 5.1 : a revised global crustal model at $5^\circ \times 5^\circ$, *EOS*, Trans. Am. Geophys. Union, **77**, F483.
- Mora, P. (1987). Nonlinear two-dimensional elastic inversion of multi-offset seismic data, *Geophysics*, **52**, 1211-1228.
- Nakanishi, I., and D. Anderson (1983). Measurements of mantle wave velocities and inversion for lateral heterogeneity and anisotropy-I. analysis of great circle phase velocities, *J. Geophys. Res.*, **88**, 10267-10283.
- Nakanishi, I., and D. Anderson (1984). Measurements of mantle wave velocities and inversion for lateral heterogeneity and anisotropy-II.

analysis by the single-station method, *Geophys. J. R. astro. Soc.*, **78**, 573-617.

Nataf, H.-C., I. Nakanishi, and D. Anderson (1986). Measurements of mantle wave velocities and inversion for lateral heterogeneities and anisotropy-III. inversion, *J. Geophys. Res.*, **91**, 7261-7307.

Nolet, G. (1990). Partitioned waveform inversion and two-dimensional structure under the network of autonomously recording seismographs, *J. Geophys. Res.*, **95**, 8499-8512.

Nowack, R. L., and L. W. Braile (1993). Refraction and wide-angle reflection tomography: theory and results, in *Seismic Tomography: Theory and Practice.*, (eds H. M. Iyer and K. Hirahara), Chapman & Hall, London.

Pan, G. S., and R. A. Phinney (1989). Full-waveform inversion of plane-wave seismograms in stratified acoustic media: applicability and limitations, *Geophysics*, **54**, 368-380.

Press, F. (1968). Earth models obtained by Monte Carlo inversion, *J. Geophys. Res.*, **73**, 5223-5234.

Rodi, W. L., Glover, P., Li, T. M. C. & Alexander, S. S., 1975. A fast, accurate method for computing group-velocity partial derivatives for Rayleigh and Love modes. *Bull. Seis. Soc. Am.*, **65**, 1105-1114.

Rothman, D. H. (1985). Nonlinear inversion, statistical mechanics, and residual statics estimation, *Geophysics*, **50**, 2784-2796.

Rothman, D. H. (1986). Automatic estimation of large residual statics corrections, *Geophysics*, **51**, 332-346.

Russell, D. R. (1987). Multi-channel processing of dispersed surface waves, Ph.D. Dissertation, Saint Louis University.

Sambridge, M. and G. Drijkoningen (1992). Genetic algorithms in seismic waveform inversion, *Geophys. J. Int.*, **109**, 323-324.

Sambridge, M., and K. Gallagher (1993). Earthquake hypocenter location using genetic algorithms, *Bull. Seis. Soc. Am.*, **83**, 1467-1491.

Sato, H., I. S. Sacks, and T. Murase (1989). The use of laboratory

velocity data for estimating temperature and partial melt fraction in low-velocity zone: comparison with heat flow and electrical conductivity studies, *J. Geophys. Res.*, **94**, 5689-5704.

Sen, M. K. and P. L. Stoffa (1992). Rapid sampling of model space using genetic algorithms: examples from seismic waveform inversion, *Geophys. J. Int.*, **108**, 281-292.

Shibutani, T., M. Sambridge, and B. Kennett (1996). Genetic algorithm inversion for receiver functions with application to crust and uppermost mantle structure beneath eastern Australia, *Geophys. Res. Lett.*, **23**, 1829-1832.

Silver, P. G., and W. W. Chan (1991). Shear wave splitting and subcontinental mantle deformation, *J. Geophys. Res.*, **96**, 16429-16454.

Sipkin, S. A. (1986). Interpretation of non-double-couple earthquake mechanisms derived from moment tensor inversion, *J. Geophys. Res.*, **91**, 531-547.

Snoke, J. A. and D. E. James (1997). Lithospheric structure of the Chaco and Parana basins of south America from surface-wave inversion, *J. Geophys. Res.*, **102**, 2939-2951.

Stein, R. S., G. C. P. King, and J. Lin (1992). Change in failure stress on the southern San Andreas fault system caused by the 1992 magnitude=7.4 Landers earthquake, *Nature*, **258**, 1328-1332.

Stoddard, P. R., and D. Abbott (1996). Influence of the tectosphere upon plate motion, *J. Geophys. Res.*, **101**, 5425-5433.

Stoffa, P. L. and M. K. Sen (1991). Nonlinear multiparameter optimization using genetic algorithms: inversion of plane-wave seismograms, *Geophysics*, **56**, 1794-1810.

Su, W.-J. and A. M. Dziewonski (1992). On the scale of mantle heterogeneity, *Phys. Earth and Planet. Int.*, **74**, 29-54.

Tarantola, A., and B. Valette (1982). Generalized non-linear inversion problems solved using the least-squares criteria, *Rev. Geophys. Space Phys.*, **20**, 219-232.

Thio, H. K., and H. Kanamori (1995). Moment-tensor inversions for

local earthquakes using surface waves recorded at TERRAScope, *Bull. Seis. Soc. Am.*, **85**, 1021-1038.

- Vidale, J. E., and D. V. Helmberger (1992). Elastic finite-difference modeling of the 1971 San Fernando, California earthquake, *Bull. Seis. Soc. Am.*, **78**, 122-141.
- Wang, C. Y. (1981). Wave theory for seismogram synthesis, Ph.D. Dissertation, Saint Louis University.
- Wessel, P., and W. H. F. Smith (1991). Free software help map and display data, *EOS Trans. AGU*, **72**, 445-446.
- Woodhouse, J., and A. Dziewonski (1984). Mapping the upper mantle: three-dimensional modeling of earth structure by inversion of seismic waveforms, *J. Geophys. Res.*, **89**, 5953-5986.
- Woodward, R. L., and G. Masters (1991). Global upper mantle structure from long-period differential travel times, *J. Geophys. Res.*, **96**, 6351-6377.
- Zelt, C. A. and R. B. Smith (1992). Seismic traveltime inversion for 2-D crustal velocity structure, *Geophys. J. Int.*, **108**, 16-34.
- Zhang, Y. S. and T. Tanimoto (1992). Ridges, hotspots and their interaction as observed in seismic velocity maps, *Nature*, **355**, 45-49.
- Zhou, L-S., and D. V. Helmberger (1991). Broadband modeling along a regional shield path, Harvard recording of Saguenay earthquake, *Geophys. J. Int.*, **105**, 301-312.
- Zhou, L-S., and D. V. Helmberger (1994). Source estimation from broadband regional seismograms, *Bull. Seis. Soc. Am.*, **84**, 91-104.
- Zhu, L., and D. V. Helmberger (1996). Advancement in source estimation techniques using broadband regional seismograms, *Bull. Seis. Soc. Am.*, **86**, 1634-1641.

VITA AUCTORIS

Tao-Ming Chang was born in Taiwan on August 16, 1966. He attended the National Central University, Chung-Li, Taiwan, from 1985-1989, and received his B.S. degree in Geophysics in 1989. After two years of military duty, he became a graduate student and research assistant in Department of Earth and Atmospheric Science of Saint Louis University. In 1993, he received his Master of Professional Geophysics degree, and since 1993 he has been pursuing a Ph. D. degree in Geophysics.